Fundamentals of Cavity Formation in α-Fe and Fe-Cr Alloys

A Dissertation Presented for the

Doctor of Philosophy

Degree

The University of Tennessee, Knoxville

Yan-Ru Lin

December 2021

To my wife, I-Hsuan Chen, and to my parents, Shun-Fu Lin and Shu-Hua Lu, who made everything possible.

Acknowledgments

Many people have provided assistance and encouragement during the course of my thesis study. This dissertation is the result of many experiences I have encountered at the University of Tennessee, the Joint Institute for Advanced Materials, Oak Ridge National Lab, Argonne National Lab, National Tsing Hua University, the University of Michigan, and the City University of Hong Kong from dozens of remarkable individuals who I wish to acknowledge.

First and foremost, I would like to express my sincere appreciation for the guidance, patience, and knowledge given by my advisor, Prof. S.J. Zinkle. I would also like to thank Dr. A. Bhattacharya for his advice and constructive criticism. Acknowledgments are also due to Prof. J.J. Kai for the TEM and FIB facility support. I am greatly appreciative of the support given to me by the thesis committee, Drs. R.E. Stoller, B.D. Wirth, W.J. Weber, and H. Xu for their insightful comments and encouragement. Special thanks to the past and present members of Dr. Zinkle's research group for their valuable discussions and assistance. These include Drs. T. Yang, S. Agarwal, C. Li, P.J. Doyle, J. Brechtl, T. Smith, A. Terricabras, L. Wang, C.P. Massey. I would also like to thank Y. Zhao, Y. Li, T. Austin, S. Levine, P. Zhu, and T. Duffin for their assistance.

The financial support of the United States Department of Energy, the University of Tennessee, and the State of Tennessee and Tennessee Higher Education Commission is greatly appreciated.

Abstract

Ferritic-martensitic steels are attractive candidate materials for fusion and advanced fission reactors primarily due to their low swelling characteristic, attractive thermo-mechanical properties, and the potential for development of nanostructured ferritic alloys. However, significant discrepancies exist regarding the effect of solutes and irradiation temperature on cavity swelling under ion versus neutron irradiation conditions. Several mechanisms have been proposed that may affect cavity swelling, but no general theory or model has received complete acceptance to explain these phenomena.

To better understand the formation of cavities in ferritic steels, we have performed multi-temperature (400-550°C) single-beam and simultaneous dual-beam irradiations (ex-situ and in-situ) on a series of ultra-high purity Fe and Fe-Cr alloys (3-14 wt% Cr), as well as nanostructured alloys. Helium production rates of 0.1, 10, and 50 appm He/dpa were selected to examine the He effects for fission- and fusion-relevant conditions. Transmission electron microscopy was used to characterize the microstructures in more than 50 different irradiated samples. As a complement to the ex-situ irradiated samples, real-time dynamic formation and evolution of defects were performed in an in-situ ion irradiation TEM facility. Atom probe tomography was used to examine the formation of Cr-rich alpha prime precipitates.

The relative importance of the solute content, irradiation temperature, sink strength and He/dpa on cavity swelling was investigated and discussed. Cavities were observed in all the irradiated samples between 400-550°C. We show that the narrow temperature range of observable cavities reported in prior ion irradiation studies is likely an artifact of the near-surface and implanted ion effects due to the use of insufficiently high ion energies. The peak swelling temperature was noticeably higher for the Fe-Cr alloys than pure Fe. A higher He/dpa level resulted in a higher peak swelling temperature for pure Fe. Bimodal size distribution of cavities was only observed in the 10 and 50 appm He/dpa irradiated samples. Peak cavity swelling occurs at intermediate He production rate ~10 appm He/dpa. Swelling as a function of Cr content is non-monotonic and depends on the ratio of biased

to neutral sink strength, which is likely associated with solute trapping of defects and the formation of α’ precipitates. Helium concentrations up to ~1 at% were well managed in nanostructured alloys with a high density of nanoparticles.

Table of Contents

List of Tables

List of Figures

Chapter 1
Introduction and General Information

Radiation damage in fission reactors and proposed fusion reactor designs can significantly change the property of the surrounding structural materials. Generally, there are five key radiation damage degradation processes [1] that can occur in structural materials, including radiation hardening and embrittlement, phase instabilities due to the radiation-induced segregation, radiation creep that adds in addition to regular thermal creep, volumetric swelling due to void formation, and high-temperature helium embrittlement. Usually, these effects, in turn, degrade the mechanical properties and shorten the lifetime of the material. Collectively, the first and last phenomena tend to define a temperature window over which the material might be usable. The estimated operating temperature windows for a few structural materials in nuclear energy systems are shown in Figure 1.1. This study focuses on the ferritic-martensitic (FM) alloys and nano-structured ferritic steels (NFAs), such as ODS steels.

Apart from the proposed fusion designs, international cooperation has selected six Generation IV (Gen-IV) advanced fission reactor concepts (including Molten Salt Reactor (MSR), Very High-Temperature Reactor (VHTR), Super Critical Water Reactor (SCWR), Lead Fast Reactor (LFR), Gas Fast Reactor (GFR), and Sodium Fast Reactor (SFR)) to improve the safety, nuclear waste management, and power conversion efficiency of typical light-water reactors [2]. The Gen-IV nuclear reactor designs require demanding operation conditions such as very high irradiation temperatures, high fluences of fast neutrons, and corrosive environments. Figure 1.2 shows the predicted displacement damage and irradiation temperature for structural materials of current and proposed fission and fusion reactors [3]. Structural materials in fusion reactors are expected to suffer more severe displacement damage than fission reactors. In terms of neutron spectrum energy, fission neutrons are predominantly between 0.1-2 MeV, while fusion neutrons are ~14 MeV. The latter energy is well above the threshold energy of (n, α) reactions in iron (~5 MeV). This leads to different helium generation rates for fusion environment (~10 appm He/dpa) and fast fission reactors (~0.1 appm He/dpa). For FM steels, a comparison of the transmutant

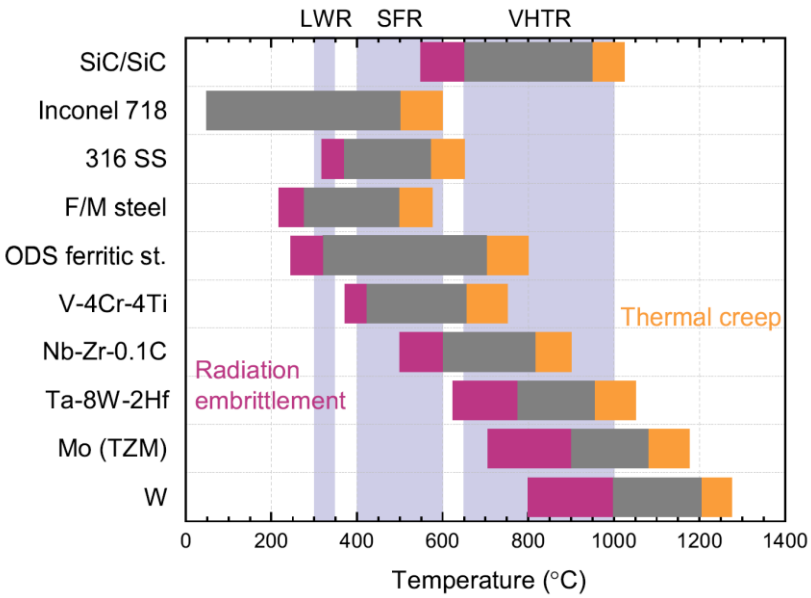

Figure 1.1 Estimated operating temperature of structural materials for damage level of 10-50 dpa. Reproduced from Ref. [1]

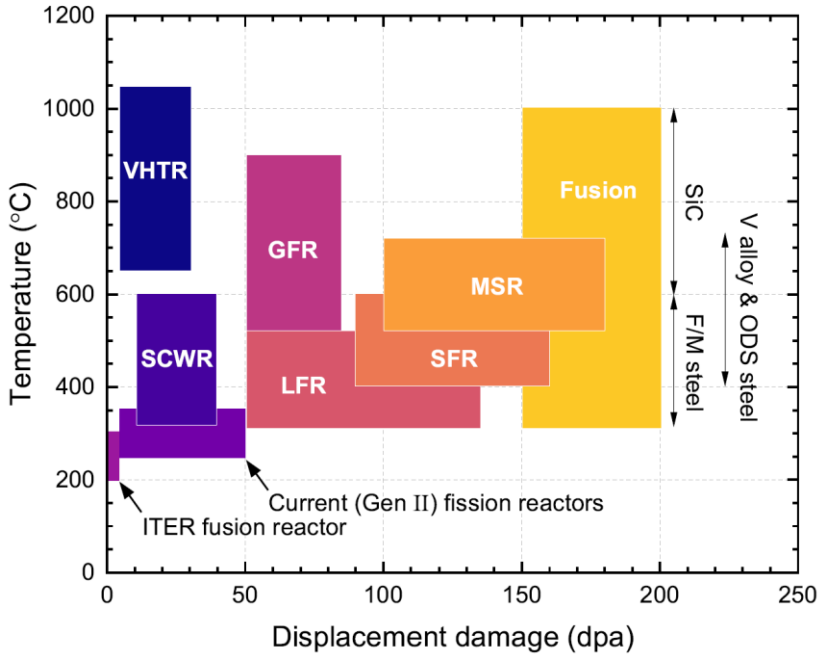

Figure 1.2 Structural material operating temperature and displacement damage dose conditions in current (Generation II) and proposed future (Generation IV) fission and fusion energy systems. Reproduced from Ref. [1]

helium and damage production of these two systems, along with other irradiation facilities, can be seen in Figure 1.3**.**

In this study, Ni and He ions were used to irradiate ultra-high purity Fe and Fe-Cr alloys as well as several experimental FM and ODS steels. Heavy ion irradiation is a valuable complementary tool to study neutron radiation damage produced in reactors [3]. With a higher dose rate than the neutron source, ion beams can be used to achieve high doses rapidly. In addition, it provides better temperature and flux-controlled experimental studies to identify the fundamental radiation effects. However, ion beams cannot completely simulate neutrons due to their wider primary knock-on atom (PKA) spectra, higher ionization per dpa, and dose rate effects (see Chapter 2 for a more detailed discussion). In addition, numerous artifacts of ion irradiation are also observed, including near-surface anomalous void swelling depth profile, chemical and injected interstitial effects by implanted ions, and anisotropic stress effects due to constraint by the underlying unirradiated material. Considering both regions affected by the free surface and injected ions, Figure 1.4 illustrates the safe analysis region of Fe-10Cr (all compositions here are in weight percent, wt%) irradiated by 5 MeV Fe ions. In general, higher energy ions (>8 MeV) are recommended to minimize these artifacts. Furthermore, heavy ion irradiation does not produce helium and hydrogen during irradiation, while neutron irradiation in specific material produces these gases via transmutation reactions. This shortcoming can be overcome to a certain degree through dual-ion irradiations, which inject heavy ions and gas ions simultaneously.

FM steels containing Cr are promising structural material candidates for fusion and advanced fission reactors due to their attractive mechanical properties and significant resistance to degradation from neutron irradiation. Ferritic and martensitic steels are Fe-Cr alloys with body-centered-cubic (BCC) and body-centered-tetragonal (BCT) structures, respectively. They have been used in fossil power stations and other industries for decades. For nuclear applications, FM steels were first proposed to replace austenitic steels (with face-centered-cubic structure, FCC) owing to their superior resistance to void swelling. A comparison of void swelling in fast neutron-irradiated austenitic steels and FM steels is shown in Figure 1.5. Generally, the cavity swelling resistance of BCC metals is superior to

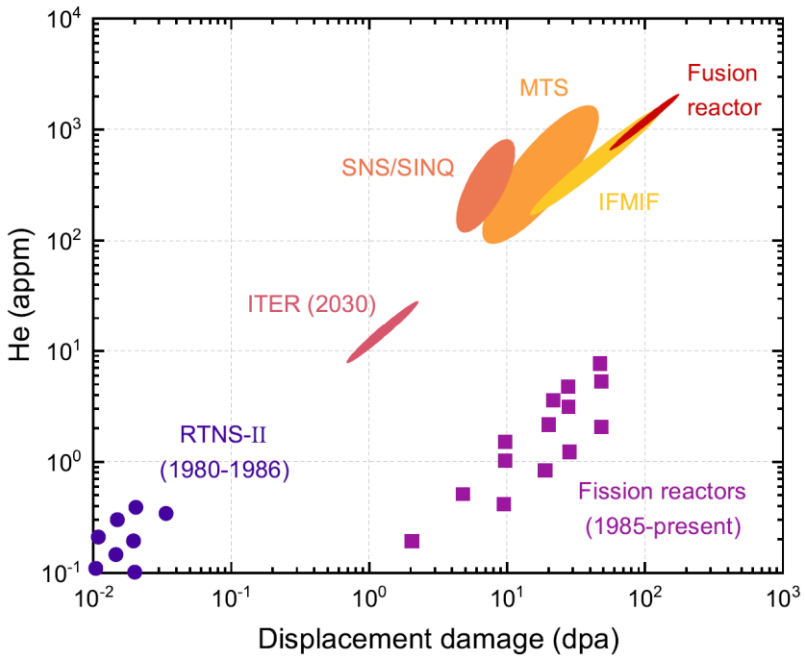

Figure 1.3 Summary of the FM steels experimental database in terms of transmutant He versus displacement damage in actual fission, proposed facility, and future fusion reactors. Reproduced from Ref. [4]

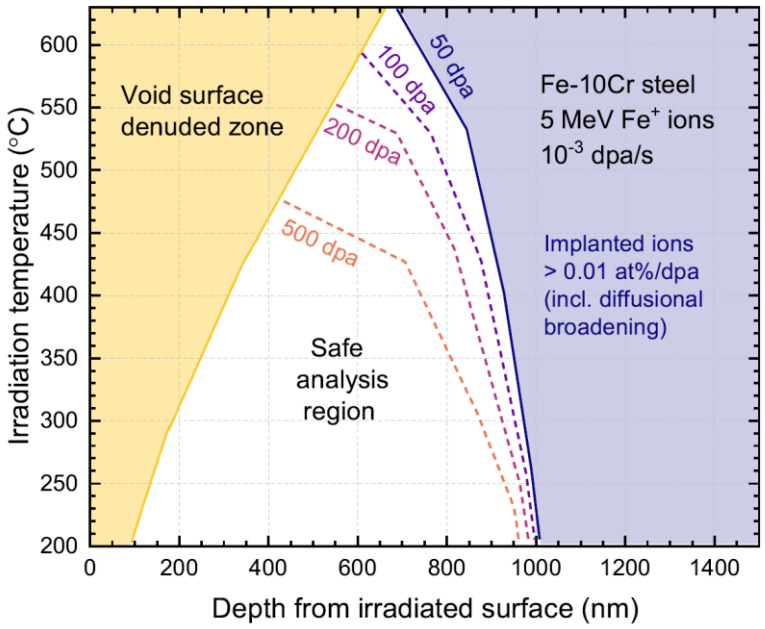

Figure 1.4 Calculated safe analysis region for Fe-10Cr irradiated by Fe ions. Reproduced from Ref. [3]

that of FCC metals. In Gen-IV reactors, FM steels are being targeted for use in fission reactors as in-core (e.g., fuel cladding, wrappers, and ducts) and out-core components (e.g., pressure vessel). For fusion reactor designs, they have been candidate materials for the first wall and blanket structures.

Despite its many advantages, FM steels are susceptible to irradiation-induced embrittlement at lower temperatures (<400°C) that leads to a substantial increase in the ductile-to-brittle transition temperature (DBTT). Along with the low-temperature hardening effect, the Cr content of the alloys can also affect the DBTT under irradiation. Figure 1.6 shows the DBTT dependent on the Cr concentration for neutron-irradiated FM steels. A minimum DBTT temperature shift occurs around 9 wt% Cr [5]. At higher temperatures (>550°C), FM steels may not be used due to their low creep strength. In addition, phase separation and radiation-induced precipitation should also be considered when using these materials in specific temperature ranges. At temperatures around 300-500°C, with the additional radiation enhanced diffusion, α' phase precipitates may form and induce hardening and embrittlement of the alloys [6]. Although FM steels containing more than 12 wt% Cr are of particular interest in nuclear plants because of their corrosion resistance, they are prone to embrittlement due to α' precipitation. Taking the dependence of Cr concentration on mechanical properties into account, the development of FM steels for use in advanced nuclear reactors has been focusing on 8-12 wt% Cr steels, including several commercial or experimental FM steels (e.g., T91 (~9%Cr-1MoVNb), F82H (~8% Cr), Eurofer97 (~9% Cr), and HT9 (~12% Cr).

Strong interest exists toward nanostructured ferritic alloys (NFAs) due to their high sink strength. There are three general strategies for engineering radiation resistance in materials [4]. The first is to produce materials containing a high density of point defect sinks, such as nanoscale precipitates (e.g., ODS FM steels), ultrafine grains, or nanolayered composites. Secondly, using materials with negligible (vacancy) point defect mobility at the desired operating temperature. Third, using materials with intrinsically superior resistance to radiation damage accumulation, such as BCC FM steels. This is generally attributed to a lower dislocation bias and more diffuse primary displacement cascade damage compared to FCC austenitic steels. Nanostructured FM steels with BCC structure

combine two of these strategies. In the light of the first strategy, extensive studies have shown that nanoscale dispersoids, stable under prolonged high-temperature neutron service, can enhance mechanical properties and improve the radiation resistance of the material based on the concept of high sink strength. The introduction of high-density point defect recombination centers reduces the point defect supersaturation and suppresses void swelling. In addition, He effects could also be mitigated by increasing the number density of these nano-dispersoids acting as He trapping sites to control the bubble size or to reduce migration of He towards the grain boundaries. However, there is no systematic irradiation data showing how the density of nanoparticles in advanced ferritic alloys affects the helium bubble density and size at elevated temperatures.

Fe-Cr alloys are the simplest representatives of FM and ODS steels on which fundamental effects of irradiation can be better understood in separate-effects studies. Although studies on the radiation effects in Fe-Cr alloys have spanned over fifty years, the knowledge of their post-irradiation properties is still far from complete. The complication is based on their non-monotonic dependence of Cr on microstructural evolution and mechanical properties under irradiations. The Cr composition should be optimized to achieve the most desirable performance. Moreover, significant discrepancies have been reported regarding the temperature dependence of void swelling (temperature range and peak swelling temperatures) under ion versus neutron irradiation conditions. In particular, some studies have reported a much narrower range of temperatures for observable void swelling in ion-irradiated samples (which may be partially affected by implanted ion and near-surface effects). In addition, He synergistic effects and the effect of impurity additions that are commonly known to interact with vacancies (like C, N, O) are not yet clearly quantified in Fe-Cr alloys. Therefore, it is valuable to study high-purity binary Fe-Cr alloys with limited variables in terms of impurities and alloying elements.

The objective of this thesis is to examine the temperature dependence of cavity swelling, the dependence of cavity swelling on the Cr content, the He synergistic effects in high purity Fe-Cr alloys, and the sink strength effect of advanced nanostructured ferritic alloys. In this study, ultra-high purity Fe, Fe-Cr alloys (with Cr content ranging from 3-14 wt% Cr), a Fe-10Cr alloy with 760 ppm C, and several experimental FM steels (Eurofer97,

CNA3, and 14YWT) were selected for dual-ion irradiation or single-beam He implantation studies to investigate the radiation damage in these materials. Coordinated ex-situ bulk material irradiation experiments with post-irradiation examination and in-situ ion irradiation were conducted to provide a better understanding of the mechanism of void swelling and He effects in Fe-Cr alloys. This study provides quantitative knowledge of fundamental radiation damage effects which could be applied in other metal or ceramic materials. There are three phases of this research project. Phase one includes a detailed examination of the cavity denuded zone, the diffusion of injected self-ions, and other experimental artifacts. Phase two involves the microstructure characterization of irradiation-induced defects (e.g., cavities, loops, dislocations, etc.) in Fe-Cr alloys with a variation of Cr levels (0-14 wt% Cr), He appm/dpa (0.1, 10, and 50), and irradiation temperatures (400-550°C). Phase three is the study on sink strength effects of He implanted nanostructured FM steels with different nanoparticle types and densities.

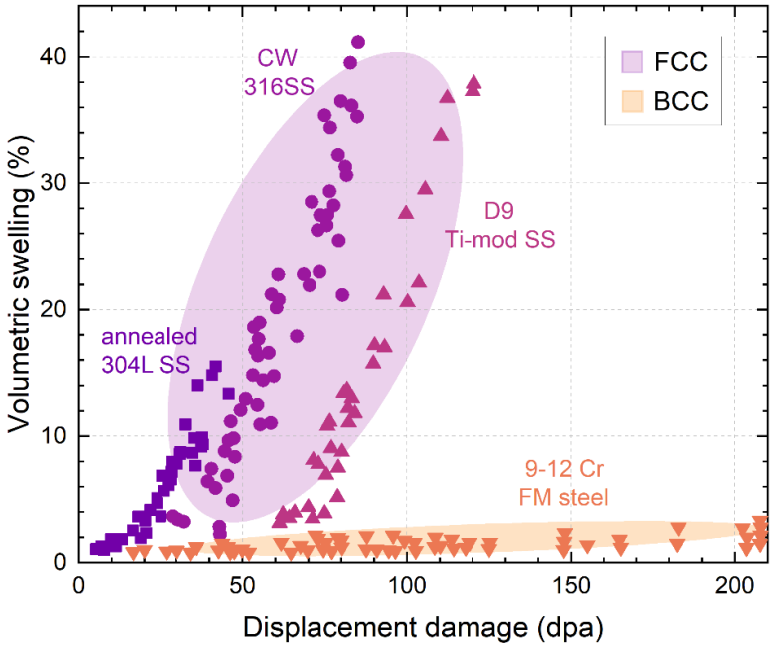

Figure 1.5 Comparison of void swelling in neutron-irradiated austenitic stainless steels (304L, 316, and D9) and 9–12Cr FM steel at 400–550°C. Reproduced from Ref. [7]

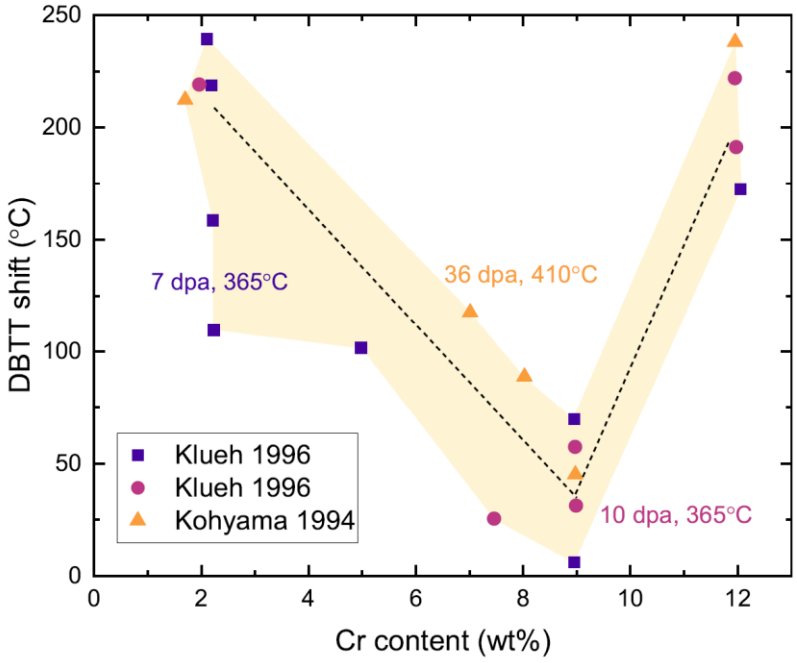

Figure 1.6 Variation of DBTT shift with Cr concentration in neutron-irradiated FM steels. Reproduced from Ref. [5]

Chapter 2
General Radiation Damage Theory

2.1 Basic Idea of Radiation Damage

Particle-matter interactions involve scattering and energy absorption processes. These interactions can be described by several interatomic potentials for different incident particles. The hard-sphere interatomic potential model is a simplified approximation to describe the ballistic collision of neutron to nucleus. In the simplest case of elastic scattering, the recoil energy from neutron-nucleus interaction is given by

$$T = \frac{\wedge}{2} E\,(1 - \cos\theta) \tag{2.1}$$

where

$$\wedge = \frac{4mM}{(m+M)^2} \tag{2.2}$$

E is the incident particle energy, m is the mass of the incident particle, and M is the mass of the struck atom. The energy transfer is maximum when a head-on collision happens, and the incident particle backscatters at an angle of 180 degrees. That is, in Eq. (2.1), when $\cos\theta = -1$, the maximum energy can be obtained as

$$T = \wedge E \tag{2.3}$$

As shown in Table 2.1 and Figure 2.1, these high energy particles (e.g., neutrons, ions, and electrons), with sufficient energy transferred above the so-called displacement energy (E_d), cause atoms of the material to be displaced. The first displaced atom, usually denoted as primary knock-on atom (PKA), then collides with other atoms initiating a sequence of displacements of atoms. During the displacement cascades, a high density of interstitial-vacancy pairs (Frenkel pairs) will be produced. These point defects (interstitials and vacancies), at specific temperatures, migrate to recombine or form defect clusters. With

Table 2.1 Comparison of 1 MeV neutron, self-ion, and electron in iron.

Parameters	1 MeV Neutrons	1 MeV Self-Ions	1 MeV Electrons
Damage range	10^{-2} m	$<10^{-6}$ m	~10^{-6} m
Damage rate	~10^{-6}-10^{-9} dpa/s	~10^{-4}-10^{-2} dpa/s	~10^{-2}-10^{-3} dpa/s
Surviving defect fraction	~0.3	~0.3	~1
Atomic mixing	~50-100	~50	~1-3
Transmutants	Yes (e.g., He, H)	No (but could be simulated by multi-beam irradiation)	No
Sample activation	Yes	No	No
Max PKA energy, $\boldsymbol{T_{max}}$	$\wedge E$	$\wedge E$	$\frac{2E(E+2m_ec^2)}{MC^2}$
$\boldsymbol{T_{max}}$ for Fe	69 KeV	1 MeV	78 eV
Average PKA energy, $\boldsymbol{T_{avg}}$	$\frac{\wedge E}{2}$	$\sqrt{\wedge E E_d}$	$\geq \frac{T_{max}}{2}$
$\boldsymbol{T_{avg}}$ for Fe (E_d=40eV)	34.5 KeV	6.3 KeV	~40 eV

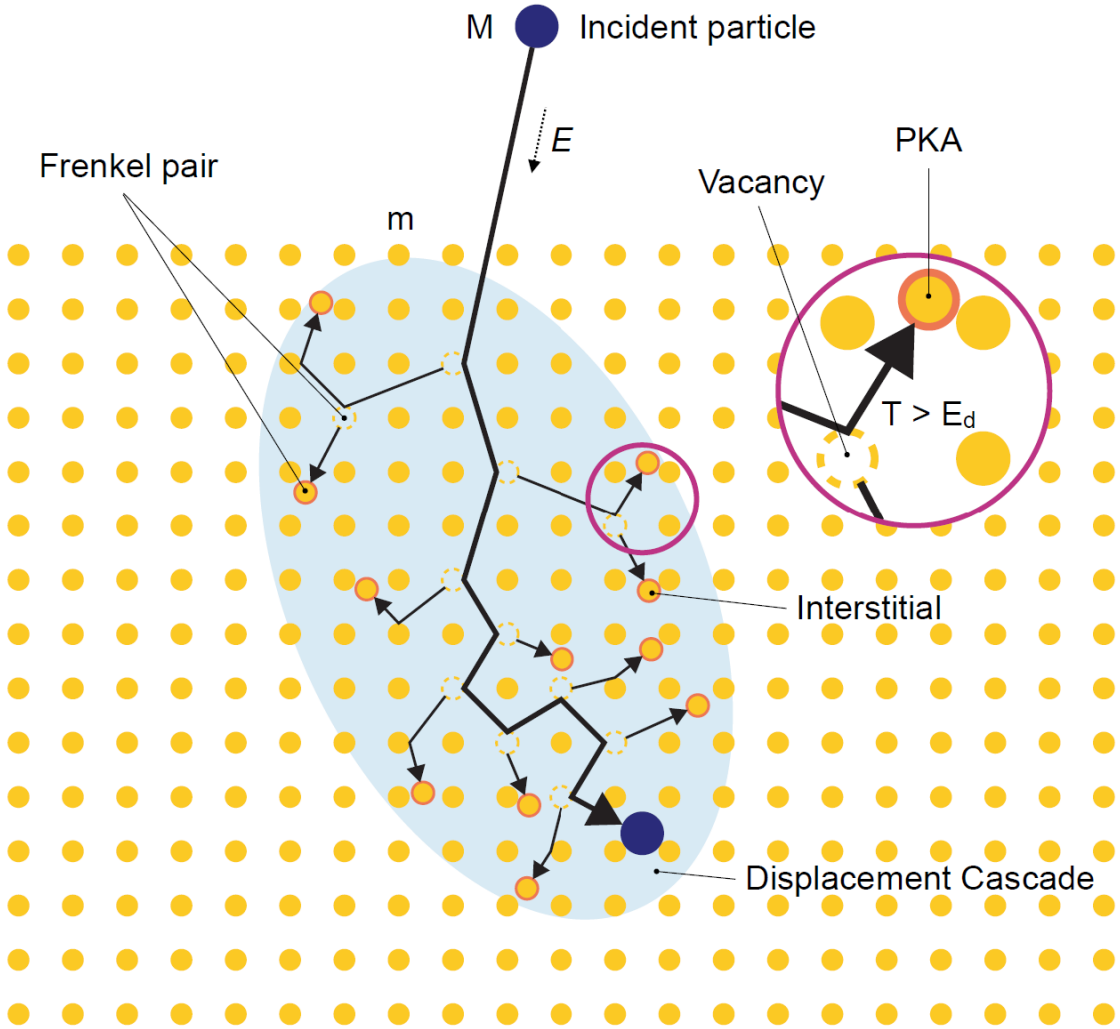

Figure 2.1 Schematic of a collision cascade.

time, they may evolve to more stable defects and alter the material properties. Because the interaction between these energetic particles and solids is distinct, significant differences exist between neutrons, ions, and electrons in the production of PKAs. The main differences among the three irradiation types are summarized in Table 2.1.

In order to compare radiation damage by different radiation sources, the theoretical number of displacements per atom (dpa) at absolute zero is the most common unit used to quantify the primary radiation damage. However, there are several limitations of this displacement model proposed by Norgett, Robinson, and Torrens [8] (known as the NRT dpa). First, it overestimates the magnitude of surviving defects without consideration of in-cascade and correlated recombination. Secondly, the model doesn't consider the crystalline effect together with the crystal-orientation dependence of E_d. Third, it does not monitor in-cascade mixing events. Lastly, it only describes the primary damage source term. Other damage correlation parameters such as temperature, mobility of defects, and dose rate are not considered. Recently, two complementary parameters, ARC-dpa (athermal recombination-corrected) and rpa (replacement per atom), were proposed to correct the in-cascade recombination and ballistic mixing effects, respectively [9].

2.2 Stopping and Range of Ions in Matter (SRIM)

In this study, the dpa values were calculated with the help of the SRIM software package. SRIM, first developed by Ziegler et al. in 1985 [10], is used widely to simulate the interaction of energetic ions in matters. Based on a Monte Carlo simulation method with the binary collision approximation assuming a straight path between collisions, the impact results of an incident ion and the recoil ions for each collision could be simulated. It provides useful predictions on the distribution of implanted ion concentration, depth profiles of energy loss (including partitioning between electronic and nuclear processes), as well as depth profiles of displacement per atom, which are valuable for irradiation effect research, ion implantation study, and ion beam technology. Other information, such as sputtering rate, ionization, and phonon production can also be obtained.

Based on the NRT model [39], the total number of displacements (or total

number of Frenkel pairs) can be obtained by

$$\nu_{NRT} = \frac{\kappa\, T_{dam}}{2E_d} \tag{2.4}$$

where κ is the displacement efficiency with a value of 0.8, T_{dam} is the damage energy that represents the portion of the PKA energy that is dissipated due to the ionization energy loss, and E_d is the displacement energy. The SRIM program, with an option of Quick calculation (Q-C) or Full Damage cascades (F-C) mode, provides the average T_{dam} and ν_{NRT} of the incident ions at a specific penetration depth for dpa calculation. However, several reports have pointed out that large discrepancies in the dpa value were found when using different F-C/Q-C modes, or when using the "vacancy" file produced by SRIM versus using the damage energy values calculated by SRIM to obtain ν_{NRT}. A recent recommendation on using SRIM for dpa calculation is to apply the damage energy method with either Q-C or F-C mode in SRIM [11-13].

2.3 Radiation Effects in Nuclear Materials

2.3.1 Radiation-induced defects

Due to the presence of unrecombined Frenkel pairs during irradiation, defect clusters can form either directly within energetic displacement cascades, or via point defect nucleation and growth processes. At sufficiently high temperatures, they may aggregate to form larger stable defects. These defects can be classified as vacancy-type or interstitial-type defects. Several typical irradiation-induced defects are summarized in Table 2.2 and shown in Figure 2.2 as a function of homologous temperature (T/T_M, where T_M is the absolute melting temperature). In Figure 2.2, three important transition temperatures were labeled as stages I, III, and V. The five defect recovery stages are the background knowledge to understand and estimate the formation of microstructures at specific homologous temperatures. At temperatures below stage I (~0.05 T_M), both interstitials and vacancies are immobile. This results in the crystalline-to-amorphous transition for many irradiated intermetallics and ceramic materials due to high levels of retained disorder. Above stage I,

where interstitials become mobile, interstitial type of dislocation loops can be observed by TEM. Stage II starts the migration of small interstitial clusters and de-trapping of interstitials from solute impurities and other trap sites. When the temperatures are above stage III (~0.2 T_M), cavity formation can be induced, and radiation-induced solute segregation or precipitation phenomena can become pronounced due to the migration of monovacancies. The migration of small vacancy clusters and de-trapping of vacancies from solute impurities and other trap sites starts at Stage IV. At higher temperatures above 0.3 T_M (stage V), small vacancy clusters or loops thermally dissociate. Stress-assisted migration of transmutant He to grain boundaries may also occur at very high temperatures. If left unchecked, these microstructural changes could induce degradation of macro material properties, as mentioned in Chapter 1 (the five key radiation damage degradation processes). For example, SFTs, dislocation loops, and cavities can cause pronounced radiation hardening and associated loss of ductility/embrittlement. In addition, cavities can produce pronounced dimensional expansion. Moreover, helium bubbles at grain boundaries cause dramatic weakening of grain boundary strength, leading to premature rupture at high temperatures.

2.3.2 Cavity nucleation and growth

The cavity-nucleation theory and cavity-growth theory were established based on the reaction rate theory of radiation effects [14]. A cavity is a general designation of three-dimensional vacancy aggregates that could be a gas-filled bubble or underpressurized void. Cavity nucleation requires migration and clustering of vacancies. Because of the relatively low migration energy of interstitials (<0.2-0.45 eV), the thermally activated diffusion of the interstitials is possible at low temperatures. On the other hand, vacancies (with higher migration energy) typically only become mobile when the temperature is above 0.2-0.3 T_M. Furthermore, at higher temperatures where thermal vacancy concentration is high, void embryos became unstable due to vacancy reemission and void nuclei dissolution. Therefore, the potential temperature range of void swelling is roughly between 0.3 and 0.6 T_M.

Table 2.2 TEM observable defects in irradiated materials

Interstitial-type defects	Vacancy-type defects
1. Planar dislocation loops (perfect or faulted) 2. Network dislocations	1. Planar dislocation loops (perfect or faulted) 2. Stacking fault tetrahedrons, SFTs (unique to FCC materials) 3. Three-dimensional cavities (bubbles or voids)

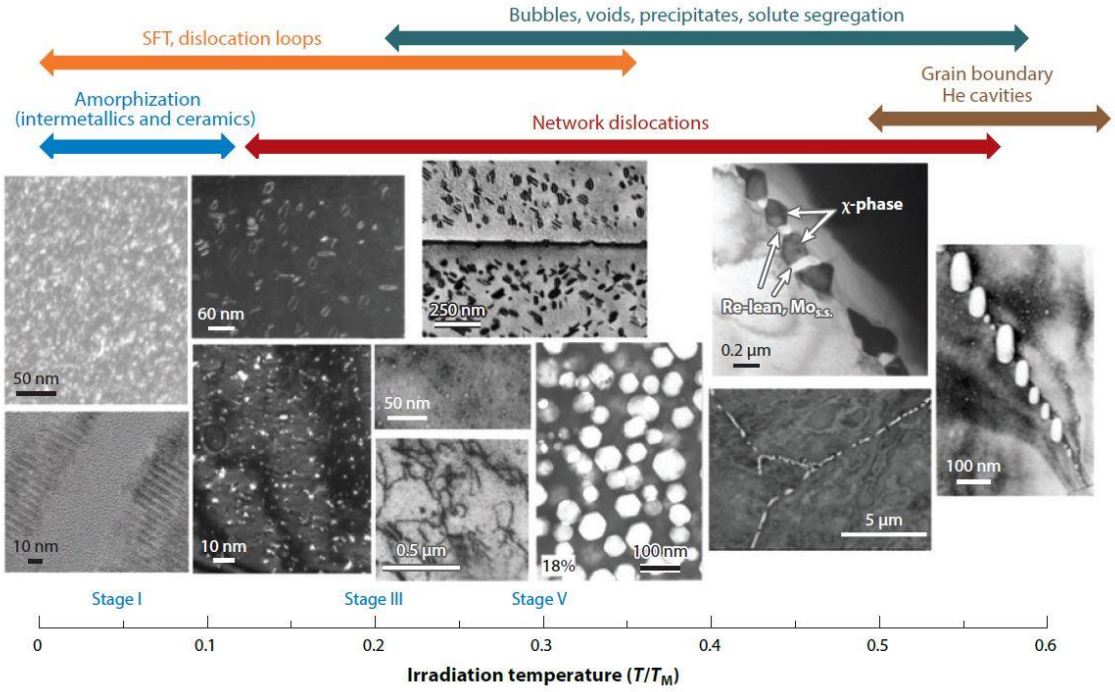

Figure 2.2 Examples of representative microstructures in irradiated materials as a function of irradiation temperature. Ref. [4]

Another important factor for void nucleation and growth is the dislocation bias mechanism. During irradiation, equal concentrations of interstitials and vacancies are produced, and the interstitials with high mobility recombine with the same number of vacancies. Dislocations have a higher absorption bias toward interstitials due to the longer-range relaxation strain of interstitials compared to vacancies. This leaves an excess flux of vacancies for the formation of cavities and macroscopic swelling. Therefore, biased sinks that are more attractive to interstitials are needed to produce the vacancy supersaturation that drives void nucleation and growth. In the past, cavities were considered to be neutral unbiased sinks. However, recent simulation results have demonstrated that small cavities may also have interstitial bias [15]. Although this finding may not affect the fundamental nucleation pathway of the dislocation bias mechanism, it has implications for understanding the incubation period and suppression of cavity swelling.

Helium stabilizes cavity formation by a pressure effect. When He concentration is low, the cavity swelling initially increases with increasing He concentration. Nevertheless, at very high He concentration, the cavity swelling decreases with increasing He concentration. According to calculations based on the critical radius model [14], the conversion of over-pressurized bubbles to voids becomes less likely at very high He concentrations. This is caused by an increase in the critical radius for the bubble to void conversion and over-nucleation in the number density of cavities. In other words, for constant vacancy flux, too many cavity sites are present at very high He/dpa for a fixed vacancy supersaturation. Therefore, the effect of He concentration on void swelling is maximized at intermediate He concentration. Figure 2.3 shows this effect clearly for the cavity swelling of FCC Cu with a maximum swelling at ~10 appm He/dpa.

During the nucleation period, the number density of cavities increases with time, but the sizes remain small. Moving to the cavity growth period that follows, the number density stabilizes, and the void size increases with time. Based on the rate theory, the cavity growth rate is given by the critical radius model [16]

$$\frac{dr}{dt} = \frac{1}{r}\left(z_v^c D_v C_v - z_i^c D_i C_i - z_v^c D_v C_v^C\right) \tag{2.5}$$

where $z_v^c D_v C_v$ and $z_i^c D_i C_i$ are the point defect flux on a cavity of radius r, $z_{v,i}^c$ is the cavity capture efficiency of interstitials or vacancies, $D_{v,i}$ is the point defect diffusion coefficients, $C_{v,i}$ is the point defect concentration, and C_v^C is the thermal vacancy local concentration at the cavity. C_v^C can be expressed as

$$C_v^C = C_v^{eq} \exp\left[\frac{\Omega}{kT}\left(\frac{2\gamma}{r} - P\right)\right] \quad (2.6)$$

where C_v^{eq} is the bulk thermal vacancy concentration, Ω is the atomic volume, k is the Boltzmann constant, T is the temperature, γ is the surface tension, and P is the pressure in the cavity. Setting $\frac{dr}{dt} = 0$, provides the critical radius for cavity growth or shrinkage as a function of the vacancy supersaturation C_V^{eq}. As shown in Figure 2.4, the critical radius r_c, gained at a critical He concentration n_c increases with increasing bubble density and or temperature. For low to moderate He concentrations (n_g<n_c), the two roots (r_b and r_v) for the radius R lead to the commonly observed bimodal cavity size distributions. In addition, the yellow curve (n_g=0) presents the growth of void without gas effects.

2.3.3 Sink strength effects

Sink represents a site for vacancy and interstitial loss due to mutual recombination. Sinks can be divided into neutral (unbiased) sinks with no preference for capturing the type of point defects, or based sinks that show a preference for capturing one type over the other. Standard rate theory provides useful approximations of the defect sink strengths for different microstructural features [17]:

1. Cavities, dislocation loops, and precipitates

$$S = 4\pi r N(1 + S_{tot}^{0.5} r) z \quad (2.7)$$

2. Dislocations

$$S_{dis} = z_{i,v} \rho_n \quad (2.8)$$

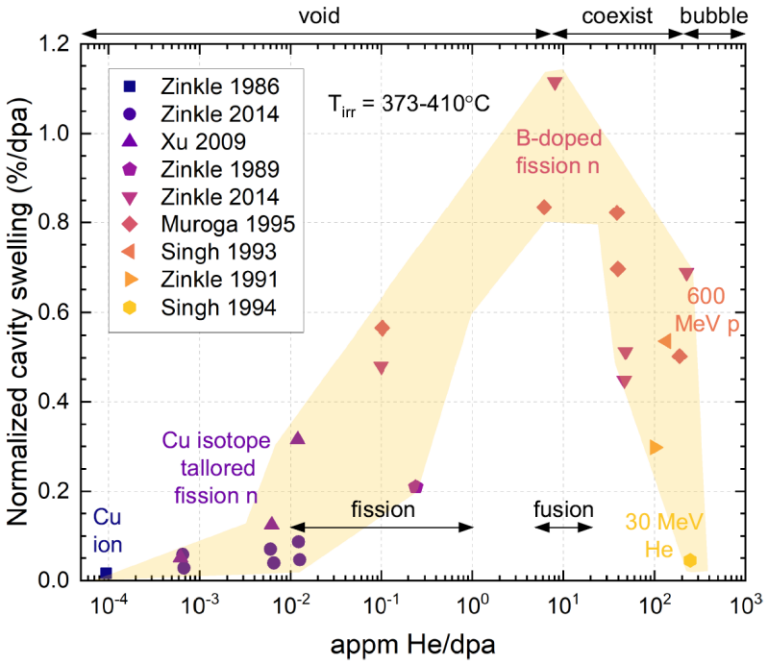

Figure 2.3 Cavity swelling of irradiated Cu as a function of He concentration per dpa. Reproduced from Ref. [4]

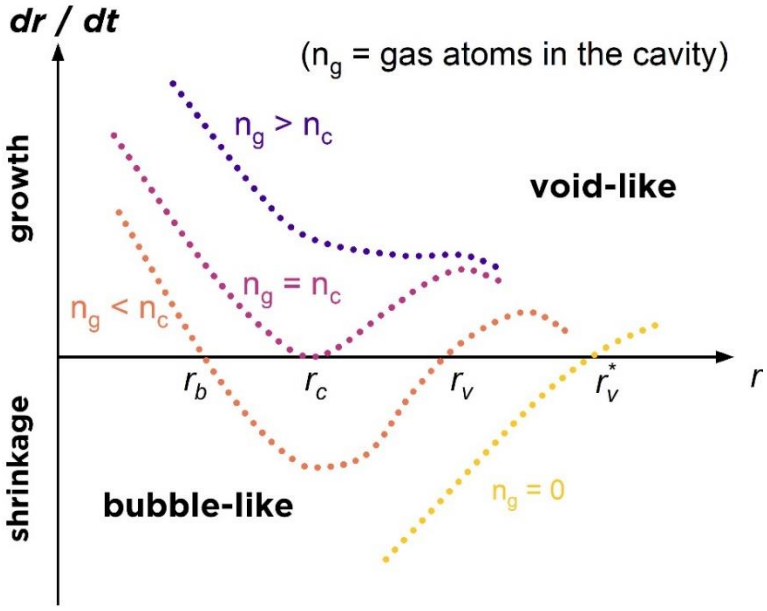

Figure 2.4 Cavity swelling of Cu as a function of He concentration per dpa. Reproduced from Ref. [16]

3. Grain boundaries (assumed spherical)

for low total sink density ($S^{0.5}d \ll 1$):

$$S_{gb} = \frac{60}{d^2} \tag{2.9}$$

for high total sink density ($S^{0.5}d \gg 1$):

$$S_{gb} = \frac{6S^{0.5}}{d} \tag{2.10}$$

where S is the sink strength, r is the radius of the defect or precipitates, N is the number density of the defect/precipitates, z is the capture efficiency (z=1 for unbiased sink), ρ_n is the dislocation density, and d is the grain diameter.

For the defect clusters associated with radiation hardening, the spacing is typically much finer and the resultant required sink strength to potentially affect the fine-scale defect cluster formation is ~10^{15} m^{-2}. At higher temperatures, defect clusters are larger and of lower density relevant for void swelling, resulting in an overall lower defect sink density required to potentially affect cavity formation and growth. Following the high sink strength concept described in Chapter 1, a significant decrease in void swelling typically can be achieved if the spacing between the sinks is much finer than the distance between void embryos, $N^{1/3} > 10\ S_{tot}^{-0.5}$. Using typically observed void densities near the peak swelling temperature as shown in Figure 2.5 (N ~10^{21} m^{-3} for neutron irradiated stainless steel), this corresponds to a required sink strength above ~10^{15} m^{-2}.

Cavity denuded zones at grain boundaries and near-surface were observed in various irradiated metals [18, 19]. The origin of these zones is considered to be connected with the sink strength of grain boundaries. In this sense, voids are not homogeneously distributed near the grain boundaries (or surface) due to the dramatic reduction in the concentration of point defects next to this sink. In other words, this point defect sink site locally reduces the vacancy supersaturation below the critical concentration needed for

void nucleation. In the framework of rate theory, the grain boundary denuded zone width can be expressed in two cases [20]

1. Sink dominant

$$L \propto \sqrt{\frac{1}{C_s}} \tag{2.11}$$

2. Recombination dominant

$$L \propto \left(\frac{D_i D_v}{\alpha G}\right)^{\frac{1}{4}} \tag{2.12}$$

here L is the denuded zone width, C_s is a function of dose rate and temperature and is proportional to the concentration of internal sinks such as dislocation loops and voids, $D_{i,v}$ is the diffusion coefficients, α is the vacancy-interstitial recombination coefficient, and G is the dose rate (dpa/s) of point defects. When the density of dislocation loops or voids is relatively high, the denuded zone width would be expected to follow the sink-dominant relationship Eq. (2.11). On the contrary, a recombination-dominant condition with low defect densities would be expected to follow Eq. (2.12). Based on this equation, it was proposed that the temperature dependence of the width of the cavity-free zone is proportional to $exp\ (\frac{-E_m}{4KT})$, where E_m is the migration energy. In addition, the dose rate dependence for the cavity denuded zone width is generally proportional to $G^{-1/4}$.

Although the width of the void denuded zone has been measured in previous studies, the distribution of bubbles, with a smaller size than voids, was not carefully characterized. The corresponding denuded zone width for helium bubbles is much smaller than that for voids. In addition, it has been reported that the growth of cavities can be enhanced in a transition regime adjacent to the cavity denuded zone along the grain boundary or near the surface of the material [21], which is mainly attributed to the escape of self-interstitial atom (SIA) loops by 1-D migration [22]. This transition regime referred

to as a localized peak swelling zone could also influence the result of lower energy (<5 MeV) self-ion irradiation studies.

2.3.4 Dose rate effects

Dose rate is one of the most significant differences between neutron and ion irradiation. For interstitial dislocation loops, previous studies have reported that dislocation loop density is enhanced with increasing dose rate [23]. In addition, the dissolution temperature (Stage V) of in-cascade SFT clusters was found to be ~70°C higher for ion irradiation (higher dose rate) [24] compared to neutron-irradiated (lower dose rate) [25]. Other studies have reported that the voids were smaller while the density was higher at the peak swelling for lower dose rate neutron irradiation [26]. Lastly yet most importantly, the dose rate can cause a temperature shift of the peak cavity-swelling temperature. The temperature dependence of swelling is determined by the number of surviving vacancies, which involves a competition between several processes, including recombination with interstitials, absorption by cavities and by sinks other than cavities, and thermal vacancy emission from cavities at higher temperatures. Ion irradiations with high dose rates can induce an increased point defect recombination (matrix recombination), and can also increase the sink density, which increases point defect losses to sinks. In other words, with a reasonable shift to a lower temperature, the high dose rate irradiations could be equivalent to normal lower dose rate neutron irradiations. Based on the rate theory, for the recombination-dominant steady-state condition, the peak swelling temperature shift between to different dose rate irradiations could be given by [26]

$$T_2 - T_1 = \frac{\left(\frac{kT_1{}^2}{E_v^m + 2E_v^f}\right)\ln\left(\frac{G_2}{G_1}\right)}{1 - \left(\frac{kT_1}{E_v^m + 2E_v^f}\right)\ln\left(\frac{G_2}{G_1}\right)} \tag{2.13}$$

where $T_{1,2}$ is the temperature at dose rate condition 1 or 2, k is the Boltzmann constant, E_v^m is the vacancy migration energy, E_v^f is the vacancy formation energy and $G_{1,2}$ is the dose rate. However, the shift of the swelling profile as a function of temperature was not simply a translation shift. The temperature shifts of swelling onset, peak swelling, and swelling cessation were all different, as shown in Figure 2.6. Temperature shifts due to the dose rate effect should always be considered when comparing ion and neutron irradiations.

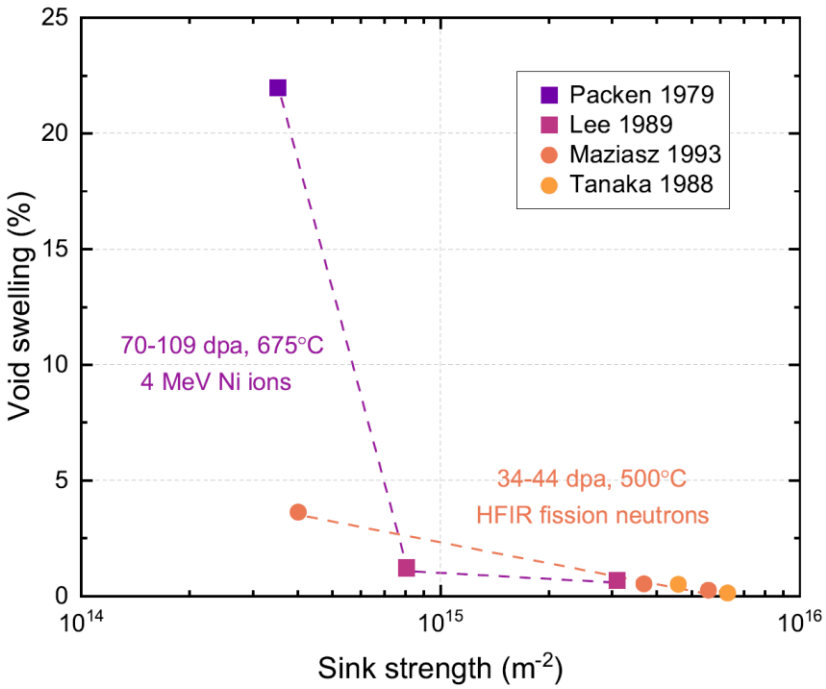

Figure 2.5 Void swelling as a function of sink strength in ion and neutron-irradiated Fe-Cr-Ni austenitic alloys. Reproduced from Ref.[4]

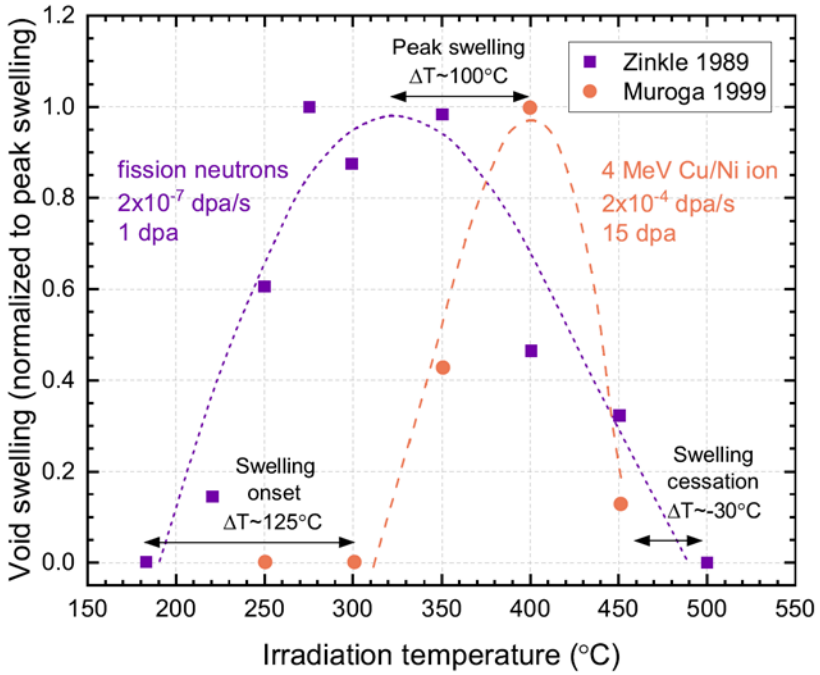

Figure 2.6 Dose rate dependence of void swelling with increasing temperature in irradiated Cu. Reproduced from Ref. [27]

Chapter 3
Literature Review of Radiation Effects in Fe and Fe-Cr Alloys

3.1 Cavity Microstructures

In 1969, Kulcinski et al. [28] first reported the observation of voids in neutron-irradiated Fe. Within the grains with visible cavity denuded zones (~1 μm), they observed homogeneously distributed faceted voids whose surface were defined by an octahedron bounded by {110} planes. However, Farrell and Houston [29] found a heterogeneous void distribution in the grain interior of similarly pure Fe. The discrepancy of these two materials could come from the reactor condition or pre-irradiation treatment of the material (the material wear annealed at 800°C for two hours). Since these initial investigations, a considerable amount of effort has been devoted to study void formation in Fe, Fe-Cr alloys and FM steels following neutron and ion irradiation.

As discussed earlier in Chapter 1, the superior resistance to cavity swelling is one of the main advantages of FM steels over the austenitic steels [7]. Garner et al. showed that FM steels have a much longer transient regime prior to the beginning of the steady-state swelling than the austenitic steels [30]. Also, the steady-state swelling rate is smaller (~0.2 %/dpa) for ferritic-martensitic steels than for austenitic steels (~1 %/dpa). However, the physical mechanisms responsible for the generally superior radiation resistance of BCC Fe based materials are not fully understood. Possible contributing mechanisms include finer dispersed point defect clusters [31], lower dislocation bias [32], and higher self-diffusion coefficients.

Furthermore, the irradiation-induced swelling in Fe-Cr alloys is strongly affected by the Cr concentration and irradiation temperature. However, the dependence of void swelling on the Cr content in Fe-Cr alloys is not simply monotonic and not entirely consistent between studies. The Cr solute dependence of void swelling in neutron-irradiated Fe and Fe-Cr alloys is summarized in Figure 3.1 under four different dose and temperature ranges. The swelling values of zero or negative were set as 0.01%. As shown

in Figure 3.1.a, at a relatively lower dose and lower temperature conditions, Porollo et al. [33] and Little et al. [34] showed that the void formation was significantly suppressed in Fe-Cr alloys compared to Fe, with a minimum swelling near 2-5 wt% Cr. However, other data [35, 36] showed that the swelling increases with increasing Cr until a local maximum around 8-10 wt% Cr, for Cr contents above 3 wt% Cr. The local maximum swelling is more pronounced at higher doses of 140 [35, 37] and 200 dpa [33, 38] as shown in Figure 3.1.c. Garner et al. [30] suggested that Cr affects the duration of cavity incubation period, with the shortest duration at ~10 wt% Cr. For Fe-Cr alloys with higher Cr levels (>12-14%), it is suggested that the reduction of swelling is associated with α' precipitation [36]. At higher temperature conditions, the Cr content causing maximum swelling in Figure 3.1b and d is still inconsistent and seems most pronounced at 9-12 wt% and 5-10 wt% Cr, respectively. The fluctuations of temperature and dose in neutron (reactor) irradiation systems could also be a challenge for obtaining quantitative experimental results.

For ion irradiation experiments, which usually have a better temperature and dose control than neutron irradiations, systemic studies of the effect of Cr on void swelling have been relatively scarce (summarized in Figure 3.2). Bhattacharya et al. (128 dpa, 13 appm He/dpa) [39] and Brimbal et al. (100 dpa, 0-25 appm He/dpa)[40] studied Fe and Fe-Cr (containing 3-14 wt% Cr) alloys irradiated with dual ion beams (2 MeV Fe and He) at 500°C. They both found that the formation of voids was strongly suppressed by the presence of Cr levels of 3-14 wt%. However, surface and implanted ion effects could also affect the result since the ion energy is relatively low. On the other hand, Johnston et al. [41] utilized 5 MeV Ni ion to irradiate Fe-Cr at 500°C to 116 dpa, and found that the addition of Cr enhanced the void swelling with a maximum near 15 wt% Cr.

In addition to Cr concentration, cavity swelling is also dependent on the irradiation temperature, dose rate effect (on void swelling temperature shift, see chapter 2), and the self-ion energy (for ion irradiation studies). Significant discrepancies have been reported regarding the temperature dependence of void-swelling, including the temperature range and the peak swelling temperature. In Figure 3.3 [42-45], a series of ion irradiation studies on Fe, Fe-Cr model alloys, and FM steels with different dose rates clearly showed variations of peak swelling temperatures. Furthermore, the temperature range of observable

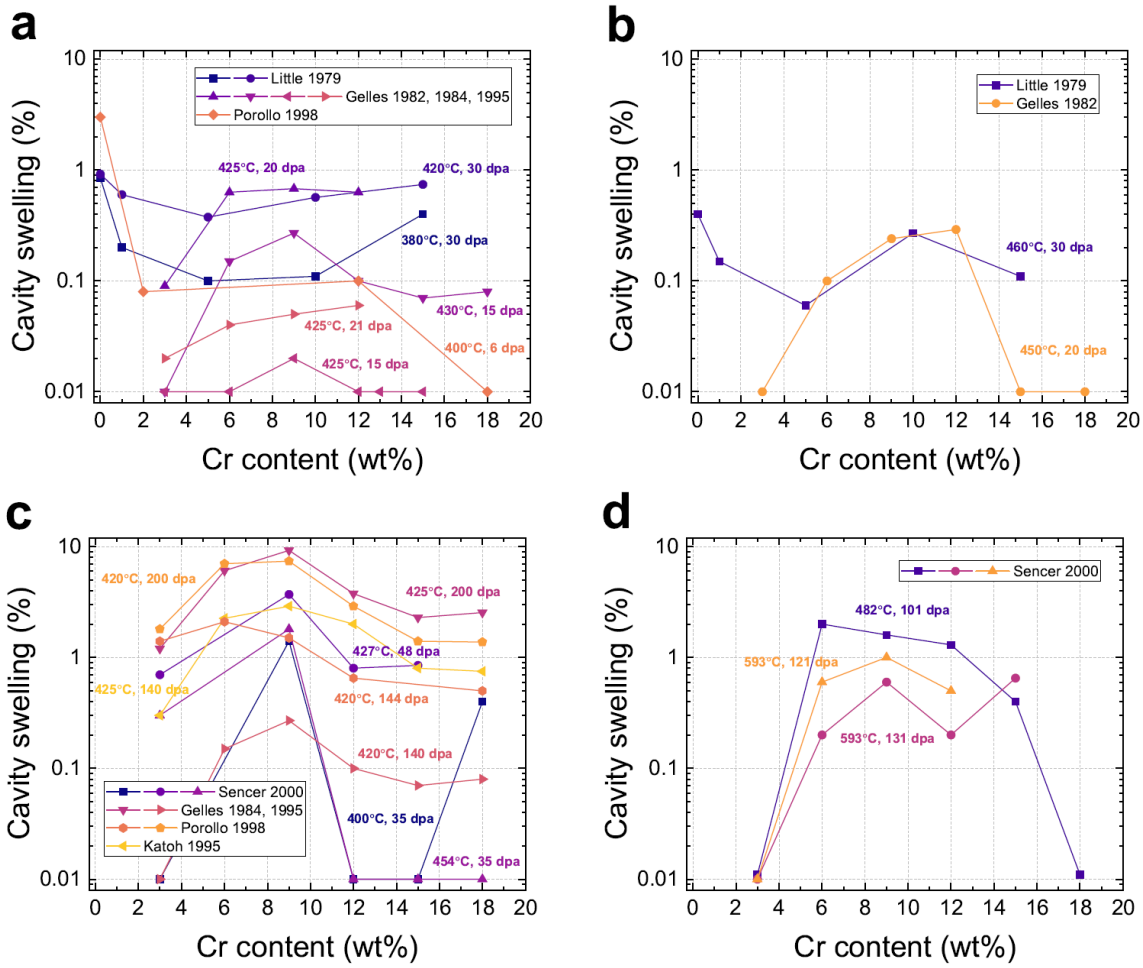

Figure 3.1 Variation of void swelling as a function of Cr concentration in neutron irradiated Fe-Cr alloys. (a) dpa ≤ 30, temperature ≤ 430°C; (b) dpa ≤ 30, temperature ≥ 450°C; (c) dpa > 30, temperature < 460°C; (d) dpa > 100, temperature > 480°C

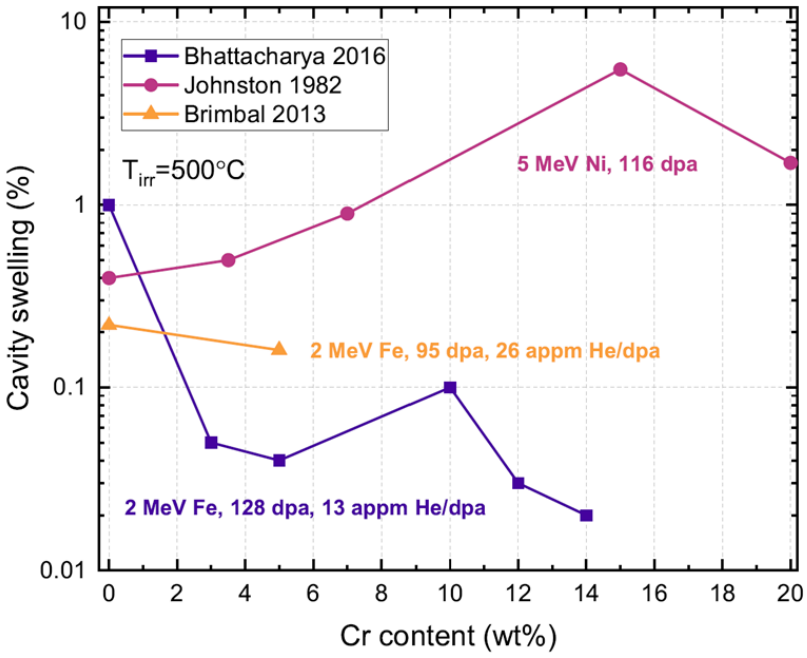

Figure 3.2 Variation of void swelling as a function of Cr concentration in ion irradiated Fe-Cr alloys at 500°C

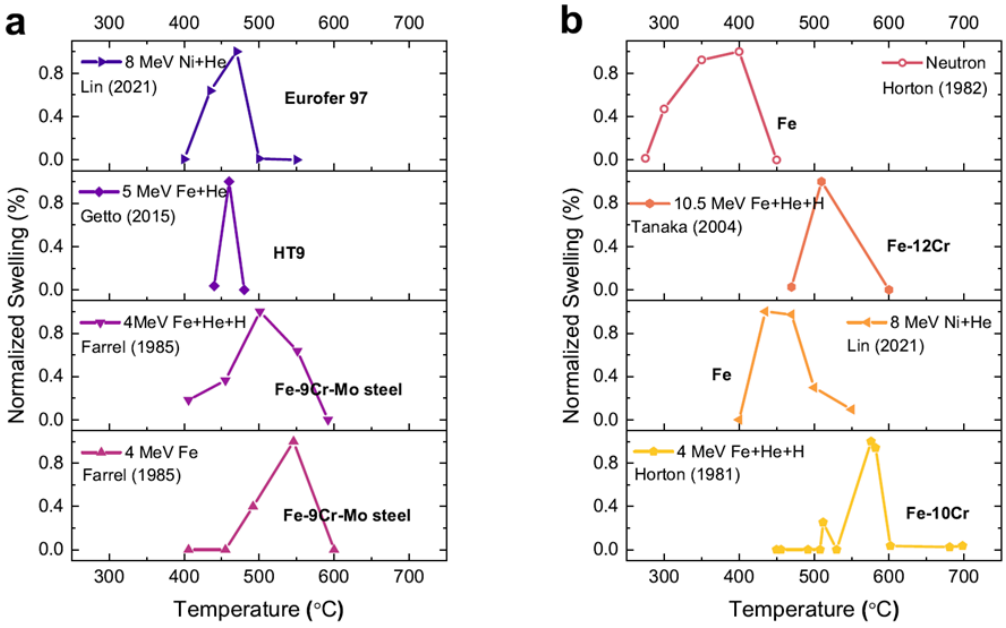

Figure 3.3 Swelling dependence on the irradiation temperature and injected particles of (a) FM steels and (b)Fe-Cr model alloys. [46]

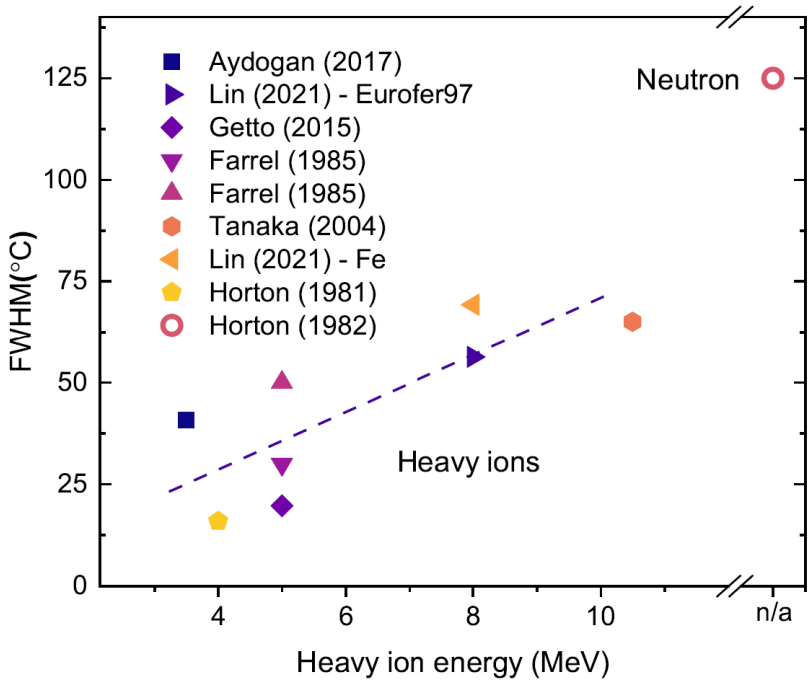

Figure 3.4 Relationship between heavy-ion energy and observable temperature range of cavities. [46] (FWHM: full width at half maximum)

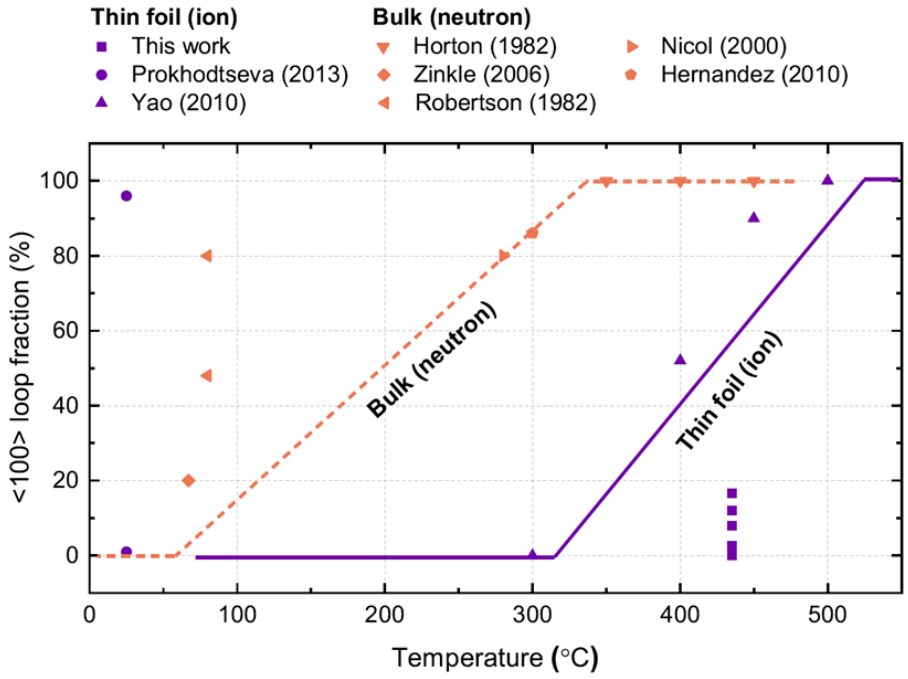

Figure 3.5 Temperature dependence of the fraction of $a\langle 100\rangle$ loops in irradiated pure iron.

void swelling increased with increasing self-ion energy (Figure 3.4). It is worth noticing that the temperature range for void swelling in ion-irradiated samples reported to date is much less than the ~100°C FWHM observed for neutron irradiation experiments. This suggests that implanted ion and surface denuded zone effects may be modifying the extent of the observed temperature regime for void swelling in these ion irradiation studies.

3.2 Dislocation Loops and Precipitates

3.2.1 Review of Fe

Beyond attractive mechanical properties and the intrinsically superior resistance to void-swelling that make ferritic alloys a promising structural material for advanced nuclear reactors [4], one of the most significant anomalies that has intrigued researchers is the proportion of two types of dislocation loops in Fe and Fe-Cr alloys. In 1962, Masters and Eyre reported the observation of dislocation loops in neutron-irradiated Fe [47, 48]. Later, Eyre and Bullough observed two types of interstitial loops in neutron-irradiated iron with Burgers vector $b = \frac{a}{2}\langle 111\rangle$ and $b = a\langle 100\rangle$, and discussed how these loops can form from $\{110\}$ planar defects by one of two shear mechanisms described as followings [49]:

$$\frac{a}{2}[110] + \frac{a}{2}[00\bar{1}] = \frac{a}{2}[11\bar{1}] \tag{3.1}$$

$$\frac{a}{2}[110] + \frac{a}{2}[\bar{1}10] = a[010] \tag{3.2}$$

The observation of loops with $a\langle 100\rangle$ Burgers vectors was surprising since this has significantly strain energy compared to $\frac{a}{2}\langle 111\rangle$ loops due to the larger length of the Burgers vector. They suggested that the later reaction with $\langle 110\rangle$ shear requires higher thermal energy and therefore only occurs at elevated temperatures. Over the past 50 years, the temperature dependence of the loop densities for the two different families of Burgers vectors has been widely studied experimentally in both neutron [42, 50-54] and ion irradiated Fe [55, 56]. The results are summarized in Figure 3.5. Experimental results, as shown in the figure, are mostly consistent with the same conclusion that $\frac{1}{2}\langle 111\rangle$ loops are

predominant at low irradiation temperatures (<400°C), whereas a higher ratio of $\langle 100 \rangle$ loops is observed at elevated irradiation temperatures. This temperature trend agrees with an elastic free energy calculation study by Dudarev et al. [57] that indicated $\langle 100 \rangle$ loops are energetically favorable above 300°C due to the magnetic effects in Fe [58]. Besides, both $\langle 100 \rangle$ and $\frac{a}{2}\langle 111 \rangle$ loops were also observed in neutron and ion irradiated Fe-Cr-Al alloys at temperatures above 300°C [59-61]. In Figure 3.5, it is worth noting that the $\langle 100 \rangle$ loop fractions are still low under 300°C for ion irradiation, while $\langle 100 \rangle$ loops are already predominating at 300°C for neutron irradiations. This is in qualitative agreement with the dose rate effects discussed previously and suggests that some sort of thermally activated transformation is involved in the creation of $\langle 100 \rangle$ loops.

In addition to the two types of loop Burgers vectors, an inhomogeneous distribution of dislocation loops has been observed under certain irradiation conditions in both neutron and ion irradiated Fe. Phenomena such as loop rafting, clustering of loops, and dislocation or grain boundary decoration were observed. Zinkle and Singh [50] found the rafting of $\frac{1}{2}\langle 111 \rangle$ loops primarily on $\{111\}$ planes and secondarily on $\{110\}$, and few on $\{100\}$ planes following neutron irradiation at ~80°C. Robertson et al. [51] observed dislocation decoration of loops with mixed Burgers vectors also at ~80°C with neutron irradiation. However, when a considerable amount of interstitial impurities (e.g., C and N) are present in Fe, the distribution of dislocation loops apparently becomes more uniform due to the high affinity of impurities to point defects and defect clusters.[49, 54] However, it is not clear if the phenomenon of rafting or dislocation decoration would diminish when the irradiated Fe has lower purity or when Fe-Cr alloys or advanced FM steels are irradiated.

3.2.2 Review of Fe-Cr alloys

Regarding the effect of Cr content, both thin foil [62, 63] and bulk material [64, 65] irradiation studies have shown that the proportion of $\langle 100 \rangle$ loops generally decreases with the addition of Cr for a given irradiation temperature. Terentyev et al. [66] reported that Cr has a strong affinity to $\frac{1}{2}\langle 111 \rangle$ interstitial clusters. *In-situ* TEM experiments in Fe-Cr alloys

have also shown that the mobility of small $\frac{1}{2}\langle 111\rangle$ interstitial loops is significantly reduced due to the segregation of Cr at the periphery of loops or the interaction of Cr with self-interstitial atoms in Fe-Cr alloys compared to pure Fe [67]. Xu et al. inferred that the reduction of $\frac{1}{2}\langle 111\rangle$ loop diffusivity due to Cr interactions may reduce the population of $\langle 100\rangle$ loops [68]. As for Fe-Cr-Al alloys, the dependence of Cr content on the loop types was more complex (generally exhibited a weak dependence on Cr content). The study by Field et al. [61] showed a decrease in the fraction of $\frac{1}{2}\langle 111\rangle$ loops to $\langle 100\rangle$ loops with the addition of Cr, which is in contradiction to previous Fe-Cr studies. Other Fe-Cr-Al studies [59, 60], however, showed a weak effect of Cr content on loop types in Fe-Cr alloys.

The effect of Cr on the size and density of dislocation loops in Fe-Cr alloys are also unclear. It should be noted that dislocation loops or clusters with sizes below the resolution limit ~1 nm could not be detected and measured under conventional TEM. That is, the actual loop density and mean loop size could be underestimated and overestimated, respectively. Due to the lack of systematic studies with fixed irradiation temperature or irradiation dose, there is not a clear correlation between the Cr content and loop evolution. As shown in Figure 3.6a, the average loop size decreased dramatically with increasing Cr content at 0-2 wt% Cr following neutron irradiation at 300-425°C [33, 69, 70]. Above 2 wt% Cr, the dependence becomes ambiguous. Porollo et al. [33] found that the loop size was strongly suppressed and independent of Cr content, while Konobeev et al. [70] reported that the loop size decreased with increasing Cr content, continuously. Distinctly, Katoh et al. [37] showed that the loop diameter is maximized at 6-9 wt% Cr under high dose irradiation to 140 dpa. Other studies with doses of 1.5 [71] and 6 dpa [33] also showed the largest loop size at around 9 wt% Cr. As for the loop density as a function of Cr content in irradiated Fe-Cr alloys, the data from previous neutron studies are plotted in Figure 3.6b. In contrast to the loop size, the loop density generally increased with increasing Cr content from 0-2 wt%, and then approached saturation above 2 wt% Cr. The exception is the work by Katoh et al. [37], in which a significant drop in loop density was observed at 6-8 wt% Cr. Furthermore, it has been proposed that Cr and other impurities (e.g., C and N) could increase the threshold dose of the formation of dislocation loops [51, 54, 72]. This agrees

with the result of smaller loops observed in high Cr content materials (Figure 3.6). The enhanced recombination due to solute trapping of interstitial loops by Cr or other impurity atoms was suggested to contribute to the reduction of size and delayed formation of loops [73]. Last but not least, dislocation decoration by small loops was also observed in Fe-Cr alloys. The dislocation decoration phenomenon was observed in irradiated Fe-Cr alloys with Cr contents of 2.5-12 wt% by Matijasevic et al. [54]. Besides, they observed that Fe-Cr alloys with higher Cr levels contain more decorating loops (near the dislocations) than the low Cr content alloys.

3.2.3 α' phase precipitation

Under high temperature and irradiation, Fe-Cr alloys and FM steels with Cr >8-9% are prone to alpha prime precipitation. However, it is suspected that conventional perditions of the binary phase diagram for Fe-Cr system may incorrectly suggested very low solubility of Cr in Fe matrix, due to which the phase diagram is not fully understood. Bonny et al. [74] has proposed a new α + α' two-phase (Fe-rich matrix and Cr-rich precipitate) domain boundary in the Fe-Cr phase diagram (Figure 3.7). Xiong et al. [75] suggested that the alteration of the Fe-Cr phase diagram observed by Bonny et al. is only a steady-state under irradiation but not an equilibrium state. For higher Cr content FM steels (>20% Cr), the σ phase is one of the risky phases that causes embrittlement and alters the corrosion resistance of Fe-Cr alloys. Typically, σ phase precipitation only occurs at 600-1000°C and its production below this temperature becomes very sluggish [76]. Therefore, Cr-enriched α' precipitates are perhaps the major problem resulting in mechanical property changes of FM alloys for nuclear energy applications. The α' phase shares the same BCC lattice with the original ferrite δ and its counterpart α phase. The lattice constants of α-Fe and α' phase are 0.2886 and 0.2885 nm, respectively. Because of the minor lattice mismatch between the two phases and the slight mass difference between Fe (Z=56) and Cr (Z=52), α'precipitates are generally difficult to be observed by conventional or analytical TEM [77].

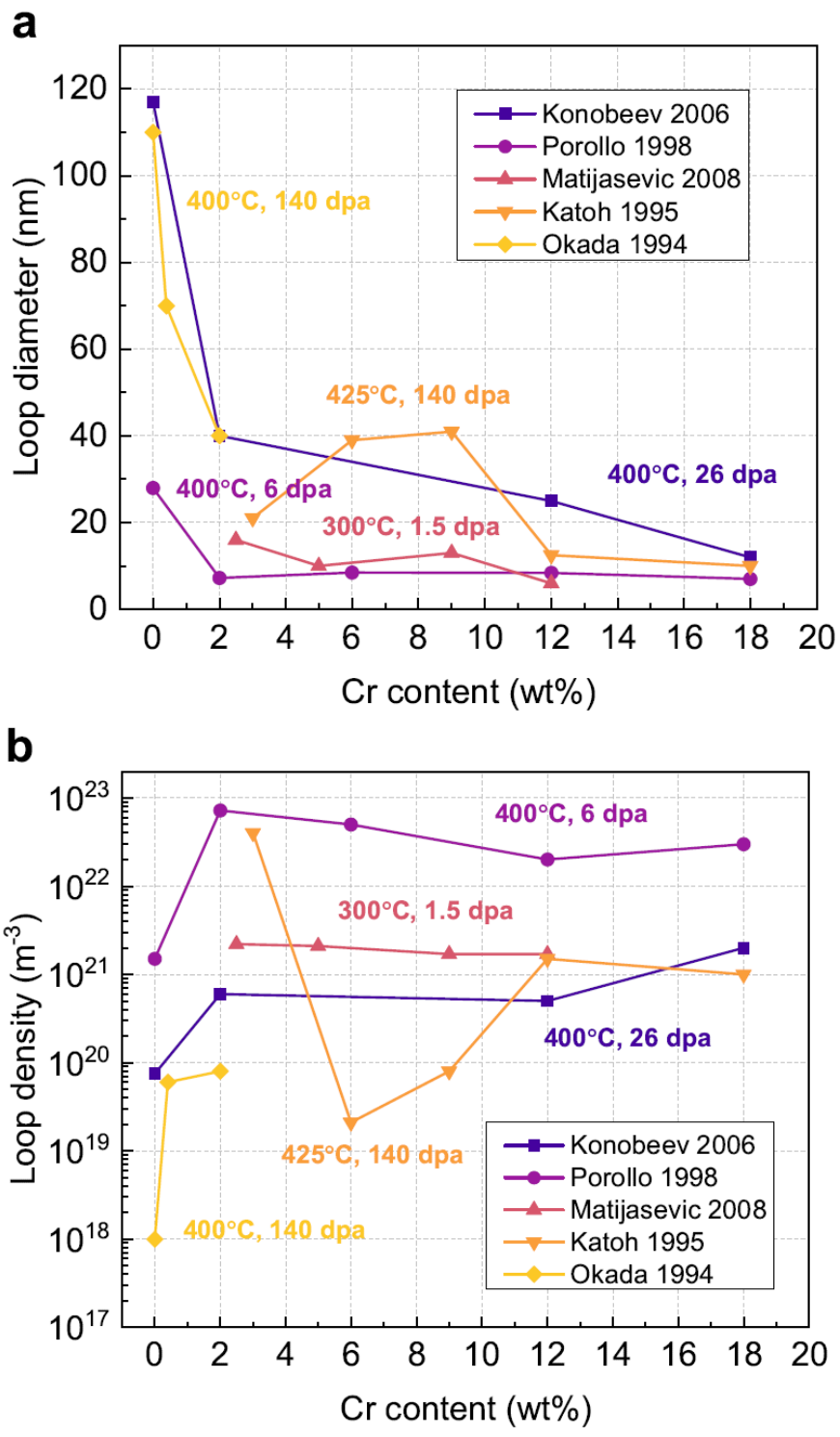

Figure 3.6 Dislocation loop (a) size and (b) density as a function of Cr content in neutron irradiated Fe and Fe-Cr alloys.

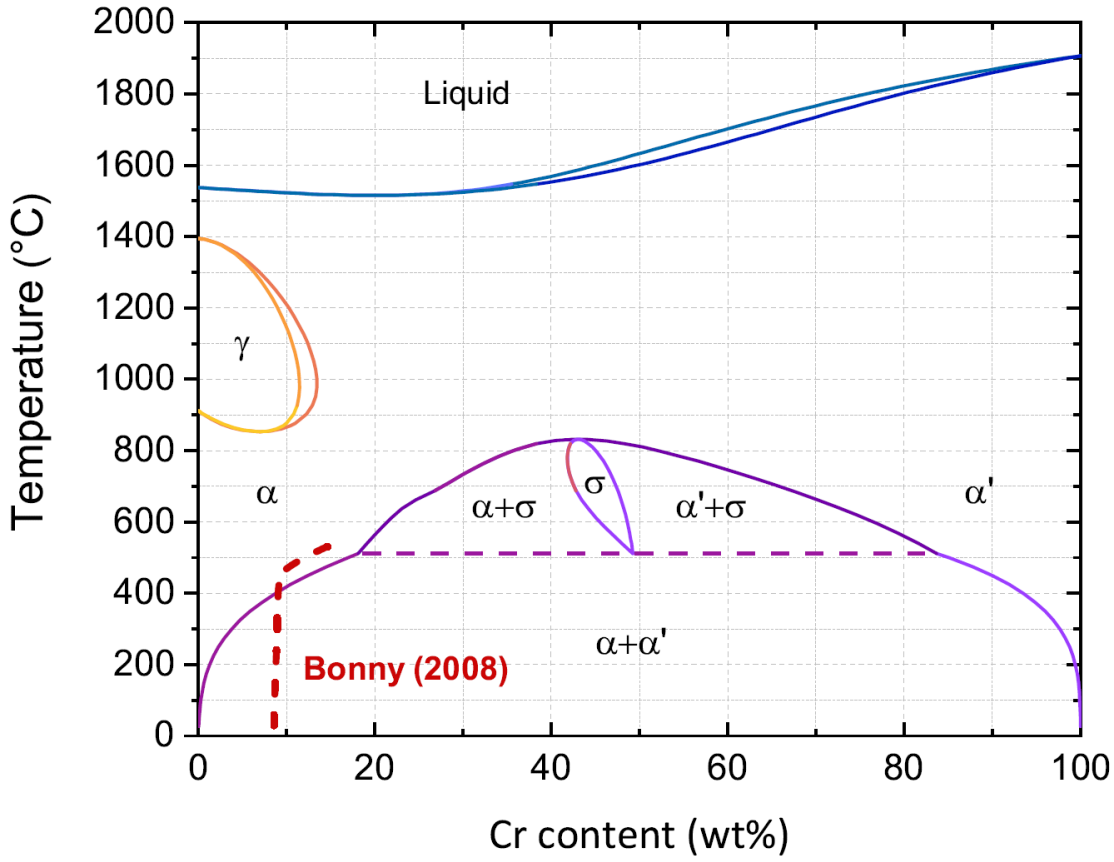

Figure 3.7 Fe-Cr binary phase diagram calculated from Thermo-Calc and the result of Bonny et al. [74]

With the contribution of radiation effects (in particular, radiation enhanced diffusion), the irradiation-enhanced α' phase precipitation could be observed at temperature ranges within the phase diagram domains. As discussed earlier in chapter 1, alloys could suffer from irradiation-induced embrittlement due to the formation of Cr-rich α' precipitates. In the study by Kuksenko et al. [6], α' precipitates were formed in neutron-irradiated Fe-Cr alloys with 9-12 wt% Cr at 300°C to a dose of 0.6 dpa. However, a significant difference in the formation of α' precipitates was found in neutron and ion irradiation bombardment of the same material [79]. Previously, α to α' decomposition in Instead, atom probe tomography (APT) has been shown to be able to detect nanoscale a' precipitates [78]. FM steels were mainly observed after ion irradiation only at dose rates below 10-5 dpa/s. [80, 81] Tissot et al. [81] also indicated that ion irradiation could enhance the formation of α' precipitates with a low dose rate ~10-7 dpa/s. Nevertheless, a recent study of Fe-18Cr by Zhao et al. [82] observed α' precipitates with 8 MeV Fe ion irradiation at 350-450°C, at dose rate ~10-4-10-3 dpa/s. The absence of α' precipitates (at 300 and 420°C) in the study by Pareige et al. [79] at higher dose rates (10^{-4}-10^{-3} dpa/s) may be due to the ballistic dissolution in ion irradiation, which is more effective than radiation enhanced diffusion at temperatures below 350°C.

Chapter 4
Methods

4.1 Materials

4.1.1 High purity Fe and Fe-Cr alloys

The high purity Fe and Fe-Cr material were prepared by induction melting at Ecole des Mines at Saint Etienne, France, under the European Fusion Development Agreement contract EFDA-06-1901 [83]. They were all heat-treated at different temperatures (for 1 hour under pure argon flow) to reach large grain sizes and low dislocation density (~10^8 cm^2). Scanning electron microscopy (SEM) images (see Appendix A) of the as-received materials revealed large equiaxed grains for the high purity binary alloys, acicular structure for the Fe-10Cr-C alloy. The composition and mean grain size of the materials are summarized in Table 4.1.

4.1.2 Advanced ferritic/martensitic steels

14YWT-SM10 ODS alloy and CNA3 advanced ferritic/martensitic steel were used in this study. The TEM images and typical compositions of the as-received materials are given in Figure 4.1 and Table 4.2, respectively. The CNAs with fine MX-type (M=Ti/Ta/V, X=C/N) nanoparticles and coarse $M_{23}C_6$ particles were developed at Oak Ridge National Laboratory (ORNL) to achieve a fine dispersion of precipitates in a tempered martensitic matrix via a well-defined thermomechanical treatment process [84]. The fine particle density and average diameter in the CNA3 alloy were around 10^{21}-10^{22} m^{-3} and 3-20 nm, respectively [85]. On the other hand, the coarse $M_{23}C_6$ particles have an average diameter greater than ~70 nm, with a lower density on the order of 10^{18}-10^{19} m^{-3}. The prior-austenite grain size was ~10-60 μm. The dislocation density of the as-fabricated CNA3 alloy was ~3×10^{14} m^{-2}. The 14YWT is an advanced ODS ferritic alloy developed at ORNL [86]. The SM10 heat of 14YWT demonstrated a uniquely fine and uniform microstructure of nanograin structure (grain size ~0.2 μm) and high density (~10^{24} m^{-3}) of Y-Ti-O nanoparticles (diameter about 2-3 nm) [87]. Other particles, such as $Y_2Ti_2O_7$, TiN, or TiC,

Table 4.1 Material composition and mean grain size of high purity Fe and Fe-Cr alloys.

Material	Cr (wt.%)	C (wt. ppm)	S (wt. ppm)	O (wt. 4ppm)	N (wt. ppm)	P (wt. ppm)	Mean grain size (μm)
Pure Fe	<2 ppm	4	2	4	1	< 5	183 ± 98
Fe-3Cr	3.05	4	2	6	2	--	390 ± 166
Fe-10Cr	10.10	4	4	4	3	< 5	82 ± 36
Fe-10Cr-C	10.10	780	2	2	3	< 5	64 ± 30
Fe-14Cr	14.25	5	7	4	5	< 10	141 ± 80

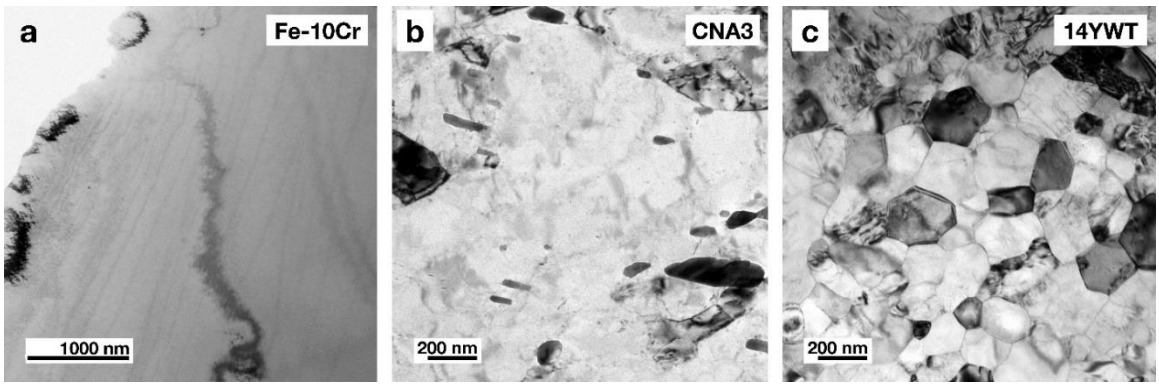

Figure 4.1 TEM images of unirradiated (a) Fe-10Cr, (b) CNA3, and (c) 14YWT materials.

Table 4.2 Compositions (wt%) with balance of iron of the FM steels used in this study.

Element	Eurofer97	CNA3	14YWT
C	0.11	0.1	0.065
Cr	8.95	8.6	13.190
Mn	0.55	1	0.06
Mo	0.005	n/a	0.002
N	0.038	0.004	0.131
Nb	0.004	n/a	< 0.02
Ni	0.003	n/a	0.03
Si	n/a	0.15	0.04
Ta	0.14	0.1	n/a
Ti	n/a	0.15	0.24
V	0.20	0.1	< 0.002
W	1.04	1.3	1.94
Y	n/a	n/a	0.199

with a relatively larger size of 5-30 nm were also observed in low number densities in 14YWT. The dislocation density of the as-fabricated 14YWT alloy was ~2×10^{14} m^{-2}. The Fe-10Cr alloy had very low impurities, whereas the Fe-9Cr alloy included 0.1-0.6 wt% of Mn, Mo, Si, V, and W. Both binary alloys were heat-treated to reduce dislocation density. The average grain size of the Fe-9Cr and Fe-10Cr alloys are ~0.6 and 82 μm, respectively. The fabrication process of the Fe-9/10Cr model alloys are described elsewhere [46, 87].

4.2 Ion Irradiations

4.2.1 Michigan Ion Beam Laboratory (MIBL)

Fission-relevant condition

The high purity Fe, Fe-Cr alloys, and Eurofer97 were simultaneously irradiated at the Michigan Ion Beam Laboratory [88] by 8 MeV Ni^{3+} ions and He^{2+} ions (0.1 appm/dpa) at each of 5 different temperatures (400, 435, 470, 500, and 550°C). Before irradiation, the bulk materials were cut into 2 mm×10 mm bar specimens by a low-speed diamond saw. After cutting, the bar specimens were mechanically polished using SiC abrasives up to 2,000 grit and diamond polishing fluids with progressively finer particles down to 0.01 μm. To minimize C contamination during the ion-irradiations, the specimens were plasma cleaned for 2 hours before loading onto the specimen holder [89]. Six bar specimens (five high purity model alloys and Eurofer 97 steel) were first attached with a thin layer of high vacuum compatible silver paste on a Cu foil. Next, the foil with samples was held with a mask covered on the top (as shown in Figure 4.2a). The irradiated area was 4 mm×6 mm (corresponding to 2 mm×3 mm region at the centrally positioned end of each of the six bars). Infrared thermal imager and thermocouple wires welded on the samples (outside the irradiation area) were used to continuously monitor the temperature during irradiation. The typical standard deviation of average temperatures measured by the thermal imager was below ±7°C (see appendix. A and C for details).

Since the diffusional broadening of implanted ions [90] is not accurately known, we purposefully selected an ion species distinct from the specimen so that the implanted ion profile could be measured post-irradiation (the Ni implanted region could then be

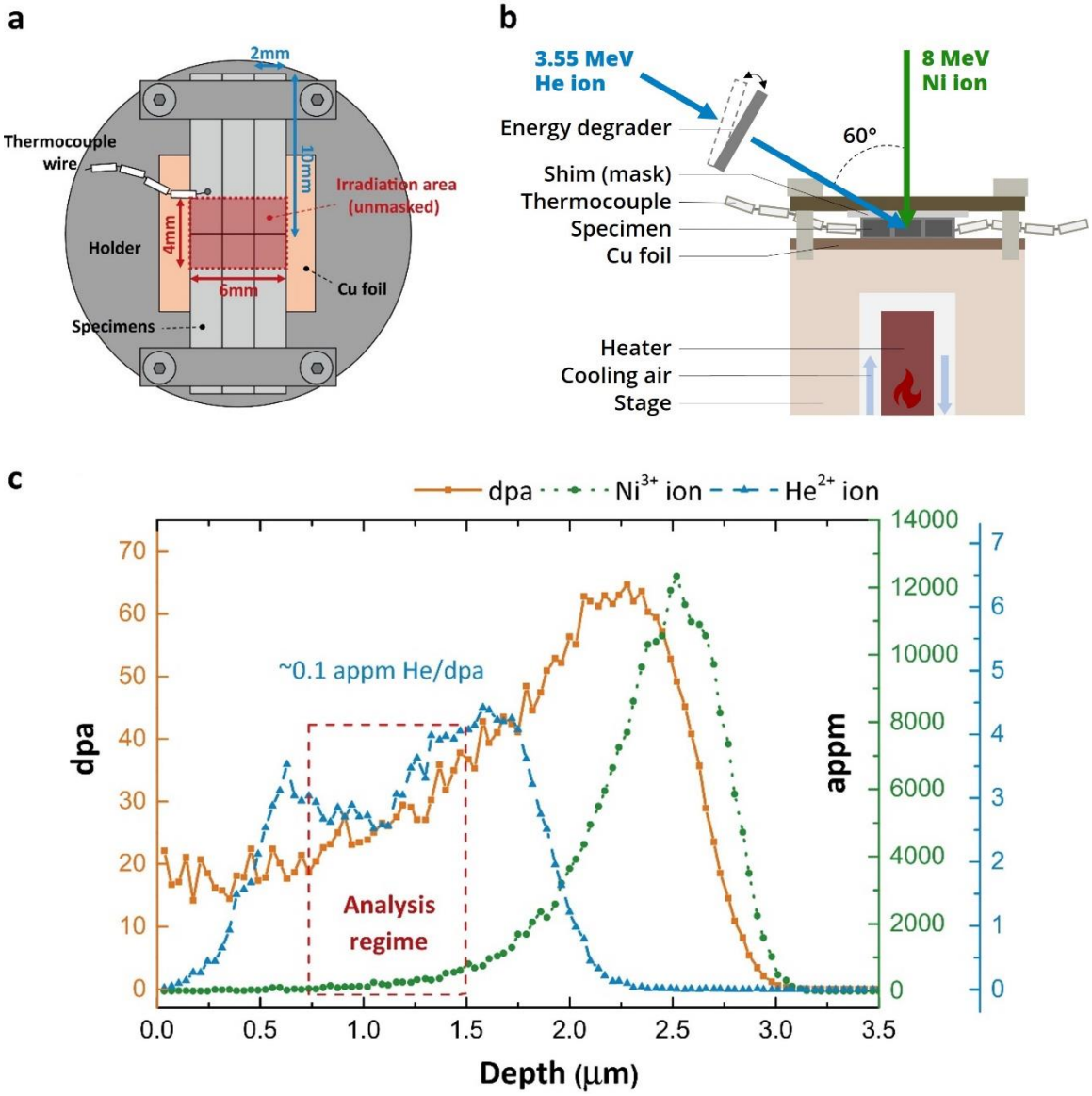

Figure 4.2 Irradiation setup: (a) sample arrangement; (b) dual ion beam directions and stage; (c) SRIM simulation for 8 MeV Ni and energy-degraded 3.55 MeV Hi ions in Fe target.

avoided for quantitative analyses). A tiltable aluminum foil was used to degrade the 3.55 MeV He ion beam to provide the desired depth-dependent He implantation in the ion irradiated midrange region. The defocused Ni ion beam (BL4: 3 MV NEC Pelletron accelerator) was perpendicular to the sample, while the angle between the Ni beam and the rastered He beam (BL7: 1.7 MV General Ionex Tandem accelerator) was 60°, as showed in Figure 4.2b. Other irradiation conditions, including the dose rate and irradiation time, are listed in Table 4.3. The total fluence to achieve a mid-range dose of 30 dpa was 9.68×10^{20} ions/m^2 by SRIM2013 full cascade damage energy method [10] assuming displacement threshold Ed=40 eV, as shown in Figure 4.2c; similar damage levels were obtained using the SRIM "quick calculation" method, whereas the SRIM full cascade vacancy text file produced erroneously high results as noted by Stoller et al. and others [11, 13]. The mid-range dose rate was about 1.4×10^{-3} dpa/s. The concentration of He was selected at a roughly constant 0.1 appm He/dpa at depths of 0.5-1.5 μm.

Fusion-relevant and high He/dpa conditions

Follow-up irradiation experiments were conducted with helium per dpa ratios of 10 and 50 appm He/dpa. The investigated conditions are a subset of the 30 samples previously investigated at 0.1 appm He/dpa. The irradiation conditions, including the total fluence and dose rate, of the 8 MeV Ni ions were the same. Plasma cleaner and cold trap were also used for the experiment. The only differences are the implanted He profile and bulk sample size, and the sample arrangement. The concentration of He produced by degraded energy He ion beam are selected at a roughly constant 10 and 50 appm He/dpa at depths of 0.5-1.5 and 0.75-1.25 μm, respectively. The narrower range of constant 50 He/dpa profile for the latter irradiation is due to the instrument restriction. The bulk materials were first cut into 2 mm×2 mm square foils by electrical discharge machining (EDM) cutting. With a similar mechanical polishing process used for the bar samples (Figure 4.2a), the final thickness of the square samples was ~0.5 μm. In order to prevent potential compressive stress during irradiation for clamped samples (Figure 4.2a), the square samples were attached on a 20 mm×30 mm Cu plate with silver paste, as shown in Figure 4.3a. The SRIM simulated damage and helium profiles of the 10 and 50 appm He/dpa experiments are illustrated in

Table 4.3 Matrix of the dual ion (Ni & He) beam irradiation conditions at MIBL.

Materials	Ion Species	Fluence (ions/m^2)	Mid-range dose & dose rate	Temperature (°C)	Estimate irradiation time (hours)
Fe Fe-3Cr Fe-10Cr Fe-14Cr Fe-10Cr-780appm C Eurofer97	8 MeV Ni^{3+} ions & 0.1, 10, 50 appm He/dpa	9.68×10^{20}	~30 dpa ($1.4x10^{-3}$ dpa/s)	400 435 470 500 550	6-8

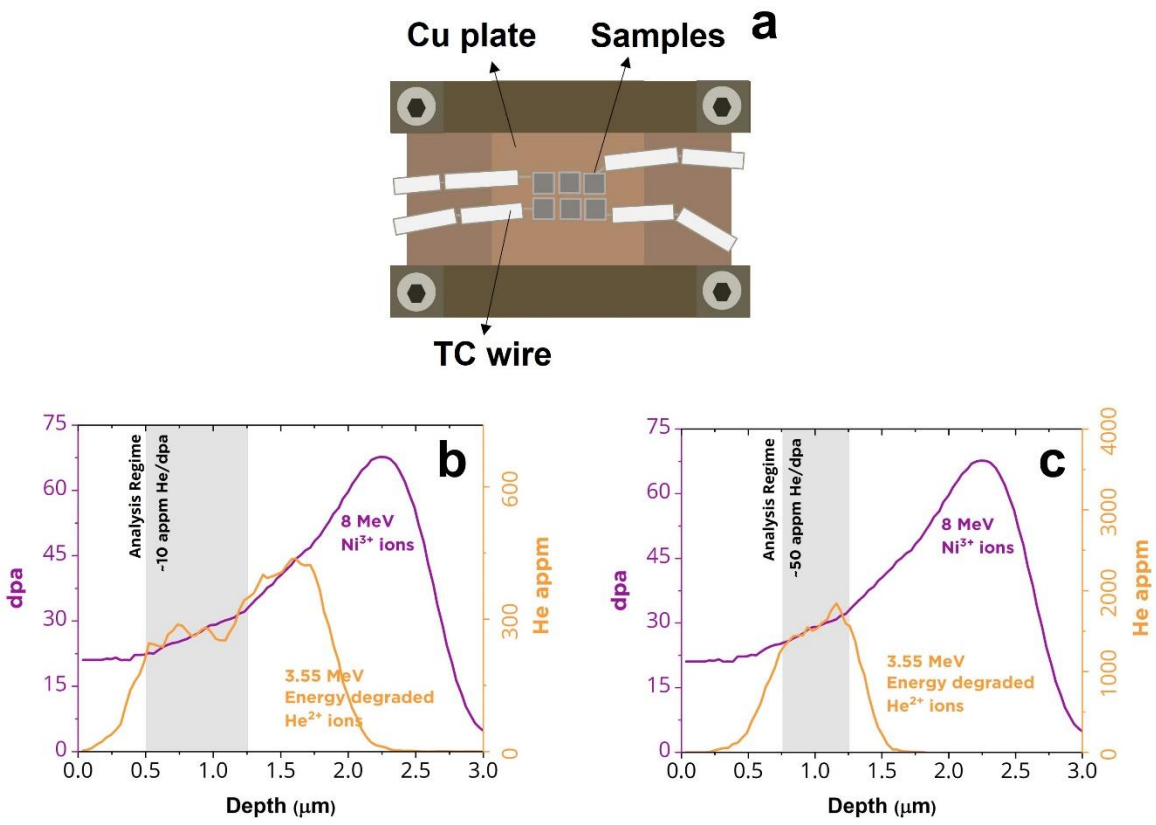

Figure 4.3 Irradiation setup: (a) sample arrangement and SRIM simulation for (b) 10 appm He/dpa and (c) 50 appm He/dpa conditions.

Figure 4.3b and 4.3c, respectively. In view of the discrepancy of Ni ion range between SRIM estimation and experimental measurements (EDS and SIMS), the SRIM profile could be modified by changing the correction factor of the SRIM calculation to fit the peak center of implanted ions measured by experimental techniques (Fig. B.6). Using a correction factor of 1.5 (Fig. B.7), would increase the midrange dose to ~40 dpa, which is 33% higher than the original SRIM estimation. However, further studies are needed to confirm the stopping power error (for Ni ion in Fe target) in SRIM, and to examine if the correction factor can accurately correct the defect production profile.

4.2.2 National Tsing Hua University (NTHU) Accelerator Laboratory

The 275 keV He implantation experiments on the Fe-10Cr model alloy and the NFAs (CNA3 and 14YWT) were carried out at 500 and 700°C with the High Voltage Engineering Europe (HVEE) implanter at National Tsing Hua University in Taiwan. Bulk materials were cut into 2 mm×2 mm square specimens by a low-speed diamond saw. After cutting, the bar specimens were mechanically polished using sandpaper up to 2,000 grit and polishing fluids with particles down to 0.01 μm. The final thickness of the square samples was about 0.5 μm. Figure 4.4a shows the overall holder and sample arrangement. The 2 mm×2 mm samples were attached on a 3 mm×15 mm Fe strip with silver paste. The strips were then placed into a groove on a Molybdenum holder. Quartz plates were placed on the periphery of the target holder (next to the Fe alloy specimens) to confirm the ion beam profile and position. Also, thermocouple wires were welded on the samples to measure the temperature during irradiation. The fluence and peak helium concentration were 1.28×10^{20} m^{-3} and 8,000 appm, respectively. Figure 4.4b shows the depth profile of the He concentration calculated by the SRIM-2013 program using the "quick calculation" vacancy.txt files with displacement energy, Ed=40 eV for Fe target. The peak He production rate at depth 0.6 μm was 2.4 appm He/sec. In addition, the dose and dose rate at depth 0.6 μm were 0.3 dpa and 2.8×10^{-5} dpa/s, respectively.

4.2.3 Intermediate Voltage Electron Microscope (IVEM)-Tandem Facility

In-Situ Single Helium Beam Implantation

The TEM thin foils of Fe-10Cr, CNA3, and 14YWT materials were irradiated with 10 keV single He ion beam, with a 15° incident angle, at 600 and 900°C. The thin TEM foils were irradiated at the Intermediate-Voltage Electron Microscopy (IVEM)-Tandem facility in Argonne National Laboratory (ANL) (Figure 4.5a) [91]. As shown in Figure 4.5b, with a total fluence near 6.82×10^{19} m^{-2}, based on the SRIM-2013 calculation (also by "QC-vacancy.txt" method and Ed=40 eV), the peak radiation damage and He concentration at depth 60 nm were roughly 0.3 dpa and 12,000 appm, respectively. For the 600°C in-situ irradiated samples, when the peak dose reached 12,000 appm, we stopped the implantation and subsequently performed post-irradiation annealing to 900°C. The annealing results were used to compare with the 900°C directly hot-implanted experiments.

In-Situ Dual Beam Irradiation

The TEM thin foils were subsequently irradiated at 435°C with 1 MeV Kr ions and 12 KeV He ions simultaneously with a 15° incident angle at the Intermediate-Voltage Electron Microscopy (IVEM)-Tandem facility in Argonne National Laboratory (ANL) [91]. The samples were heated gradually from room temperature to 435°C by a Gatan double tilt heating holder. As calculated with the Stopping and Range of Ions in Matter (SRIM-2013) program using the "quick calculation" vacancy text files with displacement energy 40 eV for Fe target, the depth profile of the atomic displacements and He concentration are shown in Figure 4.6. TEM observation was continuously performed during the damage production by Kr ions up to a total fluence of 1.3×10^{20} ions/m^2, corresponding to 18–22 dpa at the depth 50-125 nm with a constant dose rate of 1×10^{-3} dpa/s (roughly 16 min to cause 1 dpa damage). The total fluence of implanted He ion beam and He per dpa ratio were 1×10^{21} ions/m^2 and 10 He appm/dpa (at a depth of 25 nm), respectively. This experiment is used to compare with the dual-beam irradiation results conducted at MIBL (see section 4.2.1). The material and irradiation condition of the two

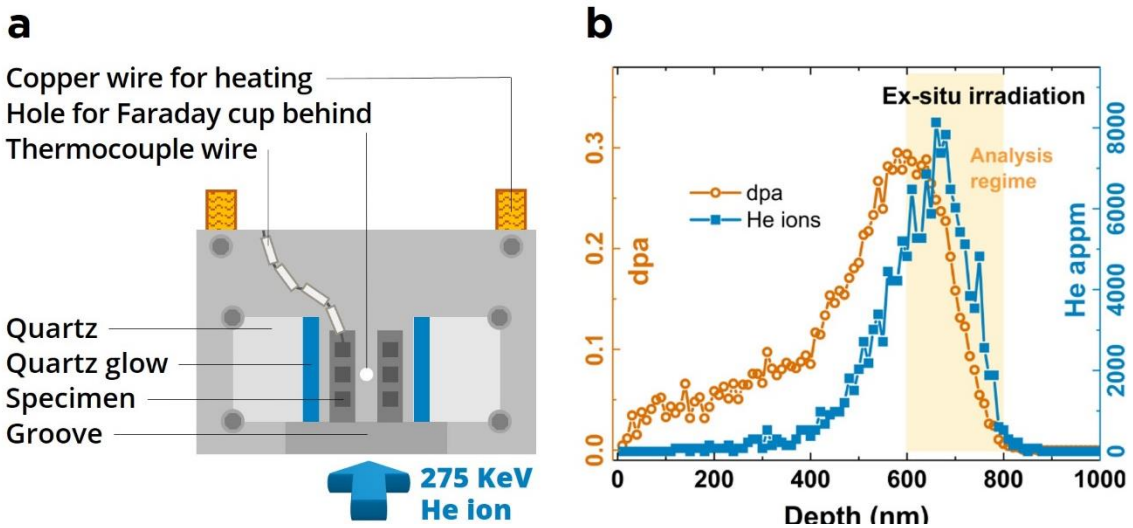

Figure 4.4 Irradiation setup: (a) Sample loading and arrangement at NTHU; (b) SRIM simulation for 275keV He ions in Fe target.

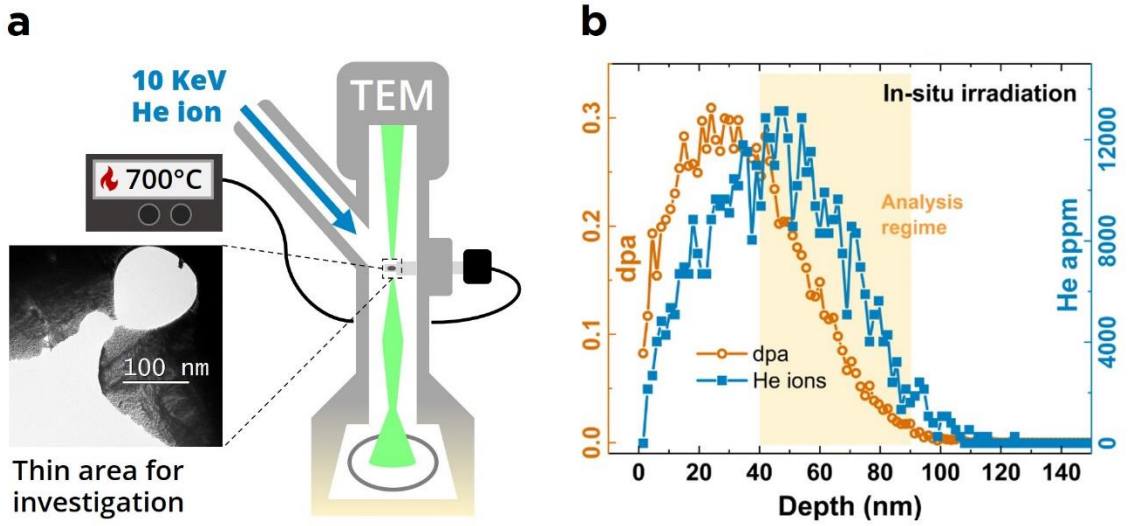

Figure 4.5 (a) Schematic diagram of the in-situ irradiation experiment at ANL; (b) SRIM simulation for 10 keV He ions in Fe target.

in-situ TEM experiments are listed in Table 4.4.

4.3 TEM Specimen Preparation

4.3.1 Focused ion beam

The focused ion beam (FIB) samples in this study were prepared by using the ZEISS AURIGA CROSBEAM FIB/SEM and the FEI Scios DualBeam system. Due to the high efficiency and small sample consumption, FIB is commonly used to prepare samples for TEM investigation. With a liquid metal ion source (LIMIS) operating at accelerating voltages ranging from 2 to 30 kV, the FIB device sputters atoms from the target material by the accelerated gallium ions. FIB can either mill, cut, or polish (thinning) at any point of interest desired on the sample. As shown in Figure 4.6, most commercial instruments have combined the FIB ion column with an SEM electron) column to monitor the sample during preparation. An example of procedures is summarized below:

1. Load sample and check the vacuum status ($<2\times10^{-5}$ Torr) before opening the column valve.
2. Align the eucentric point with an appropriate working distance (7-12 mm). This can prevent the image from moving laterally as the specimen is tilted.
3. Align the coincident point. This calibrates the relative position of the SEM-beam and FIB-beam for imaging.
4. Insert the nozzle from the gas injection system (GIS) to deposit protective Pt or C layers on the sample surface to prevent FIB damage.
5. Set up appropriate parameters for ion milling to make a 1-2 μm thin lamella. At this stage, a high current (30 kV, 12 or 8 nA) is useful to remove material more efficiently.
6. Use the micro-manipulator to lift out the lamella and mount it on a TEM lift-out grid.
7. Conduct coarse polishing from high to low currents (30 kV, 2 nA to 10 pA). The lamella thickness should be 80-120 nm after the coarse polishing.

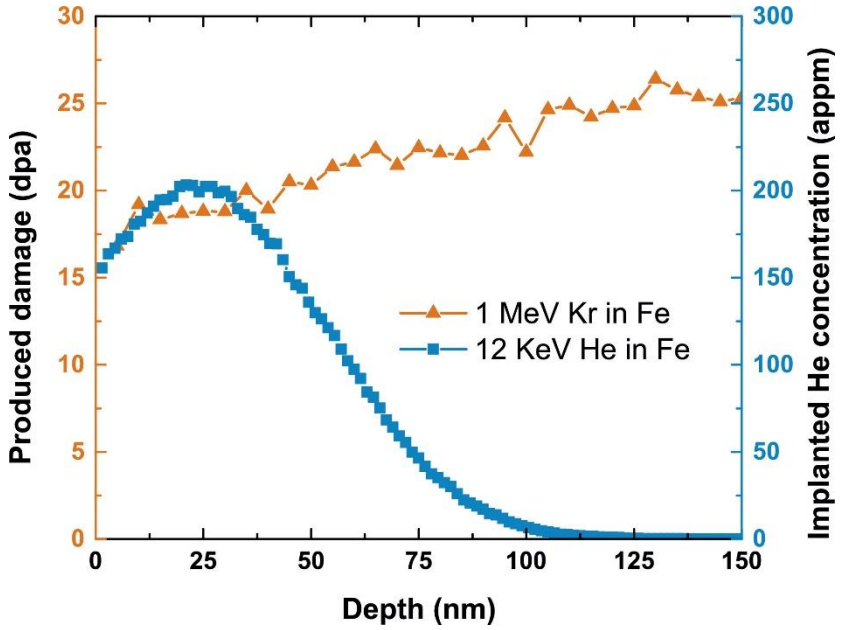

Figure 4.6 SRIM calculated profiles of the 1 MeV Kr damage and 12 keV He ion implantation in Fe target.

Table 4.4 Matrix of the IVEM in-situ irradiation experiments.

Material	Temperatures	Ion Species	Maximum dpa and dose rate	Peak He concentration	appm He/dpa
Fe-10Cr CNA3 14YWT	600°C 900°C	10 keV He	0.5 dpa 3.7×10^{-4} dpa/s	12,000 appm	24,000
Pure Fe Fe-10Cr	435°C	1 MeV Kr^{2+} & 12keV He	20 dpa 1×10^{-3} dpa/s	200 appm	10

8. Perform the final fine polishing with a very low voltage and current (2-5 kV, 10-50 pA) until a transparent area (window for TEM investigation) appears under 3 keV SEM.

4.3.2 Electropolished TEM samples

For the IVEM facility, electropolishing method for the preparation of TEM samples is recommended. This is because the sputtering damage induced by Ga ions in FIB samples could cause artifact microstructures when used in TEM in-situ irradiation studies. In the present study, a Struers-Tenupol 5 electropolisher was used to prepare the electropolished TEM samples. Procedures are summarized below:

1. The samples were first cut into 3 mm diameter disks by Electrical discharge machining (EDM) cutting.
2. After that, both sides of each sample were ground using sandpaper from 360 to 800 grit.
3. After thinning the thickness to about 15 μm, the samples were twin-jet electropolished using a mixed solution with 5% Perchloric acid and 95% methanol at -40°C to perforation for TEM observations.
4. The voltage was set as 27 V for 14YWT and 23 V for the other samples (Fe, Fe-10Cr, CNA3). The current was around 90-130 mA.

After twinjet electropolishing, the thickness of a wedge-shaped TEM sample with 3 mm in diameter would be about 100 nm near the hole produced by electropolishing. For an ideal sample, the thickness would continuously change from ∼15 μm near the edge to ∼50 nm near the perforation position, as shown in Figure 4.8.

4.4 Transmission Electron Microscopy (TEM)

In this study, the microstructures of the irradiated region were characterized using a ZEISS Libra 200HT FE MC TEM, a 300 kV Hitachi 9000 NAR TEM, a JEOL-2010F 200 keV TEM, and a 200 kV Cs-corrected JEOL JEM-ARM200F S/TEM. In general, the resolution limit of traditional TEM prevents it from resolving defects of a size less than ∼1 nm. Therefore, defects with dimensions below the TEM resolution limit could exist but are not

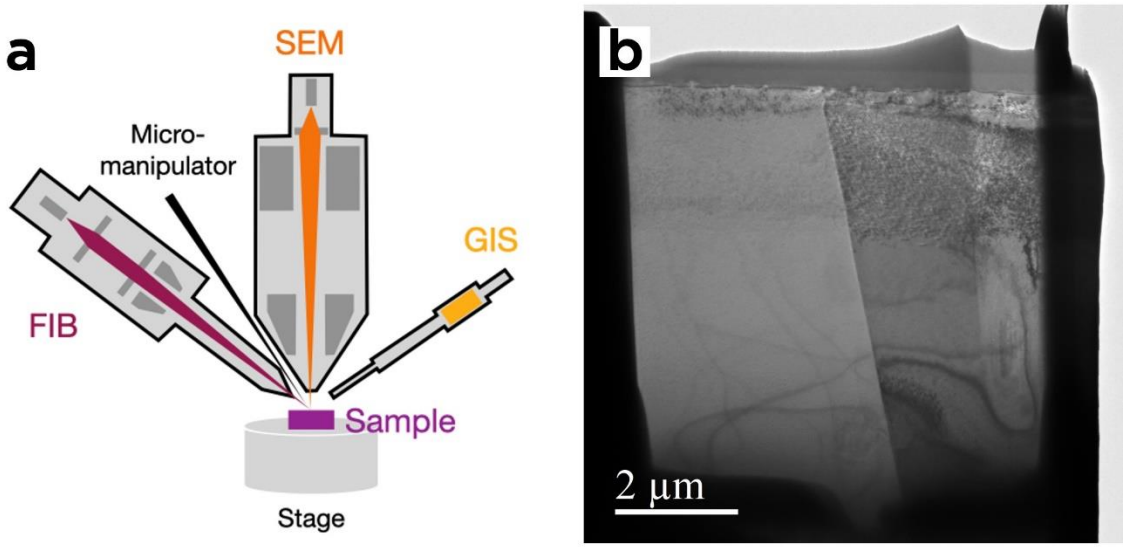

Figure 4.7 (a) Schematic of FIB+SEM crossbeam facility, and (b) example of a TEM sample prepared by FIB lift-out technique

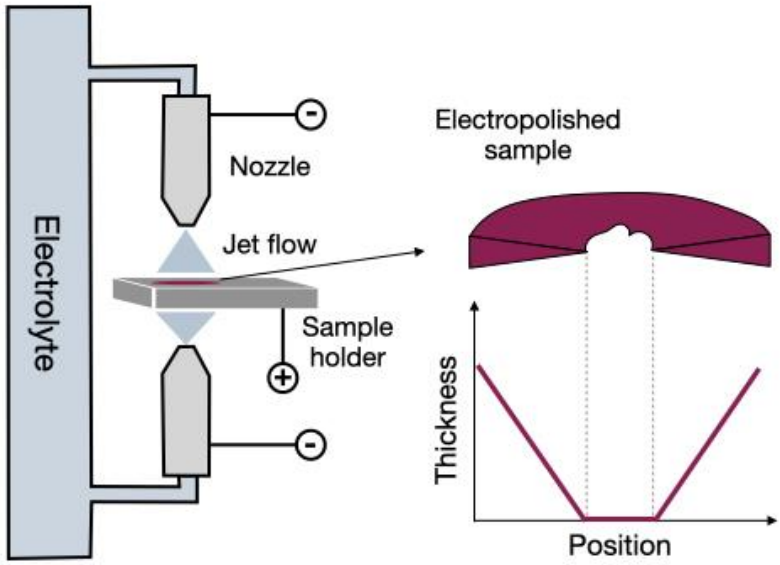

Figure 4.8 Schematic of twinjet electroplisher and electropolished samples.

observable. In addition, Energy-dispersive X-ray spectroscopy (EDS) was applied to verify the chemical composition of the specimens. Furthermore, electron energy loss spectroscopy (EELS) was used to measure the sample thickness and verify the chemical composition.

4.4.1 Basics of TEM

A basic TEM is composed of an electron emission source, a series of electromagnetic lenses, and the specimen stage, arranged in a vertical column vacuumed to a pressure below 10^{-7} Pa. As shown in Figure 4.9, similar to an optical microscope (although OMs use glass lens), TEM also has condenser lens, objective lens, and projector lens. Accelerated by the applied voltage, a coherent electron beam is first generated by the electron emission source. Traveling through the column, the beam is constrained and aligned by t electromagnetic fields produced by a series of lenses. Eventually, the electron beam interacts with the specimen, and the transmitted beam forms magnified images by focusing on a charge-coupled device (CCD) camera or a fluorescent screen. TEM can typically magnify objects up to several million times. The common accelerating voltage is 200 kV. Operating TEM with voltages above 200 kV provides higher electron beam intensity and better resolution. However, the specimens can get damaged by ionizing radiation at such high voltages.

4.4.2 STEM imaging

As its name implies, scanning transmission electron microscopy (STEM) is a combination of SEM and TEM. In STEM mode, the electron beam is converged to a fine probe (Figure 4.10). The transmitted signal is collected as a function of the beam location as it scans across the sample. With the development of a spherical aberration (Cs) corrector, which leads to a higher-intensity but smaller electron probe, a STEM equipped with the Cs corrector could provide atomic-resolution images and perform elemental analysis of one atomic column. Based on the inner- and outer- collection angle of the detectors for STEM imaging, there are ABF (annular bright-field), LAADF (low-angle annular dark-field), and HAADF (high-angle annular dark-field) images. For the high-resolution STEM images in

this study, with a camera length of 8 cm, the HAADF detector was set to collect electrons scattered between 68 and 280 mrad, the LAADF detector was set to collect electrons scattered between 30 and 120 mrad, and the ABF detector was set to collect electrons scattered between 17 and 34 mrad. In general, ABF and LAADF images would still show diffraction contrast or difference of specimen thickness dependence due to the partial collection of the Rutherford scattering (elastic) signal, which dominates at lower angles. HAADF images collect thermal diffuse scattering (quasi-elastically) signals and are more sensitive to the atomic number. When applied in a restricted zone-axis orientation, the HAADF scattering signal from a single column of atoms is strongly dependent on the atomic number (roughly $Z^{1.7}$, hence it is also referred to as Z contrast images) and the thickness of the sample.

4.4.3 Spectrometry and elemental analysis

When a high-energy electron beam transmits through the sample, the injected electrons may interact with the constituent atoms of the material and generate various types of signals for material characterization (Figure 4.11). The main types of signals used in TEM/SEM include transmitted electrons, characteristic X-rays, secondary electrons (SE), back-scattered electrons (BE), Auger electrons, etc. This section focuses on the EDS and EELS techniques used in the present study. Both techniques are widely used for chemical composition analysis. The main differences between the two techniques are summarized in Table 4.5.

Energy Dispersive X-ray Spectroscopy (EDS)

Energy-dispersive X-ray spectroscopy (EDS, EDX, XEDS, or EDXS), also known as energy dispersive X-ray analysis (EDXA or EDAX), is an analytical technique used for compositional analysis of materials. While incident electrons excite the specimen, the constituent atoms may dissipate some of the absorbed energy by ejecting a core-shell electron. When the higher energy outer-shell electron proceeds to fill an empty place, it releases the difference in energy as characteristic X-rays, which correspond to the atom types (element). This then allows for chemical characterization or elemental analysis. In

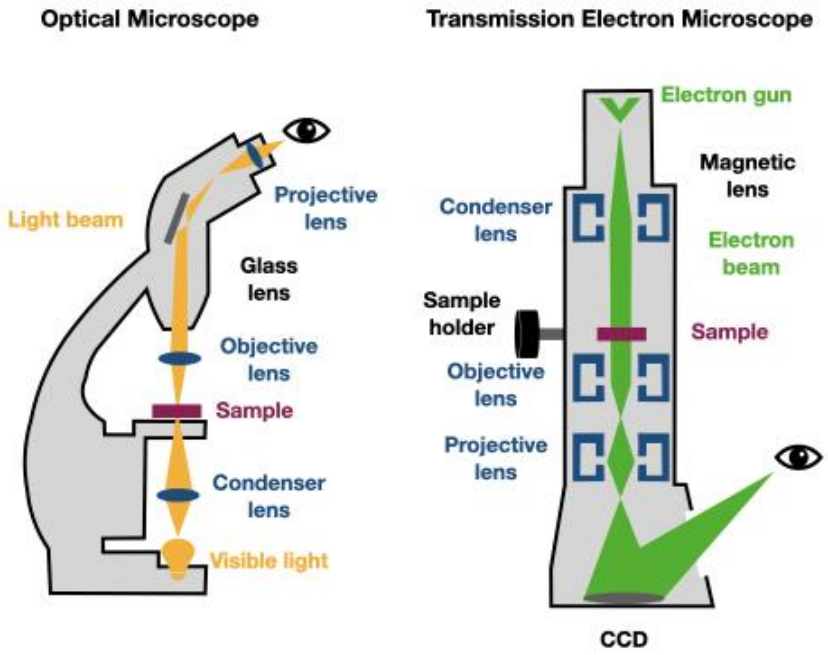

Figure 4.9 Schematic comparison of the basic components between TEM and OM.

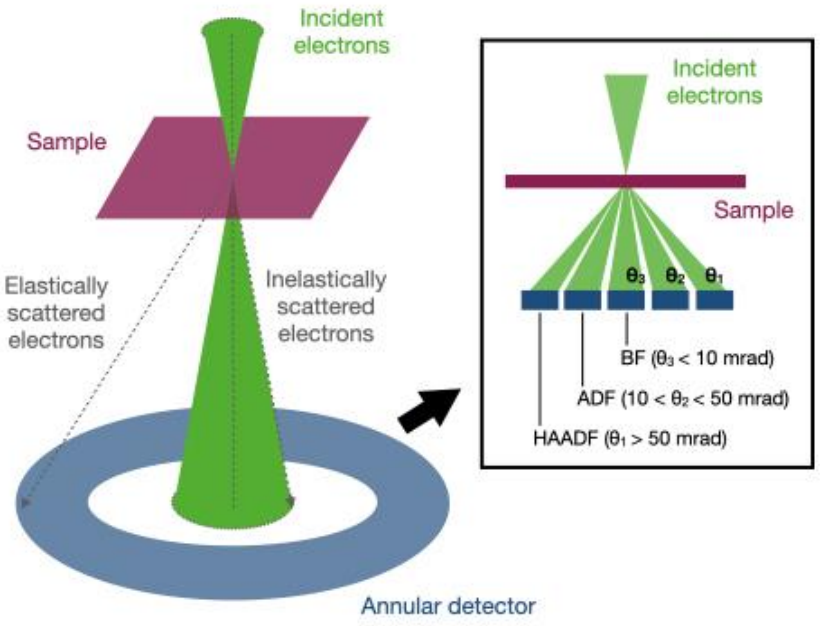

Figure 4.10 Schematic of STEM and STEM detectors.

general, the peak position of the spectrum identifies the element, whereas the intensity is related to the element concentration.

In practice, several artifacts can be produced in the spectrum and could result in misinterpretation:

1. Escape Peak (signal detection artifacts): Because of the limitation of the detector, a small fraction of X-ray energy is lost (not transformed into electron-hole pairs). An escape peak (Si) may appear in the spectrum below the true characteristic peak position.
2. Internal-Fluorescence Peak: After a long counting time, a small peak from the detector dead layer (Si, Ge, or Li) may occur in the spectrum.
3. Sum Peak: The sum peak arises when the electronics are not fast enough. In other words, two or more photons enter the detector at the same time. This could be avoided by reducing the brightness (dead time <60%).
4. Post-Specimen Scattering: Peaks that are not generated by the electron probe in the analysis region. These artifact signals may come from the pole piece (Fe) or TEM grid (Cu). To minimize the effects of post-specimen scattering, it is suggested to remove the objective diaphragm, operate as close as possible to zero tilt, and use a beryllium specimen holder and grid.

In this study, the depth profile of the implanted Ni ions was analyzed using an FEI Talos F200X analytical scanning TEM (STEM) equipped with a SuperX EDX system which consisted of four silicon drift detectors (SDD) surrounding the sample and a JEOL 2010F 200 KV TEM microscope. An Oxford AZtec software platform was used for quantitative EDS line scan analysis. The STEM-EDS line-scan profile consisting of 250 measurement points distributed over a line of 3 μm in length was recorded with an acquisition time of 20 seconds per measurement point.

Electron Energy Loss Spectroscopy (EELS)

Electron energy loss spectrum is the energy distribution of electrons that loss energies (specimen absorption energy) when passing through the specimen. Apart from EDS that only provides elemental information, EELS includes elemental, chemical, and dielectric information from the inelastic scattering electrons. EELS is typically applied to

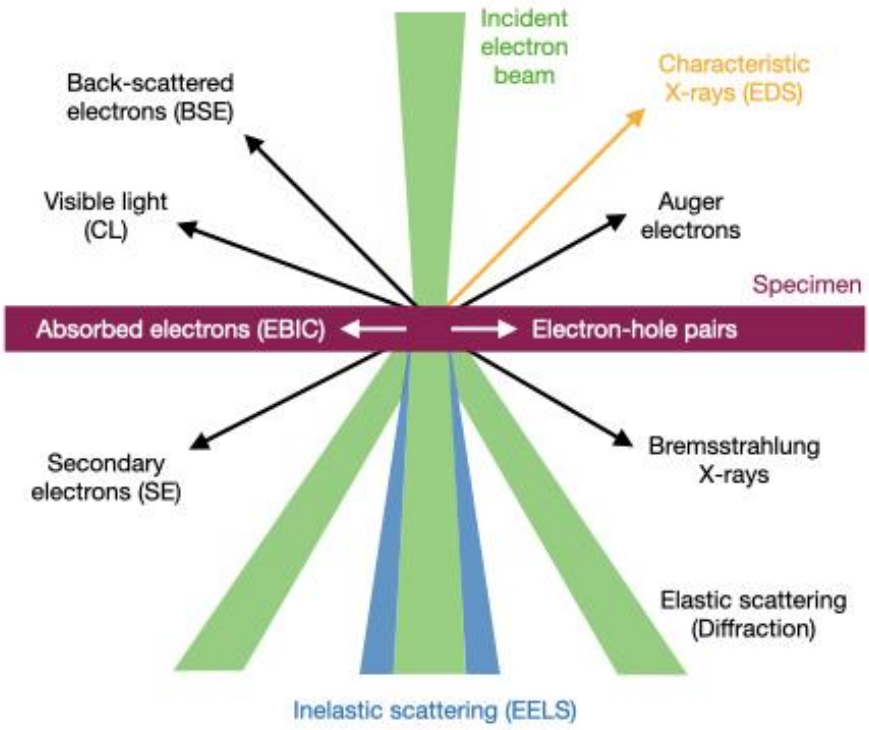

Figure 4.11 Signals from electron beam and specimen interactions. (CL: cathodoluminescence, EBIC: electron-beam-induced current.)

Table 4.5 Comparison between EDS and EELS.

EDS	EELS
Provides elemental information only	Elemental, chemical, and dielectric information
Inefficient signal generation, collection, and detection	Very efficient in every aspects compared to EDS
Slow technique (hours)	Fast technique (seconds to minutes)
Energy resolution >100 eV (frequent overlaps)	Energy resolution 0.3-2 eV (fewer overlaps)
High detection efficiency for high Z elements	High detection efficiency for low Z elements
Artifacts from column and other parts of sample	No artifacts like in EDS
Inefficient X-ray mapping	Efficient X-ray mapping
Better signal to background ration	Worse signal to background ratio

measure specimen thickness, analysis of the elemental composition, and phase identification from EELS fine structure. In addition, EELS is also applicable to studies of electronic band structure and chemical bonding, atomic radial distribution function, bandgap analysis, and dielectric response.

As shown in Figure 4.12, a complete EELS spectrum has three main regimes:

1. Zero loss regime: the zero-loss peak locates in the energy range of -2 to 5 eV (depends on the electron gun type). The peak is composed of elastically scattered electrons and quasi-elastically scattered electrons (energy loss <0.01 eV; due to phonon excitation). A zero-loss alignment is important before beginning any other analysis. Due to the energy spread of the incident beam, the tail of the zero-loss peak needs to be precisely subtracted.
2. Low loss regime: the low loss regime is in the energy range of 1 to 50 eV. The signal in this regime is mostly contributed from the plasmon excitation and inter-band transition between the valence and conduction bands. The combination of zero loss and low loss regime provides the bandgap, dielectric properties, and specimen thickness information.
3. Core loss regime: The core loss regime is typically in the energy range of 50 to 2,000 eV. In this regime, edges that arise due to inner-shell ionization are characteristic of the elements present in the specimen. In addition, for the same element, the characteristic edge profile varies with different chemical bonding, also known as the electron energy loss near edge structure (ELNES). Approximately 50 eV above the ELNES regime, spectrum oscillations due to the ejected electrons with low kinetic energies could be observed, and so-called the extended energy loss fine structure (EXELFS). This regime contains the information of short-range order and atomic radial distribution function.

In this study, the sample thickness was estimated by EELS. The most common procedure for estimating specimen thickness within a region defined by the incident beam is to record an EELS spectrum in the low-loss regime and compare the area under the zero-loss peak (I_0) with the total area under the whole spectrum (I_t) using the "Log-Ratio Model." This method is based on the kinetic energy loss of scattered electrons. Details can be found

in the textbook by Williams and Carter [92]. According to the model, the foil thickness (t) can be estimated from EELS by:

$$t = \lambda \ln \frac{I_t}{I_0} \tag{4.1}$$

$$\lambda = \frac{106F(E_0/E_m)}{\ln(2\beta E_0/E_m)} \tag{4.2}$$

Where λ is the average mean free path, E_0 is the incident electron energy, E_m is the average energy loss related to the atomic number, F is the relativistic correction term, and β is the collection semi-angle (in mrad). The volume density of cavities or loops was obtained from TEM images by dividing their areal density by the estimated foil thickness (see sec 4.4.4 for details). For the log-ratio model, the typical error in λ values ranges between 25-30% due to inherent error in estimating electron mean free paths.

4.4.4 Image contrast and analysis of defects

Defect strain field contrast

The TEM image intensity is related to the amplitude ($I \propto |\phi|^2$) of the wave function of directed (ϕ_0) and diffracted (ϕ_g) electron beam. Considering the lattice distortion (R), the modified Howie-Whelan equations are written as [92]:

$$\frac{d\phi_0}{dz} = \frac{\pi i}{\xi_0}\phi_0 + \frac{\pi i}{\xi_{-g}}\phi_g exp[2\pi i(sz + g \cdot R)] \tag{4.3}$$

$$\frac{d\phi_g}{dz} = \frac{\pi i}{\xi_0}\phi_g + \frac{\pi i}{\xi_g}\phi_0 exp[-2\pi i(sz + g \cdot R)] \tag{4.4}$$

The Howie-Whelan equations imply that a defect cannot bring on additional contrast when $g \cdot R = 0$. However, if $g \cdot R \neq 0$, the defect strain field of the distorted lattice will change the image contrast and become visible.

For a single dislocation, the lattice distortion (R) is:

$$R = \frac{1}{2\pi}\left(b\phi + \frac{1}{4(1-v)}\{b\phi + b \times u(2(1-2v)\ln r + \cos 2\phi)\}\right) \tag{4.5}$$

This equation indicates that $g \cdot R$ is proportional to $g \cdot b$ or $g \cdot b \times u$. Therefore, for most cases, if $g \cdot b = 0$, the dislocation would be invisible because the diffracting planes are parallel to R. This is also known as the g-dot-b invisibility criterion. Technically, dislocation can be visible even if $g \cdot b = 0$ when $g \cdot b \times u \neq 0$. The reason for this is the bucking of the glide planes, which leads to a relatively lower dislocation strain field contrast.

Crystal orientation and diffraction pattern

In addition to the $g \cdot b$ invisibility criterion, crystallographic information is also required to quantify the density and Burgers vector of dislocations and dislocation loops. That is, a specific zone axis of the interested phase needs to be identified by tilting the sample to match the corresponding diffraction or Kikuchi pattern of the zone axis. Based on several detailed experimental studies [93-95] combining multiple sample tilting for loop type analysis in BCC Fe, the dislocation loops considered in this study are limited to $\frac{a}{2}\langle 111 \rangle$ and $a\langle 100 \rangle$ loops. Figure 4.13 illustrates the diffraction pattern of BCC Fe under the three common low index zone axes ([100], [110], and [111]), and their corresponding dislocation loop map without considering the $g \cdot b$ invisibility criterion. For example, when the sample is tilted along the [100] zone axis, $\langle 111 \rangle$ loops would be elliptical loops, while [001] and [010] loops are edge-on loops, and [100] loops are plan-view loops.

Along the zone axis, due to the interaction of Bloch waves and atom columns (for S<0), the TEM image intensity would be relatively low with dark contrast. Here, S is the excitation error, which is the deviation from a Bragg condition for a certain reflection g. Therefore, dislocation and dislocation loops are usually imaged under weak beam conditions, where S>0. Weak beam dark field (WBDF) imaging is a relatively high-resolution imaging technique for defect analysis. The dislocation line thickness is only about 3 nm in WBDF images, while the dislocation line thickness of dark field images at two-beam conditions could be 16-40 nm. The procedure to set up a weak beam dark field condition is summarized below:

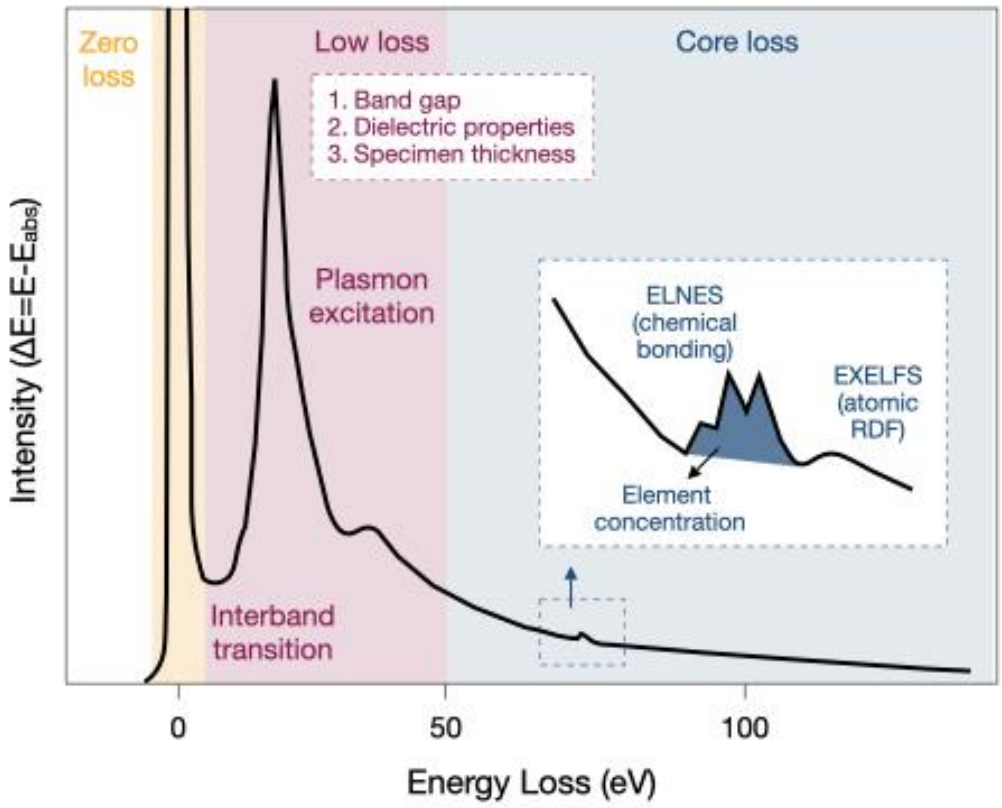

Figure 4.12 EELS spectral information.

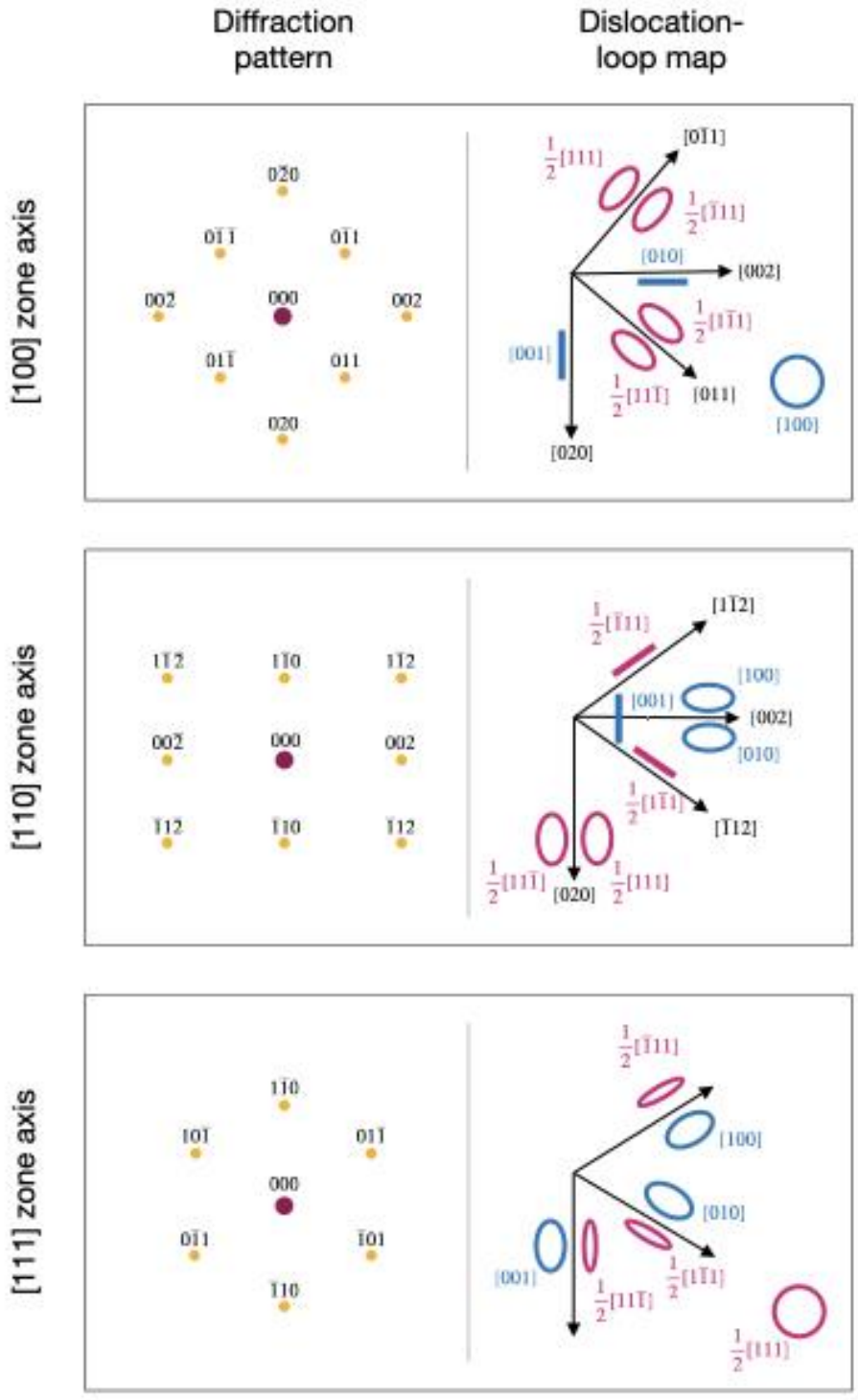

Figure 4.13 Diffraction pattern of BCC Fe and corresponding dislocation-loop map along specific zone axes.

1. In BF-DIFF mode, follow the Kikuchi line and tilt the sample to a two-beam diffraction condition, as shown in Figure 4.14a (T and g excited).
2. Switch to DF-DIFF mode, use the BEAM TILT function to tilt the direct beam (T) to the "g" position, as shown in Figure 4.14b. This condition is also known as the central dark field condition.
3. Switch back to BF-DIFF mode, tilt the sample to the other two-beam condition, where T and -g are excited (Figure 4.14c). Note that S should be slightly larger than 0.
4. Use the smallest objective aperture to select the "T" spot.
5. Switch back to BF-IMAGE mode and adjust the image focus to get a BF image at two-beam condition.
6. Switch to the DF-IMAGE mode to get the WBDF image pair. Note that the exposure time should be less than 15 seconds.
7. Switch to DF-DIFF mode. Retract the objective aperture and record the diffraction pattern. The pattern should look like Figure 4.14d.
8. Switch to BF-DIFF mode to get the diffraction pattern of the BF image taken in step 5.

Fresnel-defocused bright-field TEM images

Fresnel fringes in TEM are produced by the interference of electrons scattered from the edge of the specimen with the incident electron beam. Likewise, Fresnel fringes would also appear around the He bubbles (or cavity) in irradiated materials when an electron beam is scattered from the edge of the bubbles. As shown in Figure 4.15, for under-focused images (negative defocus value, $\Delta f<0$), the bubbles generally appear as white dots surrounded by a dark fringe, while for over-focused images ($\Delta f>0$), fringe contrast is reversed. When the TEM image is in focus ($\Delta f =0$), the bubble is almost invisible (no significant contrast). In this study, cavity size was measured from TEM under-focused images. The volume density of cavities was also obtained from TEM under-focused images by dividing their areal density by the measured foil thickness. The under- and over-focused images were taken at Δf =-1 to -3 μm and Δf =+1 to +3 μm, respectively. The volume fraction of cavities was calculated by:

$$\Delta V = \frac{4}{3}\pi \Sigma \left(\frac{d}{2}\right)^3 \tag{4.6}$$

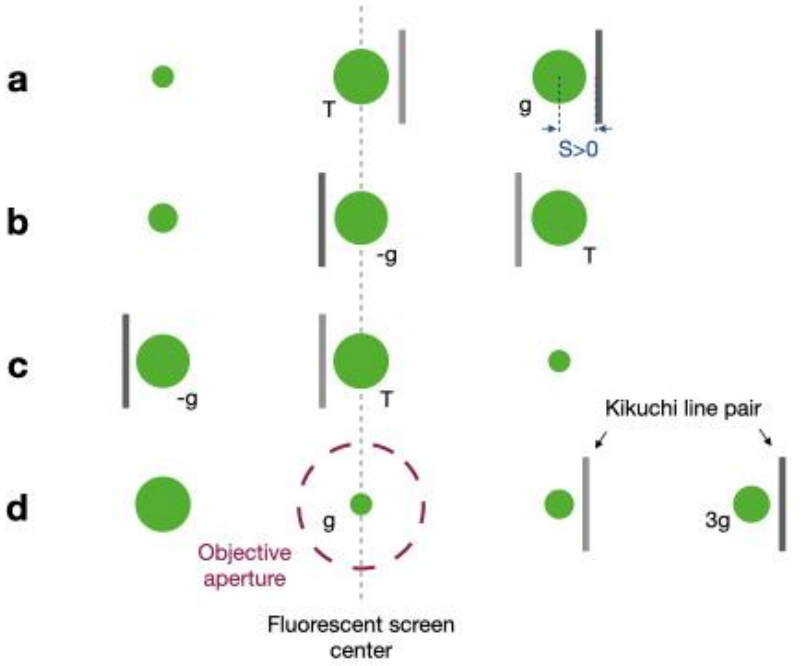

Figure 4.14 Two beam and weak beam diffraction condition

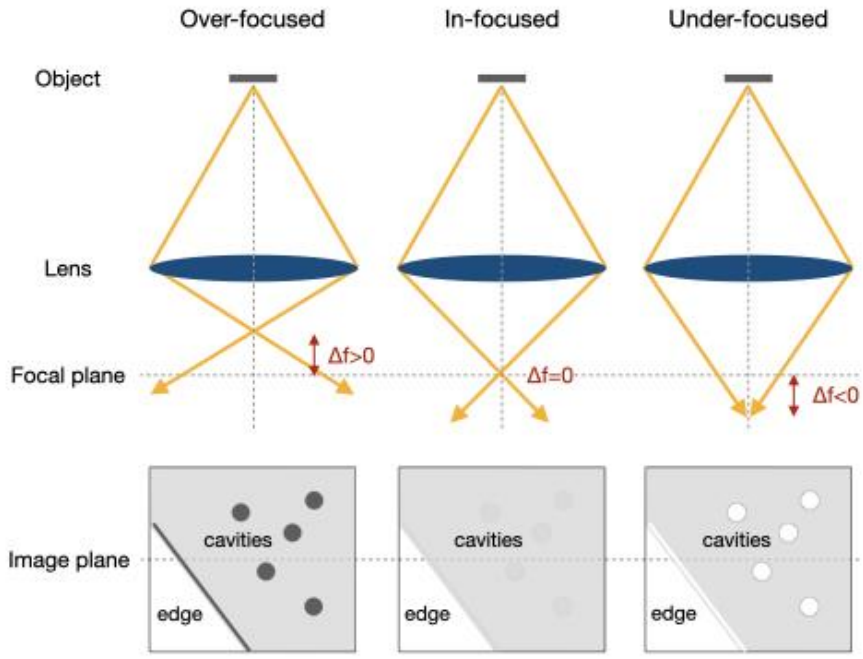

Figure 4.15 Fresnel fringes and defocus conditions.

and the volumetric swelling was determined from

$$S = \Delta V/(V - \Delta V) \tag{4.7}$$

where d is the diameter of a cavity, and V is the volume of the analyzed zone. The error bars in the figures considered the statistical counting errors and EELS thickness measurement errors (assumed ±20%) using general error propagation methods.

Chapter 5
Results

5.1 Cavities in Fission Relevant Conditions

5.1.1 Depth-dependent cavity microstructures

Identifying safe analysis regions for cavity microstructure quantification

Cross-sectional TEM images of depth-dependent cavity microstructures of Fe and Fe-10Cr for the five irradiation temperatures are compared in Figure 5.1. Cavities were observed in the midrange regions in both materials at all irradiation temperatures, with a near-surface cavity denuded zone and suppression of cavities (due to injected ions [3, 96, 97]) near the peak damage region. In most cases, the maximum cavity swelling was observed in a region immediately adjacent to the near-surface denuded zone, despite the damage dose being lower than in the deeper midrange region. Similar "peak swelling" transition regimes adjacent to the cavity denuded zone along grain boundaries or near the irradiated surface have been reported for other neutron or ion irradiated materials [21]. This enhanced swelling region has been attributed to the escape of glissile self-interstitial atom (SIA) loops by 1-D migration [22]. The near-surface and implanted ion artifacts could be clearly seen in the quantitative measurement of the depth distribution of cavity size (diameters), cavity density, and cavity swelling summarized in Figure 5.2 (corresponding to the TEM images of cavities in Fe and Fe-10Cr shown in Figure 5.1). In Fig. 3, the size and number density of cavities were used to calculate depth-dependent cavity swelling with a constant bin width of 250 nm. For depths below 750 nm, the absence or lower cavity density near the surface was found in both Fe and Fe-10Cr samples especially at higher temperatures above 500°C (Figure 5.2c-d). The local maximum of cavity size adjacent to the denuded zone at all temperatures was obvious in Fe (Figure 5.2a) but not in Fe-10Cr (Figure 5.2b). The locally larger cavity sizes were the most prominent for the irradiations at 470 and 550°C in Fe. At depths above 1500 nm, the cavity size and density were both suppressed in the two materials. Based on the cavity size and density results, the calculated

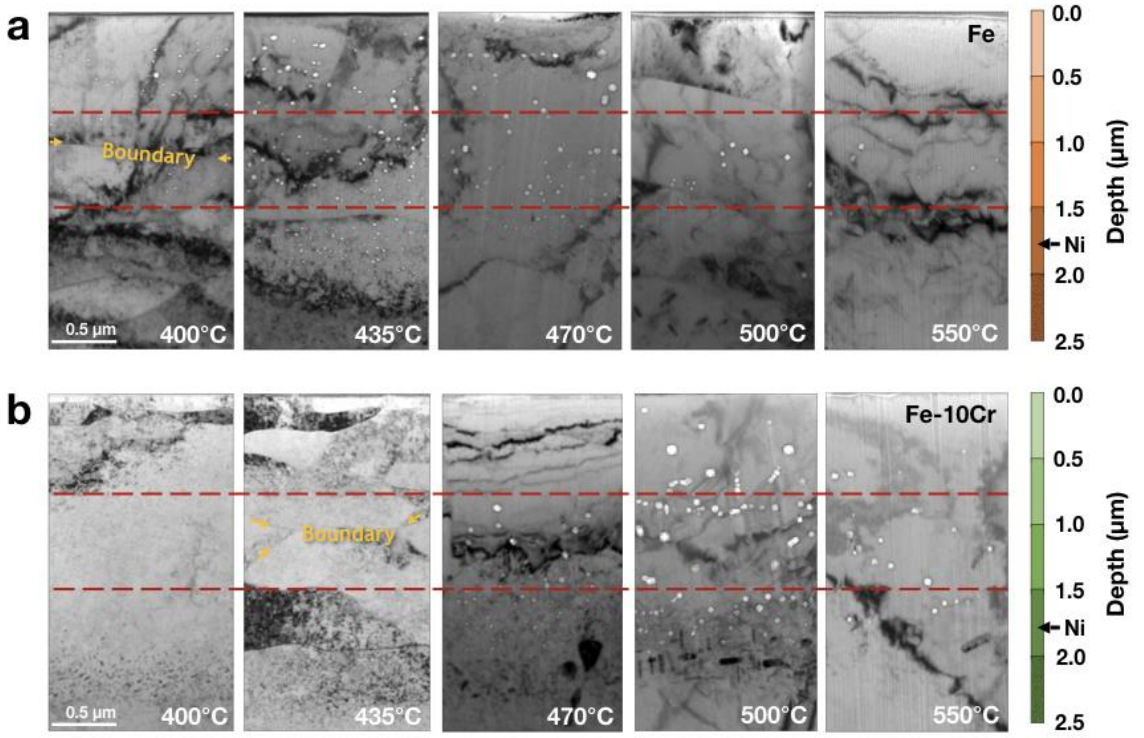

Figure 5.1 Cross-section TEM bright-field under focused images (defocus value ~ -800 to -1000 nm) of 0.1 appm He/dpa dual-beam irradiated (a) Fe and (b) Fe-10Cr alloys at 400-550°C. The black arrow indicates the depth location of the Ni peak concentration as measured by STEM-EDS.

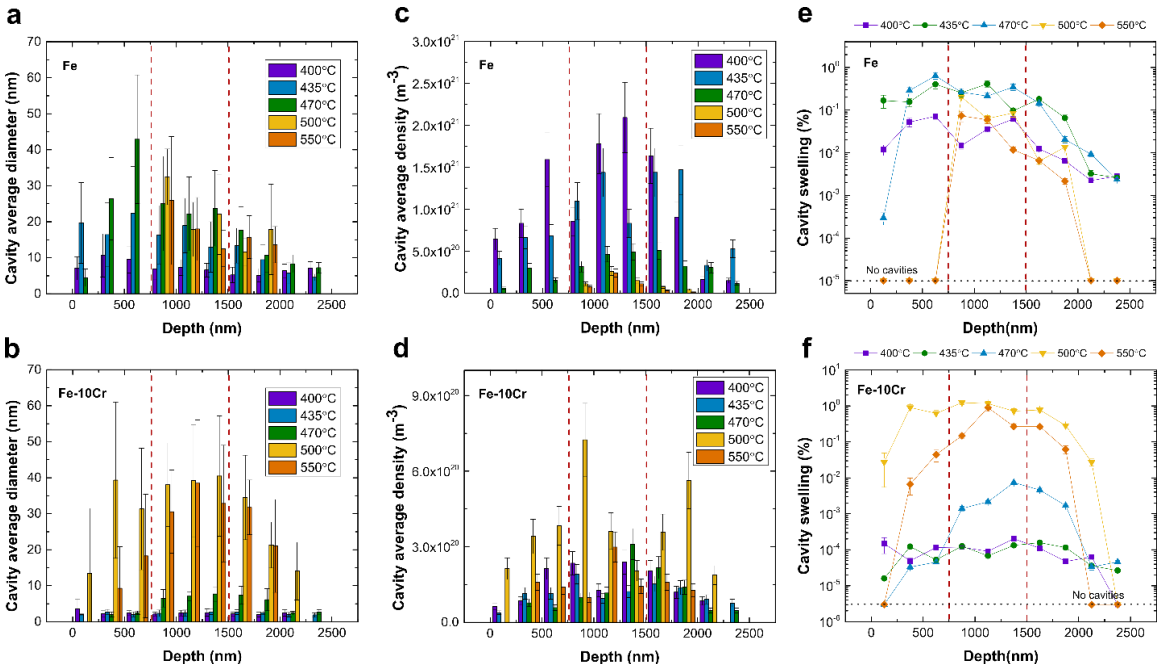

Figure 5.2 Average size, number density, and volume swelling of cavities in Fe (Figs. a, c, e) and Fe-10Cr (Figs. b, d, f) as a function of depth (0.1 appm He/dpa). The area between the red vertical dashed lines indicates the analysis midrange region.

volumetric swelling (Figure 5.2e-f) was generally suppressed near the surface (<750 nm) and at depths above ~1500 nm. At 550°C, Figure 5.2 also indicates a possible implanted ion effect for depths as low as 1100 nm, especially for pure Fe. For the implanted ion threshold, a content below 0.01 at%/dpa was suggested in the study by Zinkle and Snead to minimize artifacts [3]. Overall, the suppression of swelling at the surface and near the implanted ion regions was observed in all the 30 examined test conditions. Therefore, in this study, all the cavity sizes and densities for comparative analysis were averaged over a midrange region 750-1500 nm below the irradiated surface to minimize influence of the near-surface denuded zone (with the adjacent artificially enhanced swelling zone) and the injected interstitial region. This midrange analysis region is bounded by dashed lines in both Figure 5.1 and Figure 5.2 (as well as in subsequent figures), and corresponds to ~30 dpa and co-implanted with 0.1 appm He/dpa.

Dislocation loop and network dislocation microstructures were observed at all conditions at depths ~400-2000 nm (see Figure A.4 in supplementary for details). A brief discussion of the correlation between the cavities and loops/networks is given in the supplemental information. In addition, sub-grains were observed in most of the samples after irradiation, whereas they were not observed in the as-received materials. For cavity swelling quantification, we avoided the areas with sub-grains in the cross-sectional TEM samples as much as possible and counted the cavity areal density within a >2 μm wide range (parallel to the surface) to minimize the sub-grain artifacts. A comparison of the depth distribution of the cavities, dislocation loops (or dislocation networks), and Ni profile are demonstrated in Figure A.5.

In order to better understand the peak location and diffusion of the injected Ni ions, we conducted STEM-EDS line scans on several samples (Figure 5.3). In Figure 5.3a, the TEM bright-field image of Fe irradiated at 470°C shows a depletion of cavities near the surface (< 250 nm) and near the mean penetration depth of Ni ions (~1800 nm). An enhanced swelling (ES) region next to the cavity denuded zone (DZ) is also shown in the same figure. Gaussian curve fitting of the Ni profiles was applied to the Fe and Fe-10Cr samples (irradiated at 400-550°C) for quantitative values of the Ni peak center (Figure 5.3b) and the full width at half maximum (FWHM) of the Ni profiles (Figure 5.3c). In

Figure 5.3b, the STEM-EDS measurement of the injected Ni profile revealed the peak position of the implanted Ni ions was substantially lower than the estimated depth calculated by SRIM (~700 nm shift), which is apparently due to an error in the stopping power model given by Ziegler, Biersack, and Littmark (ZBL stopping power) used in SRIM2013 [98]. For 8 MeV Ni, the measured and predicted mean ion ranges in pure Fe are 1.8 and 2.5 μm, respectively, corresponding to a 38% overestimate of the 8 MeV Ni ion range in Fe by SRIM. Considering Fe ions, which have a similar atomic number and weight as Ni ions, the predicted 8 MeV Fe ion range in Fe by SRIM (yellow dashed line in Figure 5.3b) is only about 1.95 μm, which is much closer (8% difference) to our experimental results for 8 MeV Ni ions. Due to the large overestimation of 8 MeV Ni ion in Fe penetration depth in SRIM (and possibly for other target materials including Ni where experimental confirmation of the ion range would be difficult because the ion and target atoms are chemically indistinguishable), special care is required to identify suitable safe-analysis mid-range regions for ion-irradiation studies using the ion source of Ni. Apart from the peak location of the implanted ions, enhanced diffusivity (considering both radiation enhanced diffusivity and thermal diffusivity) of Ni atoms with increasing temperature could further broaden the injected Ni band compared to the SRIM implanted ion profile. This effect is specifically reflected in the increase in FWHM of the implanted Ni STEM-EDS line scan profile with increasing temperature in Figure 5.3c, and in the higher measured Ni levels compared to SRIM predictions at all depths from ~300 nm to the peak implanted region, i.e., the “tail” of the implanted Ni profile in the irradiated region extends considerably farther than predicted by SRIM due to radiation enhanced diffusion. In summary, as shown in Figure 5.3d, based on our TEM images and STEM-EDS analysis, to avoid the surface artifacts and the implanted ion artifact, even with a relatively high energy ion source, the safe analysis regime is limited for ion irradiation studies on radiation damage, especially at higher temperatures where the effects of the two artifacts are enhanced.

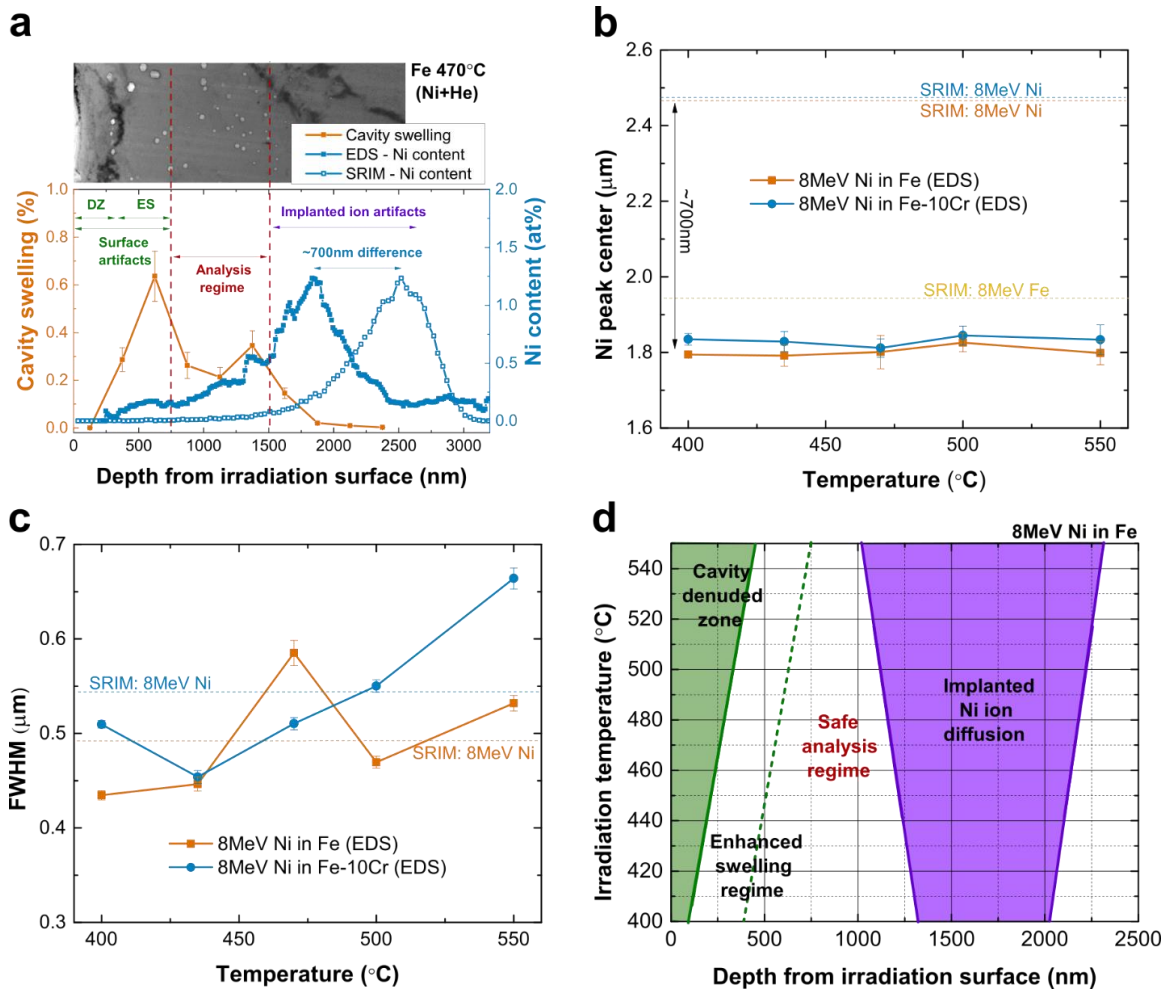

Figure 5.3 STEM-EDS analysis of (a) implanted Ni profile compared to SRIM simulation and cavity swelling (DZ and EZ stand for the cavity denuded zone and enhanced swelling region, respectively); (b) Ni concentration at the implantation peak center; EDS vs. SRIM prediction and comparison with SRIM predictions for 8 MeV Fe and (c) Full width at half maximum (FWHM) of Ni profile in Fe and Fe-10Cr observed from EDS and estimated from SRIM; (d) identification of the safe analysis depths: temperature- and depth-dependent regions affected by the surface and injected ions for Fe irradiated with 8 MeV Ni. The implanted ion region shown in Fig. d is based on experimental EDS measurements at multiple temperatures.

Temperature effect on the cavity size, density, and shapes

Cavities were observed in all thirty investigated ion irradiation conditions (six Fe and Fe-Cr alloys at five irradiation temperatures), as shown in the TEM under-focused bright-field images in Figure 5.4. All the images were taken from a relatively safe analysis regime at a depth of 750-1500 nm below the surface as outlined by the dashed lines in Figure 5.1. For all the samples, the cavities in the safe analysis regime were mostly homogeneously distributed. However, along the sub-grains formed after irradiation (see Figure 5.1 for the Fe-400°C TEM image at depth ~1 μm for an example), localized cavity denuded zones were found. Heterogeneous nucleation of cavities inside the dislocation loops or at grain boundaries, as reported in ref. [99], were not observed in this study. We observed no evidence for a bimodal cavity size distribution in any of the irradiated materials, which could mainly be due to the relatively low He production rate (0.1 appm He/dpa). Faceting in the larger cavities (>10 nm) was observed in the high-temperature irradiated samples (Figure 5.4). The three basic cavity shapes (cubic, octahedral, and dodecahedral) in ferritic alloys summarized by Gelles et al. [100] (see inset figures in Figure 5.4 for the possible ideal cavity shapes) agrees with our observed facet planes as shown in Figure 5.4 with the truncated cubic/octahedral shapes and the truncated cubic/dodecahedral shapes. The shapes of the facet cavities are summarized in Table 5.1, where F is the truncation parameter. At lower temperatures (<435°C), the small cavities were mostly spherical. After the formation of faceted cavities at elevated temperatures, the truncation parameter decreased with increasing temperature. That is, at intermediated temperatures, the cavity shapes were a mixture of truncated cubic/octahedral or truncated cubic/dodecahedral shapes, whereas the cavity shape type became less truncated (unitary) at high temperatures.

At 500°C, the cavity size in Fe-3Cr and Fe-10Cr were similar with the highest average diameter ~40 nm among all 30 irradiated samples. At 550°C, the cavity size of Fe, Fe-3Cr, and Fe-10Cr was smaller than at 500°C. Based on traditional cavity growth and nucleation theory [26, 101], the cavity size would generally be expected to increase with increasing temperature. However, at very high temperatures, the rate of thermal emission of vacancies from underpressurized cavities rapidly increases (cavity shrinkage rate

proportional to the vacancy self-diffusion coefficient) [26, 101]. In other words, cavity shrinkage rate at high temperature competes with the increasing growth rate. This agrees with the observed smaller cavity size (Fe, Fe-3Cr, and Fe-10Cr) and decreased growth rate (Fe-14Cr, Fe-10Cr-C, and Eurofer97) as the irradiation temperature increased from 500°C to 550°C. Regarding the cavity density dependence on temperature, based on the same cavity growth and nucleation kinetic rate theory concepts the cavity density should monotonically decrease with increasing temperature. Such a monotonic decrease in cavity density with increasing temperature was observed in all alloys for irradiation temperatures near or above 470°C, and in the pure Fe sample for all investigated irradiation temperatures. Nonetheless, as shown in Figure 5.5b, the measured cavity density exhibited a peak near 470°C for most of the irradiated Fe-Cr alloys. The number densities of TEM observable cavities in the five Fe-Cr alloys at 400°C were about an order of magnitude smaller than the measured cavity density in Fe. Since the measured cavity sizes at 400 and 435°C for all but Fe and Eurofer97 were below 2 nm, it is considered likely that numerous cavities in the other alloys (with TEM foil thickness ~80 nm) may not be identified and counted by the Fresnel contrast imaging technique [102]. Both the cavity size and density were relatively low for Eurofer97 over the entire investigated temperature range.

5.1.2 Peak cavity swelling temperature

Based on the cavity size and number density extracted from the midrange region (safe analysis zone), the total volumetric swelling (the sum of each cavity volume) of the Fe and Fe-Cr materials as a function of temperature at a fixed dose rate of 1.4×10^{-3} dpa/s is given in Figure 5.6. Comparing the swelling of all thirty sample conditions, Fe-3Cr at 500°C had the highest cavity swelling with a value of ~2%. The peak swelling temperature for all the Fe-Cr alloys was around 500°C. Conversely, pure Fe exhibited a ~50°C lower peak swelling temperature than the Fe-Cr alloys.

In general, the temperature dependence of cavity swelling involves a competition between point defect recombination, point defect absorption by sinks, and thermal vacancy emission at higher temperatures [103]. Previous ion irradiation studies have estimated a peak swelling temperature for both Fe and Fe-Cr alloys in the range of 450-580°C for

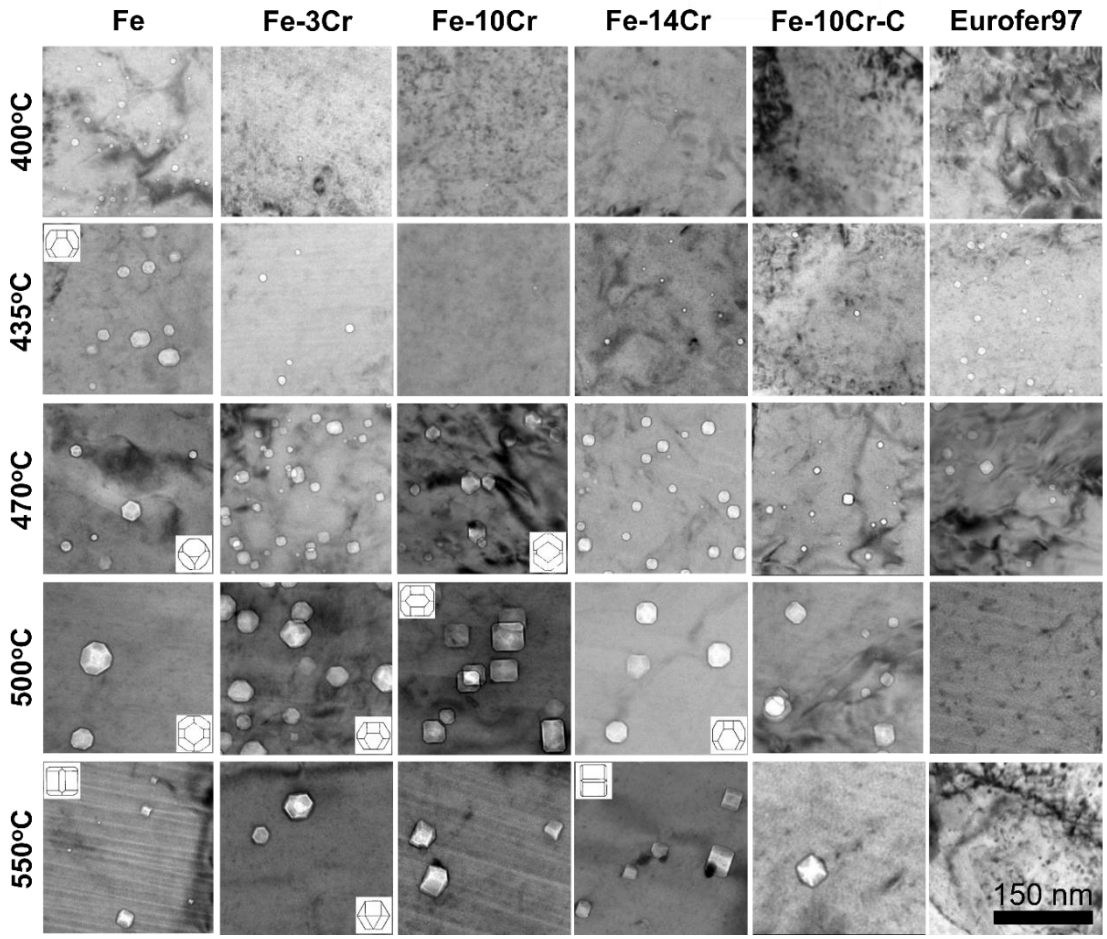

Figure 5.4 TEM images of cavities in dual-ion irradiated Fe and Fe-Cr alloys at 400-550 °C with 0.1 appm He/dpa. Images were taken from the midrange irradiated region (~1 μm depth), and the corresponding ideal truncated cubic/octahedral and cubic/dodecahedral cavity shapes are shown as inset images (inset figures are reproduced from Ref. [100]).

Table 5.1 Cavity shapes of the irradiated Fe and Fe-Cr samples at 400-550°C

	Fe	Fe-3Cr	Fe-10Cr	Fe-14Cr
400°C	spherical	spherical	spherical	spherical
435°C	truncated cubic/octahedral (F=0.6-0.7)	spherical	spherical	spherical
470°C	truncated cubic/octahedral (F=0.3-0.5)	approximately spherical	truncated cubic/dodecahedral (F=0.8-1.0)	approximately spherical
500°C	truncated cubic/dodecahedral (F=0.7-0.8)	truncated cubic/octahedral (F=0.4-0.6)	truncated cubic/dodecahedral (F=0.1-0.3)	truncated cubic/octahedral (F=0.3-0.5)
550°C	truncated cubic/dodecahedral (F=0.1-0.3)	truncated cubic/octahedral (F=0.4-0.6)	unidentified	truncated cubic/dodecahedral (F=0.1-0.3)

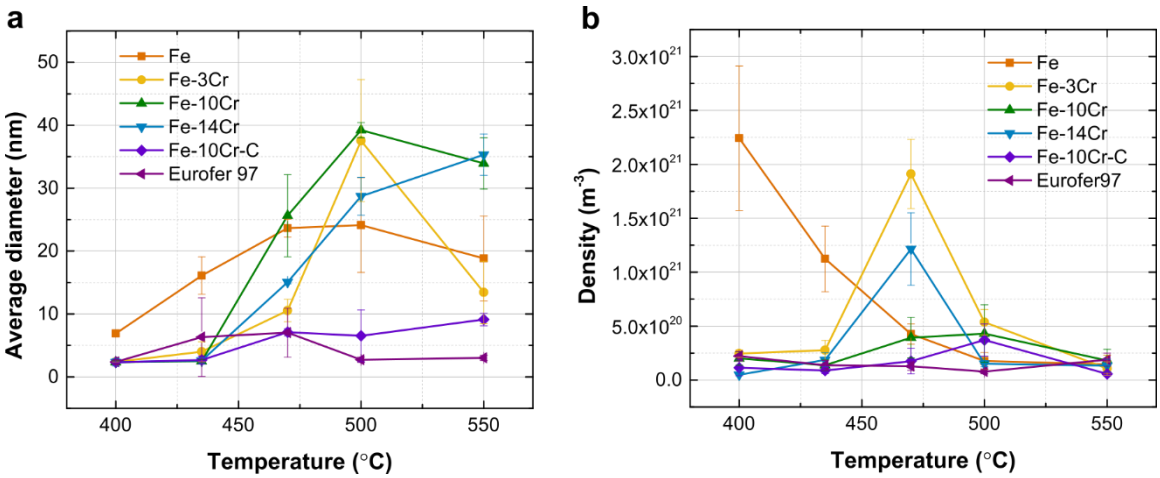

Figure 5.5 Comparison of the (a) cavity size (diameters) and (b) density in ion irradiated Fe and Fe-Cr alloys at 400-550°C, with 0.1 appm He/dpa. Cavity analysis was performed in the midrange irradiated region (~1 μm depth).

similar damage rates of ~1×10^{-3} dpa/s [39, 41, 45, 104]. The peak swelling temperature difference between Fe and Fe-Cr (observed with a ~50°C difference in the present study) has not been highly investigated. Comparing our 500°C pure Fe swelling value (~0.25%)to prior comparable dual ion beam studies with a similar dose rate of ~10^{-3} dpa/s and dose of 10-50 dpa at ~500°C [39, 40, 105, 106], our magnitude is relatively lower but in qualitative agreement with literature in the range of 0.2-1.3%. The larger swelling value in the previous studies could possibly be due to the ~100 times higher He/dpa ratio used in their studies. It is worth noticing that for studies with higher self-ion energies (4 MeV [104] and 10 MeV [106]) the average cavity size was 13-26 nm, which is closer to the average cavity diameter (~25 nm) of our Fe-500°C sample. On the other hand, for the studies using lower self-ion energies (2 MeV), the average cavity size was 2 nm [39] and 10 nm [40], at the damage rate of ~3×10^{-3} dpa/s and ~1.5×10^{-3} dpa/s, respectively. As described previously, it is possible that the injected ion effects could result in the suppression of cavity size. It should be emphasized that our results indicate that the addition of Cr above 500°C enhances the cavity swelling for the given irradiation doses. This finding is opposite to a recent ion irradiation study by Bhattacharya et al. [39] which showed that the swelling was suppressed ~10 times by the presence of 3-14% Cr, compared to pure Fe. At the dose rate of ~1.5×10^{-3} dpa/s, the maximum swelling value ~0.1% among the Fe-Cr alloys in their paper was found in Fe-10Cr at 157 dpa and 500°C, while >10% swelling occurred for the pure Fe sample.

5.1.3 Cavity swelling dependence on Cr content

The measured midrange cavity swelling as a function of Cr content in the high-purity Fe and Fe-Cr binary alloys is plotted in Figure 5.7 for all five of the investigated dual ion irradiation temperatures. This figure clearly shows that increasing Cr solute levels dramatically suppress cavity swelling in the ion irradiated Fe-Cr alloys below ~450°C. Conversely, the effect of Cr solute on cavity swelling is either very weak or leads to slightly enhanced swelling above ~450°C. Therefore, a difference in the effect of Cr on cavity swelling seems evident depending on whether the irradiation temperature is above or below

~450°C. At the two highest investigated irradiation temperatures, maximum swelling values were found for 3% Cr and 10% Cr at 500 and 550°C, respectively. However, the overall swelling variation was non-monotonic with respect to Cr content and exhibited different general behavior at different temperatures.

5.1.4 Swelling in Eurofer97, Fe-10Cr alloys, and Fe-10Cr-C alloys

Figure 5.8 shows the cavity swelling in Eurofer97 tempered martensitic steel that contained ~9% Cr, ~0.6% Mn, ~1% W, and ~0.2% V based on SEM-EDS measurements. Since the alloy composition and heat treatment for Eurofer97 was different from the high purity binary Fe-Cr alloys, the resulting microstructure is more complex. The prior austenite grain size of the as-received Eurofer97 material is ~10 μm which is roughly one order of magnitude smaller than the high purity Fe-Cr materials. The peak swelling temperature of the Eurofer97 steel with ~9% Cr was slightly smaller than the Fe-10Cr model alloy, and overall exhibited the lowest peak swelling value among all the investigated alloys with a peak swelling temperature comparable to pure Fe. However, the total swelling in the Eurofer97 steel was very small (<0.01%) at all irradiation temperatures. A comparable dual-beam study at higher He/dpa conditions (3 MeV Fe ions plus 17 appm He/dpa) on Eurofer97 at 500°C to a dose of 26 dpa also showed relatively modest swelling of 0.08% [107]. While it is possible that the impurity solute elements (e.g., C, N, O) in Eurofer97 materials could interact with point defects and thereby influence the incubation period and total volume swelling of cavities, other factors such as sink strength associated with the primitive (not radiation-induced) dislocations, smaller grain size and presence of carbides is expected to suppress the swelling.

As shown also in Figure 5.8, above 450°C, the C-containing alloy exhibits lower swelling compared to the high purity Fe-10Cr, which suggests that C (or mixed ferrite ad martensite structure) might suppress void swelling in this temperature regime. Considering dose rate effects (this will be discussed later), this temperature is equivalent to a neutron irradiation temperature of ~380°C, based on Eq 2.13. A neutron irradiation study on Fe-12Cr reported by Sencer et al. [108] indicated that the carbon impurity in Fe-12Cr

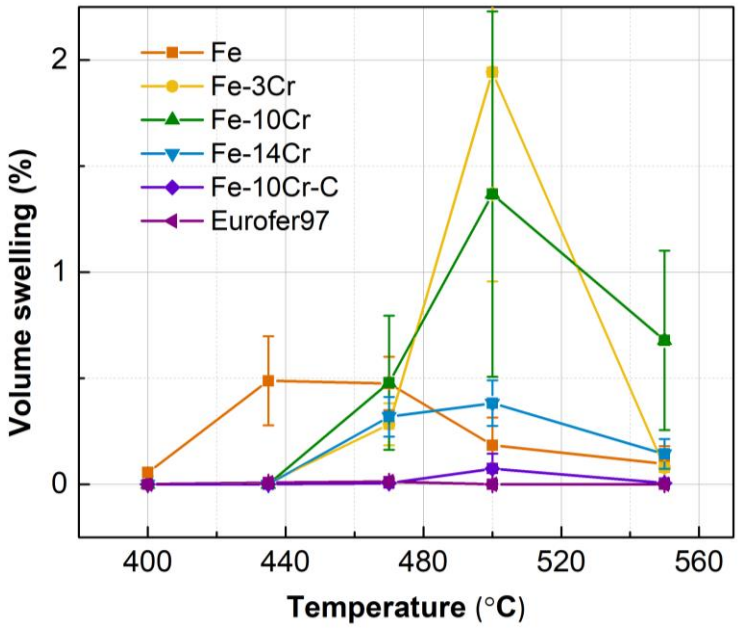

Figure 5.6 Dependence of cavity swelling on irradiation temperature in dual beam ion irradiated (0.1 appm He/dpa) Fe and Fe-Cr alloys. Cavity analysis was performed in the midrange irradiated region (~1000 nm depth).

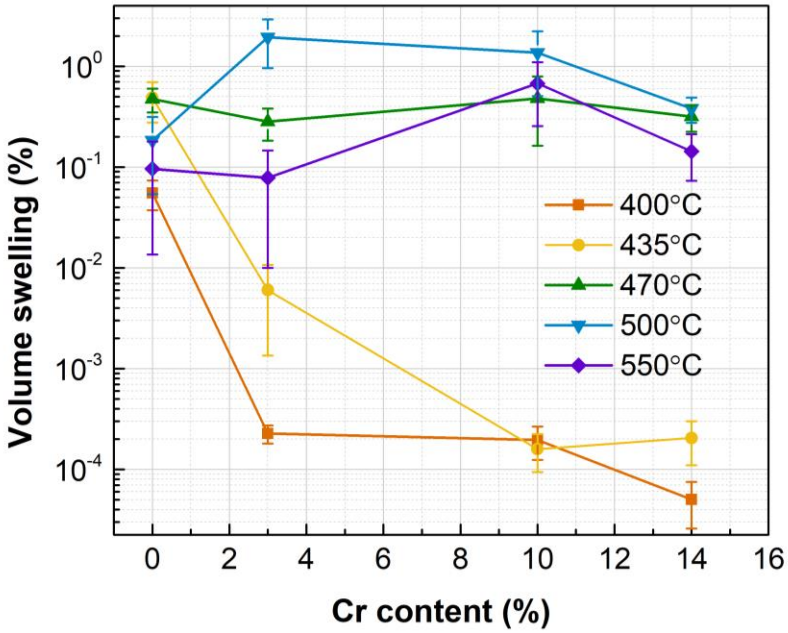

Figure 5.7 Variation of the cavity-swelling as a function of Cr concentration in the high-purity Fe and Fe-Cr dual-ion irradiated samples (0.1 appm He/dpa).

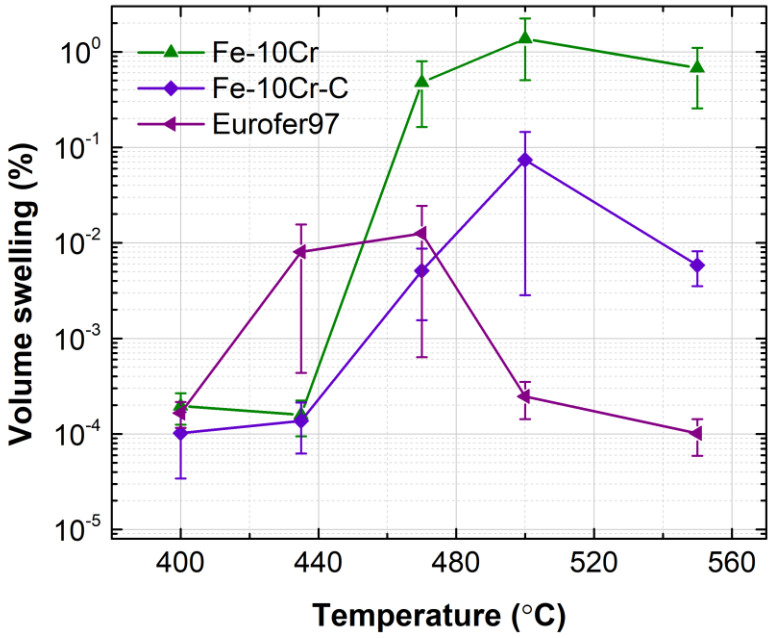

Figure 5.8 Result of carbon additions on cavity-swelling in Fe-10Cr, Fe-10Cr-C, and Eurofer97 (9% Cr) for dual ion irradiation at 0.1 appm He/dpa.

at temperatures below 454°C and doses below 48 dpa tends to monotonically decrease the swelling. At 482-650°C, however, an increase of C content to 0.1% led to very large increases in swelling. This observation seems to support our finding in the Fe-10Cr and Fe-10Cr-C alloys. But similar to the case of Eurofer97, we believe that the martensite structure present in the Fe-10Cr-C samples (Figure A.1) should be the most significant factor on the suppression of cavity swelling compared to binary Fe-10Cr [109]. The comparison of the Fe-10Cr and Fe-10Cr-C results in this study may not simply be attributed to carbon impurity effects due to the difference in matrix phases (ferrite vs. martensite). This study reveals that for studying C effect, it is imperative to verify the starting microstructure of the bcc Fe base alloys to avoid incorrect interpretation of carbon's influence.

5.1.5 APT study on the formation of Cr-enriched precipitates

Based on the Fe-Cr phase diagram (Figure 3.7), Fe-14Cr irradiated at 400°C has the highest possibility for α' precipitation compared to other samples. Although α' were not observed in the Fe-10Cr and Fe-14Cr samples by STEM-EDS, the Fe-14Cr sample irradiated at 400°C were selected for APT analysis to confirm if precipitates formed during irradiation. FIB was used to prepare samples for APT analysis. The samples were analyzed by the Local Electrode Atom Probe (LEAP) 4000X HR model APT located at the Center for Nanophase Materials Sciences (CNMS), Oak Ridge National Laboratory (ORNL). The collected data was analyzed by a self-developed cluster analysis algorithm (Python code) for the IVAS software to identify the precipitates and to quantify their size and density [82]. Cr-enriched precipitates were observed in all of the four APT samples in midrange (~1 μm) region of the irradiated Fe-14Cr sample. The midrange dose and dose rate were 30 dpa and 1.4×10^{-3} dpa/s, respectively. The APT reconstructions are presented in Figure 5.9, and the information of the precipitates are listed in Table 5.2. The average number density and average atomic radius are 1.6×10^{-3} m^{-3} and 1.53 nm, respectively. The Cr concentration in the clusters is 44-56 at%, but not around 80-90 at% for α' precipitates as estimated by the phase diagram (Figure 3.7). This could because of the artifact of APT analysis for small

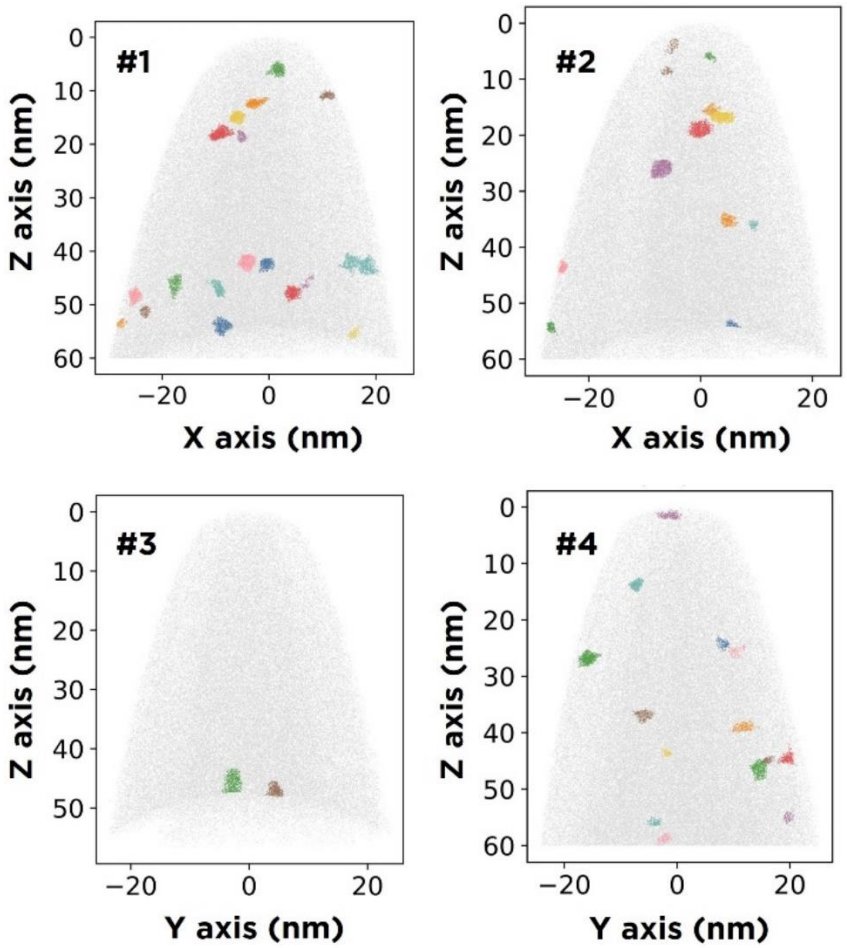

Figure 5.9 APT reconstruction of the Fe-14Cr irradiated at 400°C (30 dpa, 0.1 appm He/dpa, 1.4×10^{-3} dpa/s). The colored clusters represent the Cr-enriched precipitates.

Table 5.2 Quantification of Cr-enriched precipitates in Fe-14Cr irradiated at 400°C (30 dpa, 0.1 appm He/dpa, 1.4×10^{-3} dpa/s).

Sample #	Number density (m^{-3})	Atomic radius (nm)	Cluster core Cr (at.%)	Matrix Cr (at.%)
1	1.9×10^{23}	1.27	47.91	14.85
2	1.7×10^{23}	1.41	44.11	15.07
3	4×10^{22}	1.82	56.26	14.93
4	2.3×10^{23}	1.61	44.67	15.12
Average	1.6×10^{23}	1.53	48.24	14.99
Standard deviation	8.3×10^{22}	0.24	5.60	0.12

precipitates (radius <2 nm) or that the Cr-enriched precipitates are radiation-altered α' precipitates (not classic α' precipitates).

5.2 Cavities in Fusion Relevant and High He/dpa Conditions

5.2.1 Near surface and implanted ion effects

We performed simultaneous dual-ion (8 MeV Ni^{3+} and 3.4 MeV He^{2+}) irradiation on high purity Fe and Fe-Cr alloys (3-14 wt% Cr) at 400-550°C utilizing multiple ion accelerators at Michigan Ion Beam Laboratory (MIBL). The 22 investigated specimen in this sub-section are a subset of the 30 previous investigated samples (0.1 appm He/dpa). With the same total fluence of 9.68×10^{20} m^{-2} Ni ions, the mid-range damage (at depth ~1 μm) and dose rate were roughly 30 dpa and 1.4×10^{-3} dpa/s, respectively. He ions were degraded through a rotating Al foil to produce a graduated implanted helium concentration at constant 10 and 50 appm He/dpa at intermediate depths of 750-1250 nm. Plasma cleaner and cold trap were used to minimize contamination. The infrared thermal imaging system was calibrated by thermocouples prior to the start of the irradiation. Using TEM, cavities were observed in all the twenty investigated irradiation conditions. Quantitative information on cavity swelling of irradiated Fe (extracted from TEM images) as a function of depth is shown in Figure 5.10. The depth-dependent cavity swelling of each condition was calculated with a constant bin width of 250 nm. In Figure 5.10, for the irradiation temperature between 400-550°C, both the 0.1 and 10 appm He/dpa irradiated samples typically showed a cavity denuded zone and an adjacent enhanced swelling regime near the sample surface (around 0-750 nm). The cavity denuded zone width increased with increasing temperature. At midrange (750-1500 nm), the swelling increased with increasing depth. Based on SRIM estimation, the dose and damage would increase with increasing depth within this midrange. At depths above 1500 nm, the swelling was suppressed in the two conditions. In agreement with the results in section 5.1.1, the suppression of swelling near the surface and the peak of the implanted Ni profile was observed in all the examined irradiation conditions.

In addition, sub-grain boundaries were observed in more than half of the 0.1 appm He/dpa irradiated samples, but not found in the 10 appm He/dpa irradiated samples (Figure 5.10). To avoid strain effects on clamped bar samples, square samples were attached to a Cu plate for the 10 appm He/dpa irradiation experiments. Our results indicate that samples arranged closely without gaps may induce stress during high-temperature irradiation due to thermal expansion. The formation of sub-grain boundaries may not be observed in commercial or other complex ferritic steels because of the smaller grain size, higher initial dislocation density, or addition of impurities. However, samples irradiated under stress may potentially affect the defect evolution and mislead the fundamental understanding of irradiation effects.

SIMS study on implanted Ni ions

Ni injected ions, distinct from the Fe-rich target specimens, were chosen for the ease of post-irradiation examination. The profiles of implanted Ni ions in Fe and Fe-10Cr irradiated at 400, 470, and 550°C were analyzed by time-of-flight secondary ion mass spectrometry (ToF-SIMS) at National Tsing Hua University using a TOF-SIMS 5, manufactured by ION-TOF, Germany. The experimental conditions for the dual-beam SIMS depth profiling are summarized in Table 5.3. Intensities of recorded SIMS depth profiles (Figure 5.11) were converted into atomic concentration scales by considering the total ion dose of 9.68×10^{20} ion/m^2 given by the irradiation experiments. A background level up to ~0.003 Ni atomic fraction can introduce large and undefined errors.

Further analyses of the thermal diffusion and radiation enhanced diffusion (RED) broadening of the implanted ion profiles were conducted by fitting model-generated ion profiles to relevant profiles from SIMS (Figure 5.11). A set of MALAB routines were provided by Peter et al. [90] for RED modeling based on Fick's second law and SRIM simulation. The depth dependence of the RED coefficient was modeled following the equation

$$D_i = D_{max}\left(\frac{RD_i}{RD_{max}}\right)^E + D_{therm} \tag{5.1}$$

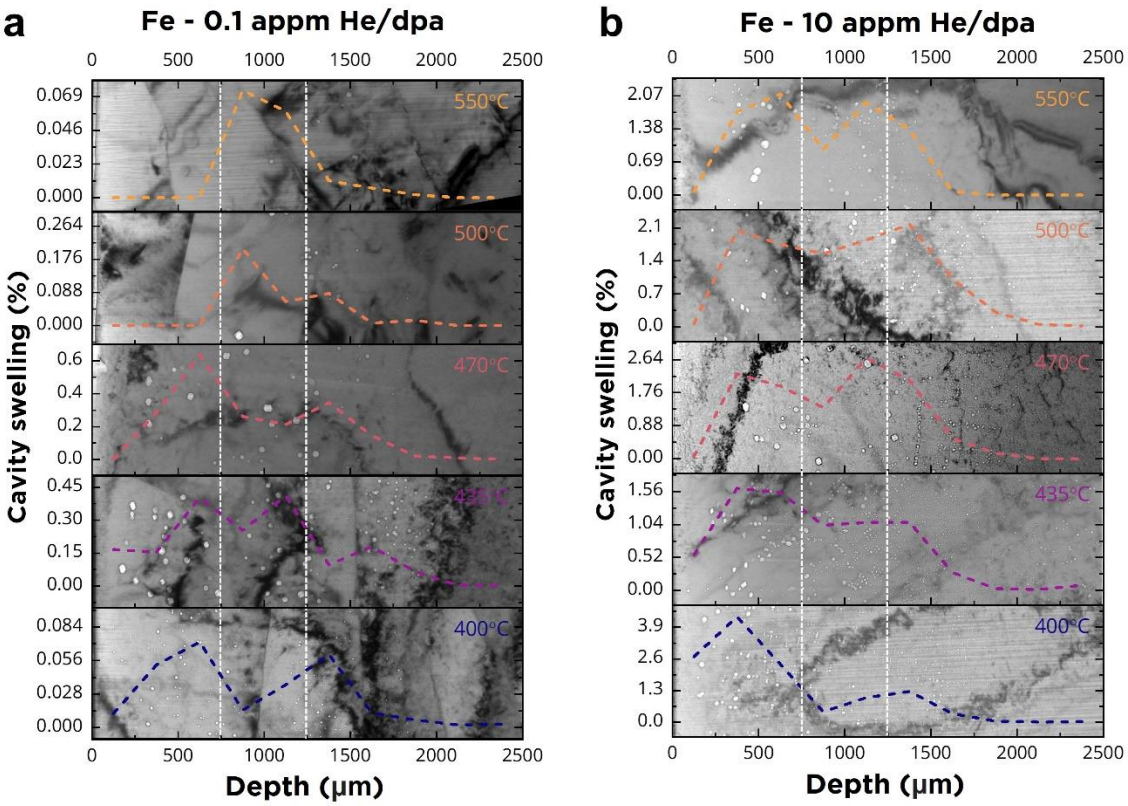

Figure 5.10 Comparison of depth distribution of cavity swelling in Fe irradiated at 400-550°C with 0.1 and 10 appm He/dpa.

Table 5.3 TOF-SIMS experiment conditions

	Analysis Beam	Sputter Beam
Ion type	Bi	O_2
Energy (KeV)	30	2
Current	1.0 pA	450 nA
Area (μm^2)	100×100	260×260
Fluence (ions/m^2)	5.8×10^{13}	3.3×10^{19}

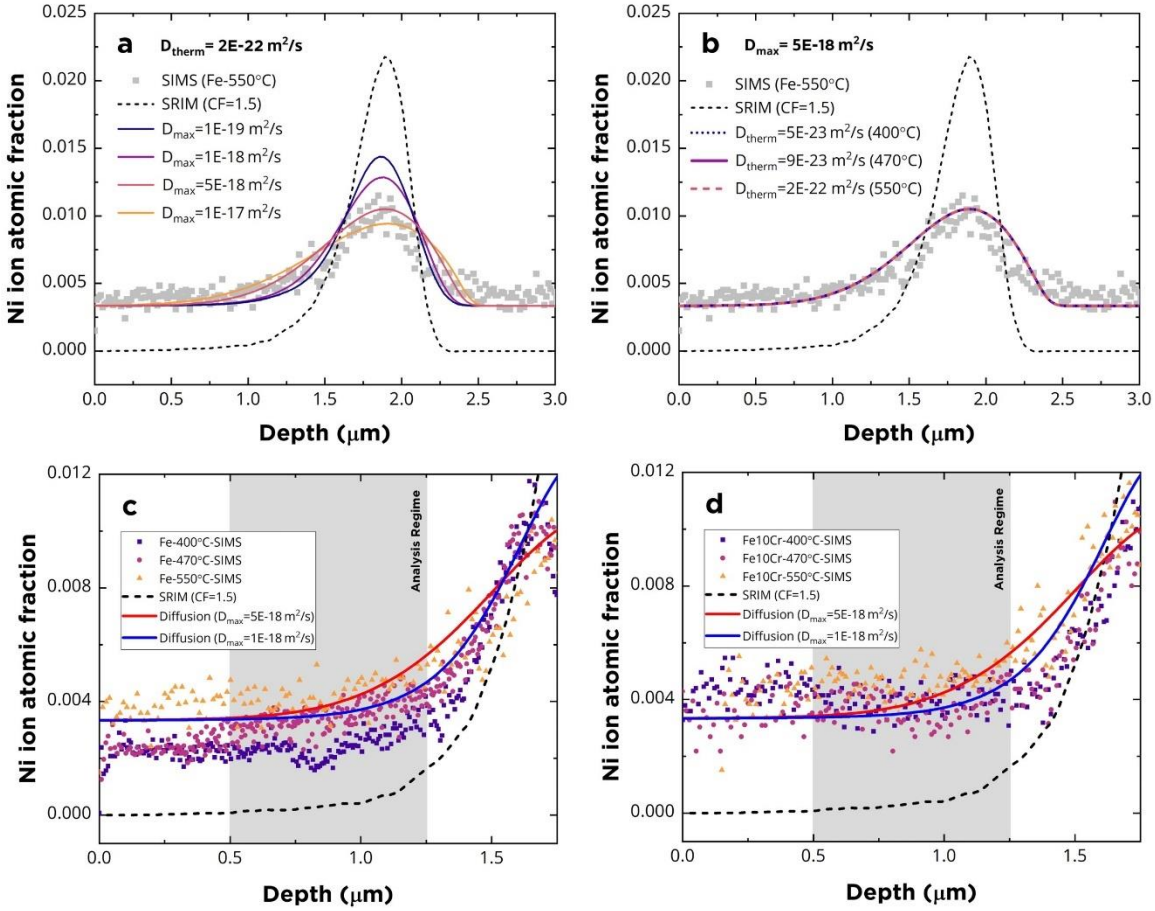

Figure 5.11 Implanted Ni profile form model and SIMS. (a) demonstration of the peak diffusion coefficient effect, (b) demonstration of the of temperature effect, (c-d) Implanted Ni profiles in Fe and Fe-10Cr near the TEM analysis regime.

where, D_i and D_{max} are the RED diffusion coefficients of bin i and the maximum damage rate, respectively, D_{therm} is the thermal diffusion coefficient, and $RD_{i,max}$ are the damage rates, E is the exponential scaling factor which is set as 0.5 for recombination-dominant conditions. By modifying the correction factor in SRIM, the peak position of the implanted Ni profiles estimated by SRIM were first shifted to overlap with the peak position of Ni profile measured by SIMS (see appendix B. for details). Further, the background level of Ni was set as 0.003 for the model calculation. Finally, with a fixed D_{therm} for 550°C, the model-generated profiles showed the best fit to the SIMS profile with D_{max} of 5×10^{-18} m^2/s (Figure 5.11a). The temperature variation from 400 to 550°C shows an insignificant effect on the diffusion broadening of the implanted ion profiles (Figure 5.11b). Comparison of the injected Ni ion profile near the TEM analysis regime for Fe and Fe-10 are shown in Figure 5.11c and d, respectively.

Cavity denuded zone width

As shown in Figure 5.12a, a cavity denuded zone and the adjacent enhanced swelling regime (with larger cavities) were observed near the sample surface and near the grain boundary. The near-surface cavity denuded zone extends to a roughly fixed distance into the material. On the other hand, the cavity denuded width near the grain boundary gradually decreases with increasing depth, and the width decreases to zero at a depth of ~2 μm. For the cavity denuded zone near the grain boundary, as shown in the inset image of Figure 5.12a, small bubbles were observed within the void denuded zones. The same image indicates that bubbles may have their own denuded zone width, which is smaller than the void denuded zone width.

In this study, two attempts were used to estimate the near-surface cavity denuded zone width. As illustrated in Figure 5.12b, the first method (X_d) is to draw a line parallel to the surface that intersects the maximum number of near-surface cavities, and then calculate the average width of the cavity to surface distance. This method would have a large uncertainty when the cavity density is low. The second method is to quantify the depth distribution of the cavity density, and then define a saturation density where the transition from the “denuded zone affected regime” to “bulk/safe analysis zone” happens.

Ideally, the transition point should be the intercept of a steep and another less steeply best-fit line. The cavity denuded zone width (X_3 or X_5) can then be determined using a criterion of 30% or 50% of cavity density. Similar to the first method, the transition may not be apparent when the cavity density is low. In addition, for this study, He ions were simultaneously implanted in the range of ~400-1500 nm. The diffusion of He atoms could strongly affect the vacancy mobility and the formation of cavities.

The calculated cavity denuded zone width of all the irradiated Fe and Fe-Cr samples is plotted as a function of inverse temperature in Figure 5.13. Overall, the cavity denuded zone width increased with increasing temperature. Below 435°C, the denuded zone width of the Fe-Cr alloys is 2-4 times smaller than in Fe. The differences reduce to below 2 times at higher temperatures. For the 0.1 appm He/dpa irradiated samples, there were only seven data points without interference from post-irradiation sub-grains. For Fe denuded zone width as shown in Figure 5.13a, the three lower temperature data points (400-470°C) of the 0.1 appm He/dpa irradiations agrees well with the 10 appm He/dpa irradiated samples. However, deviations of the denuded zone width between the 0.1 and 10 appm He/dpa irradiated samples are shown at temperatures above 500°C in Fe-10Cr (Figure 5.13c) and Fe-14Cr (Figure 5.13d).

5.2.2 Bimodal cavity size distribution

Cavities were observed in all the 22 investigated irradiation conditions within the analysis depth range of 750-1250 nm under TEM (as shown in Figure 5.14 and Figure 5.15). In accordance with traditional cavity growth and nucleation theory, the cavity size generally increased with increasing temperature (Figure 5.14). For the 10 appm He/dpa irradiated materials, faceting in the larger cavities was observed in the high-temperature irradiated samples, in agreement with the 0.1 appm He/dpa irradiation results (Figure 5.4).

A bimodal cavity size distribution with an intermediate critical radius typically has a high density of bubble-like cavities at small sizes and a lower population of void-like cavities at larger sizes, with hardly any cavities between these two size groups. As shown in the cavity size distribution plots (Figure 5.16), a bimodal cavity size distribution was

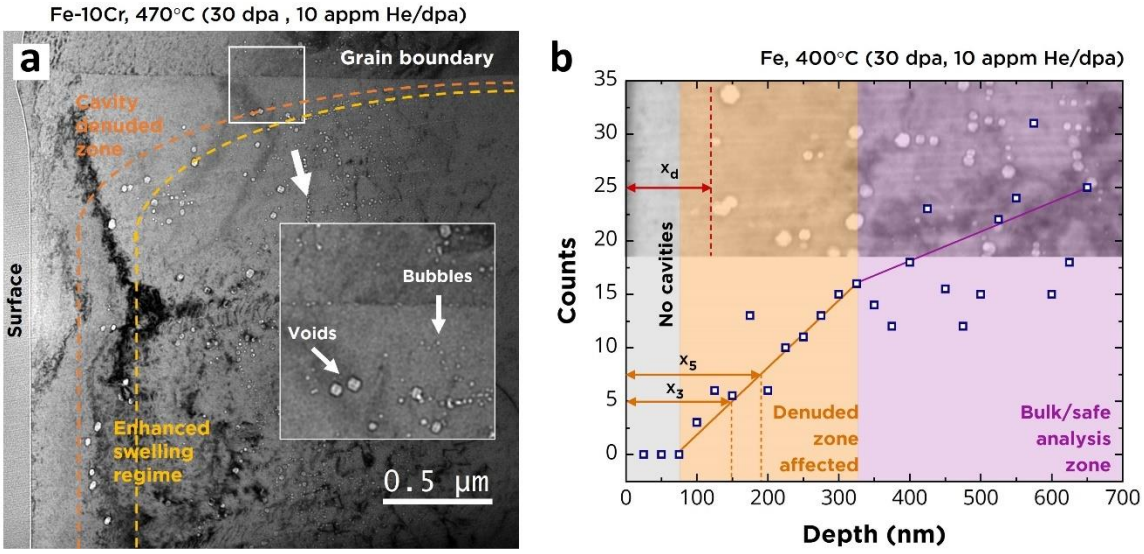

Figure 5.12 (a) cavity denuded zone width and enhanced swelling regime (b) cavity counts as a function of depth and methods for cavity denuded zone estimation.

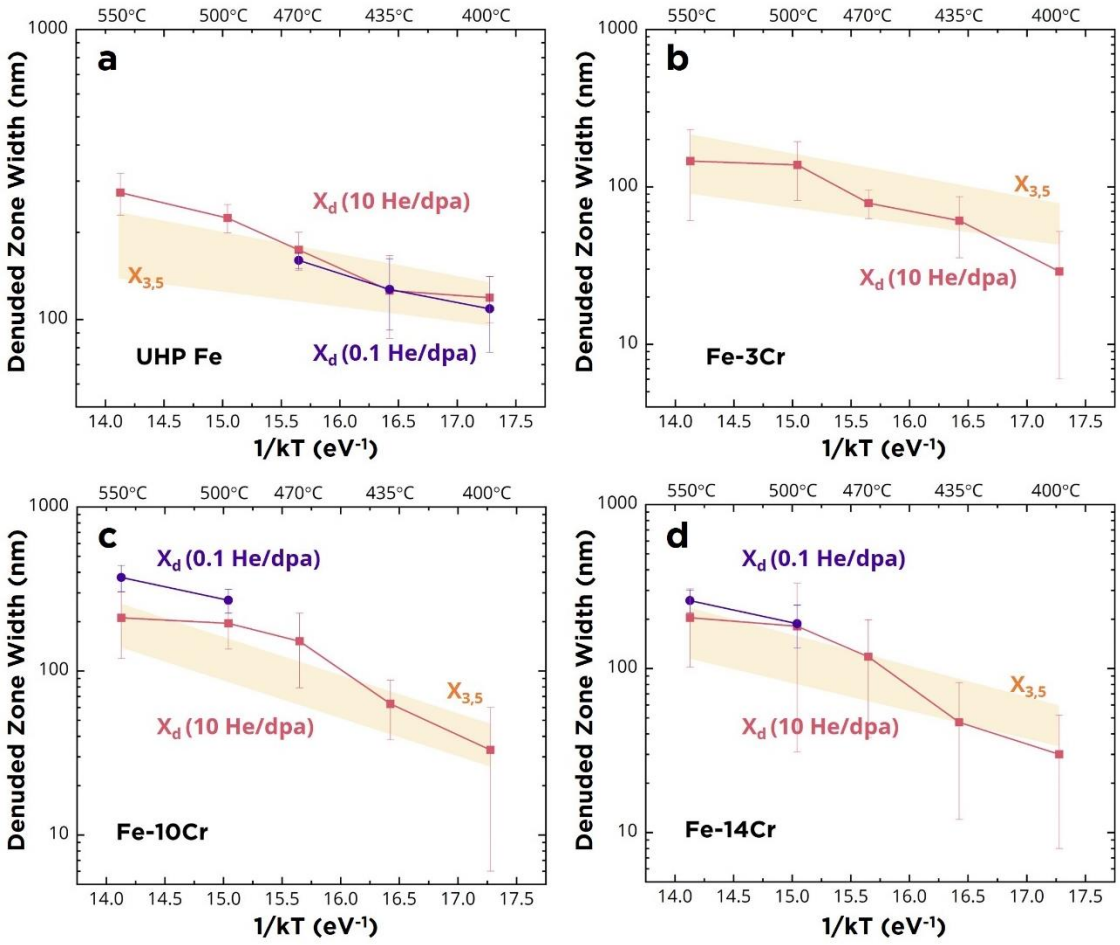

Figure 5.13 Plots of near-surface cavity denuded zone width as vs. inverse temperature in irradiated (a) Fe, (b) Fe-3Cr, (c) Fe-10Cr, and (d) Fe-14Cr alloys. The colored area indicates the slope of the linear fitted X_3 and X_5 data points.

observed in most of the 10 appm He/dpa irradiated samples, but not in the Fe-10Cr and Fe-14Cr irradiated at 400°C. In Figure 5.16, the data points represent the average cavity size, while the error bars represent the standard deviation. The histogram on the left side of each data point demonstrates the size distribution of the cavities. The violin plots on the right side of each data point show the probability density of the data smoothed by a kernel density estimator. A bimodal cavity size distribution was also observed in the two 50 appm He/dpa irradiated samples (Figure 5.17), but not in the 0.1 appm He/dpa conditions (Figure 5.4).

The critical radius estimated from the size distribution of TEM observed cavities is summarized in Table 5.4. The cross mark in the table means that a bimodal cavity size distribution was not observed. The average critical radius is 1.89 ± 0.25 nm. Like the cavity denuded zone width, there is also not a uniform method being proposed to determine the critical radius. The selected bin size for the cavity size distribution and observer bias can both cause undefined errors. However, because of the evident bimodal cavity size distribution observed in the 10 and 50 appm He/dpa irradiated samples, the size and density of the bubble-like ($r < 2$ nm) and the void-like ($r > 2$ nm) cavities were measured separately for further discussion. The selection of 2 nm for the critical radius is in between the theoretical estimated value (~1.7 nm) [110] and experimental results (~2.5 nm) by Horton et al. [111] with irradiation conditions (30 dpa and 300 appm He) similar to the present study.

5.2.3 Comparison of cavity size, density, and swelling

Figure 5.18 shows the average size of bubbles and voids of the 10 appm He/dpa irradiated materials. Following the size classification, larger voids with a diameter above 4 nm were not observed in Fe-3Cr and Fe-10Cr at 400 and 435°C. The void and bubble size increased with increasing temperature for temperatures below 500°C. However, for both the Fe and Fe-Cr alloys at 550°C, the void size either grew insignificantly or shrank by up to ~30%, likely due to the vacancy emission or diffusion of implanted Ni ions that affected the midrange analysis zone. For the 10 appm He/dpa conditions, the average void diameter in

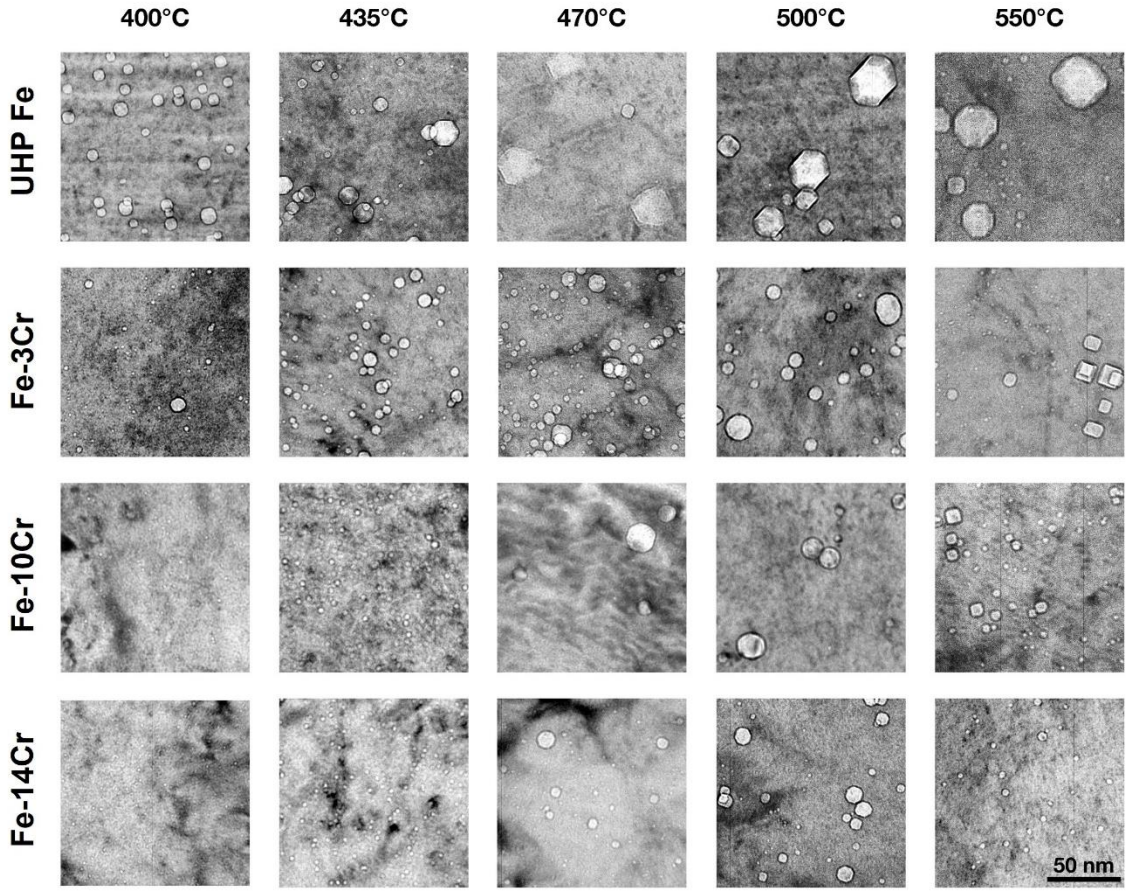

Figure 5.14 TEM Images of cavities in dual-ion irradiated Fe and Fe-Cr alloys taken from the analysis depth range of 750-1250 nm (Midrange irradiation condition: 30 dpa, 10 appm He/dpa)

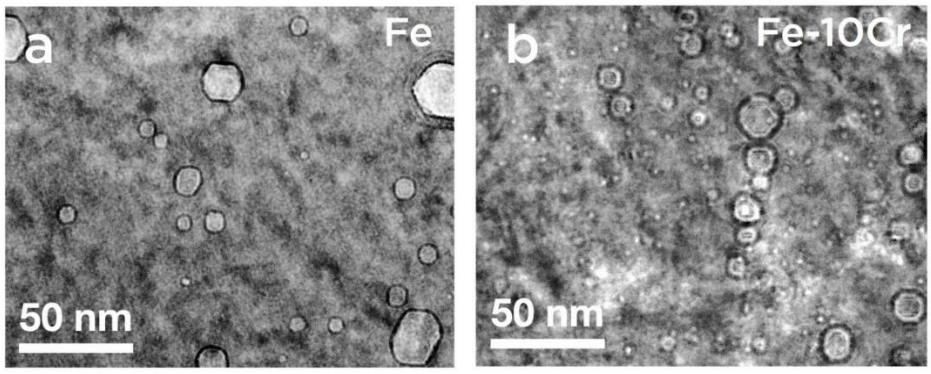

Figure 5.15 TEM Images of cavities in (a) Fe and (b) Fe-10Cr alloys irradiated at 500°C (midrange irradiation condition: 30 dpa, 50 appm He/dpa.) The TEM images were taken from the analysis depth range of 750-1250 nm.

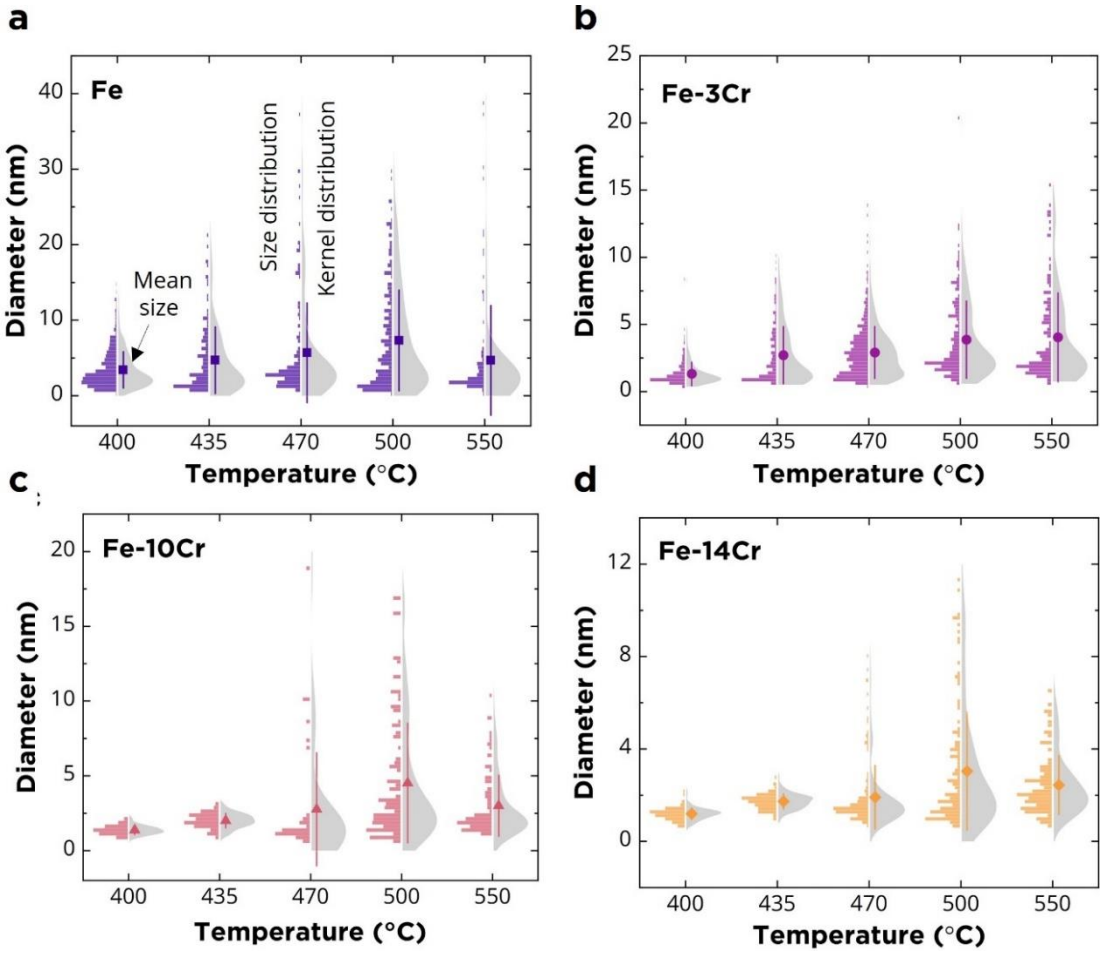

Figure 5.16 Size and Kernel distribution of the cavities in the 10 appm He/dpa irradiated (a) Fe, (b) Fe-3Cr, (c) Fe-10Cr, and (d) Fe-14Cr.

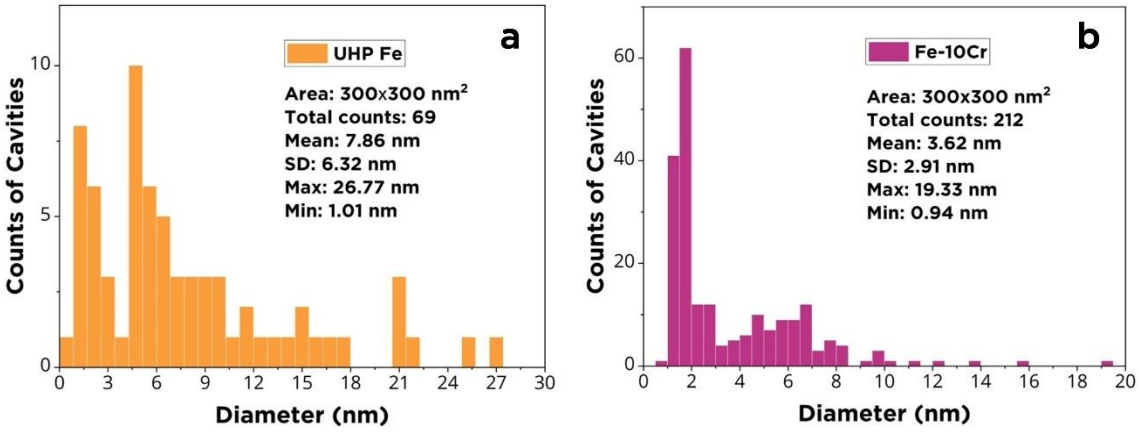

Figure 5.17 Size distribution of the cavities in the 50 appm He/dpa irradiated (a) Fe and (b) Fe-10Cr

Table 5.4 Critical radius of cavities estimated from experimental results

appm He/dpa	Temp. (°C)	Critical radius (nm)			
		Fe	Fe-3Cr	Fe-10Cr	Fe-14Cr
0.1	400-550	×	×	×	×
10	400	1.94	1.88	×	×
	435	1.72	1.69	×	×
	470	2.13	2.31	1.52	1.75
	500	1.88	2.38	1.88	1.63
	550	2.25	1.88	1.63	1.83
50	500	1.88	--	1.88	--

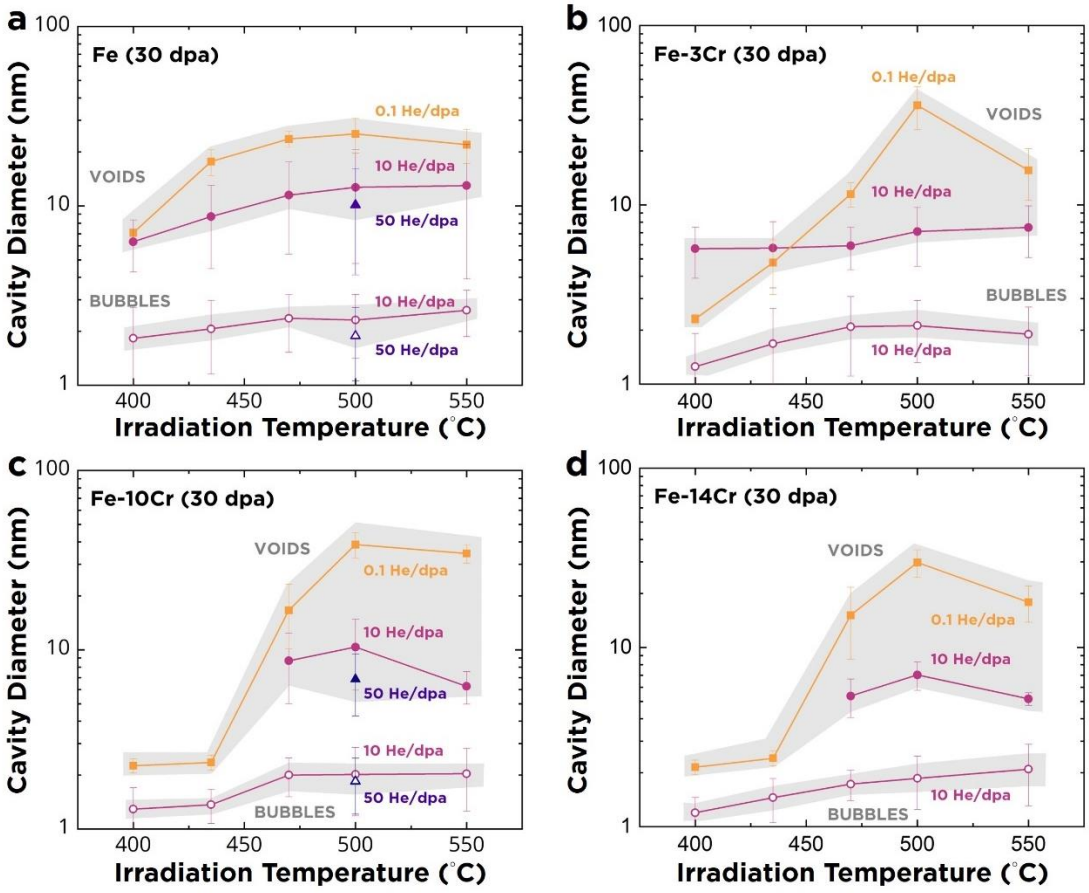

Figure 5.18 Average cavity diameter in dual beam irradiated (a) Fe, (b) Fe-3Cr, (c) Fe-10Cr, and (d) Fe-14Cr alloys at 400-550°C.

all the irradiation conditions is between 6-10 nm, while the average bubble diameter is ~2 nm. At 500°C, the 50 appm He/dpa irradiated Fe (Figure 5.18a) and Fe-10Cr (Figure 5.18c) have the smallest mean size of voids and bubbles than the same material irradiated at 0.1 and 10 He/dpa conditions.

As shown in Figure 5.19, the overall cavity density is overall in the range of ~10^{21}-10^{23} m^{-3}. The bubble density is higher than the void density by a factor of 2-10. Both the void and bubble density for all materials irradiated at 10 and 50 appm He/dpa are much higher than the void density at 0.1 appm He/dpa at all temperatures. Regarding the temperature dependence of cavity density at 10 appm He/dpa (Figure 5.19), the void and bubble density in pure Fe decreased with increasing temperature, as is typical for irradiated materials. However, for voids in the Fe-Cr alloys, the maximum density is at 470°C, and the void density is relatively low or not observed at lower and higher temperatures. In general, the variation of the cavity size and density as a function of temperature agrees with our previous 0.1 appm He/dpa results (colored in gray in Figure 5.19). The absence of voids at lower temperatures in Fe-Cr alloys could be caused by solute trapping of defects or the formation of α' precipitates that would lead to a higher sink strength which suppresses the formation of cavities.

Using the measured cavity size and density, the total volumetric swelling was measured. As shown in Figure 5.20, compared to the 0.1 He appm/dpa samples irradiated previously, the increase of 100 times in the He/dpa content overall resulted in a higher cavity swelling. The maximum swelling value of the 20 samples irradiated at 10 appm He/dpa was ~2.8% for Fe irradiated at 470°C. The peak swelling temperature was ~50-65°C higher for the Fe-Cr alloys than pure Fe. The higher He/dpa content resulted in a higher peak swelling temperature for pure Fe with a temperature difference of ~35°C compared to the 0.1 appm He/dpa case. Due to the potential effect of implanted Ni ion at higher temperatures, the effect of He on the peak swelling temperature shift of Fe-Cr alloys is unclear. In Figure 5.20, comparing the cavity swelling of Fe and Fe-10Cr at 500°C, the peak cavity swelling occurs at an intermediate helium production rate of 10 appm He/dpa, a fusion-relevant condition. Above 10 appm He/dpa, the cavity swelling decreased with increasing He/dpa ratio up to 50 appm He/dpa (Figure 5.20a and c).

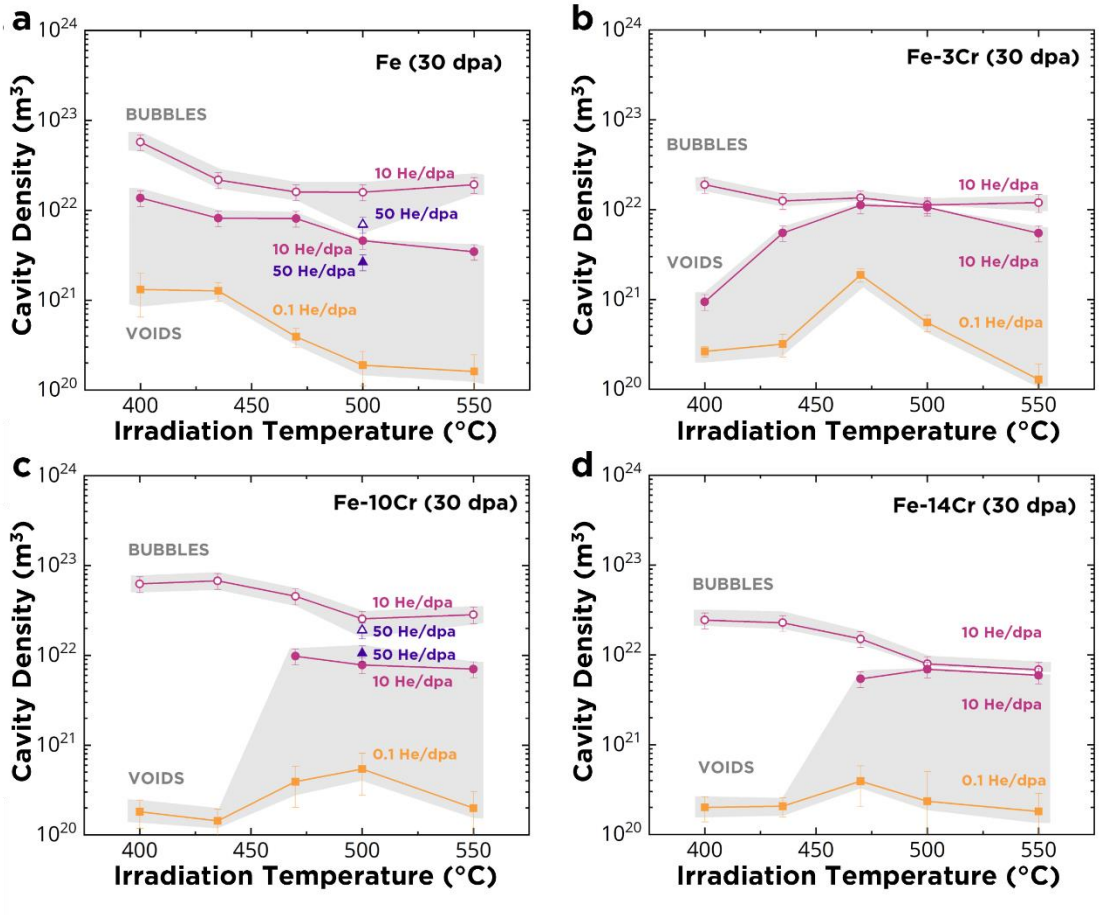

Figure 5.19 Cavity density in dual beam irradiated (a) Fe, (b) Fe-3Cr, (c) Fe-10Cr, and (d) Fe-14Cr alloys at 400-550°C.

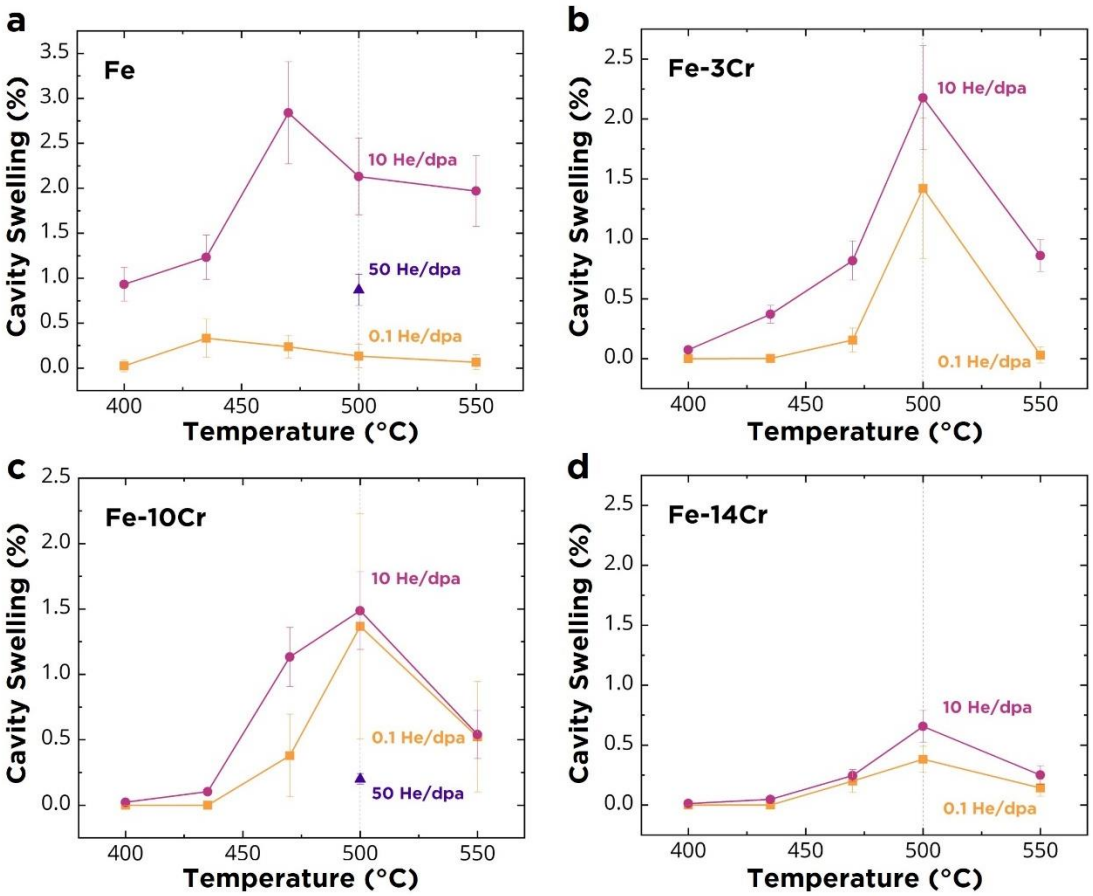

Figure 5.20 Cavity density in dual beam irradiated (a) Fe, (b) Fe-3Cr, (c) Fe-10Cr, and (d) Fe-14Cr alloys at 400-550°C.

5.3 Dynamic Observation of Defect Evolution

5.3.1 Damage evolution in the UHP Fe foil

Figure 5.21 shows the microstructural evolution of simultaneous dual-beam (Kr and He) ion irradiated Fe thin foil at 435°C with displacement damage up to 20 dpa. The corresponding dpa values and accumulated irradiation times are indicated in the upper right corner of each TEM bright-field image. The 0 dpa (unirradiated) and 0.5 dpa images were taken in a relatively thin area (<50 nm) to improve the visibility of small defect clusters. Images of 1 dpa to 20 dpa were taken in an adjacent area with an average thickness of ~78 nm (to reduce the probability of larger loop intersection with foil surfaces). Small black dot dislocation loops (~2 nm in diameter) first appeared at a dose of about 0.02 dpa (29 seconds). During the irradiation, elliptical and edge-on loops were observed for doses above ~1 dpa. The loop size increased with increasing dose and irradiation time. Based on the crystal structure of Fe and diffraction contrast of loops ($g \cdot b = 0$ criteria) [93], the shapes of visible projected dislocation loops excited by $g = 011$ near the $[100]$ zone axis should follow the geometries shown in the upper left image in Figure 5.21. For this imaging condition, $\frac{1}{2}[111]$ and $\frac{1}{2}[\bar{1}11]$ loops would be elliptical loops, while $[001]$ and $[010]$ loops are edge-on loops. At 0 to 3 dpa, most of the loops were homogeneously distributed and could be identified as predominantly $\frac{1}{2}[111]$ loops (>80%). Below 1 dpa, loop decoration was observed around pre-existing dislocations. From 0.5-1 dpa, a small number of loop strings were observed lined up mostly along the $\langle 100 \rangle$, $\langle 111 \rangle$, and $\langle 110 \rangle$ directions. Above 3 dpa, the dislocation loops grew via merging with other loops and gradually developed into irregular-shaped loops (5 and 10 dpa) and network dislocations (15 and 20 dpa). The loop decoration phenomenon was not obvious at 3 and 5 dpa. However, at ~10 dpa, the dislocation decoration phenomenon appeared where coarse finger-shaped loops were adorned with black dot loops.

Different microstructure features were observed near grain boundaries in the Fe foil. As shown in the 3-20 dpa TEM images in Figure 5.21, a defect denuded zone with a width of ~250 nm occurred next to the grain boundary. For doses of 3 to 15 dpa, several

linear defects with included angle of 90° were observed within the denuded zone. These linear defects are most likely projected $[001]$ and $[010]$edge-on loops or dislocation lines. These $\langle 100 \rangle$ linear defect population dramatically increased at ~10 dpa and evolved into grid-pattern dislocation networks at 15 and 20 dpa.

Figure 5.22 highlights the low-dose (<1 dpa) observations. From 0-0.5 dpa, a pre-existing zigzag dislocation with $\langle 111 \rangle$ and/or $\langle 110 \rangle$ Burgers vector gradually straightened into a linear dislocation (Figure 5.22a). Also, in the same sequence of figures, dislocation decoration was observed at ~0.5 dpa. A higher density of black dot loops was observed in the near vicinity of the pre-existing dislocation. Below 1 dpa where the average diameter of loops was 2-6 nm, some $\frac{1}{2}\langle 111 \rangle$ and $\langle 100 \rangle$ loops were observed mobile. The 1-D diffusion of loops and other dynamic effects such as the growth (via absorption of other loops) and loss of loops were also observed. In Figure 5.22b, considering that $\langle 110 \rangle$ faulted loops at TEM-visible sizes have never been observed in irradiated Fe (due to stacking fault energy considerations), the moving black dot loop could be a $\frac{1}{2}\langle 111 \rangle$ loop indicated by an arrow following the $[00\bar{1}]$ direction corresponding to the projection of a $\frac{1}{2}[\bar{1}1\bar{1}]$ Burgers vector. The same sequence of figures also showed that the $\frac{1}{2}\langle 111 \rangle$ loop migrated next to another black dot loop and formed an array of clusters along the $[001]$ direction. In addition to the motion of $\langle 111 \rangle$ loops, the migration of dislocation loops along the $\langle 100 \rangle$ direction is also shown in Figure 5.22c. Near the sample edge where the sample thickness is below 50 nm, several loops were lost and were not found either migrating to neighbor sites or interacting with other loops (Figure 5.22c). The movement, growth, and loss of loops were all within a one-second frame. More details on the motion of $\langle 100 \rangle$ loops (that could be an illusion under TEM) will be given in the next section.

Other results of the dynamic evolution of the Fe microstructure at intermediate-damage doses (1-7 dpa) are shown in Figure 5.23. Above 1 dpa, the mobility of black dot loops decreased. This could be due to the increased strain field interaction from a higher dislocation loop density that constrained the mobility of the smaller black dot loops. As shown in Figure 5.23a, the black dot loops could migrate to adjacent loops resulting in loop

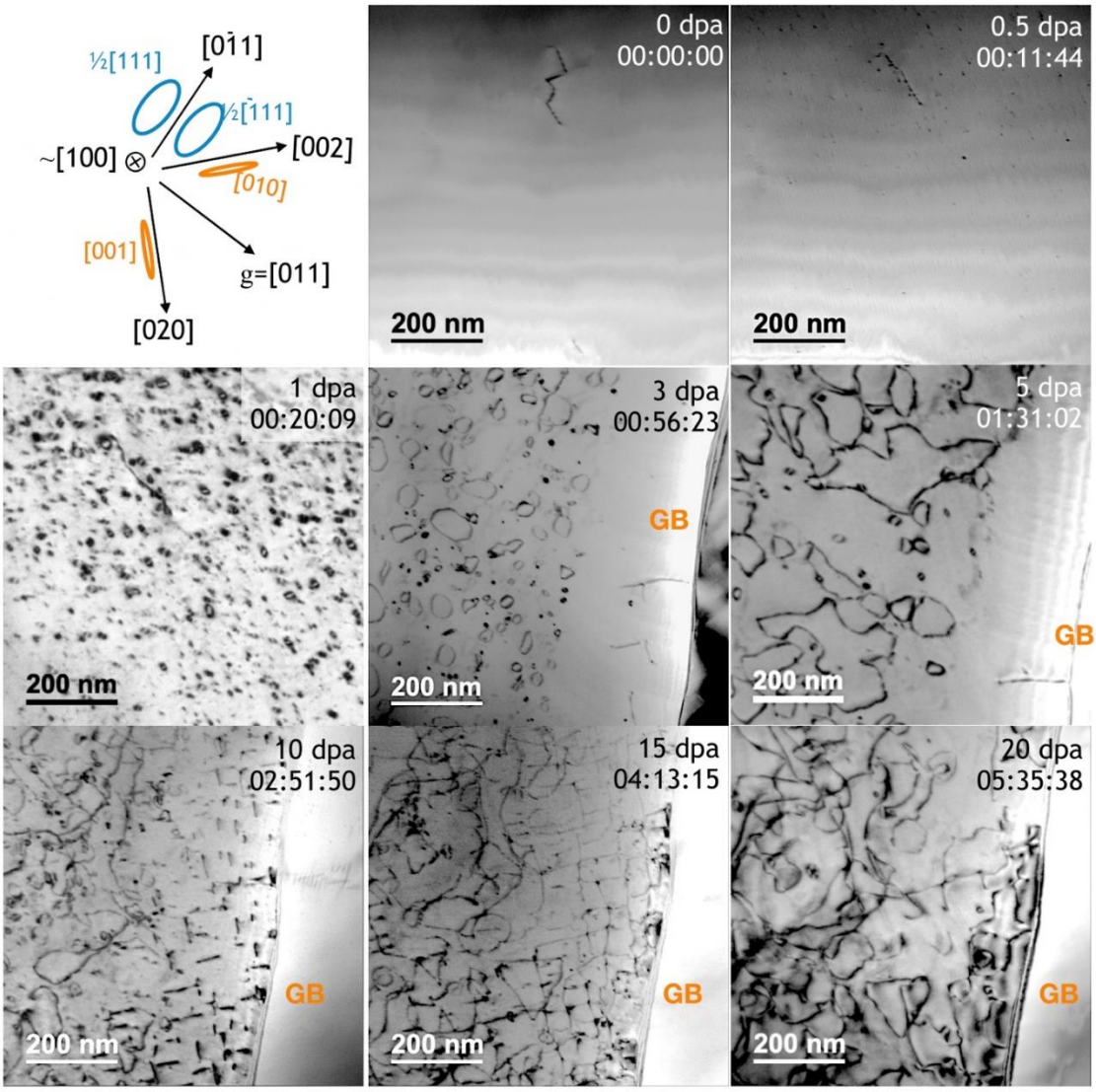

Figure 5.21 Sequence of snapshots showing the dynamic evolution of dislocation loops and dislocation networks in dual-beam (Kr + He) irradiated Fe foil. The microstructure evolution near a grain boundary (GB) is shown in images at 3-20 dpa. All are bright-field images taken with g=011 near the [100] zone axis. The g vector slightly deviated during the irradiation.

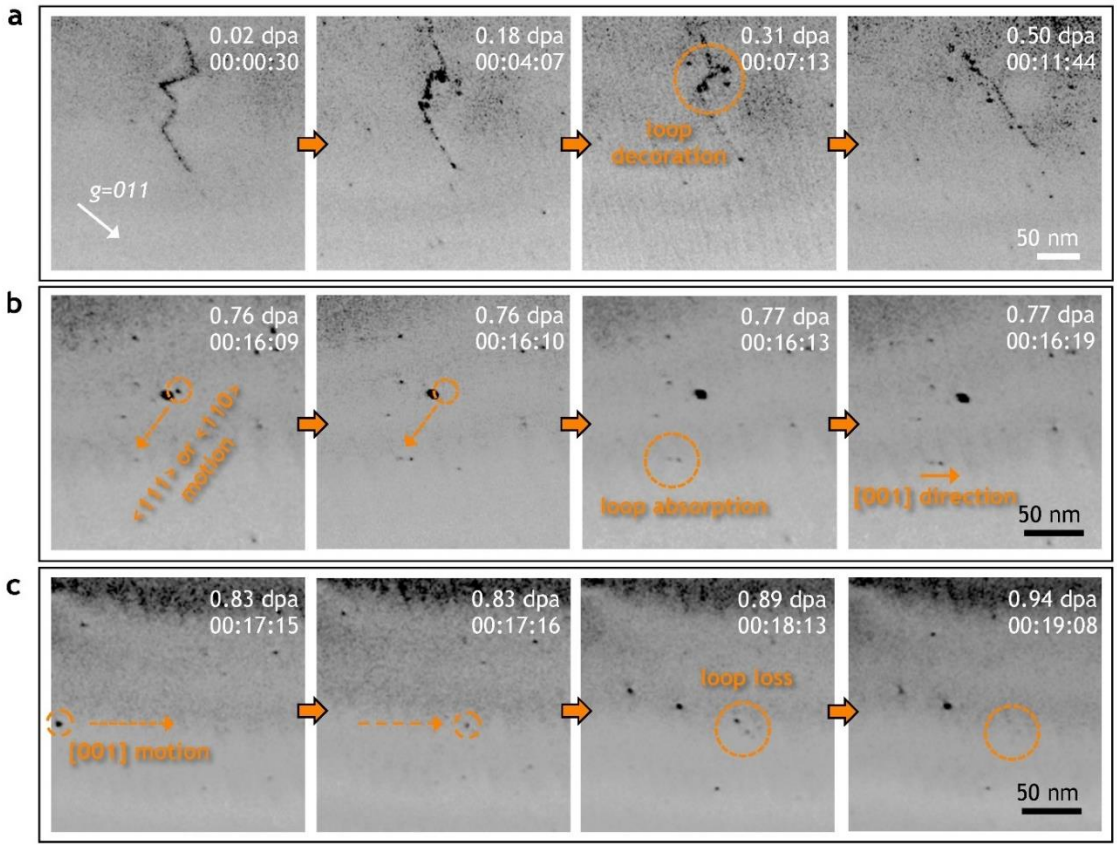

Figure 5.22 Examples of dynamic observations in Fe foil below 1 dpa: (a) dislocation straightening and loop decoration; (b) mobile ½<111> loop and loop interaction along [001] direction; (c) mobile [010] loop and loop loss. (with g=011 near the [100] zone axis)

growth (via loop absorption) of elliptical $\frac{1}{2}\langle 111\rangle$ loops and transformation to $\langle 100\rangle$ loops. The loop absorption process took about one minute. In Figure 5.23b, a high proportion of $\langle 100\rangle$ linear defects and loop strings along the $\langle 100\rangle$ directions were found near a grain boundary. The array of defects along $\langle 100\rangle$ directions could be $\langle 100\rangle$ loops or dislocation lines. When these features were close to black dot loops, they absorbed the small loops. The sequence of images (Figure 5.23b) shows that black dot loops moved along the $\langle 100\rangle$ directions and gradually developed into linear defects. Also, some of the loop strings merged to form a larger defect and eventually formed a local dislocation network. Loop growth and shrinkage were also found at higher (5-7 dpa) damage levels (Figure 5.23c), where smaller loops developed into large irregular-shaped loops. However, it took about 10 minutes for two neighboring loops to complete the coalescence.

At relatively high doses above 9 dpa, loop growth through absorption of neighboring loops was still observed (Figure 5.24). At 5-10 dpa, black dot loops were frequently observed to co-exist with large coarse loops. However, the black dot loops were not rapidly absorbed and did not rapidly vanish like the situation at lower and higher doses. Instead, at 5-10 dpa, the black dot loops gathered near the large coarse loops (Figure 5.24a) and showed a feature similar to the loop decoration observed at lower doses (<1 dpa) near primitive dislocations (Figure 5.22a).

Cavities were first detected at ~10 dpa as shown in the under-focused image at ~11 dpa in Figure 5.24b. Cavities are highlighted in green for better visibility. In the same figure, only in the near vicinity of the grain boundary, loop arrays were visible along $\langle 100\rangle$ directions. The evolution of dislocation networks of edge-on or in-plane $\langle 100\rangle$ loops and the absorption of loops by the grain boundary were also demonstrated. Also in the vicinity of a grain boundary, Figure 5.24c reports the dynamic change of the grid-pattern dislocation network with continued irradiation. Above 15 dpa, the grid-pattern dislocation network interacts with each other and became similar intertwined network types like the in-grain dislocation networks without rectangular patterns.

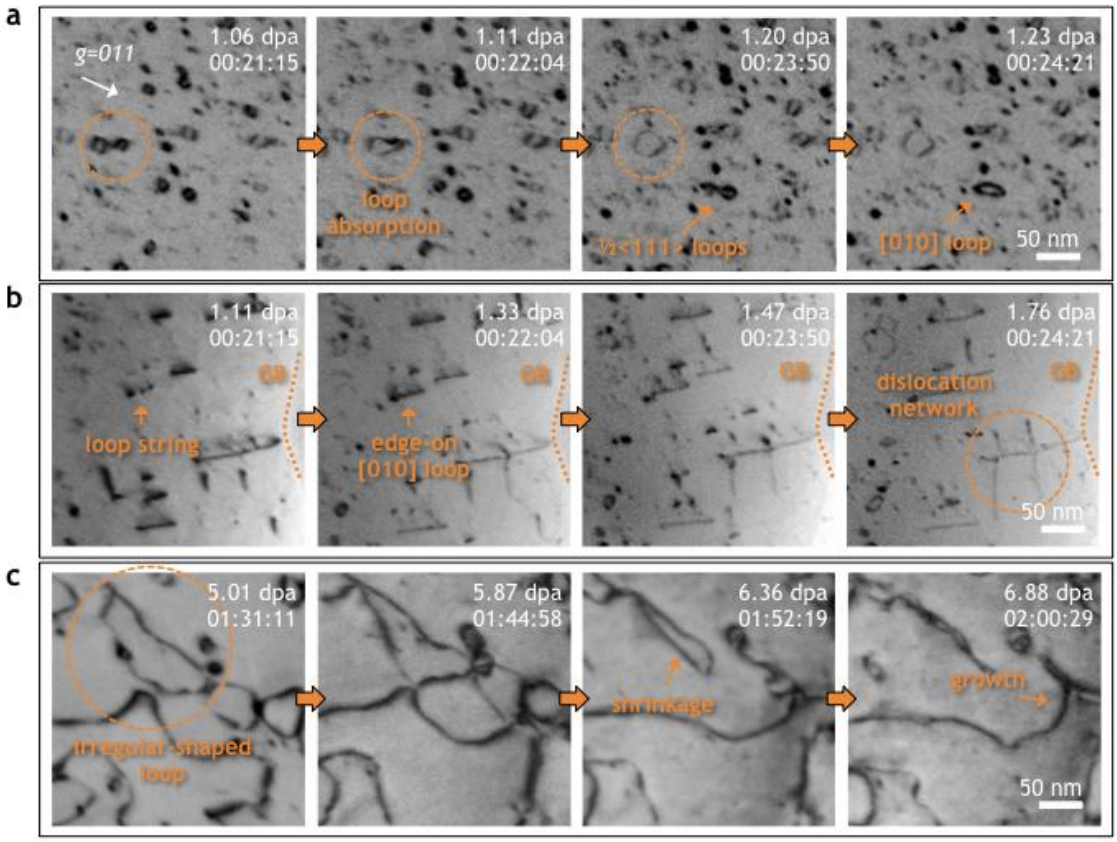

Figure 5.23 Examples of dynamic observations in Fe foil at 1-7 dpa: (a) loop absorption and interaction of ½<111> loops; (b) edge-on <100> loops, loop strings, and dislocation networks at initial state; (c) irregular-shaped loops, loop growth, and loop shrinkage above 5 dpa. (with g=011 near the [100] zone axis)

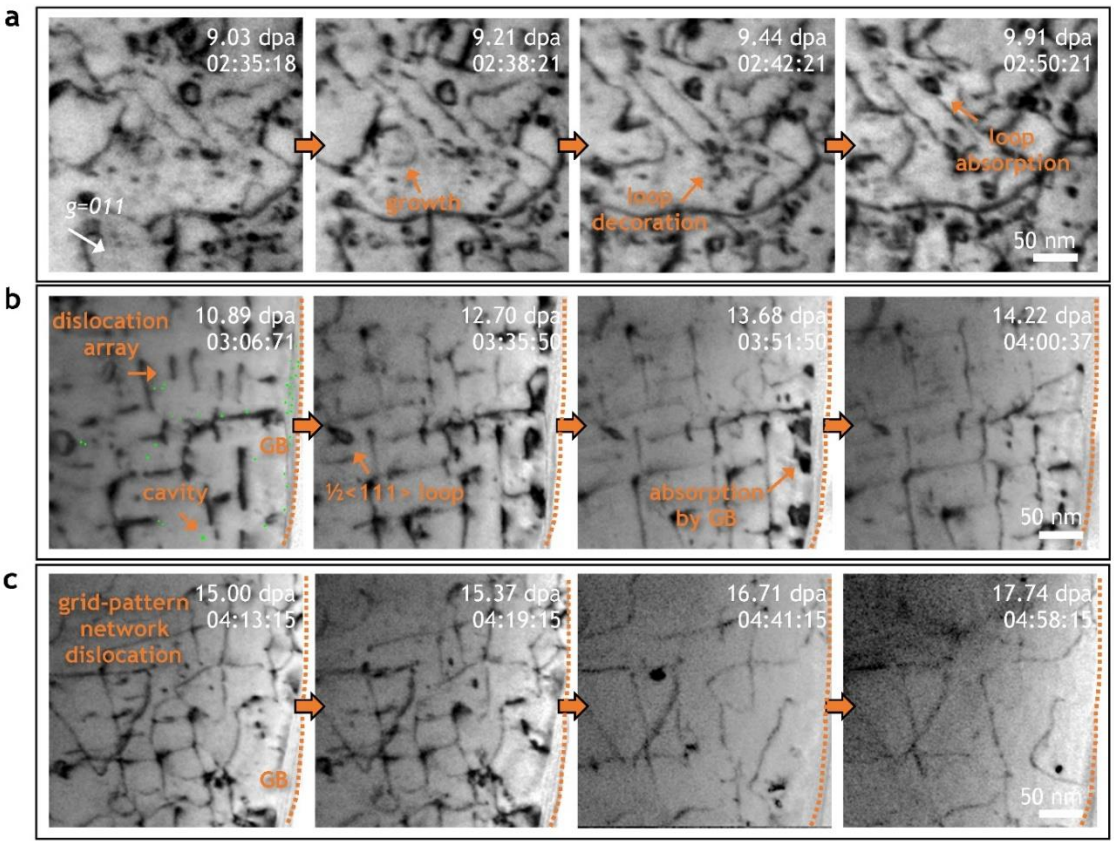

Figure 5.24 Examples of dynamic observations in Fe foil at 9-18 dpa: (a) loop growth and loop decoration; (b) loop array, loop absorption by grain boundary (marked with dotted line), and cavities (highlighted in green); (c) evolution of grid-pattern network dislocation. (with g=011 near the [100] zone axis)

5.3.2 Damage evolution in the Fe-10Cr foil

The dynamic observation of defects in irradiated Fe-10Cr is shown in Figure 5.25 for the same [100] zone axis and a similar diffraction contrast condition as in Fe. The 0-1 dpa images were taken at a foil thickness of ~58 nm, and the 3-10 dpa images were taken at areas with a thickness of ~84 nm. The 15-20 dpa image was taken at a further thicker regime of ~101 nm. Similar to the case in irradiated pure Fe, the black-dot defects initially appeared at ~0.02 dpa (31 seconds). However, even at low doses with a low population of defects, the black dot loops in Fe-10Cr were mostly immobile and in general were only observed to move a short distance to another adjacent black dot.

At low dose (~1 dpa), similar to the result in Fe (Figure 5.22a), dislocation decoration was found near a pre-existing dislocation in Fe-10Cr, as shown in Figure 5.26a. With increasing dose from 1-6 dpa, loop strings (array of black dot loops) along the $\langle 100 \rangle$ directions emerged (Figure 5.26b). Even though these lined up black dot loops were very close to each other (distance <10 nm), it took more than 10 minutes for some of them to interact (migrate and merge) and develop into embryonic forms of edge-on $\langle 100 \rangle$ loops. The string of loops along the $\langle 100 \rangle$ directions that remain as separated black dot loops might not necessarily be $\langle 100 \rangle$ loops. It is likely that they might be other types of loops laying along the $\langle 100 \rangle$ directions. In the same image sequence in Figure 5.26b, elliptical $\frac{1}{2}\langle 111 \rangle$ and edge-on $\langle 100 \rangle$ loops were also observed. Unlike the loop growth via absorption of another loop that was completed within 1 second in Fe, the loop combination in Fe-10Cr took more than 5 seconds. After the loop absorption, the loop sizes were still relatively small (~10 nm in diameter) in Fe-10Cr compared to Fe where loops could grow up to 200 nm irregular-shaped loops. Figure 5.26c demonstrates a dislocation pinning process in Fe-10Cr that was not clearly evident in Fe. The images show that $\frac{1}{2}\langle 111 \rangle$ loops acted as pinning points and bent a dislocation that was trying to travel through the lattice. The dislocation pinning was not a rare event in Fe-10Cr and was extensively observed at 3-5 dpa.

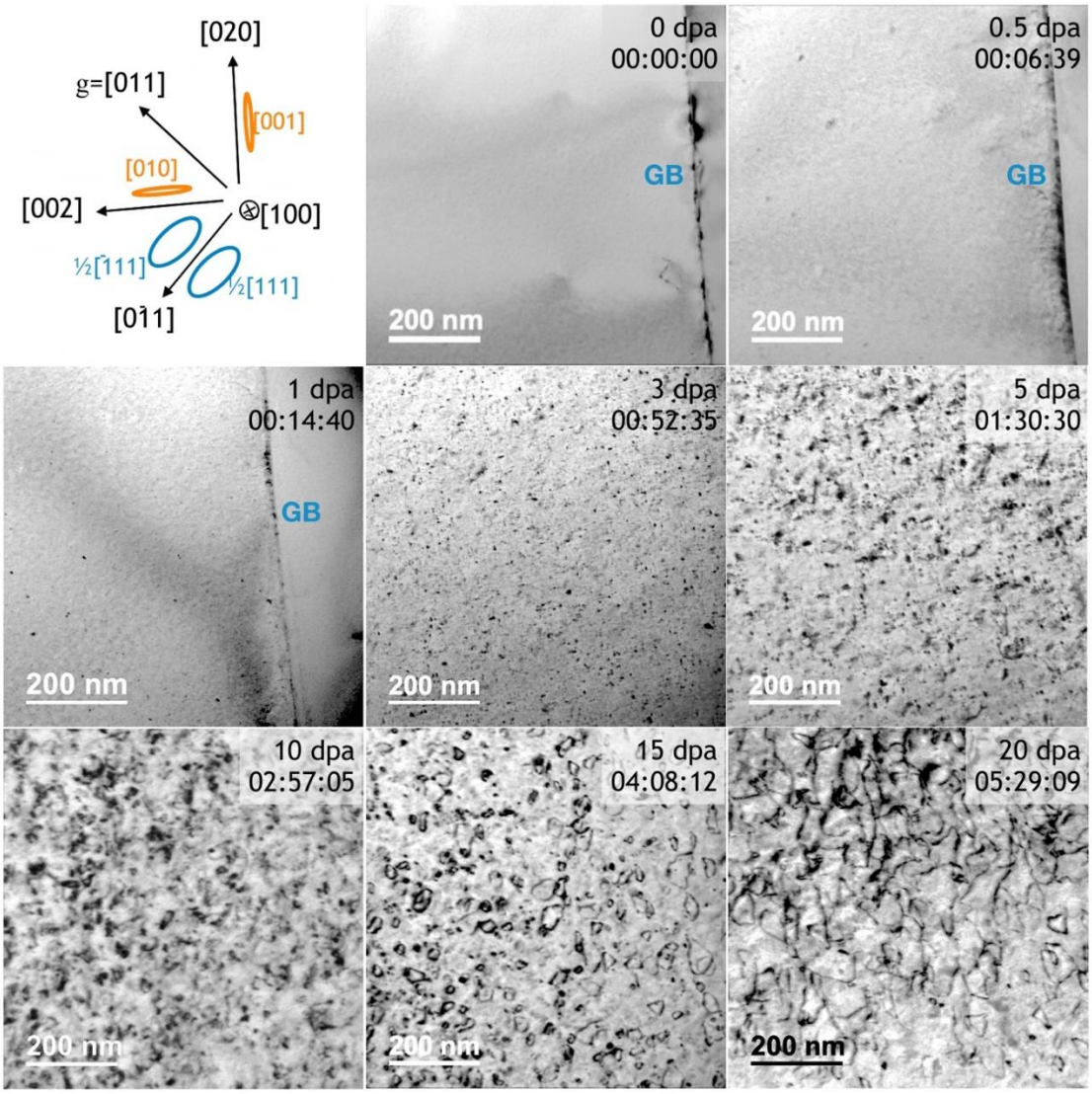

Figure 5.25 Sequence of snapshots showing the dynamic evolution of dislocation loops and dislocation network in dual-beam (Kr + He) irradiated Fe-10Cr foil. All are bright-field images taken with g=011 near the [100] zone axis. The g vector slightly deviated during the irradiation.

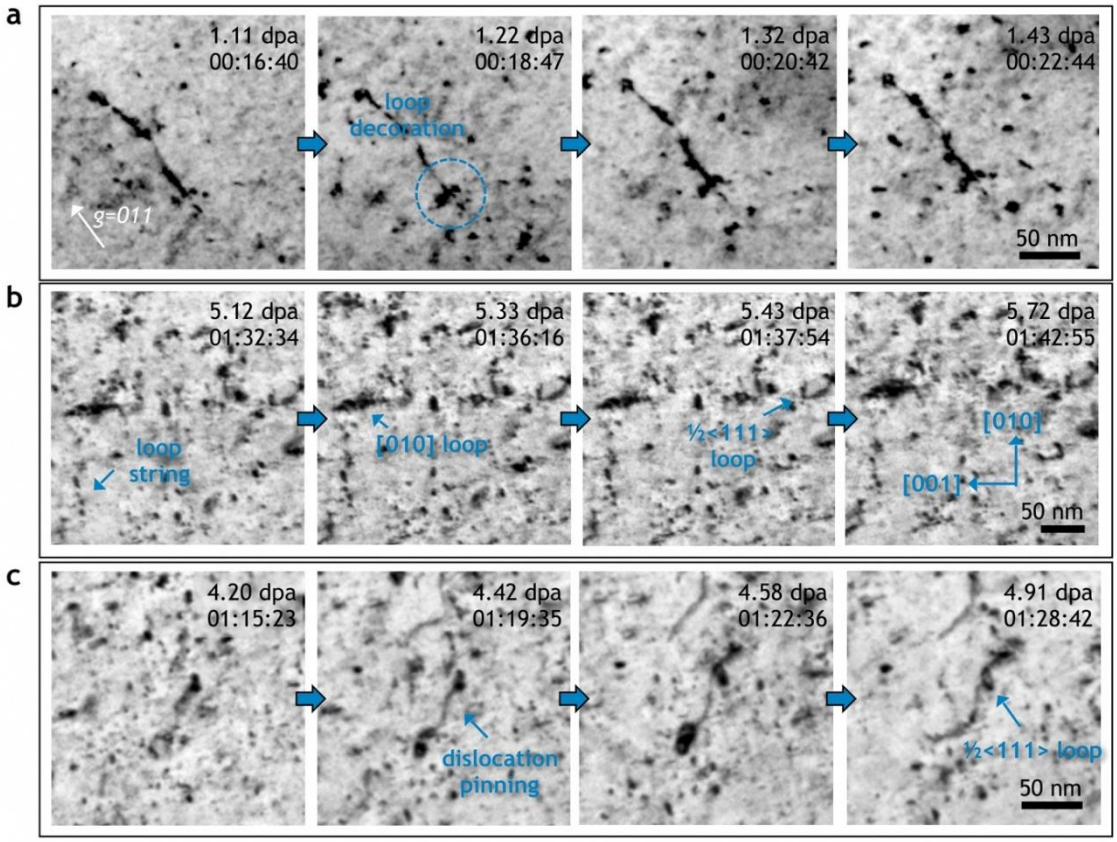

Figure 5.26 Examples of dynamic observations in Fe-10Cr foil at 1-6 dpa: (a) loop decoration; (b) <100> loop string, elliptical ½<111> loops, and edge-on <100> loops; (c) dislocation pinning. (with g=011 near the [100] zone axis)

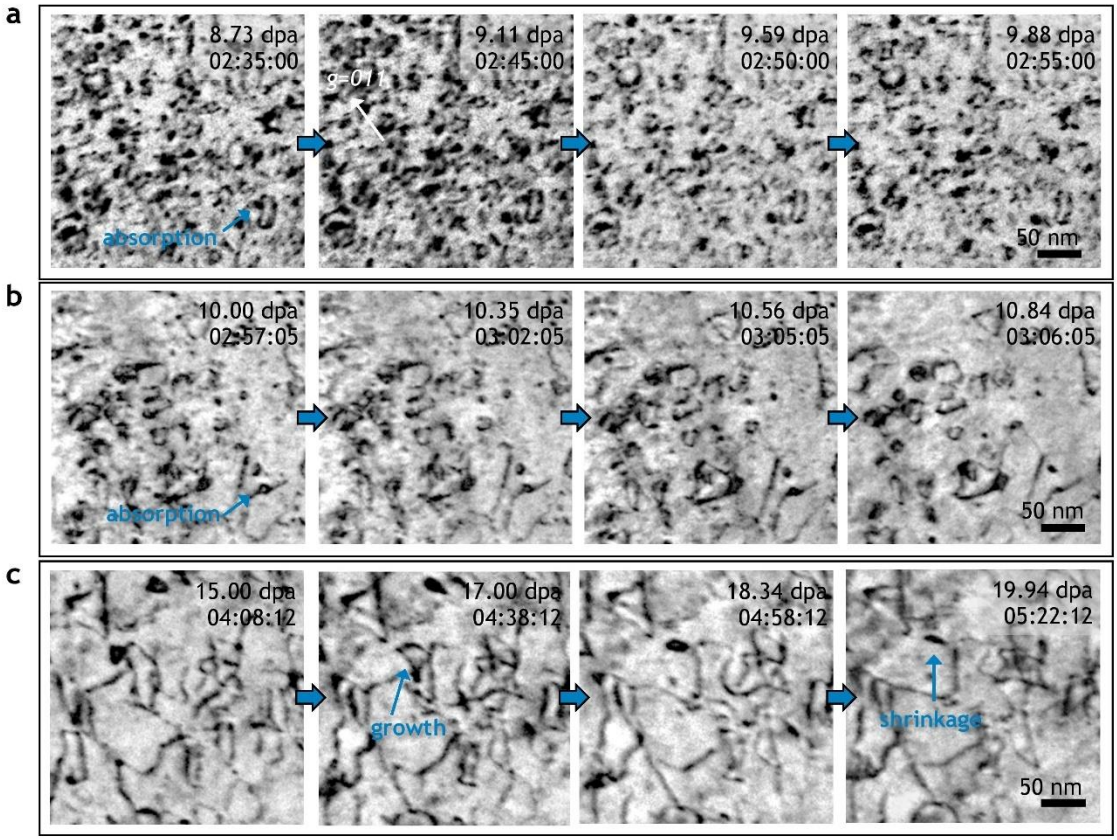

Figure 5.27 Examples of dynamic observations in Fe-10Cr foil at 8-20 dpa: (a) loop absorption; (b) irregular-shaped loops and loop absorption; (c) network dislocations. (with g=011 near the [100] zone axis)

Above 8 dpa, loop absorptions that took 10-50 minutes to complete were continually observed (Figure 5.27). Larger loops seemed to take more time to complete the absorption of a nearby loop. At 5-8 dpa, as part of the loop size increased, the density of other stable black dot loops (typical diameter of ~5 nm) kept increasing. At higher doses ~8-10 dpa (Figure 5.27a-b), the black dot loops started to interact with each other or other larger loops, resulting in a reduction of loop density. This reappearance of stable black dot loops in Fe-10Cr at ~10 dpa could be an analogy to the black dot decoration near the finger-shaped loops that was also observed at ~10 dpa in Fe (Figure 5.21). For all damage levels, the maximum loop size in Fe-10Cr is only about 100 nm, which is 2-3 times smaller than the irregular-shaped loops in Fe. The smaller size of loops reduced the probability of interaction between these immobile elliptical loops. Therefore, the embryonic type of network dislocation was only found in Fe-10Cr after 15 dpa. The networking of larger loops is presented in Figure 5.27c. At higher doses above 15 dpa (Figure 5.27c), two adjacent loops took about 70 minutes to complete the loop coalescence process. For a similar size of two neighboring loops in Fe as shown in Figure 5.23c, it took only ~15 minutes to complete the loop absorption.

5.3.3 Formation of cavities at high doses

Cavities were also observed in the Fe and Fe-10Cr foils in under-focused TEM images (Figure 5.28a-b). The defocus values of the two figures were approximately -1 μm. Some of the cavities in Figure 5.28a-b are highlighted in green for better visibility. While cavities were observed in Fe at ~10 dpa and above, the cavities were observed in Fe-10Cr only for doses close to 20 dpa. In the Fe foil, the cavity density was saturated at ~15 dpa, while the cavity size did not change significantly as the dose was increased to 20 dpa. The cavity density in Fe was lower, but the cavity size was larger than in Fe-10Cr. A particularly large cavity in diameter of ~5.7 nm was observed in Fe (Figure 5.28a). As shown in Figure 5.28c, at 20 dpa, the average diameter of cavities in Fe (~1.6 nm) was ~33% larger than those in Fe-10Cr (~1.2 nm). The cavity density (Figure 5.28d), in contrast, was slightly (~20%) lower in the Fe foil. In addition, cavities in Fe were found in the grain boundary and the

grain interior. However, for the Fe-10Cr foil, cavities were observed only in the grain interior. There was not a clear band of cavity denuded zone next to grain boundaries for either material.

5.4 Bubble Formation in Helium-Implanted NFAs

5.4.1 Bubbles in in-situ He-implanted Fe-10Cr alloy and NFAs

We performed in-situ He implantation on TEM samples of high purity Fe-10Cr alloy and two nanostructured alloys (14YWT and CNA3) utilizing the IVEM facility at Argonne National Laboratory. As shown in Figure 5.29 and Figure D.5 (for lower magnification images), He bubbles were observed in all the He-irradiated materials at 600 and 900°C. The bubbles are visible in the matrix and also at the grain boundaries. For the Fe-10Cr model alloy, the mean matrix bubble diameter significantly increased from 2.8 to 14.4 nm with increasing temperature. Conversely, the matrix bubble density decreased from 6.3×10^{22} to 2.5×10^{21} m^{-3} at 600 and 900°C, respectively. At the same temperature range, in CNA3, the average bubble diameter increased from 3.3 to 5.7 nm, and the density slightly decreased from 2.9×10^{22} to 1.5×10^{22} m^{-3} with increasing temperature. The variation of bubble size and density with irradiation temperature was more moderate for the 14YWT alloy. The average bubble diameter slightly increased from 1.8 to 2.1 nm between 600 and 900°C. However, at both 600 and 900°C, the bubble density of 14YWT remained almost constant around 2×10^{23} m^{-3}. In general, the average bubble size in the matrix was in the order of Fe-(9-10)Cr > CNA3 >14YWT, while the cavity density showed exactly the opposite sequencing.

Figure 5.30 and Figure D.6 (for lower magnification images) provide TEM images of the cavities in the He-implanted samples annealed at 750 and 900°C. These samples were irradiated at 600°C (for ~15 min) and then annealed at 750°C (for ~15 min) and 900°C (for ~15 min). The temperature was reduced to below 150°C during the interval between irradiation and annealing. Similar to the hot-implanted results, bubbles were visible in both

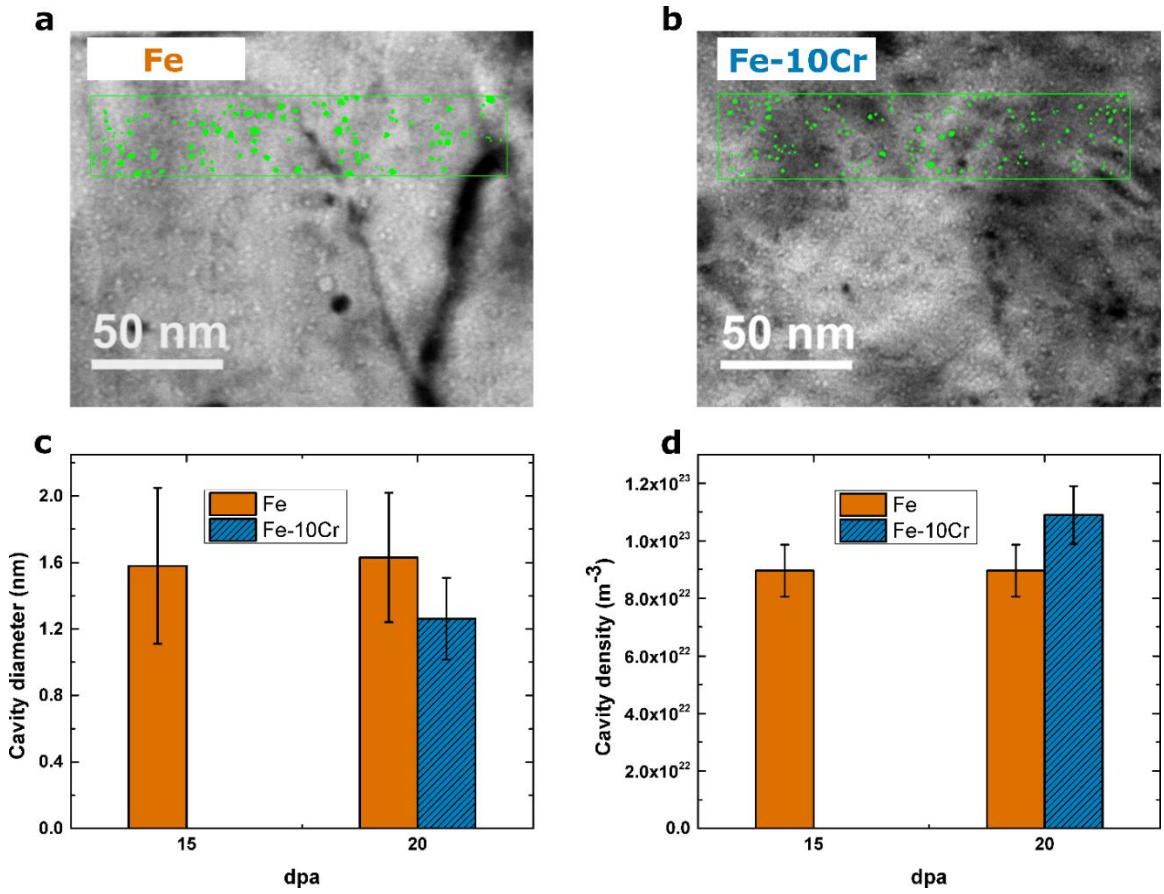

Figure 5.28 Cavities observed in dual-beam irradiated Fe and Fe-10Cr at 435°C: (a-b) TEM under-focused images of cavities in Fe and Fe-10Cr foils at 20 dpa; (c-d) average size and density of cavities at 15-20 dpa. Some of the cavities in a and b are highlighted in green for better visibility.

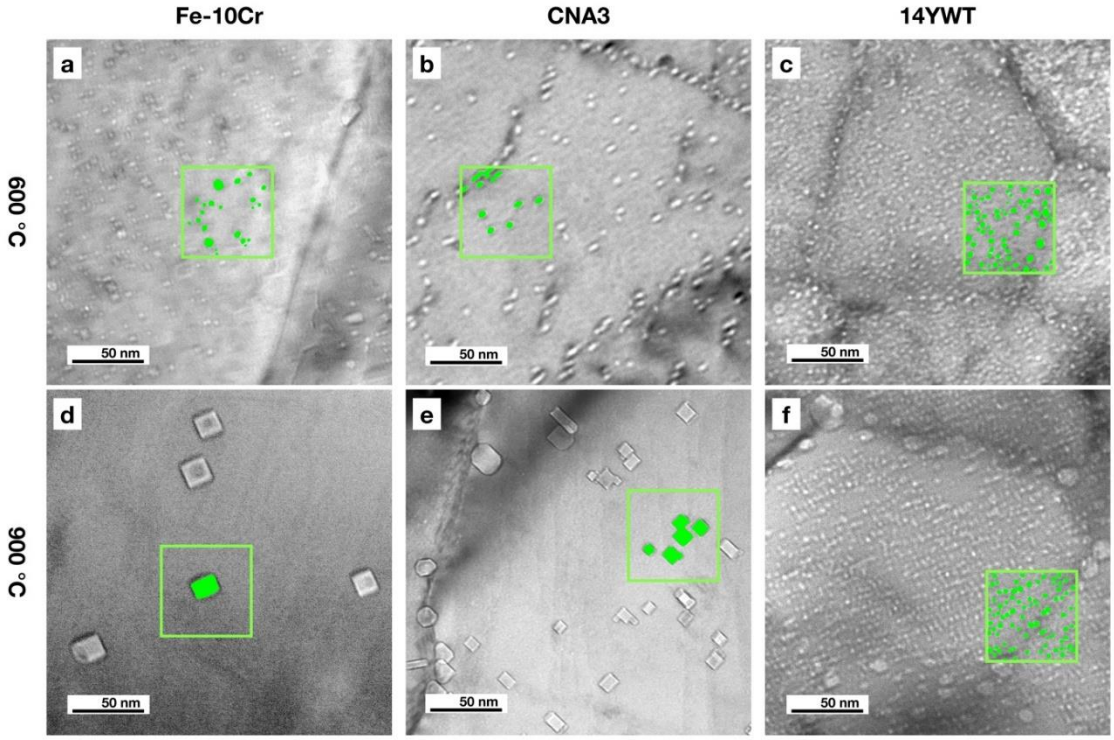

Figure 5.29 Under-focused TEM images of bubbles in in-situ He implanted Fe-10Cr and NFA thin foils at 600°C (a-c) and 900°C (d-f). The light green-filled portions of the micrographs highlight the bubbles in the materials.

grain matrices and grain boundaries. Also, the bubble size gradually increased from 600 to 900°C. Comparing the 900°C annealing results with the 900°C directly hot implanted experiments, the bubble size (in the grain matrices) was only slightly larger in the annealed 14YWT and CNA3 samples, while the average bubble diameter of Fe-10Cr was 6 nm for the 900°C annealed case compared to 14.4 nm observed in the 900°C directly implanted sample. On the other hand, the density decreased relatively less than the directly hot implanted experiments for all the three materials. The bubble density remained constant for the annealed 14YWT alloys. At 600°C, it is worth noting that the visible bubble density of CNA3 was lower than the Fe-10Cr alloy (Figure 5.29a-b). However, the bubble density in CNA3 abnormally went up when annealed at 750°C (comparing Figure 5.29b to Figure 5.30b). It is considered likely that a portion of small cavities (diameter below 2 nm) in the CNA3 alloy, irradiated at 600°C, may not be detected and counted by the Fresnel contrast imaging technique.

Figure 5.31 summarizes the average size and density of the He bubbles in the Fe-Cr matrix. The annealing time and direct implantation time were both set to be ~15 minutes at each temperature. From 600 to 900°C, the general trend showed that bubble size increased and the density decreased in Fe-10Cr and CNA3. However, the visible bubble size and density for 14YWT remained constant within the listed error bars. The changes were most pronounced for Fe-10Cr and relatively moderate for the two alloys with nanoparticles.

5.4.2 Bubbles in of ex-situ He-implanted Fe-9Cr alloy and NFAs

For the study on bulk irradiated materials, 275 keV He ions were used to irradiate a Fe-9Cr alloy and the two nanostructured alloys (14YWT and CNA3) at 500 and 700°C with a fluence of 1.28×10^{20} m^{-2}. Based on the SRIM calculation, the peak radiation damage (at ~700 nm) and He concentration were roughly 0.3 dpa and 8000 appm, respectively. Figure 5.32 and Figure 5.33 show the cavity distribution of the three materials following He implantation at 500 and 700°C in cross-sectional TEM images. Cavities are visible in the He-implanted region for all of the six ex-situ irradiated samples. The peak damage depth at ~700 nm is indicated in red dashed lines in both Figure 5.32 and Figure 5.33.

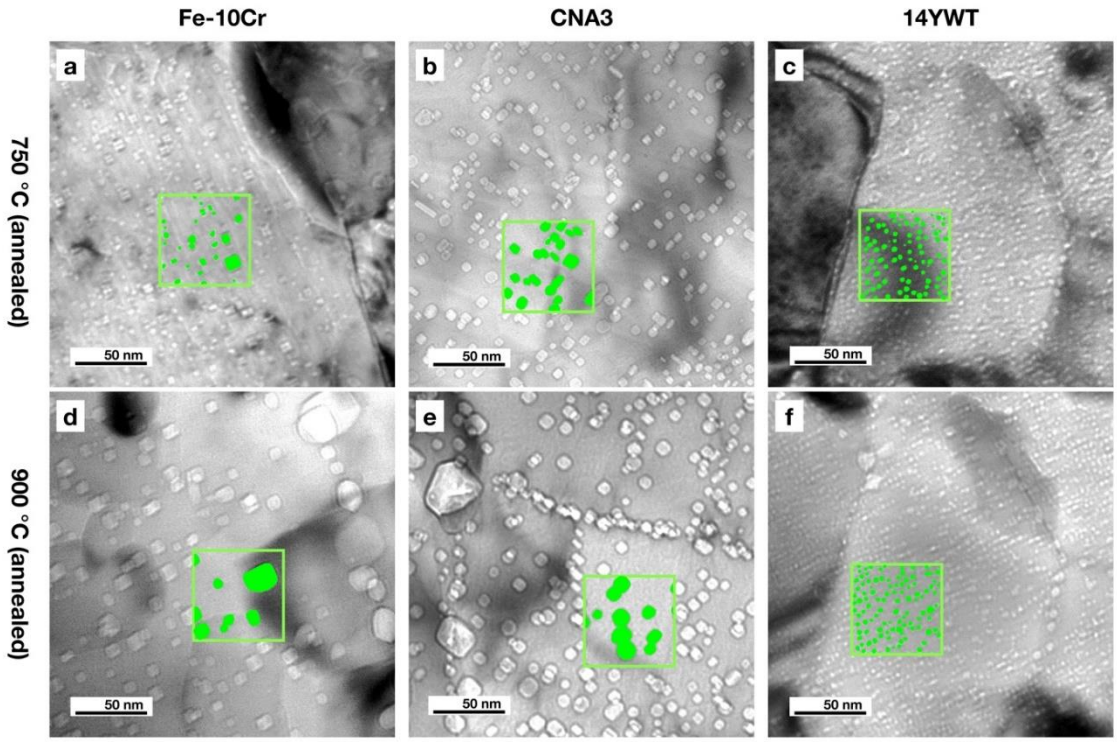

Figure 5.30 Under-focused TEM images of bubbles in post-irradiation annealed Fe-10Cr and NFA thin foils at 750°C (a-c) and 900°C (d-f). The light green-filled portions of the micrographs highlight the bubbles in the materials.

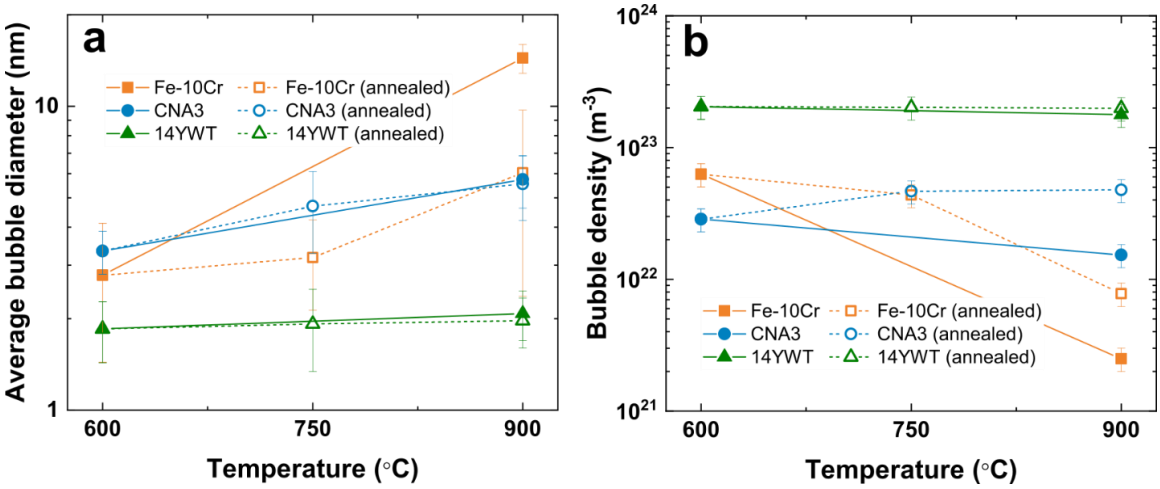

Figure 5.31 Comparison of the (a) average size and (b) density of bubbles in the in-situ irradiated Fe-10Cr and NFA thin foils at 600-900°C. The filled symbols (and solid lines) represent the directly hot-implanted experiments, and the open symbols (and dashed lines) denote the 600°C implanted specimens followed by sequential annealing at 750 and 900°C.

Most of the cavities were distributed in the range of 500-800 nm from the implanted surface. However, for the 700°C He-implanted Fe-9Cr model alloy (i.e., without the addition of nanoparticles), bubbles were agglomerated along the primitive dislocations/grain-boundaries showing a heterogeneous distribution. This is evidence that He bubble precipitation can be more heterogeneous at high temperatures, due to higher mobility of small He-vacancy clusters compared with lower temperatures (discussed in detail elsewhere [87]).

To quantify the bubble size and density, higher magnification TEM images of all the samples were taken near the depth of 700 nm, as shown in Figure 5.34 and Figure D.7 (for lower magnification images). TEM examinations showed that the size of the bubbles increased with increasing irradiation temperature, while the bubble density decreased with increasing temperature. The bubble size and density measurement results are plotted in Figure 5.35. At both 500 and 700°C, Fe-9Cr (without nanoparticles) had the largest average diameter (3.7 and 8.8 nm, respectively) and the lowest density (1.0×10^{23} m^{-3} and 2.0×10^{22} m^{-3}, respectively). In accordance with the in-situ results, the bubble size of the irradiated bulk samples was also in the order of Fe-9Cr > CNA3 >14YWT, and the density had the opposite sequencing. Considering the temperature effect, the size increment and density decrement also have the same order, i.e., for a given implanted material the smallest size and largest density occurred at the lower temperature. Looking at the two materials with the lowest and highest nanostructure density, with increasing temperature (from 500 to 700°C) the cavity sizes in Fe-9Cr and 14YWT increased by a factor of 2.35 and 1.01, respectively. Regarding the density dependence on temperature, Fe-9Cr and 14YWT decreased by a factor of 5.33 and 1.37, respectively.

5.4.3 STEM-EELS characterization of bubbles attached to nanoparticles

Previous APT and TEM results showed that the nanoparticle density of the 14YWT [86] and CNA3 [84] alloys were around 10^{23}-10^{24} and 10^{21}-10^{22} m^{-3}, respectively. These nanoparticle densities are consistent with our EELS elemental mapping results discussed in this section. The cavity appears dark in the STEM annular dark-field (ADF) images, which is opposite to the TEM bright-field images. As shown in our EELS results, the

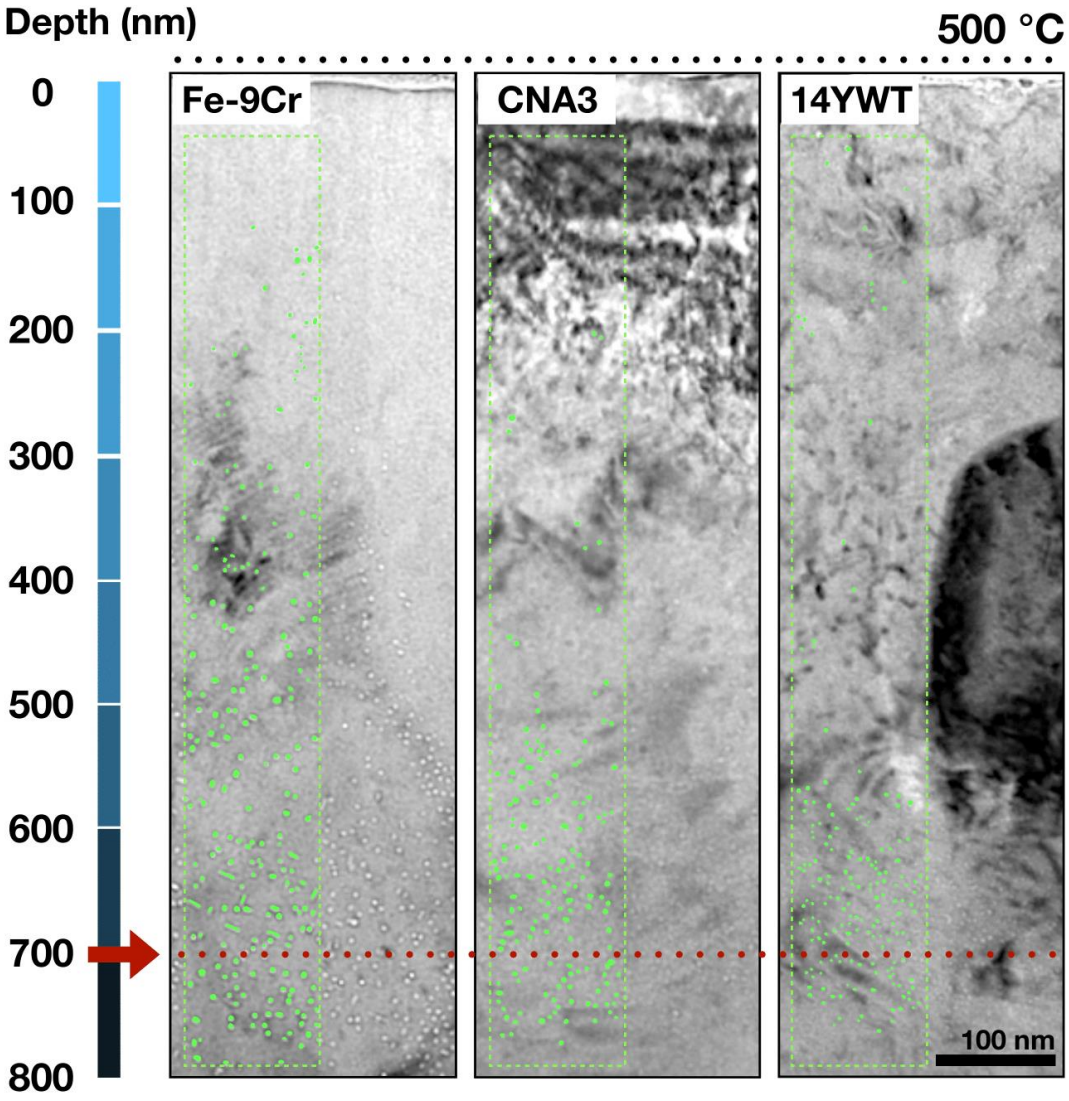

Figure 5.32 Cross-sectional defocused TEM images of the bubble distribution in He-implanted bulk Fe-9Cr and NFAs at 500°C. The red dashed horizontal line indicates the depth location of the peak concentration of He as estimated by SRIM. The light green-filled portions of the micrographs highlight the bubbles present in the matrix, due to the relatively low contrast of the small cavities.

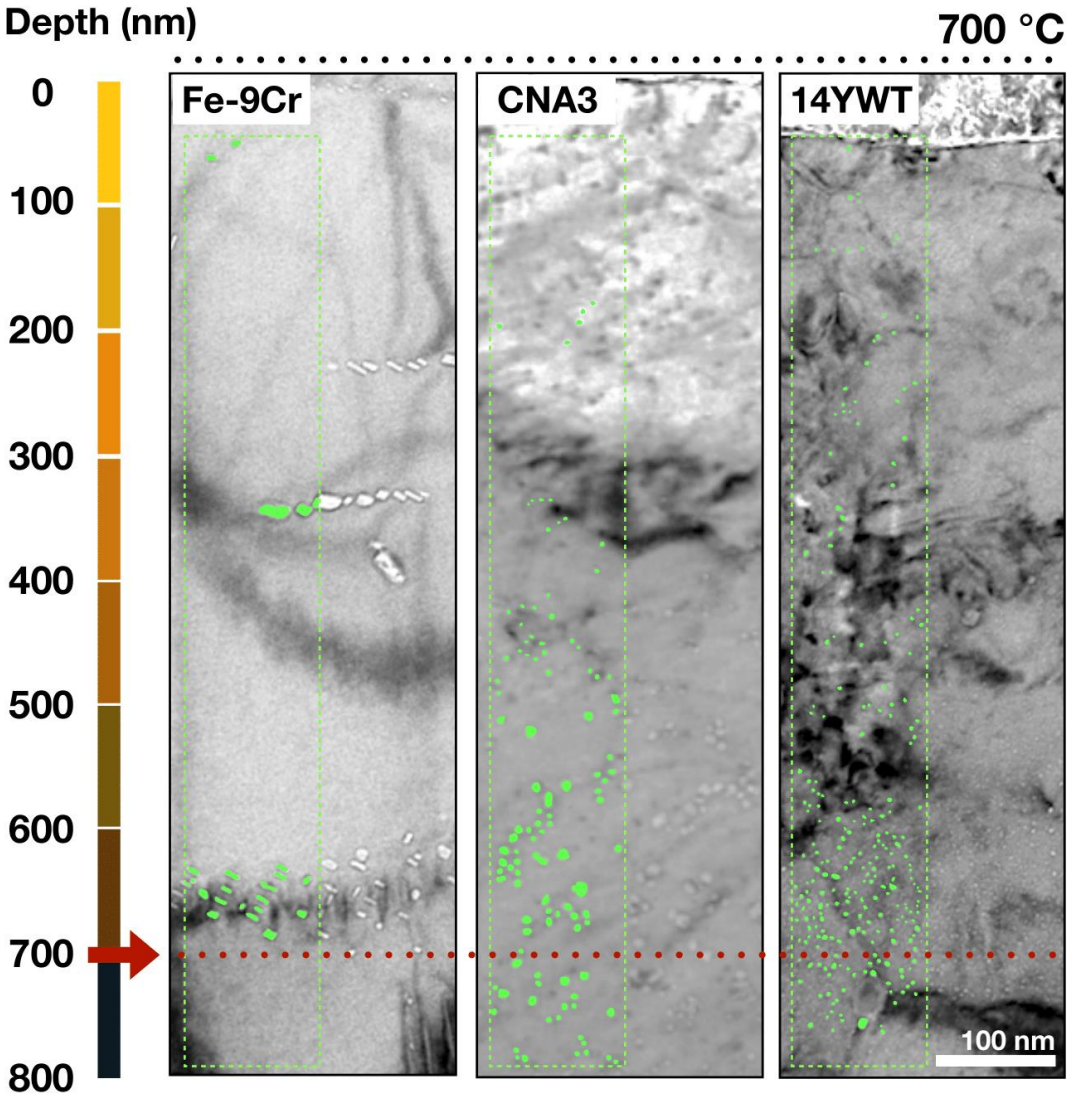

Figure 5.33 Cross-sectional defocused TEM images of the bubble distribution in He-implanted bulk Fe-9Cr and NFAs at 700°C. The red dashed horizontal line indicates the depth location of the peak concentration of He as estimated by SRIM. The light green-filled portions of the micrographs highlight the bubbles present in the matrix, due to the relatively low contrast of the small cavities.

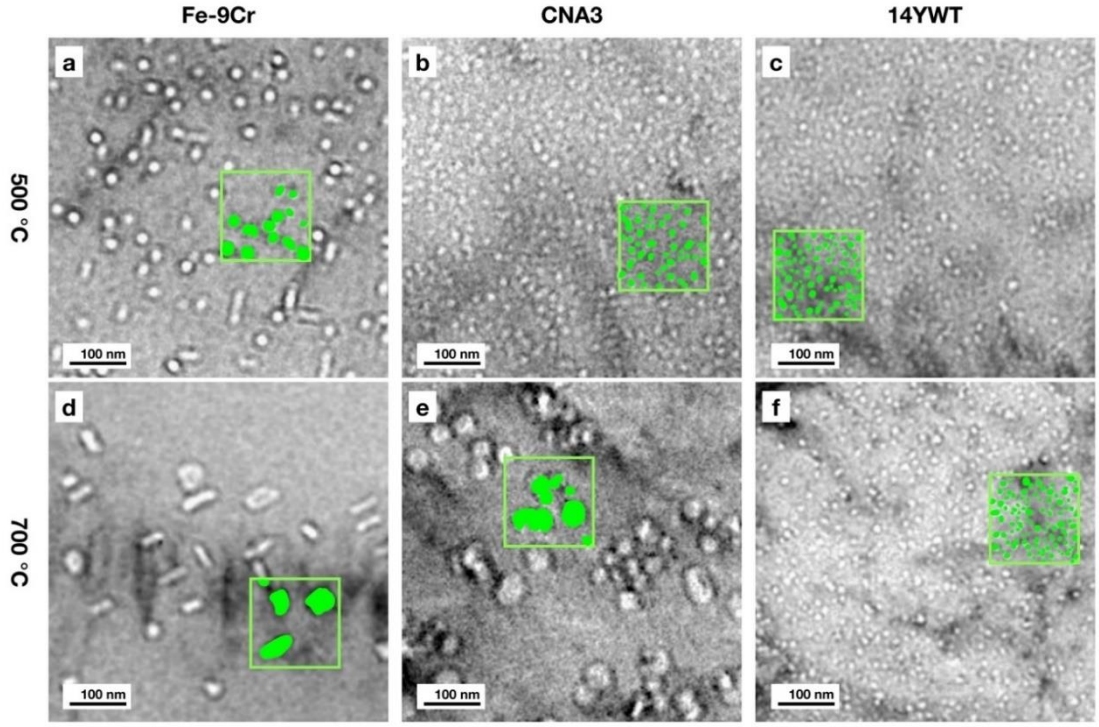

Figure 5.34 Under-focused TEM images of bubbles in He implanted bulk Fe-9Cr and NFAs at 500 and 700°C. The light green-filled portions of the micrographs highlight the bubbles in the materials.

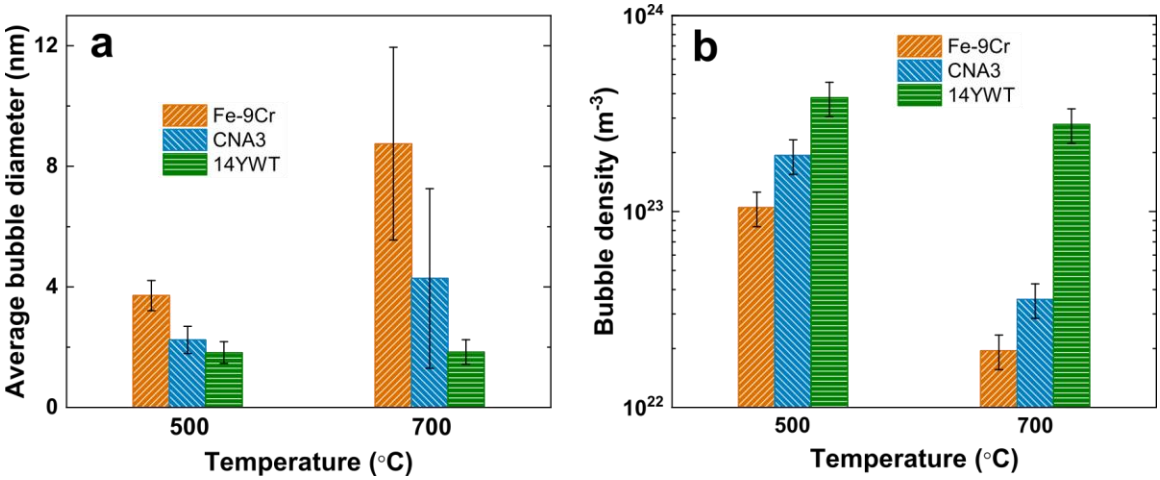

Figure 5.35 Comparison of the (a) average size and (b) density of bubbles in bulk Fe-9Cr and NFAs at 500 and 700°C.

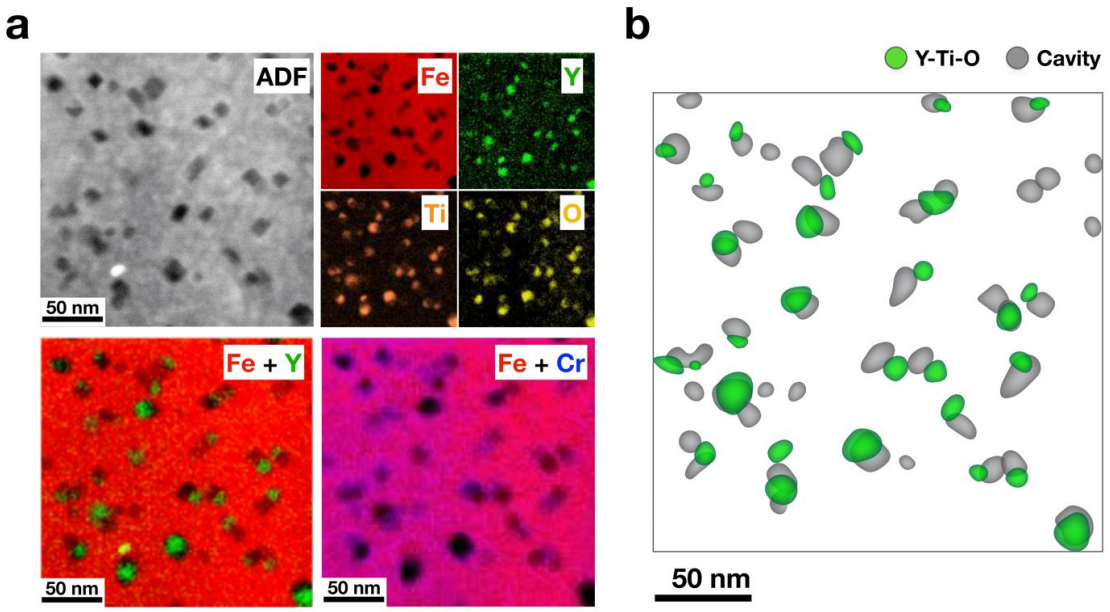

Figure 5.36 (a) STEM-EELS elemental mapping of ex-situ He implanted 14YWT at 700°C. (b) Schematic diagram of Y-Ti-O nanoparticles and cavities based on Fig. a.

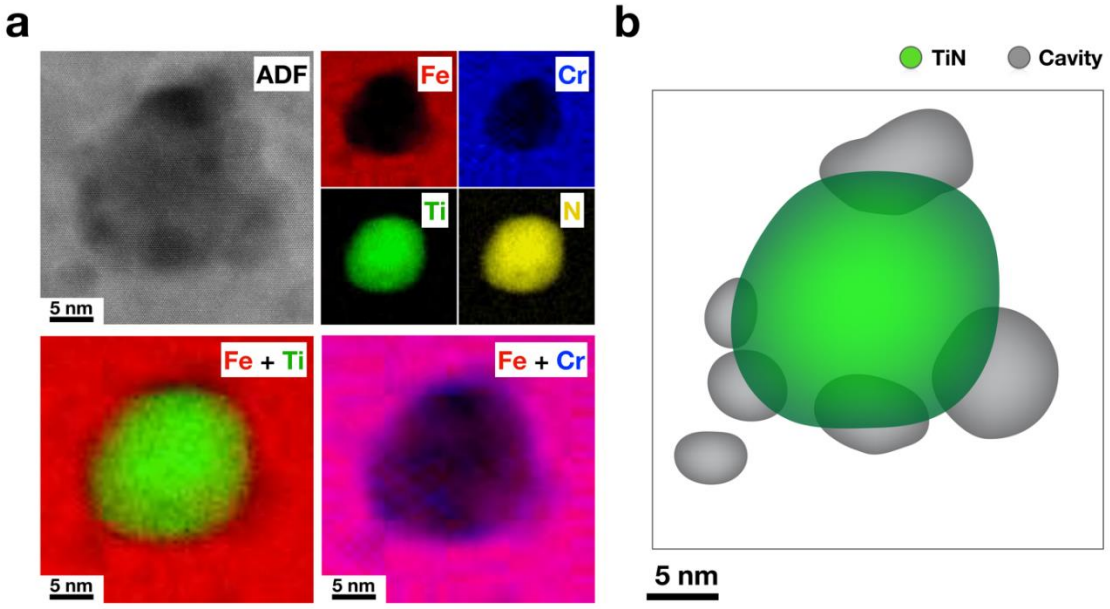

Figure 5.37 (a) STEM-EELS elemental mapping of ex-situ He implanted 14YWT at 700°C. (b) Schematic diagram of Ti-N nanoparticles and cavities based on Fig. a.

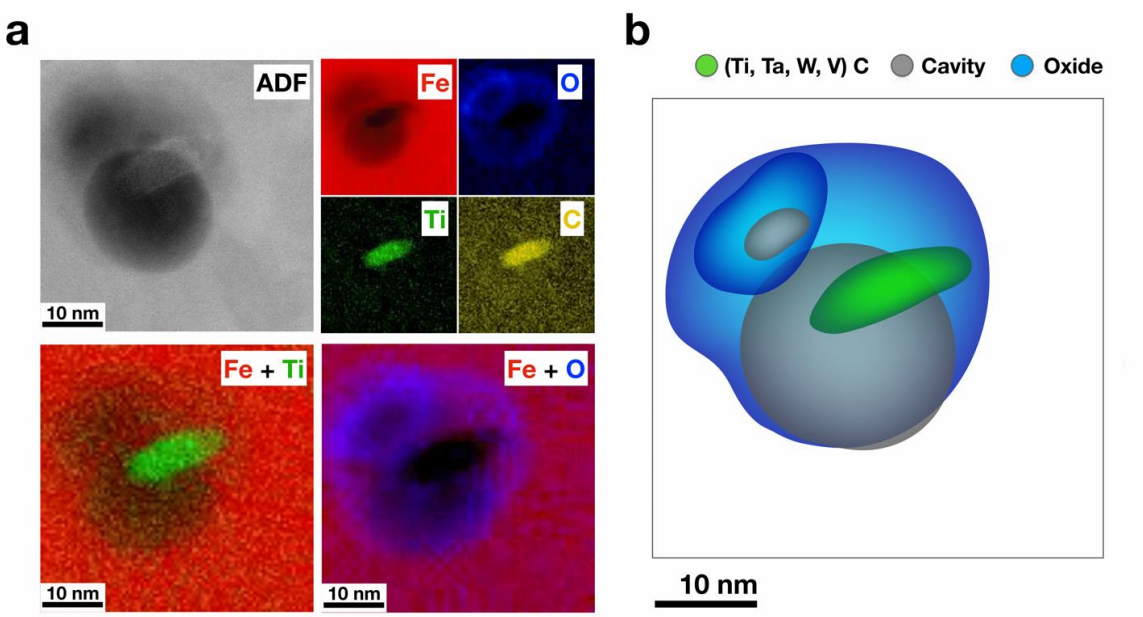

Figure 5.38 (a) STEM-EELS elemental mapping of ex-situ He implanted CNA3 at 700°C (W, V, Ta has the same site distribution as Ti). (b) Schematic diagram of a Ti, W, V, Ta-C nanoparticle, oxides, and cavities based on Fig. a.

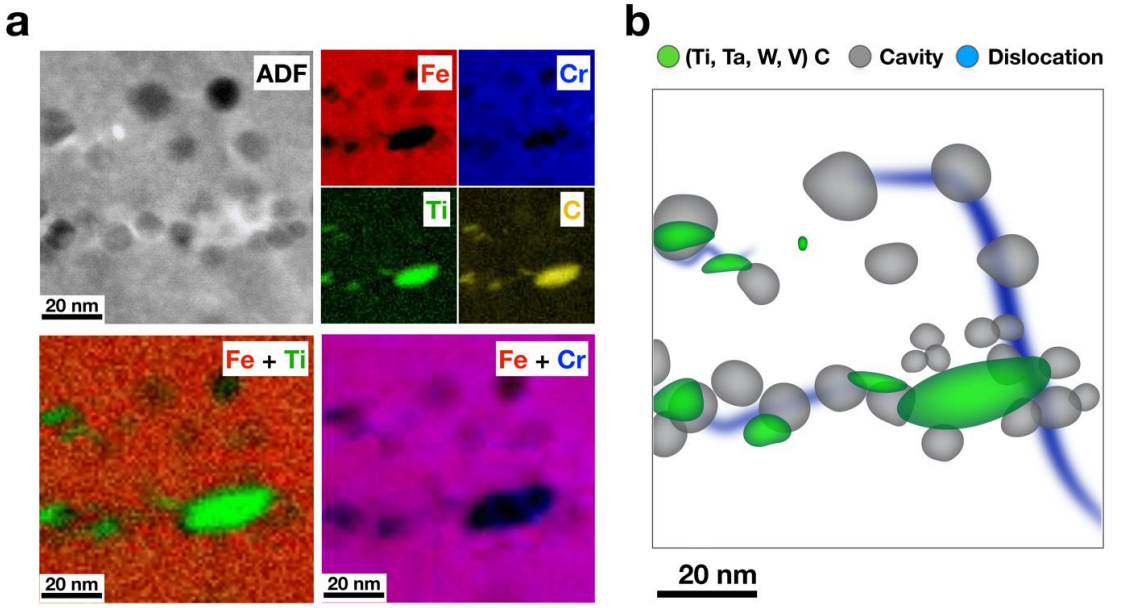

Figure 5.39 (a) STEM-EELS elemental mapping of ex-situ He implanted CNA3 at 700°C (W, V, Ta has the same site distribution as Ti). (b) Schematic diagram of Ti, W, V, Ta-C nanoparticles, dislocations, and cavities based on Fig. a.

nanoclusters in 14YWT were mainly Y-Ti-O nanoclusters (Figure 5.36), whereas coarse Ti-N particles were also observed (Figure 5.37). Cr segregation was observed on the bubble surface in 14YWT, but not in CNA3. Note that the schematic diagrams of nanoparticles and cavities are produced from projected images. The exact 3D position of the nanoparticles and cavities is undetermined. However, the projected images indicate a near one-to-one spatial correlation of cavities and Y-Ti-O nanoparticles in 14YWT. Conversely, multiple cavities tended to be associated with each relatively coarse Ti-N nanoparticle in 14YWT.

A high density of nanoscale MX precipitates (M=Ti, W, V, Ta; X=C, N) were observed in the EELS mapping of CNA3 (Figure 5.38 and Figure 5.39). In both figures, the elemental mapping of W, V, and Ta have the same site distribution as Ti. Our EELS elemental mapping results are qualitatively consistent with other atom probe tomography (APT) results of CNA3 with primarily Ti, W, V, Ta-C particles [85]. However, we also observed that a few of the domains were lacking MX particles. Figure 5.38 shows an isolated particle overlapped with possible oxides. Other studies indicated that inclusions (oxygen- and/or nitrogen-rich) in the CNA3 materials may affect the distribution of MX particles.

Our STEM-EELS elemental mapping results demonstrated that the MX carbides in CNA3 and Y-Ti-O oxides or TiN particles in 14YWT have good capability for trapping He bubbles. In this study, we focused on the fine-scale particles in 14YWT and CAN3. Other coarse particles such as M23C6 and TiC were not investigated. Among our EELS results, the Y-Ti-O nanoparticles in 14YWT have the most uniform distribution and exhibited an apparent one-to-one relationship for bubble attachment to the Y-Ti-O nanoclusters. The Ti, W, V, Ta-C dispersoids in CNA3 (~ two orders of magnitude lower nanoparticle density than 14YWT) attached ~3-10 small He bubbles to a single particle. In the CNA3 sample irradiated at 700°C, some bubbles were observed to be trapped not by nanoparticles but by network dislocations (Figure 5.39). The same phenomenon is clearly revealed by STEM images in the same CNA3 irradiated sample (Figure 5.40), where bubbles appeared at the nodes of dislocation networks.

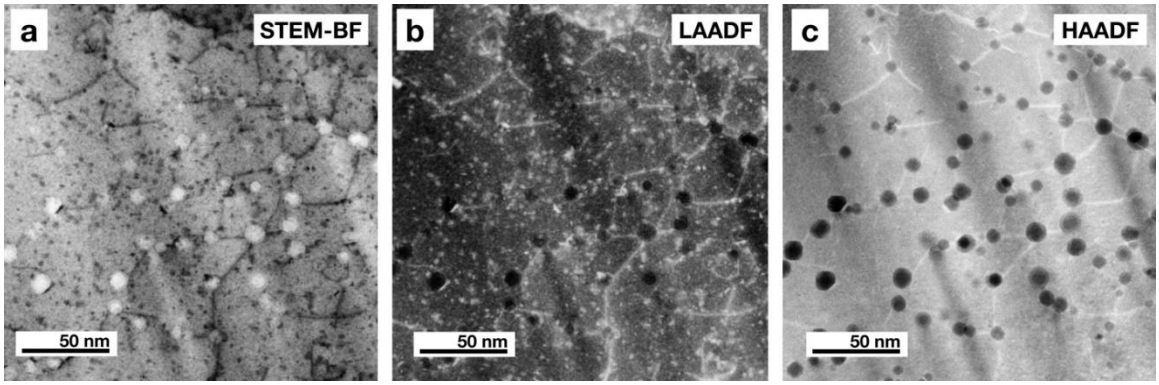

Figure 5.40 STEM images of cavities in ex-situ He implanted CNA3 alloy at 700°C, showing preferential location of cavities on intersecting dislocations: (a) STEM-BF, (b) STEM-LAADF, and (c) STEM-HAADF

The difference between the low-angle annular dark-field (LAADF) and the high-angle annular dark-field (HAADF) images is the collection angle of the detector [112-114]. LAADF images would still show diffraction contrast or difference of specimen thickness dependence due to the partial collection of the Rutherford scattering (elastic) signal which dominates at lower angles. HAADF images collect thermal diffuse scattering (quasi-elastically) signals and are more sensitive to the atomic number.

Chapter 6
Discussion

6.1 Experimental artifacts

6.1.1 Implanted ion effects

Radiation enhanced diffusion

For pure metals, the radiation-enhanced diffusion (RED) coefficient is defined as [89]:

$$D_{rad} = D_v C_v + D_i C_i \tag{6.1}$$

where $D_{i,v}$ is the point defect diffusivity and $C_{i,v}$ is the point defect concentration. With a high dose rate of ion irradiation, the vacancy and interstitial concentration can be much greater than those produced thermally. Therefore, the radiation-enhanced diffusion coefficient is typically much larger than the thermal diffusion coefficient. This agrees with the estimated D_{max} (5×10^{-18} m^2/s) and D_{therm} (2×10^{-22} m^2/s) values in the present study, for Fe-10Cr irradiated at 550°C (Figure 5.11). As shown in Figure 5.11, RED and the co-effect of thermal diffusion (Eq. (5.1)) can result in a considerable broadening of injected ion profiles, drastically different from the original SRIM predictions. Although it has been well known that implanted ions can suppress cavity swelling, there is a lack of detailed studies on RED broadening of the implanted ion profiles and its implications on microstructure evolution. Previous studies [90] showed a large variation in estimated RED values ranging from 10^{-20} to 10^{-17} m^2/s, for comparable irradiation conditions. In the present study, the best fit of D_{max}= 5×10^{-18} m^2/s is at the high end of this range. It is suggested that a buffer zone between the safe analysis regime and the SRIM estimated implanted ion band could be considered to avoid the implanted ion effects. This would narrow down the area of the safe analysis regime. In addition, implanting ion species distinct from the target material elements can cause potential chemical effects. Within the midrange, there was no

evidence of nitrides or other nitrogen compounds under STEM Z-contrast images or EDS/EELS elemental mapping.

Effect of self-ion energies on safe analysis zone and swelling temperature range

For ion irradiation studies, utilization of relatively low self-ion energies ($\leq$ 5 MeV) increases the potential overlap of near-surface and implanted ion artifacts that can suppress the formation and growth of cavities [3]. Significant discrepancies have been reported regarding the reduced temperature range for observable swelling and the temperature-dependent artifacts causing an apparent shift in the peak swelling temperature. As summarized in Figure 3.3., a series of ion irradiation studies on Fe, Fe-Cr model alloys, and FM steels with different dose rates clearly showed variations of peak swelling temperatures [42-45, 104, 115]. This is mainly due to the dose rate effect and could be approximately normalized using Eq. (2.13). Here, we focus on the temperature range of observable cavity swelling, which appears to increase with increasing self-ion energy. A potential complicating effect is associated with the influence of implanted H and/or He on expanding the cavity swelling temperature regime. In Figure 3.3a, the result of triple beam irradiated Fe-9Cr-Mo steel showed a larger temperature range of observable cavities (400-550°C) than the single beam 4 MeV irradiated result (cavities detected only at 493 and 546°C) [115]. Another triple beam study on Fe by Roldan et al. [106] also showed a relatively large temperature range (350-550°C) of observable cavities for ion irradiation studies. As discussed in the previous paragraph, the role of He/H in expanding the temperature range where cavities are visible could be due to the effect of co-implanted gas ions (He/H) that are expected to enhance the nucleation of cavities. In the same figure, comparing our 8 MeV Ni plus He ion irradiation study on Eurufer97 to another dual-beam study on HT9 with lower energy (5 MeV) Fe self-ions (at roughly comparable dose rates), the apparent effect of ion energy on suppressing the breadth of the cavity swelling regime could be clearly seen on the narrower peak of HT9. As shown in Figure 3.3b, the suppression of the cavity swelling temperature range at lower ion energies was not only observed in complex FM steels but also in Fe-Cr model alloys. However, even the swelling

temperature breadth of 8-10 MeV heavy ion results were still ~30% narrower than the neutron-irradiated study on pure Fe [42]. Figure 3.4 shows that with increasing ion energy from 3.5 MeV Fe (1.7×10^{-3} dpa/s), 5 MeV Fe (2×10^{-3} dpa/s), 8 MeV Ni (1.4×10^{-3} dpa/s), to 10.5 MeV Fe (3.5×10^{-3} dpa/s), the full width at half maximum of the observable cavity profile increases. The corresponding dose rate at peak displacement depth of each high-energy ion source is indicated in the parentheses. It is worth noticing that the temperature range for cavity swelling in all ion irradiated Fe-Cr samples reported to date is much less than the ~100°C FWHM observed for neutron irradiation experiment.

Figure 5.10 shows the variation of cavity swelling as a function of depth in Fe, with 0.1 and 10 appm He/dpa irradiation conditions. In general, the cavity swelling should increase with increasing dose [116]. That is, cavity density typically saturates at relatively low doses, but their size monotonically increases with dose. Therefore, within the midrange analysis zone, swelling would be expected to monotonically increase with increasing depth (dpa level). However, indications of an increase of swelling with increasing depth within the relatively safe analysis midrange region (750 to 1500 nm) were only clear in about half of the investigated specimen conditions. For example, in the midrange regions of Figure 5.2 e and f, cavity swelling decreased with increasing depth in both the Fe and Fe-10Cr samples irradiated at 500 and 550°C. These results highlight that even with the relatively high (8 MeV) ion energy used in this study, the safe analysis zone width seems to be quite small, especially for samples irradiated at relatively higher temperatures (where more pronounced diffusion of the implanted ions and near-surface artifacts are predicted, Figure 5.3d). Therefore, implanted ion and free surface effects may be modifying the extent of the observed temperature regime for cavity swelling in the current ion irradiation studies, even for ion energies as high as 8-10 MeV. Both the decreasing of cavity swelling in the midrange region and the suppressed temperature region of observable cavities (Figure 5.2 and Figure 5.3) suggest that for ion irradiation studies on radiation effects, higher injected ion energies that provide a wider safe analysis regime are recommended in order to minimize the two main artifacts of ion irradiation (near-surface and implanted ion effects). However, very high ion energies also require some caution since so-called “swift heavy

ion effects" associated with intense ionization can lead to artifacts that may either enhance or suppress radiation damage [3].

6.1.2 Cavity denuded zone

Vacancy migration energy and relation to peak swelling temperature

Collecting the near-surface denuded zone width data of the fifty ion-irradiated Fe and Fe-Cr samples, the seven 0.1 appm He/dpa data points without interference from post-irradiation sub-grains near the surface and the 10 appm He/dpa results are plotted in Figure 5.13. The calculated denuded zone width by the average width of the cavity to surface distance (X_d) and by the criterion of 30% (X_3) or 50% (X_5) of saturated cavity density (see 5.2.1 for details) were applied to estimate the vacancy migration energy (for recombination dominant condition) [20]. Following Eq.(2.2) where the relationship that the width of cavity denuded zone is proportional to $exp(-E_m/4kT)$, the slope of the lines can be used to estimate the vacancy migration energies (E_m) of each material. The vacancy migration energies are summarized in Table 6.1. The estimation based on the cavity denuded zone data indicates that Fe-3Cr (0.96-2.01 eV), Fe-10Cr (1.22-2.32 eV) and Fe-14Cr (1.31-2.36 eV) have larger vacancy migration energies than Fe (0.96-1.14 eV). However, DFT studies [117] predict lower vacancy migration energies for Fe-3Cr (0.52 eV), Fe-10Cr (0.43 eV) and Fe-14Cr (0.51 eV) as compared to Fe (0.71 eV). The estimated vacancy migration energy of Fe from our experimental data is larger than corresponding typical values measured by several techniques (0.55-0.71 eV) [117-120]. The estimated values based on the cavity denuded zone data also infers that the Fe vacancy formation energy (1.9 eV) and migration energy (0.55 eV) suggested in some previous studies could be underestimated [120].

In Figure 5.13a, the three lower temperature data points (400-470°C) in Fe of the 0.1 appm He/dpa irradiations agree well with the 10 appm He/dpa irradiated samples. However, deviations of the denuded zone width between the 0.1 and 10 appm He/dpa irradiated samples are shown at temperatures above 500°C in Fe-10Cr (Figure 5.13c) and Fe-14Cr (Figure 5.13d). This infers that the diffusion of implanted helium atoms or the

formation of He-V complexes near the surface may affect the vacancy migration energy calculation. In Figure 5.13, when selecting the lower (X_d^{LT}) and higher (X_d^{HT}) three temperatures for slope fitting, the calculated vacancy migration energies were significantly different. In any cases, large uncertainties (up to 50%) exist in the vacancy migration energies based on the error bars in (Figure 5.13). By redesigning the irradiation condition, a higher density of voids without the interference of helium could reduce uncertainty. Nevertheless, the near-surface void denuded method represents a useful experimental approach to estimate vacancy migration energies or obtain qualitative trends when comparing different alloys. Notable drawbacks of this approach are the requirement of high-density cavities and the number of experimental data points to minimize statistical errors. In addition, the potential effects associated with Cr-rich alpha prime precipitation in the high-Cr alloys were not examined. The formation of alpha prime precipitates (section 5.1.5) could reduce the low temperature (<450°C) swelling due to their high sink strength effect, and the lattice distortion with the accompanying formation of high-density network dislocations [121]. However, alpha prime precipitates were not observed in our Talos STEM-EDS results. Future APT analyses would be useful to confirm the preferential conditions for precipitate formation during irradiation.

Formation of subgrain boundaries

The depletion of cavities near the sub-grains observed in the 0.1 appm He/dpa samples could affect the calculation of cavity swelling. However, as mentioned earlier, by quantifying the cavity size and density over a large lateral range (>2 μm) of the FIB samples and avoiding regions near subgrain boundaries, the sub-grain effect could be effectively minimized. As shown in Figure 5.10, in a companion series of higher He/dpa ratio irradiation experiments using the same material, same mechanically thinning process, and same ion irradiation facility, we did not observe sub-grains. The main difference in the experiment results without subgrains was the sample arrangement (see section 4.2.1). Therefore, the formation of these sub-grains might be caused by the strain associated with thermal expansion for samples arranged closely without gaps (see Figure 4.2a for the sample holder and arrangement). The thermal expansion associated with heating Fe bars to

400°C is ~0.5%. Since a thermal expansion gap was not provided between the ends of the clamped samples near the center of the irradiation region, compressive stress above the yield strength of Fe-Cr alloys may have been induced during irradiation due to the thermal expansion and may have caused the observed subgrain formation. This artifact could be eliminated by simply reserving spaces between the pre-irradiated samples, as shown in Figure 4.3a.

6.2 Temperature dependence of cavity swelling

6.2.1 Peak swelling temperature

The mobility of point defects is strongly dependent on the five stages of irradiation temperatures, as discussed in section 2.3.1. In particular, voids are typically not observed below the stage III temperature where mono-vacancies are immobile. In general, the variation of cavity swelling with increasing temperature presents a bell-shaped distribution between 0.3-0.6 T_M [122], as shown in Figure 6.1. At lower temperatures, the high density of dislocation loops and the low mobility of vacancies restrict the growth of cavities due to the recombination of point defects. Therefore, the on-set of the bell-shape distribution is correlated to the vacancy migration energy. At higher temperatures, vacancies may emit out of the cavities due to the increase of the thermal equilibrium vacancy concentration (C_V^{eq}), thereby, limiting cavity growth or causing cavity shrinkage. The addition of gas atoms (such as He) can affect the stability of cavities and thereby modify the vacancy thermal emission term. Besides, Cr atoms if segregate or assemble on the cavity surface may also affect surface energy and modify the vacancy thermal emission term. Therefore, the implanted He content or addition of Cr may both affect the cessation of the bell-shaped distribution.

In Figure 6.2, the peak cavity swelling temperature of several different neutron-irradiated materials is plotted as a function of their recommended vacancy migration energies (values ranging from ~ 0.5-1.7 eV) [25, 34, 42, 123, 124], showing that peak

Table 6.1 Vacancy migration energy calculated from cavity denuded zone width

Material	Vacancy migration energy, E_m (eV)				
	10 appm He/dpa			0.1 appm He/dpa	DFT
	X_d	X_d^{LT} / X_d^{HT}	X_3 / X_5	X_d	Costa (2014)
Fe	1.14 ± 0.53	0.76 / 1.28	0.44 / 0.44	0.96 ± 0.33	0.71 (0.55)
Fe-3Cr	2.01 ± 1.15	2.48 / 1.51	0.97 / 0.96	--	0.52
Fe-10Cr	2.32 ± 1.24	3.74 / 0.82	1.27 / 1.28	1.22 ± 0.61	0.43
Fe-14Cr	2.36 ± 1.41	3.34 / 1.36	0.91 / 0.91	1.31 ± 0.82	0.51

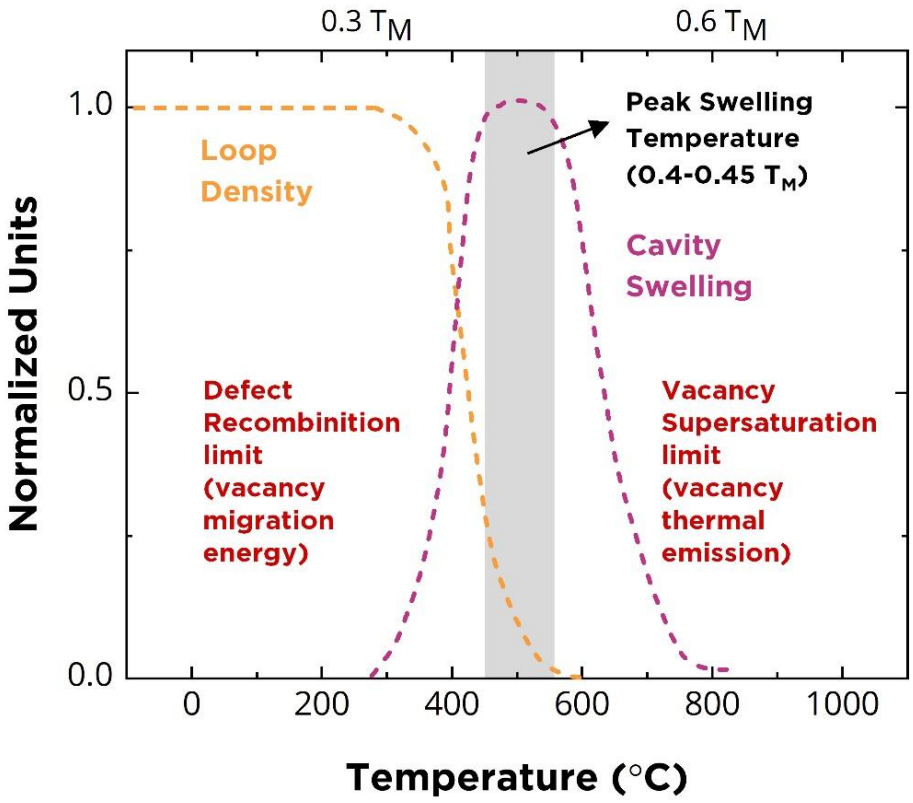

Figure 6.1 The typical trend of cavity swelling with irradiation temperature

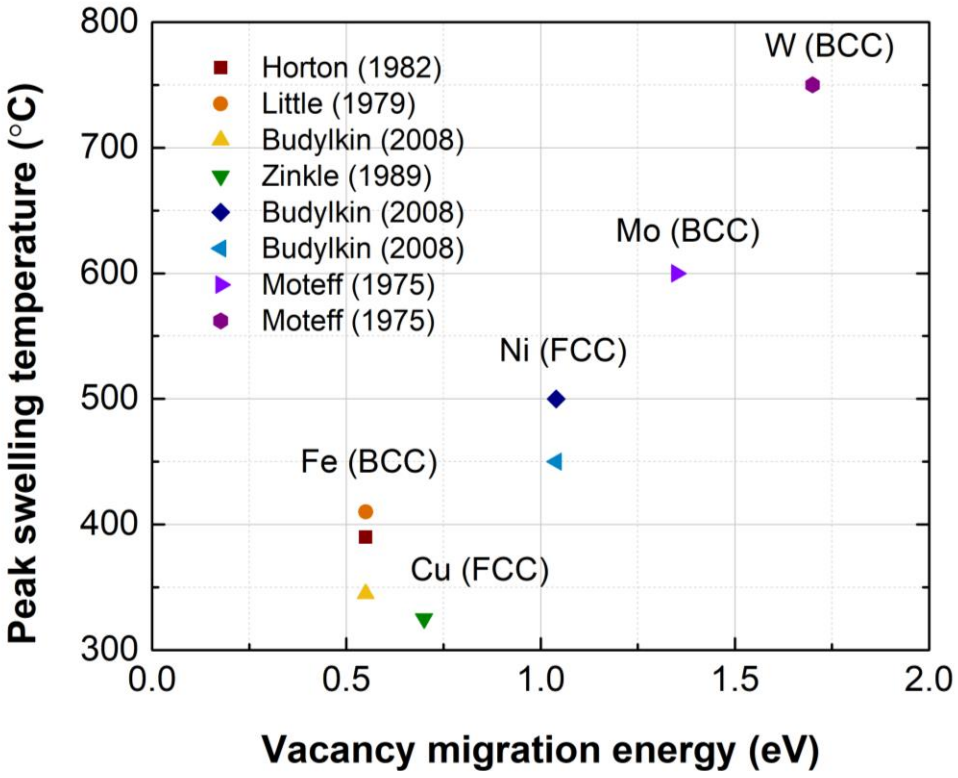

Figure 6.2 Peak cavity-swelling temperatures of neutron irradiation studies (with dose rate ~10^{-6}-10^{-7} dpa/s) in different materials as a function of vacancy migration energy. [25, 34, 42, 123, 124]

swelling temperature increases monotonically with increasing vacancy migration energy. The dose rates of the neutron irradiation studies plotted in Figure 6.2 were in the range of 2×10^{-7} to 1.5×10^{-6} dpa/s. The linear relationship between the peak swelling temperature and the vacancy migration energy (see Table A.1) also supports our finding of high vacancy migration energies for Fe-Cr vs. pure Fe, based on the observed higher peak swelling temperature of Fe-Cr alloys (Figure 5.6). In summary, both the vacancy migration energy estimation (section 6.1.2) and peak swelling temperatures obtained from this study indicate that Fe-Cr alloys may have slightly larger vacancy migration energies than pure Fe. DFT and ab initio studies [117, 125], however, found that the vacancy migration energy as a function of Cr content is complex: while vacancy migration energy in Fe-Cr alloy containing 1-5% Cr was reported lower than in Fe, vacancy migration energy tended to increase for Cr content >5%, and the energy surpassed pure Fe at higher Cr content. Therefore, more modeling research is needed to clarify such discrepancies.

In addition, higher He/dpa ratio resulted in a higher peak swelling temperature for pure Fe, but not for the other Fe-Cr alloys (Figure 5.20). The He effect on peak swelling temperature is probably because of the decrease of cavity shrinkage rate by the pressure effect of helium. This would extend the bell-shaped cavity swelling to a higher temperature. The absence of peak swelling temperature shift in Fe-Cr alloys is likely due to the artifact of injected ions at higher temperatures (see section 6.1.1). Another speculation is the addition of Cr may modify the cavity surface energy and weaken the He pressure effect.

6.2.2 Dose rate effect on swelling temperature shifts

Dose rate is one of the biggest differences between neutron and ion irradiations. The high dose rate ion irradiation results in high concentration of point defects compared to neutrons and a lower ratio of thermal emission of vacancies at a given temperature. The cavity swelling results obtained with high dose rate ion irradiations can be roughly compared to lower dose rate neutron irradiations by employing a shift in the irradiation temperature. Based on classical rate theory for recombination-dominant steady-state conditions, the

temperature shift between two different dose rate irradiations that produces a constant net flux of vacancies vs. interstitials to cavities is given by Eq. (2.13) [26, 126].

To compare our ion irradiation results to previous neutron studies, we substituted the peak swelling temperature values obtained from Figure 5.6 (T_1 = 450 and 500°C for Fe and Fe-Cr alloys, respectively) into Eq. (2.13) to estimate the peak swelling temperature shift. The Fe mono-vacancy formation energy and migration energy were set as 2.02 and 0.67 eV, respectively [118, 119]. This gives a predicted temperature shift of about 64°C, when comparing our ion irradiation cavity swelling result on Fe (1.4×10^{-3} dpa/s) to previous neutron irradiation studies on Fe performed at ~8×10^{-7} dpa/s [34, 42]. Likewise, assuming Fe-Cr alloys with the same value of formation and migration energy as pure Fe, the predicted temperature shift of Fe-Cr alloys was approximately 74°C lower for neutron studies [36, 108]. Experimentally, the peak swelling temperature shifts determined from Gaussian curve fitting of the temperature-dependent swelling profiles of Fe and Fe-Cr alloys for ion and neutron irradiation (Figure 6.3) of Fe, Fe-10Cr, and Fe-14Cr were 54°C (449°C vs 395°C), 78°C (503°C vs 425°C), and 73°C (498°C vs 425°C), respectively. The experimental ion vs. neutron irradiation peak swelling temperature shift values of ~50-75°C is close to the theoretically estimated values.

The temperature range over which swelling occurs appears to be broader for neutron-irradiated Fe [34, 42] compared to our dual beam ion irradiated Fe. In addition, it should be emphasized that the temperature profile did not have a simple translation shift for the entire swelling curve. Instead, the shift in the onset and cessation swelling temperatures were different than the shift in peak swelling temperature. Theoretically, the onset of swelling is related to the point defect recombination or sink-dominant limit, while the cessation of swelling is due to the limitation of vacancy supersaturation [116]. According to the cavity growth rate as shown by Eq. (2.5) and (2.6), at low temperatures, the supersaturation can be very high, which should make nucleation easy. However, low D_v and high C_i and C_v can lead to high matrix recombination for low sink strengths. Or alternately, high dose rates can lead to high sink strengths and increase C_i and C_v absorption at sinks. Either way, nucleation and growth of small cavity nuclei becomes

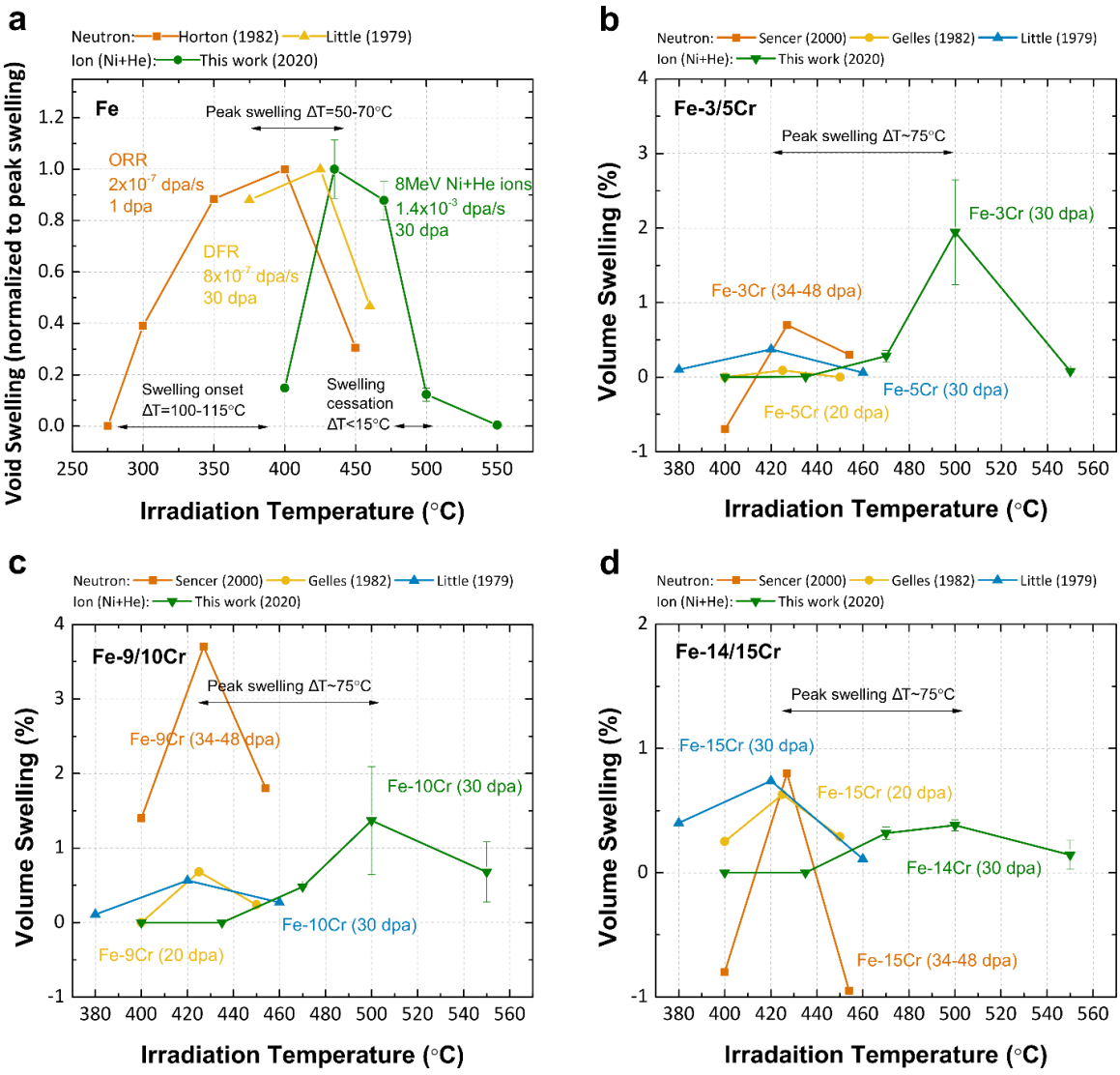

Figure 6.3 Comparison of cavity swelling as a function of temperature in previously reported neutron studies and the current dual ion irradiation study (a) Fe; (b) Fe-3/5Cr; (c) Fe-9/10Cr; (d) Fe-14/15Cr [34, 35, 42, 108]. The densification observed by Gelles (1982) in Fe-15Cr at 400 and 453°C is attributed to precipitation effects.

difficult. At high temperatures C_v^{eq} increases, this reduces the vacancy supersaturation $(D_vC_v - D_iC_i)/(D_vC_v^{eq})$. Nucleation becomes difficult at high temperatures because of the low supersaturation. Growth also becomes difficult because the growth rate is proportional to $(D_vC_v - D_iC_i - D_vC_v^{eq})$, which is reduced by increased emission. In other words, at higher temperatures, the swelling cessation is more strongly influenced by vacancy emission from cavities instead of vacancy flow to cavities.

Note that Mansur et al. [126] derived six different temperature shift relationships for sink-dominant (relevant for low irradiation temperature) and recombination-dominant conditions. Most of the temperature shift expressions are valid for the upper-temperature limit for cavity swelling, and considered to be approximately accurate also for the peak swelling temperature. However, these expressions are generally not valid for the onset of cavity swelling. The net result is generally to produce a narrowed temperature range for cavity swelling at high dose rates compared to reactor-relevant dose rates. This shifted and narrowed temperature range in accelerated-rate irradiation experiments must be considered when evaluating accelerated dose rate studies. Besides, the Mansur model is based on an extremely simplified version of the rate theory (steady-state conditions do not exist because of the long-term evolution of the irradiated microstructure) and does not consider temperature dependent stability of different microstructural features. Therefore, the model should be used with care. Future studies are needed to examine if other factors could affect this simplified model established in the 1970s.

6.3 Dislocation loops and network dislocations

6.3.1 Dislocation loop types: ⟨100⟩ and ½⟨100⟩ loops

Figure 5.23a shows an apparent dynamic transformation of two $\frac{1}{2}\langle 111\rangle$ loops to a $\langle 100\rangle$ loop. The reaction involved coalescence of two $\frac{1}{2}[111]$ and/or $\frac{1}{2}[\bar{1}11]$ loops to form a $[010]$ edge-on loop. However, based on vector summation and consideration of Frank's energy criterion from dislocation theory [127], the $[010]$ edge-on loop should not

be possible from the Burgers vector sum of $\frac{1}{2}[111]$ and/or $\frac{1}{2}[\bar{1}11]$ loops. The observed transformation infers that the formation of $\langle 100 \rangle$ loops may not follow the conventional direct (one-step) Burgers vector summation assumption of dislocation theory. This finding supports the study by Xu et al. [68] using the self-evolving atomistic kinetic Monte Carlo (SEAKMC) method. Their analysis suggested rearrangement of interstitials occurred during the loop transformation, as opposed to a direct dislocation reaction. Besides, immediately before the formation of the [010] edge-on loop (Figure 5.23b), the two reacting loops were lying along the projected [011] orientation. If the two loops reacted along $\langle 110 \rangle$ direction, this reaction would support the observation in the MD study by Marian et al. [128], where a two-step reaction with intermediate $\langle 110 \rangle$ configuration was proposed. The Marian et al. two-step reaction is also distinct from the simple one-step "111 to 100" loop reaction. Although our experimental evidence shows that the "111 to 100" loop reaction may not be a traditional one-step loop reaction, further studies are needed to confirm the details. In summary, the "111 to 100" loop reaction could involve complex interstitial rearrangement (not following the vector summation and Frank's energy criterion, supporting Xu et al. [68]), and/or the reaction could involve multi-step reactions in accordance with dislocation theory (supporting Marian et al. [128]).

The relative fraction of $\langle 100 \rangle$ loops in Fe and Fe-10Cr as a function of increasing dose are shown in Figure 6.4a. Since $\langle 100 \rangle$ and $\frac{1}{2}\langle 111 \rangle$ loops are the two main types of loops observed in Fe and Fe-Cr alloys, the $\frac{1}{2}\langle 111 \rangle$ loop fraction could be roughly given by subtracting the $\langle 100 \rangle$ loop fraction from the whole (100%). The loop types (away from the grain boundary) in the Fe foil irradiated at 435 °C (Figure 6.4) are predominantly $\frac{1}{2}\langle 111 \rangle$ loops at all investigated doses. As for the Fe-10Cr foil, the quantitative dose dependence of $\langle 111 \rangle$ vs. $\langle 100 \rangle$ loops for Fe-10Cr in our study depends on whether the observed $\langle 100 \rangle$ loop strings are considered to consist of small $\langle 100 \rangle$ loops or $\frac{1}{2}\langle 111 \rangle$ loops. If the observed $\langle 100 \rangle$ loop strings in Fe-10Cr (Figure 5.26b) consist of ordered arrays of $\langle 100 \rangle$ loops, the dominance of $\langle 100 \rangle$ loops in Fe-10Cr at doses <10 dpa (Figure 6.4; dashed line) is contradictory to the unfavorable self-energy of $\langle 100 \rangle$ loops at lower temperature [57] and

also the "111 to 100 reaction" [68]. A possible explanation could be that the ⟨100⟩ loop strings observed in Fe-10Cr below 10 dpa (Figure 5.26b) may actually be $\frac{1}{2}\langle 111\rangle$ loops arrayed along the projected ⟨100⟩ direction. For this postulated scenario, it would be puzzling why these lined up black dot loops which were very close to each other (distance <10 nm) did not coarsen to larger loops. Nevertheless, if we assume that the ⟨100⟩ loop strings were assemblies of $\frac{1}{2}\langle 111\rangle$ black dot loops (Figure 6.4; solid line), the ⟨100⟩ loop fraction would dramatically decrease to ~10 % or less over all doses. The loop type in Fe-10Cr would then become consistent with the Fe result with predominantly $\frac{1}{2}\langle 111\rangle$ loops at all irradiation doses at 435 °C. In addition, the lower fraction of ⟨100⟩ loops in Fe-10Cr would agree with previous studies that indicated the Cr interaction could reduce the $\frac{1}{2}\langle 111\rangle$ loop diffusivity and reduce the population of ⟨100⟩ loops [66]. Conversely, Schaublin et al. [94] reported that Cr solute additions could favor the formation of ⟨100⟩ loops. Due to the restriction of the *in-situ* irradiation study, we could not recheck the loop types at doses <5 dpa with different g vectors in the post irradiated sample.

In Figure 6.4b, regarding the temperature dependence of the two different families of loop Burgers vectors in pure Fe, previous ion irradiation results [55, 56, 129] are qualitatively consistent with the neutron irradiation results [42, 50-53] that ⟨100⟩ loops are progressively favored over $\frac{1}{2}\langle 111\rangle$ loops at higher irradiation temperatures (please refer to Table C.1 for the details of irradiation conditions in the references). Nevertheless, previous ion irradiation studies reported that the $\frac{1}{2}\langle 111\rangle$ loops are predominant at irradiation temperatures <400°C, whereas large fractions of ⟨100⟩ loops occur above ~450°C. Therefore, the observed predominance of $\frac{1}{2}\langle 111\rangle$ loops in 435°C ion irradiated Fe and Fe-10Cr is in moderate quantitative disagreement regarding ⟨100⟩ vs. $\frac{1}{2}\langle 111\rangle$ temperature-dependent loop stability compared to prior ion irradiation studies at comparable dose rates. Also, in Figure 6.4b, it should be noted that ⟨100⟩ loops typically do not become predominant until ~400-450°C for ion irradiation, while ⟨100⟩ loops are already predominating at ~300°C for neutron irradiation. This apparent dose rate effect [23, 130]

suggests that some sort of thermally activated transformation is involved in the creation of $\langle 100 \rangle$ loops. Another contributing factor to the different loop-type transformation temperatures between neutron and ion irradiation could be caused by the loss of the more mobile $\frac{1}{2}\langle 111 \rangle$ loops to the surface for *in-situ* ion irradiated thin foils.

At low dose <1 dpa where the loops were in the form of black dot defects, the loop types could be identified by the moving direction of the black dot defects. Table 6.2 summarizes the frequency of different loop motion events that happened between 0.3-0.8 dpa. The corresponding irradiation time (recorded video time) is approximately eight minutes. We focused on the loops that moved or disappeared from their original site. The number of newly-formed and static loops were not counted. In Table 6.2, the event of absorption with a specified migration direction means that a loop was attracted by another nearby loop and migrated toward the adjacent loop along the indicated direction. Within a 500 nm × 500 nm area, the total motion event frequency in Fe and Fe-10Cr were 26 and 11, respectively. This also infers that the addition of Cr impedes loop mobility. In both materials, loop migration and absorption along $\langle 111 \rangle$ or $\langle 110 \rangle$ directions accounted for about half of the motion events, and approximately one-third of the motions were along $\langle 100 \rangle$ directions. About 10% of the loss of loops and migration of loops occurred in an undefined direction.

It is worth noting that most previous studies reported $\langle 100 \rangle$ loops should be sessile (or have very low mobility) [129, 131]. However, a few studies reported that $\langle 100 \rangle$ loops could be glissile (mobile) at 500°C [132, 133]. It is possible that the motion of $\langle 100 \rangle$ loops shown in Figure 5.22c was actually an illusion of two loops (the first loop vanished by gliding to the surface, and a new loop was formed in the next frame). At low dose and thinner sample areas, as shown in Table 6.2, the loss of loops to the surface was seen frequently during the *in-situ* irradiation observation. A further way to confirm the motion of loops is to check if the loops were hopping in the recorded video. Unfortunately, in the present study, the electron beam was fixed at a single zone axis, and rapidly hopping of loops was not observed in the recorded videos. Jenkins et al. [129] observed the hopping of loops (only for $\frac{1}{2}\langle 111 \rangle$ loops) between successive 1/30 s video frames. This study,

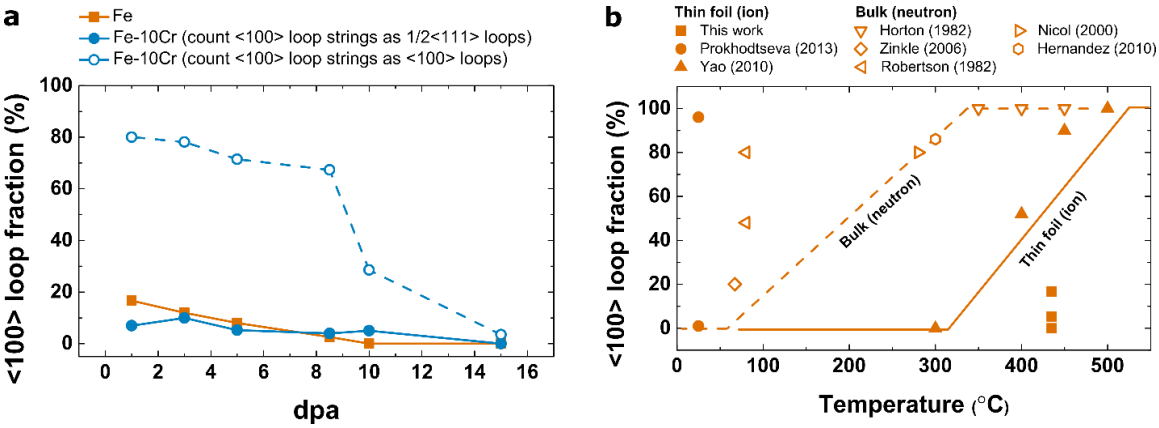

Figure 6.4 (a) Dose dependence of the fraction of ⟨100⟩ loops in dual-beam irradiated Fe and Fe-10Cr foils at 435 °C; (b) temperature dependence of the fraction of ⟨100⟩ loops in irradiated pure iron materials. (Ref. [42, 50-53, 56, 63])

Table 6.2 Frequency of small black dot loop motions for in-situ irradiated Fe and Fe-10Cr at 435°C between 0.3-0.5 dpa.

Motion events	UHP Fe		Fe-10Cr	
	Counts	Fraction	Counts	Fraction
⟨100⟩ migration	3	12 %	1	9 %
⟨111⟩ or ⟨110⟩ migration	8	31 %	3	27 %
Undefined orientation migration	2	8 %	1	9 %
⟨100⟩ absorption	4	15 %	2	18 %
⟨111⟩ or ⟨110⟩ absorption	3	12 %	1	9 %
Undefined orientation absorption	1	4 %	0	0 %
Loop loss	5	19 %	3	27 %

however, recorded the video with an exposure time of one second. Even though the motion of black dot ⟨100⟩ loops could not be scrupulously verified with the present results, the migration of ⟨100⟩ loops near the grain boundary as shown in Figure 5.23b seems to be credible.

In addition, Prokhodtseva et al. [63] reported that the foil orientation could also affect the fraction of the ⟨100⟩ and $\frac{1}{2}$⟨111⟩ loops observed during *in-situ* thin-foil ion irradiations. In ref.[63], for a dual Fe and He ion irradiated (1 dpa and 1,000 He appm) Fe-10Cr at room temperature, the ratio of ⟨100⟩ and $\frac{1}{2}$⟨111⟩ loops were 86:14 and 32:68 for the foil orientations of [001] and [111], respectively. In the present study (as shown in Figure 6.4a), with foil orientation near the [100] direction, ⟨111⟩ loops were predominant at all doses. Only for the assumption in Figure 6.4a that the ⟨100⟩ loop strings are composed of ⟨100⟩ loop arrays does the ⟨100⟩ fraction become predominant (for doses below 8 dpa). It should be emphasized that the observation of ⟨100⟩ loops in ref. [63] was at room temperature. According to prior experimental [56] and simulation studies [57], ⟨100⟩ loops should only become energetically favorable above 300°C. Future studies to confirm the effect of free surface/grain boundary on the mobility of ⟨100⟩ loops would be valuable to understand the formation mechanism of ⟨100⟩ loops.

6.3.2 Distribution of dislocation loops: loop decorations and loop strings

Loop strings were observed in the Fe and Fe-10Cr foils for doses starting at 1 dpa (Figure 5.21) and 5 dpa (Figure 5.25), respectively. The fraction of different line orientations of the overall loop strings is summarized in Table 6.3. Within an 800 nm × 800 nm area, the orientation of around 50 loop strings was counted and identified for both samples. As discussed previously, due to the fixed zone axis along [100] used in this study, we could not distinguish the loop string orientation between ⟨111⟩ and ⟨110⟩ directions. However, even counting the ⟨111⟩ and ⟨110⟩ loop strings together, both the Fe and Fe-10Cr samples showed a dominance of ⟨100⟩ loop strings (over 50%). In the Fe foil at 1 dpa, it is obvious that the ⟨111⟩ and ⟨110⟩ loop strings mostly consisted of 10-20 nm elliptical $\frac{1}{2}$⟨111⟩ loops, while the ⟨100⟩ loop strings were an array of smaller black dot

loops. In an *ex-situ* ion irradiation study on UHP Fe at 300°C and 6.5 dpa, Hernandez et al. [62] also observed $\langle 111 \rangle$ or $\langle 110 \rangle$ loop strings consisting of large (10-100 nm) elliptical loops at a similar $[001]$ pole with $g = [1\bar{1}0]$. However, they did not observe loop strings laying along other directions.

The phenomenon of black dot loops decorating pre-existing dislocations was observed in both Fe (Figure 5.22a) and Fe-10Cr foil (Figure 5.26a), but the decoration of black dot loops around the pre-existing dislocations in Fe was more pronounced. Based on the motion of the black dot loops in the recorded video, both $\langle 100 \rangle$ loops and $\frac{1}{2}\langle 111 \rangle$ loops were observed to be attracted to the dislocations. The dislocations in both Figure 5.22a and Figure 5.26a were either pure edge (Burgers vectors perpendicular to the dislocation line) or mixed dislocations. This observation is different than the neutron irradiation study on model Fe-9Cr alloy (at 325°C and 1.6 dpa) reported by Haley et al. [134], where vacancy defects interacted with pre-existing screw dislocations and resulted in the gathering of defect clusters near dislocations. For the Cr effect, it has been reported that when a considerable amount of interstitial impurities (e.g. Cr, C, and N) are present in Fe, the distribution of dislocation loops apparently becomes more uniform due to the high affinity of impurities to point defects and defect clusters [49, 54]. This statement supports the above-mentioned finding in this study, suggesting the phenomenon of rafting or dislocation decoration would diminish when the irradiated Fe has higher impurity content or when Fe-Cr alloys are irradiated.

6.4 Initial sink strength

6.4.1 Features of in-situ irradiated thin foils

Several differences have been observed between *in-situ* irradiated foils and *ex-situ* irradiated bulk materials. Although *in-situ* irradiation studies can provide valuable dynamic information on the microstructural evolution, possible major surface effect contributions such as defect denuded zones must be kept in mind when comparing *in-situ* studies to the

results of irradiated bulk materials. Kirk et al. [135] verified a pronounced reduction of loop density for *in-situ* irradiated Fe thin foils compared to bulk irradiations due to the loss of mobile loops to the nearby surface. The loss of mobile loops was also observed frequently in the present study especially in the thin area of the samples. However, in Figure 6.19, at comparable temperatures and higher doses, ion irradiated thin foils generally show a higher density and smaller size of loops compared to neutron-irradiated bulk materials. Another noteworthy difference that could also be related to the loop size and density is that *in-situ* ion studies usually are performed with a dose rate of 10^{-3}-10^{-4} dpa/s, while neutron irradiation studies have a dose rate ~10^{-7} dpa/s.

A defect denuded zone near the grain boundary (denuded zone width ~250 nm) was clearly observed in the Fe foil (Figure 5.22). Assuming that the grain boundary has an equal point defect sink strength effect as the foil surface, the grain boundary loop denuded zone implies loops should not be observed anywhere in the TEM foils with a thickness only ~100 nm; the defect denuded zone covering the upper and lower surface of the TEM foil would suppress dislocation loop formation in foils with thickness <500 nm. However, dislocation loops and network dislocations were obviously observed in both the Fe (Figure 5.22) and Fe-10Cr (Figure 5.26) thin foils with thickness ~100 nm. One possible hypothesis is that the defect denuded zone near the grain boundary could be strongly affected by the 1-D migration of loops migrating parallel to the ⟨001⟩ oriented foil surface. In Figure 5.22, with increasing dose, different types of loops were observed near and away from the grain boundary. An analogous heterogeneous difference in loop formation near grain boundaries was also reported for Fe-Cr-Al alloys after neutron irradiation in bulk materials at 382 °C to 1.8 dpa [60]. The observation of ⟨100⟩ types of loops predominantly near the grain boundary seems to support the "111 to 100 reaction" mechanism, where the formation of ⟨100⟩ loops involves interactions between two $\frac{1}{2}\langle 111\rangle$ loops [68, 128]. As shown in Figure 5.23b, the "111 to 100 reaction" could be enhanced near the grain boundary, resulting in a high population of ⟨100⟩ loops. A probable explanation is that the lower loop density in the vicinity of the grain boundary might favor certain types of dislocation loop interactions compared to the grain interior. At intermediate doses, the increasing population of ⟨100⟩

loops migrating along [001] and [010]directions toward the grain boundary (Figure 5.24b) interweaved into a grid-pattern dislocation network. The absence of ⟨100⟩ loops near the grain boundary in the Fe-10Cr foil could be due to Cr solute effects that reduce the $\frac{1}{2}\langle 111\rangle$ loop mobility [68].

6.4.2 Overall bubble behavior in NFAs

Radiation-induced defects that have been observed in irradiated FM alloys by TEM include small "black spot" loops, perfect loops with ⟨100⟩ or ½⟨111⟩ Burgers vectors, network dislocations, and cavities [136]. In this study, the materials were irradiated at temperatures well above recovery stage III (onset of vacancy migration; ~230 K in Fe) and stage V (vacancy cluster evaporation; ~550 K in Fe) [118, 136] with relatively low damage of 0.1-0.3 dpa produced by He ions. At such conditions, the main types of defects are network dislocations and cavities (Figure 5.40). Previous studies proposed that swelling could be reduced by dislocation loops [137]. However, the physical impingement-induced transformation of loops to network dislocations at high doses/high temperatures reduces the total dislocation sink strength to a moderate value and promotes the formation of cavities [138]. In the present study, we focus on the relationship between cavities (He bubbles) and nanoparticles. The implantation of ~10,000 appm of helium corresponds to the assumed lifetime He accumulation in FM steel for DT fusion reactor blanket structures (~100-200 dpa corresponds to ~10,000 to 20,000 appm He for DT fusion spectrum [4]). As summarized in Figure 6.5, for both ex-situ and in-situ experiments, in general the He bubble size increased and the density decreased with increasing temperature from 500 to 900°C for all three alloys, as expected based on simple cavity coarsening considerations.

It is worth noting that different microstructures have been observed between in-situ and ex-situ experiments at similar irradiation conditions [135, 138]. The most influential difference is the surface effect, which could result in near-surface cavity denuded zones for both sides of in-situ irradiated thin foils. However, such surface effects have been observed to be minimized for nanostructured or nanocrystalline materials [139, 140], which can be

understood based on standard rate theory sink strength considerations [141]. The high interior sink strength reduces the vacancy supersaturation and thereby suppresses the foil surface sink effect. For the two nanostructured alloys, the grain boundary to surface ratio and their high matrix sink strengths are large enough to assume that the in-situ data is not very affected by the surfaces. Besides, according to the analysis of cavity areal density as a function of the thickness in the present study (Figure. D.3), the denuded zone width seems to be undetectable within experimental uncertainties for the nanostructured alloys. In Figure 6.6, the cavity swelling of nanostructured alloys also infers that the cavity features in the two types of irradiation experiments are comparable at relevant temperatures. Therefore, in Figure 6.5, we assumed that the thin foil denuded zone effect is minimized in the nonstructured alloys and combined the in-situ and ex-situ results as one dataset.

Based on Figure 6.5, the 14YWT alloy appears to sequester the helium into smaller bubbles more effectively, and has the highest bubble density among the three investigated alloys at all temperatures. The CNA3 alloy exhibited good He trapping at 500 and 600°C but relatively inefficient trapping at 700 and 900°C, based on the decrease in measured cavity density and the observation of cavities preferentially attached to dislocations rather than exclusively being associated with MX particles (Figure 5.40). This may indicate that MX particles in CNA3 may not be stable or have an insufficient He binding energy (lower He trapping ability) at high temperatures above 700°C. In addition, at 900°C, the irradiation temperature exceeds the austenite transformation temperature (~ 848°C) for 8-10 at% Cr in Fe-Cr binary system. Therefore, phase transformation has a chance to occur in the matrix and affect the formation of bubbles for the 900°C anneals. Generally, the cavity swelling resistance of body-centered cubic metals (e.g., ferritic/martensitic steels) is superior to that of face-centered cubic metals (e.g., austenitic steels) [7, 122].

Dauben et al. [142] and Yan et al. [87] reported two different apparent activation energies at low-temperature and high-temperature regimes for helium bubbles in Fe-Cr alloys. The activation energies were evaluated from the line slope of the Arrhenius plot of bubble size (or bubble density) vs. inverse temperature. The activation energies exhibit a weak dependence on temperature below ~600°C and a stronger temperature dependence

Table 6.3 Fraction of loop string orientations in dual beam irradiated Fe (at 1 dpa) and Fe-10Cr (at 5 dpa). The loop string orientations were determined under TEM images with g=011 near the [100] zone axis.

Orientation	Fraction	
	UHP Fe at 1 dpa	Fe-10Cr at 5 dpa
⟨111⟩ or ⟨110⟩	45 %	30 %
⟨100⟩	52 %	56 %
undefined	3 %	14 %

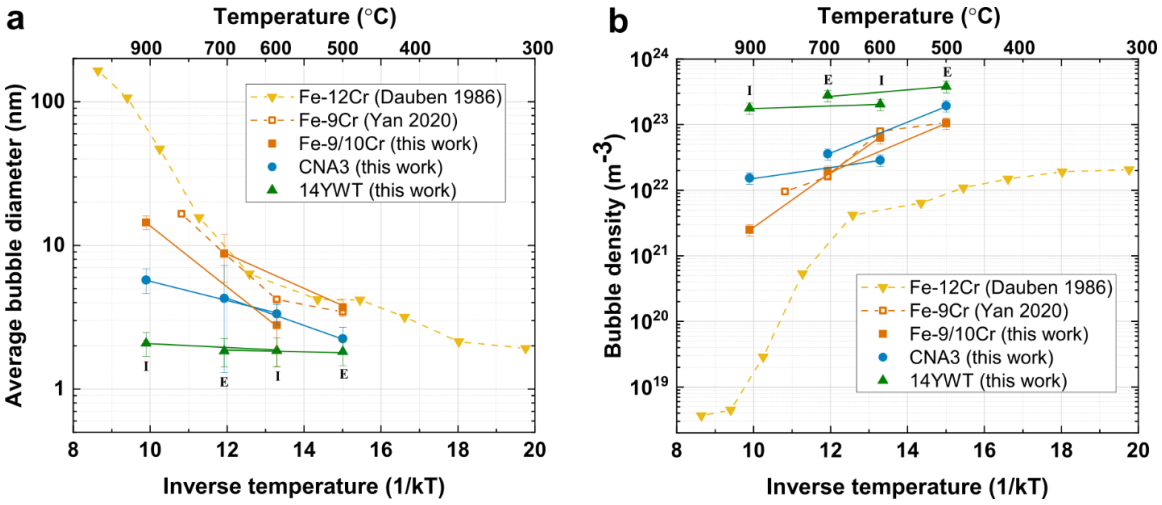

Figure 6.5 Arrhenius plot of (a) matrix bubble size and (b) density as a function of inverse absolute temperature. The "I" and "E" labels in the figures stand for in-situ irradiation and ex-situ irradiation, respectively. (Refs. [87, 142])

above ~600°C. Yan et al. suggested that the activation energy difference is related with different point defect evolution processes at different temperatures [87] Dauben et al. inferred that the activation energy for bubble size (E_R^{act}) is one-quarter or one-sixths of the helium migration energy in the low-temperature regime [142]. For the high-temperature regime (>600°C), the activation energy was attributed to helium desorption or migration of helium bubbles [143]. In Figure 6.5, Arrhenius plots were examined for the different He implanted materials to compare the effective activation energies and their temperature dependence. The 600 and 800°C data for Fe-9Cr in Figure 6.5 are reproduced from the study by Yan et al. [87], where the same Fe-9Cr material and irradiation facility were used. The estimated activation energies for bubble size (E_R^{act}) and density (E_N^{act}) are summarized in Table 6.4. The activation energies (obtained from the linear regression slope) of Fe-9/10Cr are consistent with previous studies [87, 142] showing a pronounced change at around 600°C (Figure 6.5). Overall, the E_R^{act} of the Fe-Cr alloys is in the range of 0.11-0.17 and 0.48-0.82 eV for the low- and high-temperature regime, respectively. The corresponding E_N^{act} of the Fe-Cr alloys is 0.17-0.21 and 0.86-1.95 eV for low and high temperatures, respectively. Conversely, the two NFAs did not show distinct shifts in their apparent activation energies over the entire investigated temperature regimes of 500-900°C. The activation energies of CNA3 are in-between the low- and high-temperature activation energies of Fe-9/10Cr, while the activation energies of 14YWT are even lower than the low-temperature activation energies of Fe-9/10Cr. This indicates that nanoparticles in NFAs (particularly for 14YWT) can impede the high temperature (>600°C) helium bubble coarsening that naturally occurs in the Fe-9/10Cr single phase alloys. It is suggested that, at high irradiation temperatures (>600°C), a sufficiently high binding energy of He bubbles attached to nanoparticles could suppress the helium desorption or migration of helium bubbles in the Fe-Cr matrix.

From a different perspective, previous studies suggested that the coarsening mechanisms of helium bubbles are mainly attributed to migration and coalescence (MC) or Ostwald ripening (OR) which occur at lower and higher temperatures, respectively [144, 145]. Ostwald ripening via helium resolution and reabsorption is expected to become predominant at temperatures above 0.5 Tm (the absolute melting point (T_M) of pure Fe is

1811 K). Therefore, in Figure 6.5, above 600°C it is possible that the high density of bubbles (partitioning of the available He among lots of bubbles) in NFAs could naturally decrease the coarsening rate, which results in the nearly constant linear regression slope for NFAs up to 900°C. In other words, the nanoparticles in CNA3 and 14YWT alloys may have effectively suppressed Ostwald ripening of He cavities for temperatures up to ~900°C. This implies the critical temperature for transitioning cavity behavior from MC-dominant mechanisms to OR is shifted by at least ~300°C for the nanostructured alloys.

Cavity swelling (determined by calculating the total volume of each spherical bubble with respect to the volume of the analyzed zone) increased steadily with increasing irradiation and/or annealing temperature (Figure 6.6). For any given temperature, the 14YWT alloy showed the lowest total volume swelling, while Fe-9/10Cr had the largest swelling value. Further, the Fe-9Cr ex-situ specimen exhibited higher swelling at all temperatures compared to the in-situ Fe-10Cr specimen, reaching 10% swelling at 800°C. At comparable temperatures, the bubble density is lower for the in-situ studies (especially for the Fe-9/10Cr model alloys). This could partially be due to the low-swelling surface effect of in-situ irradiated thin foils or the difference in grain size, impurity, and primitive dislocation density between the two binary alloys. Also, the swelling variation with increasing temperature was much more moderate for the 14YWT alloy, which had the highest nanocluster density. With the same amount of implanted He content, both the ex-situ and in-situ experiments demonstrate that distributing He to a higher density but smaller size of bubbles reduces the total swelling value. This is evidence that the dispersoids in both of the nanostructured alloys (particularly 14YWT) were rather effective in trapping He-vacancy complexes at their dispersoids. In addition, once these bubbles formed on nanoparticles, they could act as sinks for He as well as point defects (vacancies or interstitials).

As shown in Figure 5.30, Figure 5.31, and Figure 6.6, the 600°C in-situ irradiated samples were annealed to 900°C to compare with the 900°C directly hot implanted experiments. In general, there are important quantitative differences between post-irradiation annealing and direct irradiation at elevated temperatures. Post-irradiation annealing at elevated temperatures can modify the microstructure of irradiated materials

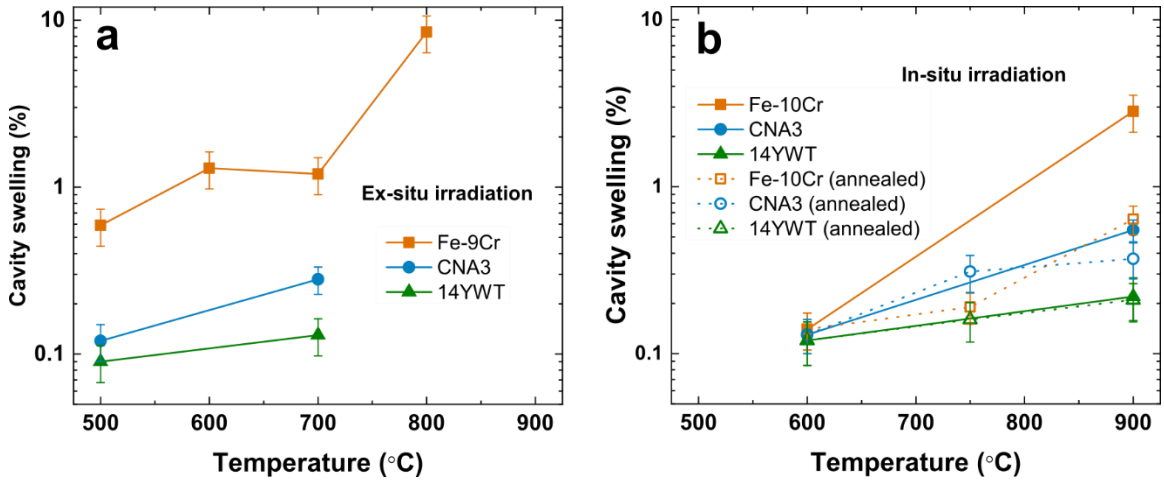

Figure 6.6 Cavity swelling of the (a) ex-situ (bulk) and (b) in-situ (thin foil) irradiated Fe-9/10Cr alloy and NFAs at 500-900°C. The Fe-9Cr swelling values in Fig. a are reproduced from Ref.[87]

Table 6.4 Effective activation energy for bubble size (E_R^{act}) and density (E_N^{act}) obtained from the Arrhenius plot in Figure 6.5. The values in the parentheses are the calculated E_N^{act} using a corrected thickness considering the surface denuded zone (see Table D.2.) at high temperatures.

Activation energy (eV)	Fe-12Cr [142]	Fe-9Cr [87]	Fe-9/10Cr	CNA3	14YWT
E_R^{act}	0.17±0.06* & 0.82±0.08**	0.12* & 0.64**	0.11±0.02* & 0.48±0.01**	0.18±0.02	0.02±0.01
E_N^{act}	0.21±0.05* & 1.95±0.21**	0.17* & 0.99*	0.17±0.05* & 0.86±0.20** (0.66±0.18)	0.45±0.16 (0.40±0.13)	0.12±0.07 (0.09±0.04)

*Experiments at temperatures below 600°C
**Experiments at temperatures above 600°C

due to the recombination and coalescence of the defects formed during lower temperature irradiation. Conversely, in the directly hot irradiated experiments the point defects and addition of helium are dynamically interacting during the irradiation at elevated temperatures. For the irradiation condition of this study, at relatively high temperatures above ~750°C, the steady-state vacancy population produced by ion bombardment is calculated to be comparable to the thermal-equilibrium vacancy concentration (see Figure. D.8. for the steady-state and thermal vacancy concentration as a function of temperature in Fe). This suggests that at temperatures near or above 750°C both approaches should produce qualitatively similar trends for helium-filled cavities due to relatively rapid kinetics for establishing near-thermal-equilibrium cavities. However, comparing the 900°C annealing results with the 900°C directly hot implanted experiments (Figure 6.6), the cavity swelling was ~6 times lower in the annealed Fe-10Cr samples. The 900 s anneal at 900°C is likely insufficient to enable sufficient Ostwald ripening of the Fe-10Cr cavities. In addition, based on the cavity growth rate estimation for ideal gas (see supplemental file for details), the annealing time of 900 s at 900°C produces a calculated cavity radius of 2.5 nm, which infers that the annealing time is not sufficient for the cavities to grow into the average cavity size (~7 nm) observed in the 900°C directly hot implanted Fe-10Cr. Therefore, the insufficient annealing time could result in a smaller cavity size (Figure 5.31a), higher density (Figure 5.31b), and lower volume swelling (Figure 6.6) in the post-irradiation annealed Fe-10Cr without nanoparticles.

On the other hand, the difference between the hot implanted and post-irradiation anneal cases was moderate or remained constant within the listed error bars for the nanostructured CNA3 and 14YWT alloys. This indicates that He bubbles attached to nanoparticles in the 600°C implanted specimens may have a relatively high binding energy. As long as the bubbles are well attached to particles, the mobility of these cavities could then be restrained when the specimens were sequentially annealed at 750 and 900°C. As discussed earlier, the relatively narrow size distribution of cavities for the two nanostructured alloys also suppresses the driving force for Ostwald ripening, since the He-vacancy concentration profile in the vicinity of the cavities (driving force for Ostwald ripening) is ~1/r (where r is the cavity size). Further studies on the He content in the bubbles

and the He binding energy (or He desorption) of bubbles attached to nanoclusters, dislocations, or grain boundaries would be useful to understand the detailed mechanism of the formation of bubbles in nanostructured alloys. For example, thermal desorption spectroscopy (TDS) could be applied to identify the He binding energy at different sites from the He desorption peaks [146].

For the ex-situ irradiated bulk materials, apart from examining the bubbles near the peak He concentration depth (~700 nm), it is also worth understanding the overall bubble distribution from the sample surface to depth >700 nm. Figure 6.7 illustrates the depth distribution of the number of bubbles in the irradiated bulk materials (see Figure 5.32 and Figure 5.33 for the cross-sectional defocused TEM images). As shown in Figure 6.7, the bubble distribution is concentrated near the peak He concentration depth (~700 nm), which is in agreement with the SRIM estimation (Figure 4.4b). At 700°C (Figure 6.7b), the cavity number fraction in 14YWT, CNA3, and Fe-9Cr model alloy at the 500-800 nm depth interval were 76%, 70%, and 38% of the total cavities detected at all depths, respectively. This indicates that the addition of a higher density of nanoparticles could better confine the diffusion of He-vacancy complexes, i.e., close to the implanted region. However, a small amount (cavity number fraction <3%) of He bubbles in 14YWT were observed near the sample surface (at depth <100 nm), but not in CNA3. This may due to the much smaller mean grain size (~0.2 μm) of the 14YWT material compared to the prior-austenite grain size of CNA3 (10-60 μm). The longer total length of grain boundaries may enhance the diffusion of He via a pipe diffusion along grain boundaries, as discussed in Chapter 6.6.3 [147].

6.4.3 Bubbles in grain boundaries of NFAs

In addition to the evolution of bubbles in the matrix, the bubbles at the grain boundaries (GB) have also been examined. Apart from the bubble density in the grain interiors, Singh and Foreman [148] proposed that grain boundary cavity density depends on absolute He production rate (He/s), but not the He per dpa ratio. Also, Han et al. reported that the cavity size and density differ for grain boundaries with different misorientations and normal planes [18]. They indicated that the grain boundary sink efficiency is dependent

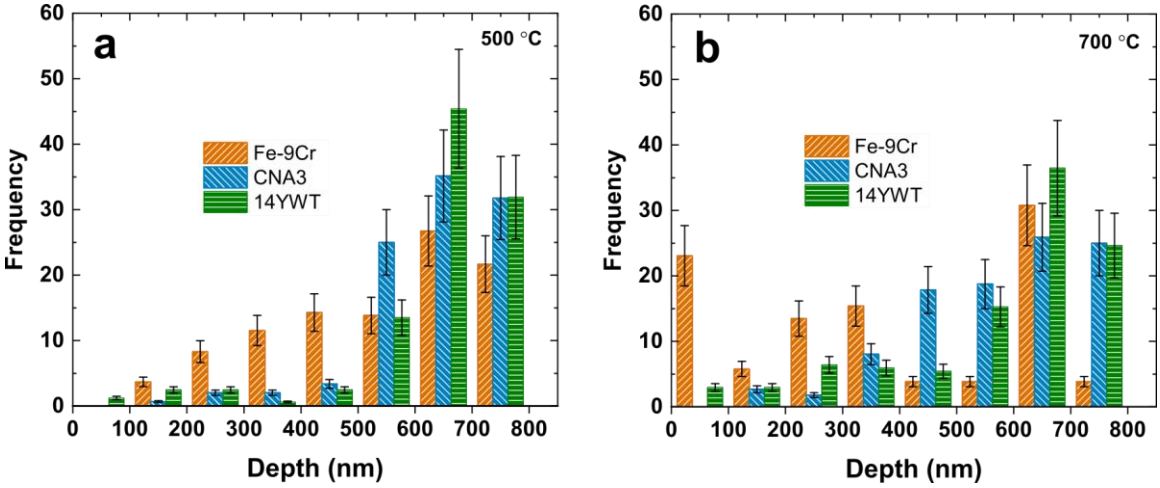

Figure 6.7 Depth variation of the number of bubbles in the ex-situ irradiated bulk samples at (a) 500 and (b) 700°C.

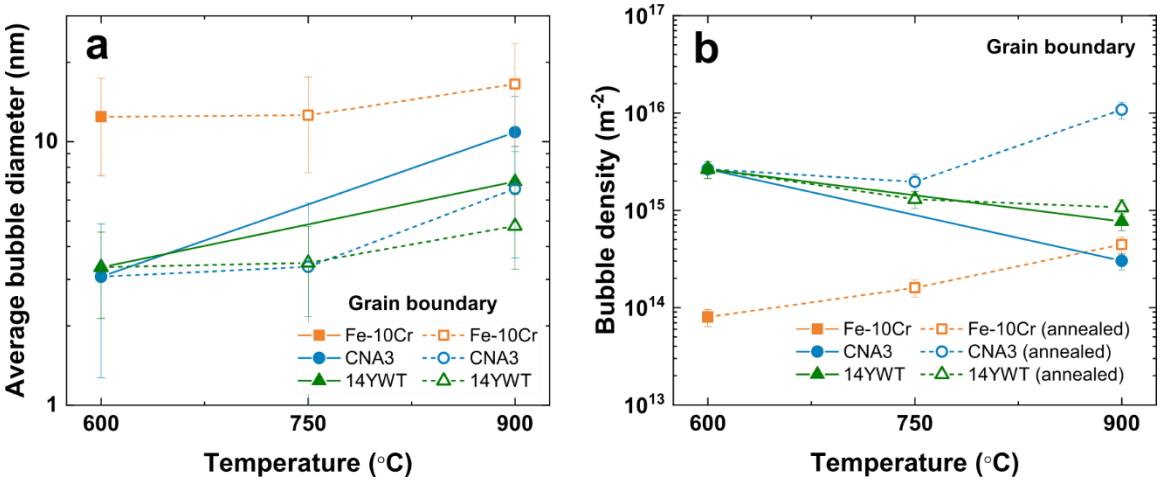

Figure 6.8 Comparison of the (a) average size and (b) areal density of cavities at grain boundaries in the in-situ irradiated Fe-10Cr and NFA thin foils at 600-900°C. The filled symbols (and solid lines) and the open symbols (and dashed lines) represent the directly hot-implanted and the sequential annealing experiments, respectively.

on the grain boundary character and structure. In the present study, we did not include possible sink efficiency variability in the analysis of the results.

Statistical information on the bubbles at grain boundaries is summarized in Figure 6.8. As shown in Figure 6.8, grain boundary cavities are the largest and have the lowest areal density for Fe-10Cr. Nanostructured alloys have smaller grain boundary cavity sizes and higher areal densities. The bubble density in the unit of "m^{-2}" is the linear density of cavities (the number of cavities per unit length of grain boundary) divided by the foil thickness estimated by EELS method. Errors can occur in the grain boundary bubble size and density if there is a significant probability of overlap of the projected bubbles (when $Nd>1/t$, where N is the areal density, d is the cavity diameter and t is the foil thickness).

Based on this inequality, a slight overlap effect may be possible at all investigated temperatures for the nanostructured alloys but generally should not be a problem for Fe10Cr. In the three materials, the average bubble size at grain boundaries increased with increasing irradiation temperature and with a higher temperature annealing process (see Figure 5.29 and Figure 5.30 for the TEM images). Also, the size distribution was inhomogeneous with large standard deviations. However, the temperature dependence of the cavity density at grain boundaries exhibited a mixture of temperature dependences. Helium bubble nucleation along grain boundaries is likely to be aided by the enhanced diffusion of He along grain boundaries by a pipe diffusion mechanism, which occurs with lower activation energy [147]. At sufficiently high irradiation temperatures, larger helium-vacancy complexes become mobile and may be trapped by the grain boundaries resulting in a net growth of the bubbles [149, 150]. As shown in the in-situ post-irradiation annealed TEM images (Figure 5.30d-f), because bubbles can diffuse more readily along grain boundaries due to the increased free volume, the growth of bubbles is expected to be further facilitated by a migration and coalescence mechanism. The potential effect of the grain size differences of the three materials is discussed and analyzed in Chapter 6.6.4.

As for the comparison between He bubbles at grain boundaries in materials with and without nanoclusters, Figure 6.8 shows that the grain boundary average bubble diameter in Fe-10Cr at 600°C is 2-4 times larger than in the two nanostructured alloys.

Besides, at 900°C, grain boundary cracking was severe in Fe-10Cr (Figure 6.9). Therefore, the grain boundary bubble size and density of the Fe-10Cr sample could not be measured at this irradiation temperature. Figure 6.9b shows possible traces of large faceted cavities with a side length up to ~1 μm, near and along a grain boundary. For the in-situ heated samples, a sequence of TEM images (Figure 6.9c-e) taken at the same area near the perforated hole (relatively thinner) also shows the formation of a large cavity at grain boundary in the Fe-10Cr material. In the same figures, some unidentified precipitates (with cavities on the surface) seem to be agglomerating to the grain boundary with increasing temperature. As discussed earlier, the austenite (gamma phase) transformation temperature is about 848°C for 8-10 at% Cr, and gamma phase Fe with FCC crystal structure generally has less resistance to cavity swelling. There is a possible influence of alpha-gamma phase transition-induced stresses in addition to standard thermal annealing bubble coarsening effects for the 900°C Fe-9/10Cr annealed samples. However, the overall significant difference between model single-phase and nanostructured alloys in the formation of cavities/bubbles at grain boundaries demonstrates the effectiveness of nanoparticles as preferential sites for He bubble nucleation in the matrix, thereby suppressing the amount of He-vacancy clusters that diffuse to grain boundaries. This also emphasizes the ability of nanoparticles to reduce the nucleation of large He bubbles along grain boundaries that would result in the degradation of material properties (e.g., high-temperature grain boundary embrittlement).

6.4.4 Relation of bubbles to nanoparticles

In Figure 5.36, Figure 5.37, Figure 5.38, and Figure 5.39, the EELS spatial maps show that the bubble number densities are comparable to the nanoparticle densities for the CNA3 and 14YWT alloys and that the He bubbles are preferentially associated with nanoparticles, suggesting that the nanoparticles are rather effective at trapping He-vacancy complexes at the particle-matrix interface. In order to further quantify the relation of bubbles to nanoparticles, the cavity density as a function of nanoparticle density in various irradiated

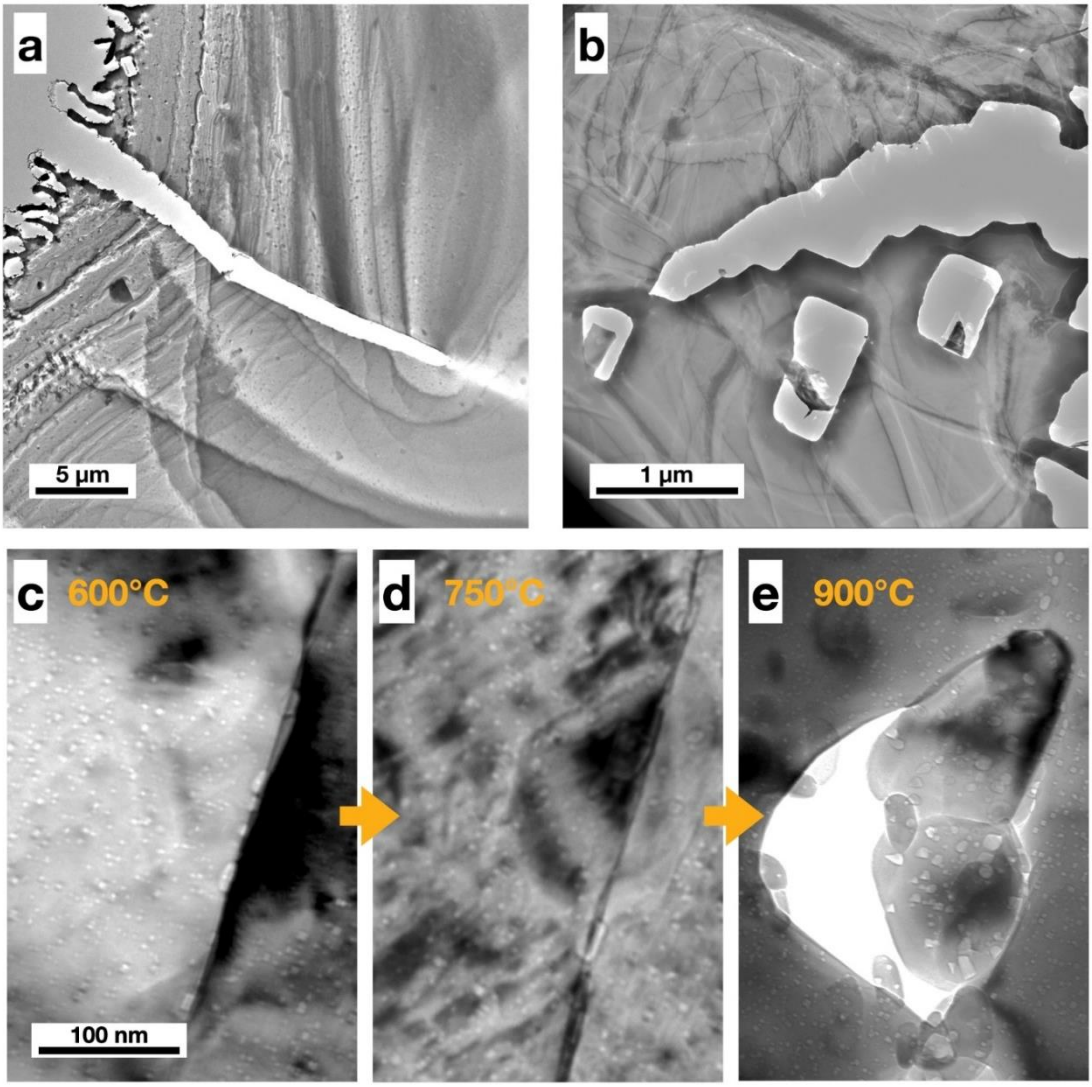

Figure 6.9 TEM images of (a) grain boundary cracking and (b) possible traces of large faceted cavities/bubbles in the in-situ irradiated Fe-10Cr thin foil at 900°C; Cavities at a grain boundary in the (c) 600°C implanted Fe-10Cr sample followed by sequential annealing at (d) 750 and (e) 900°C.

NFAs are compiled in Figure 6.10 for irradiation temperatures below and above 600°C (corresponding to migration and coalescence regime and Ostwald ripening regime, respectively). Note that the irradiation conditions of each data point were different: Lu et al. (460°C, ~0.5 appm He/dpa) [151]; Parish et al. (650°C, ~15 appm He/dpa) [152]; Brimbal et al. (460°C, ~17 appm He/dpa) [153]; Yamamoto et al. in 2007 (500°C, ~42 appm He/dpa) [154]; Yamamoto et al. in 2014 (650°C, ~47 appm He/dpa) [155]; Edmondson et al. (400°C, ~12,000 appm He/dpa) [156]; ex-situ study of this work (500 and 700°C, ~2,700 appm He/dpa); in-situ study of this work (600 and 900°C, ~4,000 appm He/dpa). In addition, the nanoparticle densities in each study were measured by different methods (e.g., EELS, EDS, or APT). The reported densities could be off by an order of magnitude due to differences in resolution limits at small particle sizes. However, these errors are difficult to statistically analyze. It should also be noted that the materials in Figure 6.10 with the same nominal material label may be processed differently, which resulted in different reported particle densities.

As shown in Figure 6.10, the cavity density increased with increasing nanoparticle density, with a near one-to-one correspondence both for irradiation temperatures < 600°C and > 600°C. At irradiation temperatures below 600°C, the cavity density in several NFAs with relatively low nanoparticle densities (below ~10^{22} m^{-3}) did not show a pronounced difference compared to Fe-9/10Cr model alloys (without nanoclusters). However, above 600°C, where the number density of cavities in Fe-9/10Cr dramatically declined (Figure 6.5b), the cavity density in NFAs was several orders of magnitude higher than in Fe-9/10Cr. Overall, the data points exhibited a 1:1 correspondence between cavity density (N_c) and particle density (N_{ppt}) within one order of magnitude deviation for nanoparticle densities of ~10^{22} m^{-3} to ~10^{24} m^{-3}. The cavity density of NFAs with high particle density ~10^{24} m^{-3} showed a slight deviation of $N_c < N_{ppt}$, while the NFAs with particle density ~10^{22} m^{-3} had $N_c > N_{ppt}$. This could be related to the average nanoparticle size difference between CNA3 (~8 nm) and 14YWT (~4 nm). As shown in the EELS elemental mapping results (Figure 5.39), a single nanoparticle in CNA3 could attach 3-10 small He bubbles, and a single particle in 14YWT attaches roughly one helium bubble (Figure 5.36). It is

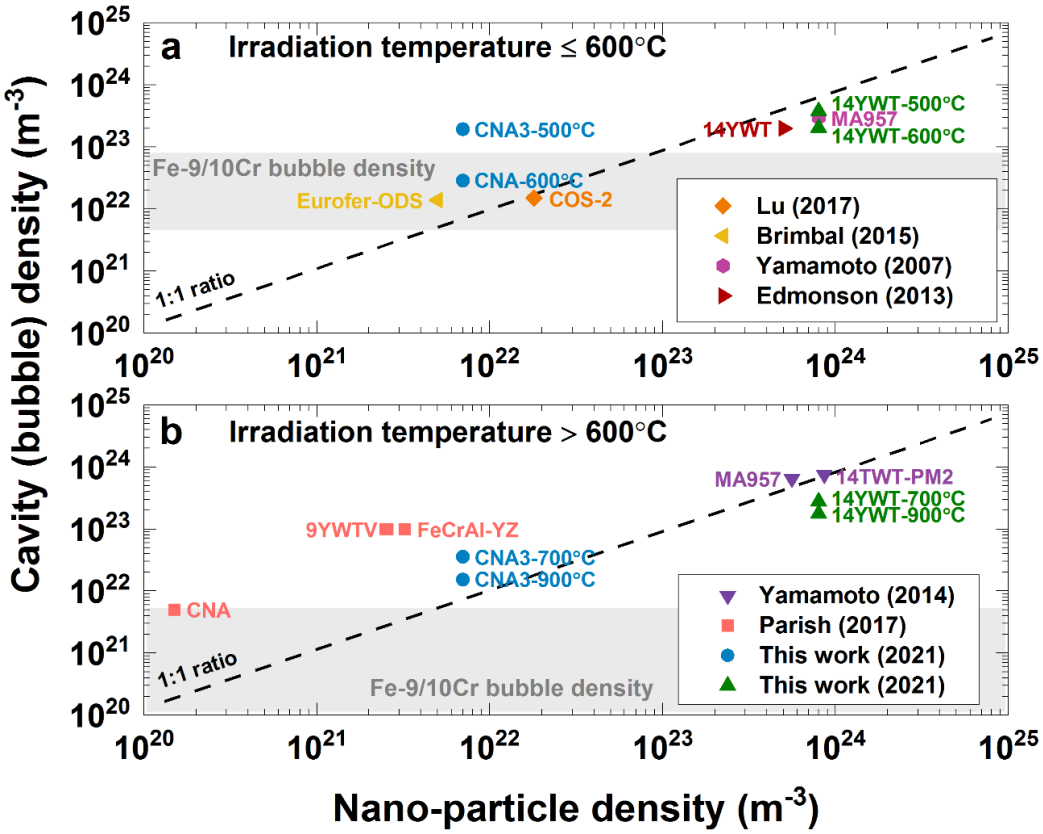

Figure 6.10 Variation of bubble density as a function of nanoparticle density in He implanted alloys. (a) Irradiation temperature <600°C, (b) Irradiation temperature >600°C. Data from Refs. [151-156] are plotted along with the results from the current study. The dashed line indicates the 1:1 relationship between cavity and nanoparticle density, and the gray shaded regions represent the cavity densities for single-phase Fe-9/10Cr alloys.

expected that the nanoparticle size or surface area and interface property could also affect the N_c/N_{ppt} ratio. The analysis of different types of precipitates on bubble formation behavior at a comparable sink density (similar precipitate size and density) could provide insight into whether there are significant differences in sink efficiency for various precipitates. Although the sink strengths (see Appendix D. for details) for the evaluated nanostructured alloys in this study did not overlap. Comparison with some literature results (Figure 6.10) indicates that similar behavior was observed in several ODS nanostructured alloys for a comparable sink strength, indicating that minor modifications in the specific oxide nanocluster composition may not strongly affect cavity evolution.

With a simplified estimation, the mean inter-particle distance ($\bar{r}$) could be calculated by:

$$\bar{r} = \frac{1}{\rho^{1/3}} \tag{6.1}$$

where ρ is the nanoparticle density. Substituting the nanoparticle density of CNA3 (~10^{22} m^{-3}) and 14YWT (~10^{24} m^{-3}) into the equation finds the average interparticle distance of 46 and 10 nm, respectively. On the other hand, the implanted He can escape to a free surface or sinks (e.g., dislocations, grain boundaries, sample surface, etc.) if the mean free path (L) for He-vacancy cluster diffusion between the bubbles is larger than the distance to a free surface. The mean free path can be estimated by [142]:

$$L = \frac{1}{2}(\pi NR)^{-0.5} \tag{6.2}$$

where N is the bubble density and R is the bubble radius. Owing to the temperature dependence of bubble size and density (as shown in Figure 6.5), the value of L for Fe-Cr alloys without particles varies strongly with temperature. This spacing can be considered to be the "natural" temperature-dependent cavity clustering behavior for single phase Fe-Cr alloys. If the interparticle distance of NFAs is less than L, then significant refinement of the cavity distribution may occur (assuming sufficient binding energy exists between the particles and the cavities).

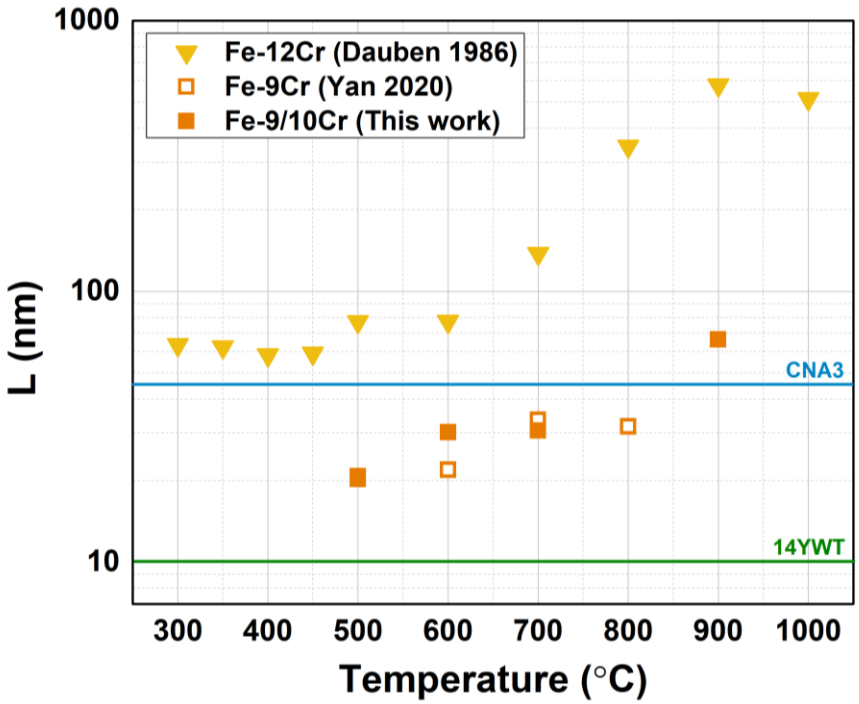

Figure 6.11 The mean free path (L) for He-vacancy cluster diffusion in particle-free Fe-Cr alloys as a function of temperature (Refs. [87, 142]). The blue and green horizontal lines indicate the temperature-independent value of the interparticle spacing for CNA3 and 14YWT, respectively.

Figure 6.11 plots the calculated He-vacancy complex diffusion mean free path from the current study and from two prior studies (Refs. [87, 142]), as calculated by substituting the bubble density and size for He-implanted Fe-9-12Cr into Eq. (6.2). Larger values of the diffusion mean free path L were observed in the study by Dauben et al. [142] which can be attributed to the lower He implantation rate (1 vs. 2.4-13 appm He/s) and much lower total implanted He levels (600 vs. 8,000-12,000 appm He) compared to Ref. [87] and the present study. The He diffusion length in Fe-9/10Cr at 500-800°C for the current study and Ref. [87] was 20-30 nm, which is about a factor of two smaller than the average interparticle distance of nanoparticles in CNA3 (~46 nm). This could partially explain the observation of some bubbles trapped by dislocations rather than exclusively at particles in CNA3 (Figure 5.40). As for 14YWT, the interparticle distance is 2-6 times smaller than the He-vacancy mean free path in Fe-9/10Cr over the temperature range of 500-900°C, which indicates that the He-vacancy complexes have a high probability of encountering a nanoparticle (inducing heterogeneous nucleation at the nanoparticle-matrix interface) rather than homogeneously nucleating as a bubble in the matrix. The above estimation indicates that the particles in CNA3 with relatively lower density might only cause a modification in the cavity nucleation behavior at higher temperatures around 600-900°C. This result is consistent with Figure 6.10, where the cavity density in several NFAs with relatively low nanoparticle densities (below ~10^{22} m^{-3}) did not show an obvious difference compared to particle-free Fe-9/10Cr alloys at temperatures below 600°C.

Although Figure 6.10 and Figure 6.11 infer that the nanoparticle density could be positively correlated with cavity density, other factors such as different types of sink (e.g. dislocation, grain boundary, α' precipitates), the He trapping ability (binding energy) of the nanocluster, He/dpa ratio, Cr solute effects on atomic diffusion, and temperature could all affect the formation of cavities. To go a step further, the growth of cavity is dependent on the point defect concentration and the thermal vacancy concentration, which are both affected by the sink strengths. Based on the standard rate theory [17], approximations of the defect sink strengths for different microstructural features of the as-received materials were evaluated (see appendix for details). Our calculation results (Table D.3) showed that the total initial sink strength (unirradiated material) is dominated by the dispersoids when

the particle density is above ~10^{21} m^{-3}. The sink strength associated with a grain size above ~0.1 μm and dislocation density below ~1×10^{14} m^{-2} would be an order of magnitude less than the nanoparticle sink strength (when the nanoparticle density is above ~10^{21} m^{-3}). The estimated total initial sink strengths of as-received Fe-10Cr, Fe-9Cr, CNA3, and 14YWT material were 1×10^{12}, 1×10^{14}, 2×10^{15}, and 3×10^{16} m^{-2}, respectively. Based on the equations for foil surface sink strength estimation developed by Bullough et al. [141], the sink strengths associated with a defect depleted zone width ~25 nm and foil thickness ~75 nm are 10^{12}-10^{14} m^{-2} in the range of temperatures between 500-900°C. Therefore, the foil surface sink strength of our in-situ study should have a minor effect compared to the total (nanoparticle-dominated) sink strength of CNA3 and 14YWT. Figure 6.12 shows the bubble size, bubble density, and swelling in the He implanted materials as a function of the total sink strength. The bubble size decreased (Figure 6.12a) and the bubble density (Figure 6.12b) increased with increasing sink strength, particularly for temperatures above 600°C. For the cavity swelling, Figure 6.12c suggests that a significant decrease in cavity swelling can be achieved if the sink strength is above ~10^{15} m^{-2}, which corresponds to a nanoparticle density above ~10^{22} m^{-3}. Similar significant suppression of void swelling has been observed for precipitate sink strengths above ~10^{15} m^{-2} in neutron and dual ion irradiated steels [4, 122, 157].

STEM-HAADF characterization was performed to identify the nanoparticle structure and the attached bubbles in the ex-situ He-implanted CNA3 and 14YWT nanostructured alloys at 700°C (Figure 6.13). The HAADF scattering signal from a single column of atoms is strongly dependent on the atomic number and the number of atoms in a single atom column [112-114]. Hence, the bubbles exhibit black contrast in HAADF images due to the absence of atoms. In Figure 6.13, a series of high-resolution HAADF images were taken at the junction of the bubble (B) and nanoparticle (P) (Figure 6.13a-c), or junction of bubble and grain boundary (Figure 6.13d). For the fine Y-Ti-O and (Ti, Ta, W, V)C clusters with diameter <10nm (Figure 6.13a and b), the atomic structure under TEM as well as their fast Fourier transform (FFT) images taken at the B and P regions remains the same as the matrix ferritic structure. The cavity and nanoparticle with a diameter of less than ~10 nm are

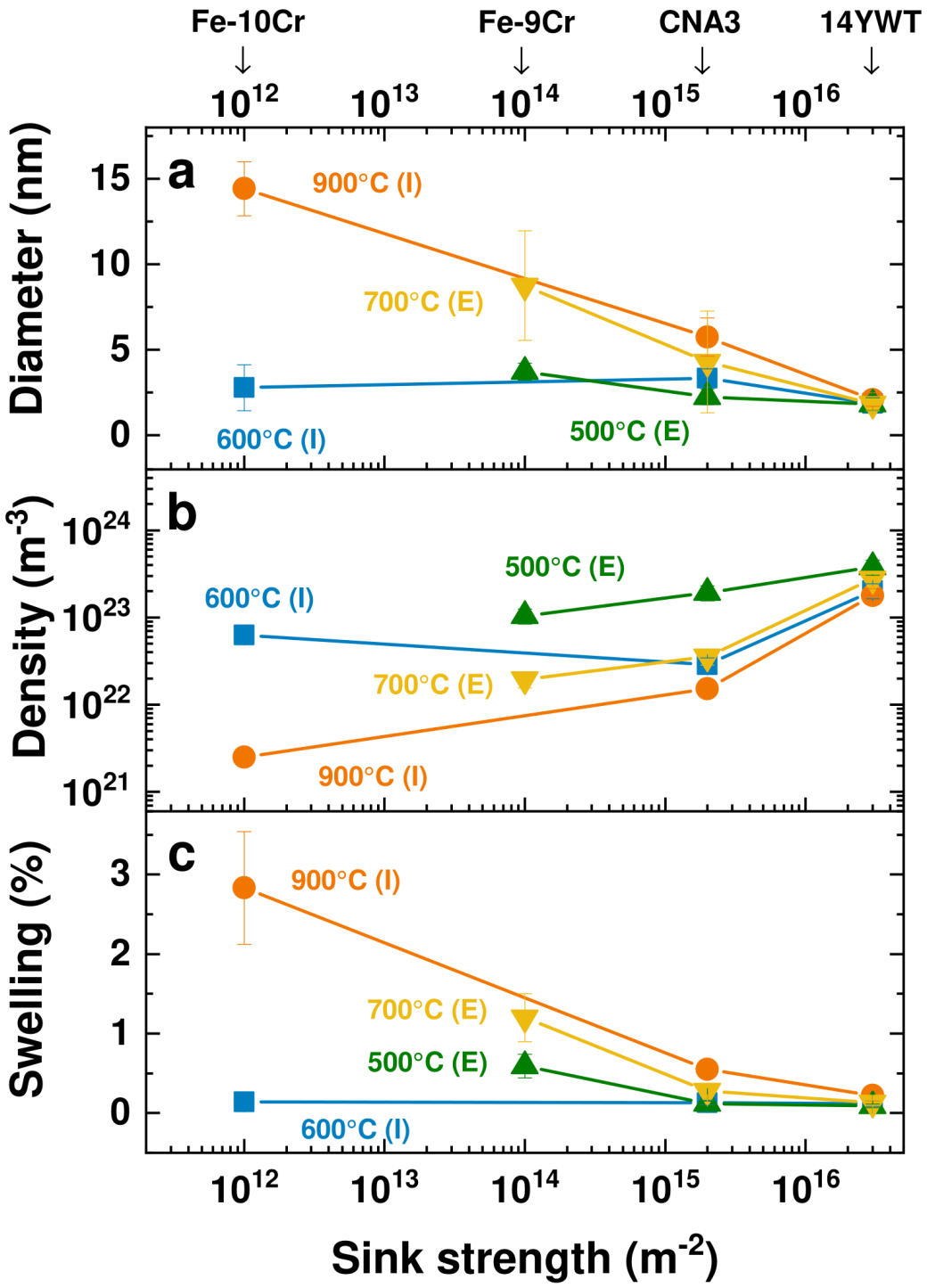

Figure 6.12 Variation of (a) bubble size, (b) bubble density, and (c) swelling as a function of initial sink strength. (E: ex-situ experiments; I: in-situ experiments)

embedded in the matrix structure. Considering a sample thickness of ~80 nm, at least seven-eighths of the atoms in an atomic column would be the surrounding Fe or Cr matrix atoms. Therefore, an overlap of atoms may occur and impact the contrast in the STEM images. For the coarse TiN particles with diameter >10 nm (Figure 6.13c), a possible NaCl atomic structure was observed, which agrees with a previous report that indicated Ti(N,C,O) precipitates in 14YWT may have a NaCl structure [156]. However, the distinct structure was observed in the bubble (B) region, but not the particle (P) region. The overlap of particles and cavities, which reduces the number of matrix atoms in the analyzed column height, could aid the imaging of the atomic structure of particles. Figure 6.13d shows a few bubbles attached to a grain boundary. The atomic structures on the left (L) and right (R) regions are obviously different. In order to minimize the matrix atom distribution, a thinner TEM sample or conducting heat treatment to coarsen the bubbles or nanoparticles (as reported by Stan et al. [158]) would be valuable to visualize the atomic structure of the nanoparticles.

6.5 Defect and precipitate sink strength

6.5.1 Dynamic evolution of defect sink strength

To investigate the possible interconnection between the evolution of dislocation loops and the formation of cavities, the sink strength of the observed loops, network dislocations, and cavities was calculated and summarized in Figure 6.14. Sinks represent a site for vacancy and interstitial loss. According to standard rate theory [17], sinks can be divided into neutral (unbiased) sinks that have no preference for capturing the type of point defects, or biased sinks that show a preference for capturing one type over the other. As discussed in Chapter 2.3.3, the defect sink strengths for different microstructural features could be estimated individually.

As shown in Figure 6.17 and Figure 6.18, with increasing dose between 0.5 and 5 dpa, dislocation loops monotonically became larger and of lower density, resulting in an

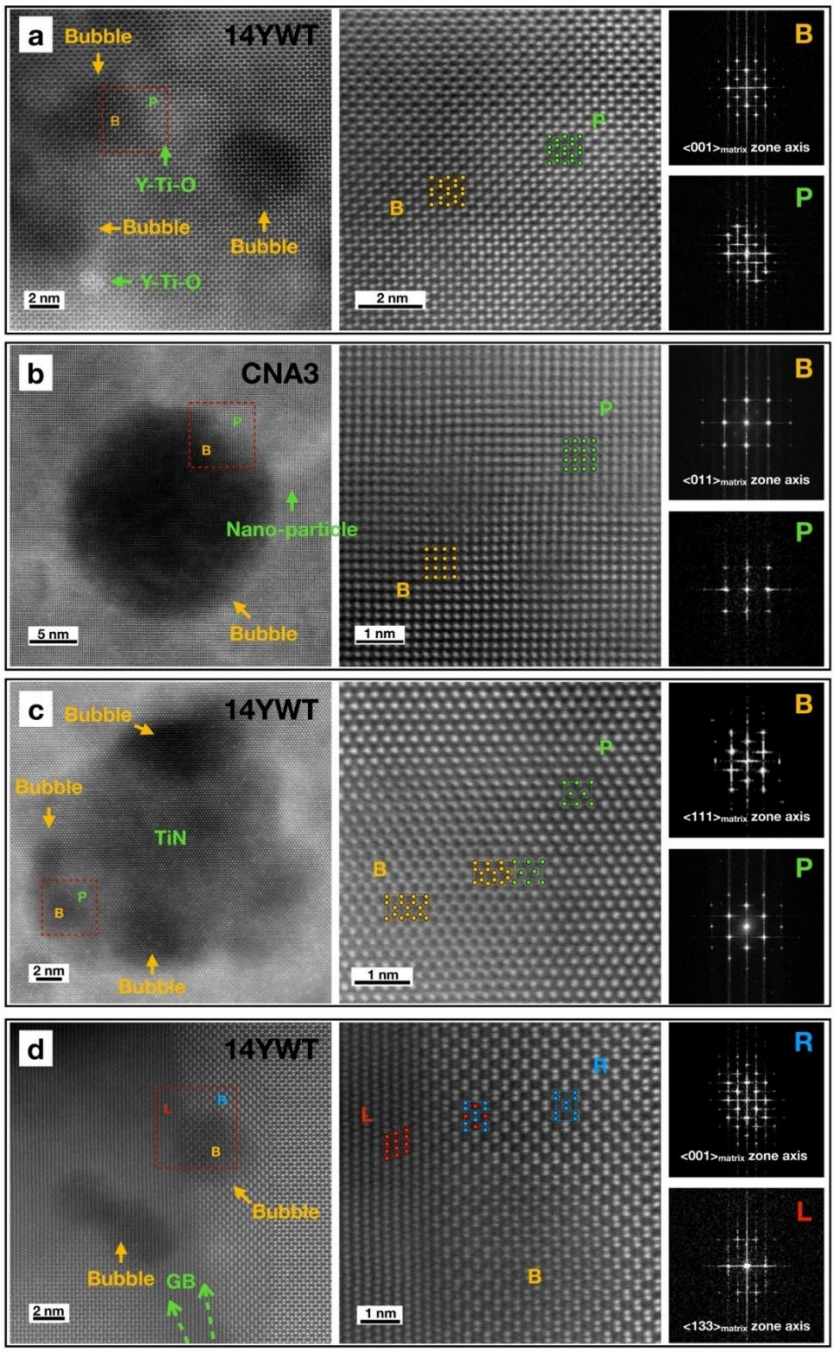

Figure 6.13 Atomic resolution STEM-HAADF images of nanoparticles (a-c) or grain boundary (d) and associated helium bubbles in 14YWT and CNA3 nanostructured alloys *ex-situ* irradiated at 700°C. (a) Y-Ti-O, viewed along the ⟨001⟩ Fe-Cr matrix zone axis; (b) (Ti, Ta, W, V)C particle, viewed along the ⟨011⟩ Fe-Cr matrix zone axis; (c) Ti-N, viewed along the ⟨111⟩ Fe-Cr zone axis; and (d) grain boundary, viewed along the ⟨133⟩(L)/⟨001⟩(R) Fe-Cr matrix zone axis. The corresponding FFT patterns of the labeled area are on the right of each figure. (B: He bubble, P: nanoparticle, L: left-grain, R: right-grain)

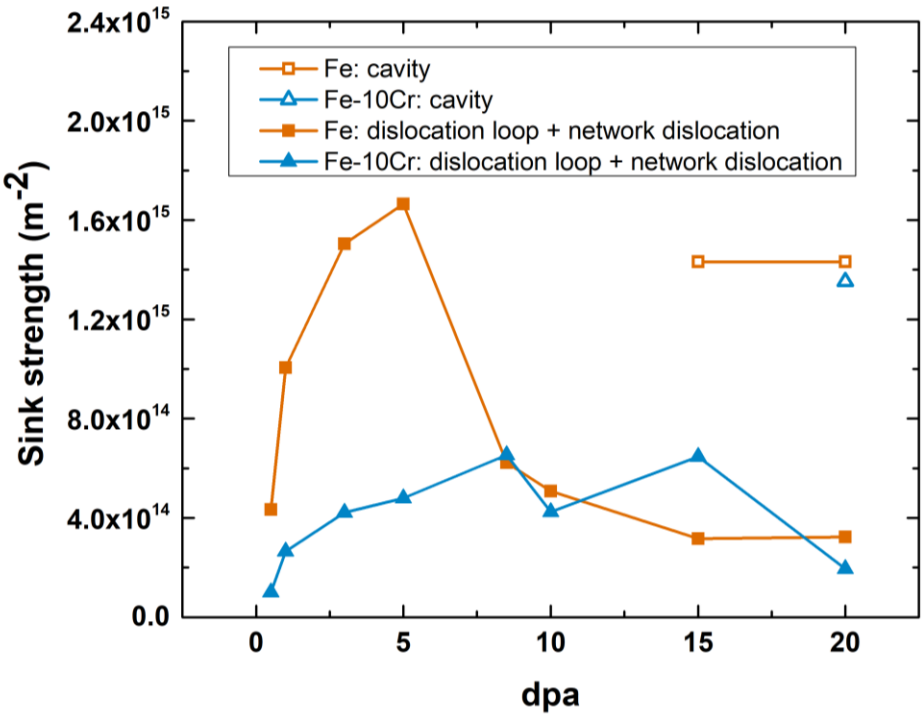

Figure 6.14 Calculated sink strength of dislocation loops, network dislocations, and cavities for in-situ dual-beam irradiated Fe and Fe-10Cr as a function of dose at 435°C.

overall higher sink strength to potentially affect cavity formation and growth. At high doses >5 dpa, Figure 6.14 shows that the transformation from loops to network dislocations at ~5 dpa for Fe and ~20 dpa for Fe-10Cr significantly reduced the total dislocation sink strength. In both Fe and Fe-10Cr foils, cavity formation required an incubation dose of ~10-20 dpa, and cavities were observed only when the total sink strength of loops and networkdislocations was below ~4×10^{14} m^{-2}. Furthermore, formation of cavities in the grain boundary was found in the Fe foil for doses above 10 dpa (Figure 5.24b), but not in Fe-10Cr. Since dislocation loops can act as sinks (trapping sites) for helium as well as vacancies and interstitials, it is likely that the 2-3 times higher density of dislocation loops in Fe-10Cr at 5-15 dpa (Figure 6.18b) can more effectively shield He-vacancy clusters from the grain boundaries. Besides, by MD simulation, Terentyev et al. [159] reported that the presence of Cr in Fe-10Cr matrix can retard the mobility of pure helium clusters, but small He-vacancy clusters were not significantly affected by the presence of Cr.

6.5.2 Sink strength of irradiation-altered α' precipitates

In the Fe-14Cr sample irradiated at 400°C with displacement damage and dose rate of 30 dpa and 1.4×10^{-3} dpa/s, respectively, Cr-enriched precipitates were observed by APT (Figure 5.9) but not by conventional or analytical TEM (EDS and EELS). The reason why precipitates in the Fe-14Cr sample were undetectable under TEM is most likely due to the slight lattice mismatch between α (a=0.2886 nm) and α' (a=0.2885 nm) phase, and the tiny mass difference between Fe (Z=56) and Cr (Z=52) [77]. As discussed in section 3.2.3, the observation of these irradiation-altered α' precipitates by APT at such a high dose rate is not common. It is also worth noting that the precipitates seem to reach a steady-state and were not dissolved under the severe displacement damage to 30 dpa. Our observation indicates that radiation enhanced diffusion could be more effective than ballistic dissolution at 400°C, even with a dose rate up to 10^{-3} dpa/s. To examine how the dose rate could affect the ballistic dissolution and radiation enhanced diffusion would require future study with different irradiation conditions (e.g., dose, dose rate, or irradiation temperature).

If irradiation-altered α' precipitates are effective sinks such as oxides (Figure 5.36) or MX type particles (Figure 5.39), the average size and average density of the α'

precipitates (Table 5.2) observed in the irradiated Fe-14Cr sample could led to a sink strength of 6.2×10^{15} m^{-2} (by Eq. (2.7)). As shown in Figure 6.14 and Figure 6.12, when the defect sink strength or the initial sink strength of nanoparticles are above 10^{-14}-10^{-15} m^{-2}, the cavity swelling could be suppressed. Therefore, the formation of α' precipitates in the Fe-14Cr sample with such a high strength above 10^{-15} m^{-2} can likely reduce the cavity swelling significantly. Based on the Fe-Cr phase diagram (Figure 3.7), the Fe-10Cr and Fe-14Cr materials with relatively higher Cr content are favorable for α' precipitation at 400-435°C. Additional APT analyses are needed to confirm if α' phase precipitation occurred in these materials.

6.5.3 Q value evaluation

Conventionally, Q value is defined as the ratio of dislocation sink strength to cavity sink strength and is given by [26]

$$Q_{i,v} = \frac{Z_{i,v}^{d}\rho_d}{4\pi r N Z_{i,v}^{c}} \tag{6.3}$$

where r is the radius of the cavities, N is the number density of the cavities, Z is the capture efficiency (Z =1 for unbiased sink), ρ_d is the dislocation density (see section 2.3.3 for details). For sink dominant conditions, the cavity swelling rate would be dependent to the Q value with a relation of

$$\frac{d(\Delta V/V)}{dt} \propto \frac{Q}{(1+Q)^2} \tag{6.4}$$

Theoretically, with a fixed dose, the maximum cavity swelling is observed at $Q = 1$, when the flow of vacancies to cavities and dislocations is equal. $Q > 1$ is when vacancy loss to dislocations dominates, while $Q < 1$ is when vacancy loss to cavities dominates. Here, dislocations as biased sinks (more attractive to interstitials) play a key role in the formation of cavities and swelling. If the flow of defects is the same, and more interstitials are absorbed by dislocations, then more vacancies must flow to cavities. Therefore, $Q = 1$ is when the bias sinks are most effective in promoting cavity growth.

However, other sink strengths such as dislocation loops or irradiation-induced α' precipitates could be comparable to the dislocation or cavity sink strength, and should not be overlooked. In addition, cavities (for both voids and bubbles) were considered to be neutral unbiased sinks in the past. However, a recent simulation study by Kohnert et al. demonstrated that small cavities might have an interstitial bias as well [15]. In a broad sense, the Q value represents the ratio of biased sink strengths to neutral sink strengths. On this basis, we proposed a general Q value as

$$Q = \frac{S_d + S_l + S_p + S_b}{S_v} \tag{6.5}$$

where S_d is the dislocation sink strength, S_l is the dislocation loop sink strength, S_p is the precipitate sink strength, S_b is the bubble sink strength, and S_v is the void sink strength. Details regarding the estimation of the sink strengths for these different features are discussed in section 2.3.3. Note that in Eq. (6.5) cavities with smaller sizes are simply considered to be biased sinks. In the work by Kohnert et al. [15], the net bias as a function of cavity size was a continuously descending curve.

In order to evaluate the Q value effect on cavity swelling, two sets of dual ion irradiated samples at the fusion relevant condition (30 dpa, 10 appm He/dpa) were selected for detailed microstructural investigation. The first set is Fe-10Cr samples irradiated at 400-550°C, and the second is Fe and Fe-Cr (3-14 wt%) samples irradiated at 470°C. The former was chosen to examine the temperature effect on defect sink strengths, while the latter provides insights into the impact of Cr on defect sink strengths. For sink strength calculation, the size and density of dislocation loops and dislocation networks are quantified under STEM ADF images. The size and density of the loops and dislocations are summarized in Table 6.5 and Table 6.6. With doses up to 30 dpa, the loop density was relatively low and network dislocations were distributed all over the STEM ADF images. The sink strength calculations of voids and bubbles were using the cavity size and density information from Figure 5.18 and Figure 5.19. All of the TEM or STEM images were taken at the midrange depth of ~1 μm.

Table 6.5 Dislocation and loop information of Fe and Fe-Cr samples irradiated at 470°C under fusion relevant condition.

Material	Loop diameter (nm)	Loop density (m^{-3})	Dislocation density (m^{-2})
Fe	13.12	1.27×10^{21}	7.14×10^{13}
Fe3Cr	11.07	3.06×10^{20}	2.90×10^{14}
Fe10Cr	16.52	5.10×10^{20}	3.57×10^{14}
Fe14Cr	17.18	6.12×10^{20}	1.29×10^{14}

Table 6.6 Dislocation and loop information of Fe-10Cr samples irradiated at 400-500°C under fusion relevant condition.

Temperature (°C)	Loop diameter (nm)	Loop density (m^{-3})	Dislocation density (m^{-2})
400	7.56	1.90×10^{21}	7.10×10^{13}
435	9	1.43×10^{21}	5.71×10^{13}
470	16.52	5.10×10^{20}	3.57×10^{14}
500	33.16	4.69×10^{20}	1.71×10^{14}
550	0	0	1.14×10^{14}

The variation of sink strengths of dislocations, loops, and cavities in irradiated Fe-14Cr with increasing temperatures are illustrated in Figure 6.15a and b. The sink strengths of these defects are overall in the order of 10^{-14}-10^{-15} m^{-2}. Substituting these sink strength values into Eq. (6.5) gives the corresponding Q values. As shown in Figure 6.15c and d, the Q values were then compared to the corresponding cavity swelling value. For the 400 and 435°C data points in Figure 6.15c and d, the sold symbols considered the possible contribution of α' precipitates, assuming the precipitate radius and density are the same as in the Fe-14Cr sample examined by APT (Table 5.2). The unfilled symbols in Figure 6.15c are the Q values of the 400 and 435°C data points assuming that α' precipitates were not formed. In Figure 6.15c bubbles (cavity radius <2 nm) were regarded as natural sinks in the conventional way, while cavities were assumed to be biased sinks in Figure 6.15d. The cavity swelling in both Figure 6.15c and d is maximized at an intermediate Q value of 0.51 and 1.34, respectively. In a similar way, the variation of defect sink strengths and the Q values as a function of Cr is demonstrated in Figure 6.16. The cavity swelling assuming bubbles are neutral (Figure 6.16c) or biased (Figure 6.16d) sinks are also peaked at an intermediated Q value of 0.39 and 0.88, respectively. In both Figure 6.15 and Figure 6.16, the cavity swelling shows a strong dependency on the "general" Q values. The deviation of the Q values from 1 in Figure 6.15c and Figure 6.16d could be due to the variation of cavity bias with decreasing size. Besides, some of the small loops may not be identified under relatively low magnification STEM images. As a secondary effect, this can also result in a smaller Q value.

6.6 Effect of chromium

6.6.1 Dynamic microstructural evolution in Fe vs. Fe-10Cr

The threshold dose for observing black dot loop defects (under TEM bright-field images) in both Fe and Fe-10Cr foils was ~0.02 dpa. This observation is consistent with prior

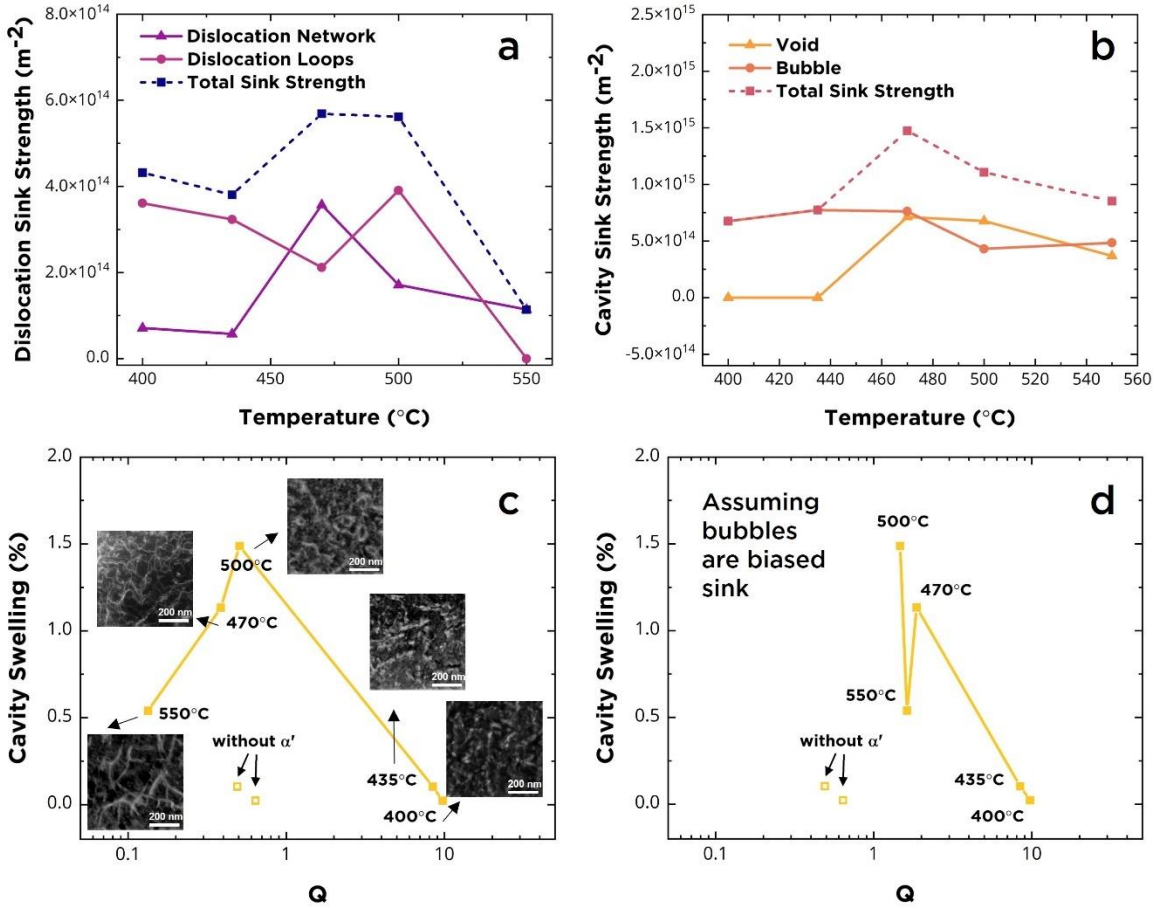

Figure 6.15 (a) dislocation and loop sink strength, and (b) void and bubble sink strength in irradiated Fe-10Cr (with 10 appm He/dpa) as a function of temperature; Dependence of cavity swelling on Q values: (c) assuming bubbles are natural sinks, and (d) assuming bubbles are biased sinks.

experimental studies [160, 161], and is generally interpreted as evidence for a low probability for direct in-cascade production of TEM-visible defect clusters during irradiation of Fe under energetic displacement cascade conditions (at low damage level). This interpretation also agrees with prior MD simulations of cascades [162, 163], whereпronounced defect clustering is predicted during the displacement cascade quenching, but the resulting defect cluster sizes (<50 interstitials; <1 nm loop radius) are near or below the TEM resolution limit. In order to further quantify the in-situ TEM results, the dose-dependent evolution of the dislocation loop size and density are summarized in Figure 6.17 and Figure 6.18, respectively. Above 5 dpa, the loops in Fe started to overlap and evolve into network dislocations due to physical impingement of large sessile loops. Network dislocations were not well developed in Fe-10Cr until ~18 dpa (Figure 6.18b). Three major loop evolution phases were observed (with some overlap): individual loop nucleation and growth (0.5-1 dpa for Fe; 0.5-5 dpa for Fe-10Cr), loop coalescence (1-8 dpa for Fe; 5-15 dpa for Fe-10Cr), and network dislocation formation (>5 dpa for Fe; >18 dpa for Fe-1Cr).

In Figure 6.18a, with an increasing dose, the loop density of pure Fe increased rapidly and saturated at ~0.5 dpa with a loop density of ~1.2×10^{22} m^{-3}. The loop density in Fe-10Cr exhibited a more sluggish evolution and did not reach saturation until a higher dose of ~3 dpa, with a corresponding loop density of ~9×10^{21} m^{-3} (Figure 6.18b). As indicated in Figure 6.18a, the loop production rate (i.e., increase in visible loop density per unit dose) before loop saturation in Fe-10Cr was roughly 6 times lower than in Fe. The loop density of Fe-10Cr could be underestimated due to smaller defect clusters (compared to Fe) that were near or below the TEM resolution limit. Above the loop saturation dose, the loop size increased with increasing dose in both materials, whereas the loop density decreased with the passage of irradiation time. The increase in loop size in this dose range (above loop density saturation dose) was mainly due to the absorption (coalescence) of loops (Figure 5.23 and Figure 5.27). The loop absorption reaction was also observed by Arakawa et al. [131] who reported the growth of loop size from ~4 nm to ~26 nm via loop absorption. As shown in Figure 6.17, the loop size in Fe grew rapidly to the average

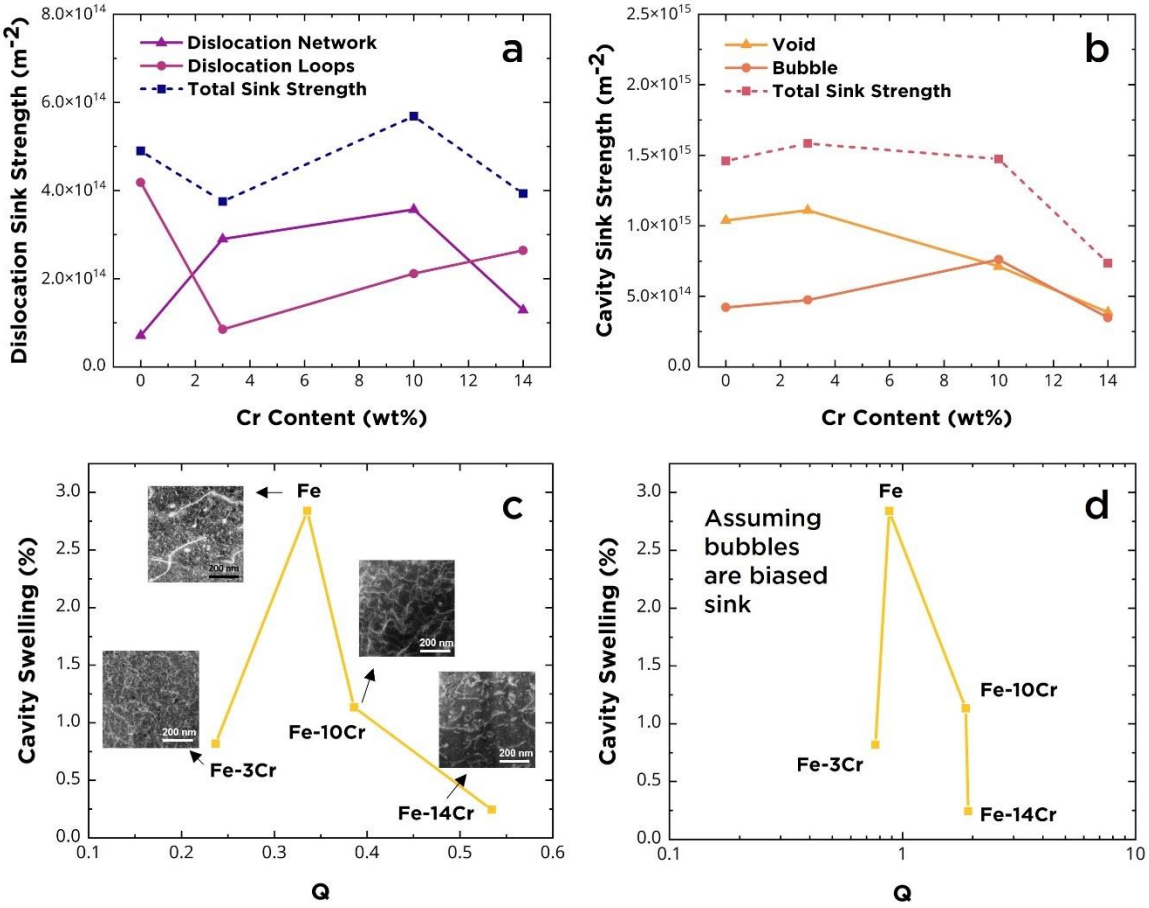

Figure 6.16 (a) dislocation and loop sink strength, and (b) void and bubble sink strength in 470°C-irradiated samples as a function of Cr content; Dependence of cavity swelling on Q values: (c) assuming bubbles are natural sinks, and (d) assuming bubbles are biased sinks.

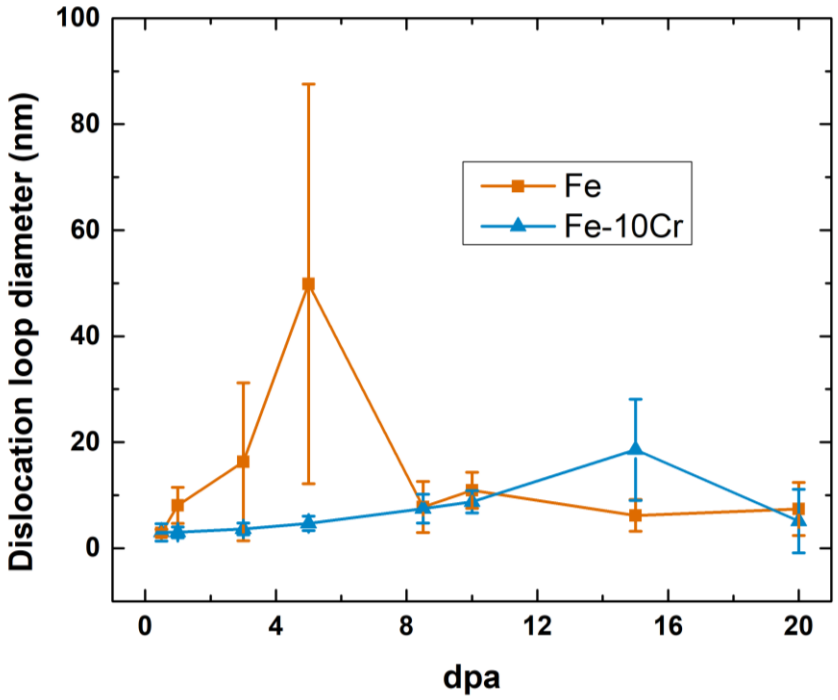

Figure 6.17 Average size of dislocation loops in in-situ dual-beam irradiated Fe and Fe-10Cr as a function of dose (irradiation time) at 435°C.

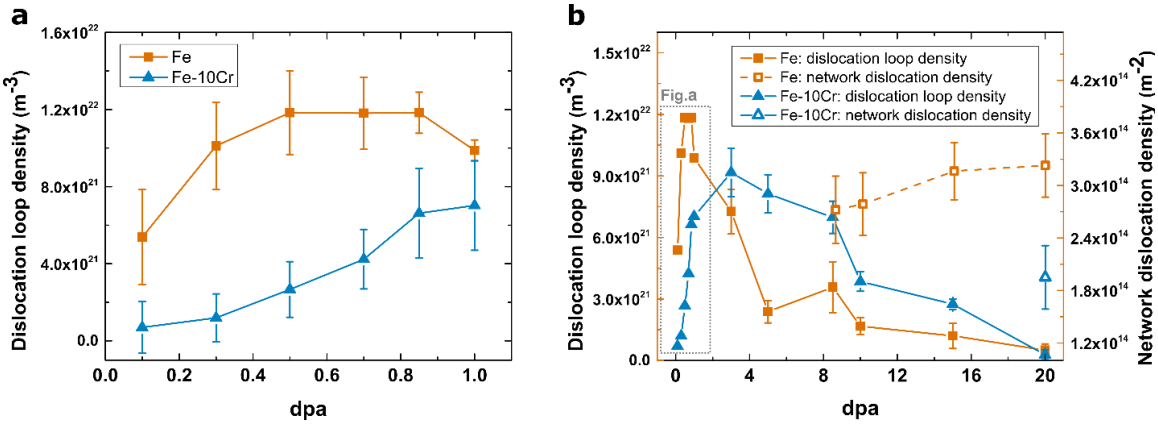

Figure 6.18 Defect density in in-situ dual-beam irradiated Fe and Fe-10Cr at 435°C as a function of dose: (a) Number density of dislocation loops at low doses (<1 dpa); (b) Number density of Dislocation loop and network dislocation at 0-20 dpa.

diameter of ~50 nm with increasing doses up to 5 dpa. At the same dose level of 5 dpa, the loop size in Fe was approximately 10 times larger than the average loop size in Fe-10Cr (~5 nm). Regarding the network dislocation density (Figure 6.18b), the average density of network dislocations in Fe-10Cr (~2×10^{14} m^{-2}) was slightly (1.75 times) lower compared to Fe (~3.5×10^{14} m^{-2}).

Figure 6.19 illustrates the comparison of loop size and density in previous ion and neutron irradiation studies [33, 42, 62, 70, 132, 164, 165]. In Figure 6.19, thin foil *in-situ* ion-irradiation studies were selected to compare with this study. The detailed irradiation conditions of these references are listed in the supplemental information (Table C.1). The measured loop size and density in the present work are comparable with previous *in-situ* irradiation studies on Fe and Fe-8/10Cr. Overall, at doses below 20 dpa and temperature between 300-500°C, the loop size and density are in the range of around 1-100 nm and 10^{20}-10^{22} m^{-3}, respectively. For *in-situ* Fe and Xe ion irradiation, at 500°C and 6.5 dpa, Jenkins et al. [129] reported the loop size of Fe and Fe-8Cr were several hundred nanometers and a few tens of nanometers, respectively. In the *in-situ* Fe and He ion irradiation study by Brimbal et al. [132], at 500°C with dose up to 0.8 dpa, the loop size in irradiated pure Fe was 40-80 nm. In the *in-situ* proton irradiation study by Chen et al. [164], the loop size of Fe and Fe-10Cr at ~400°C and 0.3 dpa were ~25 nm and ~10 nm, respectively. A higher density and a smaller size of irradiation-induced dislocation loops were also observed with increasing Cr content in neutron-irradiated bulk Fe-Cr model alloys [166].

Even though black-dot loops, elliptical loops, and network dislocations were observed in both pure Fe and Fe-10Cr, the microstructural evolution in Fe-10Cr took much more time (dose) than in Fe. The Fe-10Cr loop size grew with increasing dose, but the average size was smaller compared to Fe at corresponding doses. It was suggested that the finer size and higher density of loops or cavities observed in Fe-Cr (> 1dpa) are mainly due to the lower mobility of point defects or defect clusters compared to Fe [130, 167]. The lower diffusivity of point defects in Fe-Cr alloys also appeared to affect the required time for loop coarsening/absorption. In the present study, the required time of loop coarsening

in Fe for two adjacent loops was 1-10 minutes (Figure 5.23a and b). However, in Fe-10Cr, it took more than 30 minutes to complete a loop absorption reaction (Figure 5.27c). The elliptical loops started to show up at ~1 dpa (20 minutes) for Fe, whereas only a small proportion of elliptical loops were found in Fe-10Cr even for doses above ~5 dpa (90 minutes). For the loop to network dislocation transformation, the transformation happened at around 5 dpa (1.5 hours) and 18 dpa (5 hours) for Fe and Fe-10Cr, respectively. Besides, the maximum migration distance of black dot loops in Fe-10Cr at 1 dpa was ~30 nm, which is roughly five times smaller than in pure Fe.

Several other differences between the microstructural evolution of Fe and Fe-10Cr were observed as the damage level increased. The population of loop strings aligned along <100> directions was much higher in Fe-10Cr than in Fe. Besides, unlike the heterogeneous microstructural features in Fe, the defects in Fe-10Cr had no significant difference between the near-grain boundary area and the in-grain area. The ⟨100⟩ edge-on loops or ⟨100⟩ dislocation (Figure 5.23b) were not found near the Fe-10Cr grain boundaries. At ~10 dpa for the Fe foil, formation of a new population of small loops (black dot defects) with an average diameter of 3-4 nm (Figure 5.21 and Figure 6.18) was observed to co-exist with the network dislocations or inside large loops. The formation of black dot defects inside network dislocations/large loops was rarely reported for neutron or ion irradiation studies on bulk Fe-Cr materials [42, 104], but was observed in a previous *in-situ* electron irradiation study by Yoshida et al. [168]. In addition, it is worth to notice that, at 5-10 dpa, the pinning of dislocations by the irradiation-induced black dot loops was observed in Fe-10Cr but not in Fe. The dislocation pinning process that was only found in the Fe-10Cr foil at low doses (< 5 dpa) could be due to the ~4 times higher density of loops (Figure 6.18) that enhanced the pinning possibility of gliding dislocations. Additionally, the infrequent occurrence of dislocation pinning effects in Fe could be also influenced by the fast-growing loops in Fe with shorter dose (time) required for loop absorption and coarsening.

Identifying the nature of the loops (interstitial- vs. vacancy-type) is generally important for understanding the loop formation mechanism. This is typically performed

using the so-called inside-outside contrast technique, which is best performed on loops with sizes of ~5-50 nm [169]. At low doses, where the loop size is < 2 nm (black dot loops), determining the nature of the loops is difficult by traditional TEM techniques. At higher doses, where loop size grows to few nanometers, a majority of observed loops have been reported to be interstitial-type in neutron and ion irradiated Fe and Fe-Cr alloys [54, 62]. Nevertheless, some vacancy loops were also observed in neutron irradiation studies [59], and also in-situ ion irradiation studies [160] where many interstitials might be preferentially lost due to the thin foil surface effect [170]. Unfortunately, in the current study, the main type of defects in the post-irradiated samples (to 20 dpa) have evolved to network dislocations. Due to the time-dependent feature of the in-situ irradiation study (no irradiation pauses for detailed loop analysis), we couldn't trace back to low dose and check the loop types in our samples.

6.6.2 Cr effect on formation of cavities

As summarized in Figure 6.20, a dramatic synergistic effect appears to exist between

temperature and Cr content on cavity swelling. For both the 0.1 and 10 appm He/dpa condition, rather than a simple monotonic dependence on Cr content, our cavity swelling results summarized in Figure 6.20 indicate that Cr solute exerts a strong suppression on cavity swelling for irradiation temperatures up to 435°C but has a relatively weak or even slightly enhancement effect on cavity swelling at 470-550°C for the studied irradiation conditions. For the Cr effect, most of the previous experimental studies of ion irradiated Fe-Cr model or commercial alloys have reported cavity swelling suppression by the addition of Cr to the Fe matrix [39, 40, 43, 171]. Below 450°C, our results agree with the relatively recent study by Bhattacharya et al. [39, 171], using the same high purity Fe-Cr material as ours, that indicated the addition of Cr could suppress the swelling. Since their dose rate is ~2 times higher than ours, an additional positive temperature shift of ~8°C could be considered between the current study and that by Bhattacharya et al [39]. As shown in Figure 6.21a, the study by Bhattacharya (with dose up to 128 dpa) and our low-temperature results (<500°C) both showed the suppression of swelling by addition of Cr and a local peak swelling at Fe-10Cr (at 470°C in our case) among the Fe-Cr alloys.

However, our higher temperature results (≥500°C) seem to indicate that the addition of Cr could slightly enhance the cavity swelling. The Ni ion irradiation study by Johnston et al. [41] also found that the addition of Cr enhanced the cavity swelling with a maximum near 15% Cr at 500°C. The increased swelling with the addition of Cr was reported not only after ion irradiation but also in some neutron irradiation studies. For neutron irradiation at temperatures above 425°C (equivalent to ion irradiation at ~500°C considering the dose rate effect), maximum swelling around 8-10% Cr was reported [33, 34, 38, 108]. At higher neutron irradiation temperatures (>480°C), maximum swelling peaks near 5-7% Cr were also observed [108]. In Figure 6.21, we selected several neutron irradiation studies with similar doses of ~30 dpa as ours for comparison. The equivalent ion irradiation temperatures considering the dose rate effect are annotated in the braces. Figure 6.21 shows that Cr produces swelling suppression at low temperatures, but less pronounced effect at high temperatures. A similar trend as our ion irradiation study on the effect of Cr content seems to also emerge in the previous neutron studies [34, 108].

For lower irradiation temperatures (400-435°C), a possible physical cause for this effect could be related to the sink strength effect of the formation of alpha prime precipitation during the irradiation of Fe-Cr alloys containing >9% Cr. Previously, a significant difference in the formation of alpha prime precipitates was reported in neutron and ion irradiated materials [79]. Alpha prime decomposition in Fe-Cr alloys and FM steels had been mostly observed after ion irradiation only at dose rates around 10^{-5} dpa/s [81]. Nevertheless, recent ion irradiation studies reported the formation of alpha prime formation at temperatures as low as 300°C, and dose rate as high as ~10^{-4}-10^{-3} dpa/s [78, 172]. In this work, α' precipitates were observed by APT in the Fe-14Cr sample irradiated at 400°C and dose rate of 1.4×10^{-3} dpa/s. The suppression of swelling in our Fe-Cr samples at lower temperatures could be related to the formation of α' precipitates. Based on the equilibrium Fe-Cr phase diagram [78], at temperatures >500°C, the alpha prime phase does not form for Cr content <15 %.

Based on the consistency of our experimental results to the theoretical Q value dependence of swelling (Figure 6.16), the variation of cavity swelling as a function of Cr

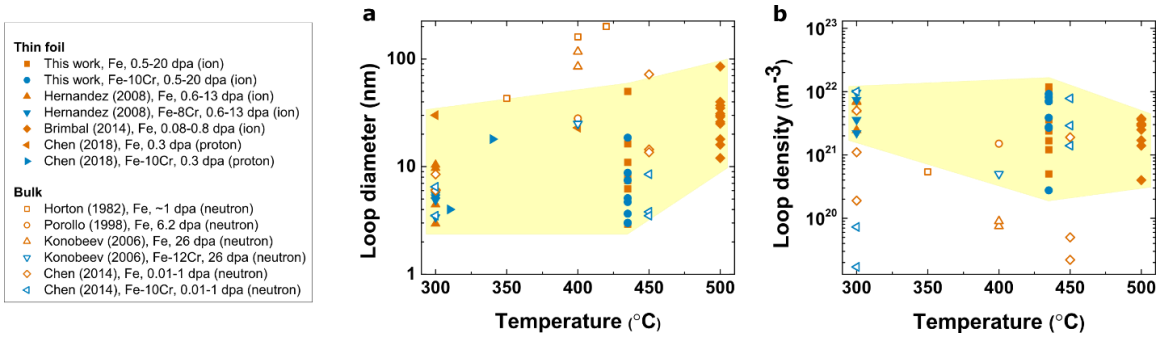

Figure 6.19 Comparison of (a) loop size and (b) density in previous thin foil (ion) and bulk material (neutron) irradiation studies. (Ref. [33, 42, 62, 70, 132, 164, 165])

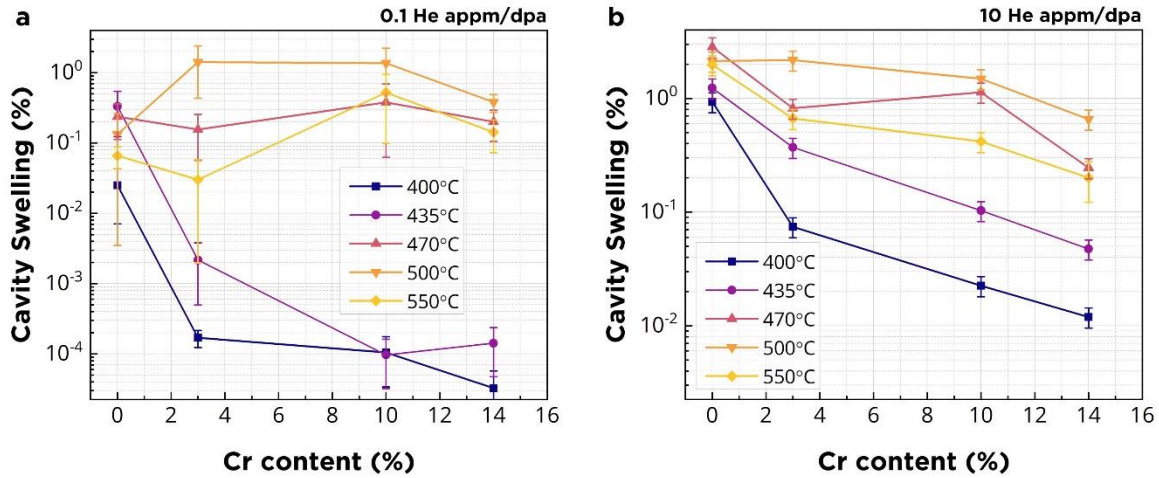

Figure 6.20 Variation of the cavity-swelling as a function of Cr concentration in the high-purity Fe and Fe-Cr dual-ion irradiated samples: (a) 0.1 appm He/dpa, and (b) 10 appm He/dpa.

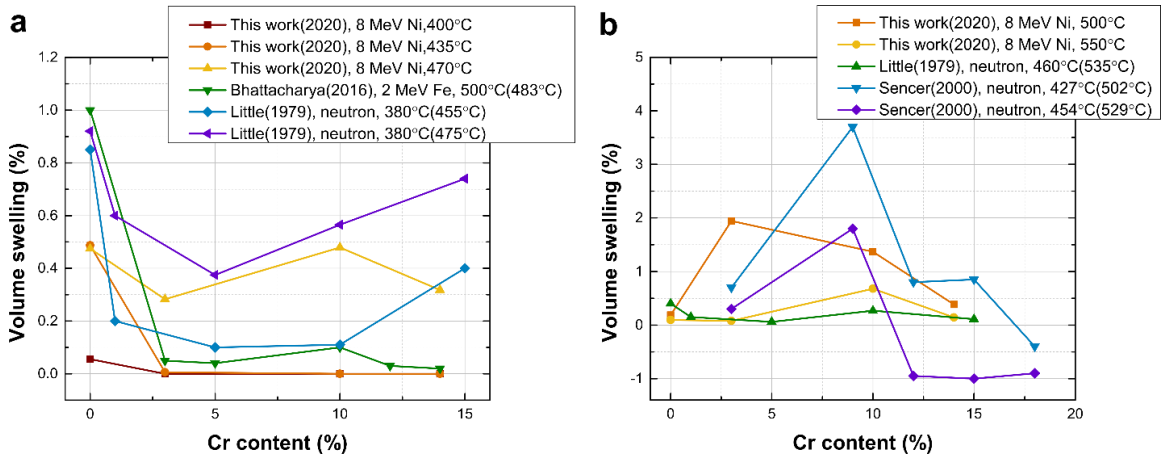

Figure 6.21 Variation of cavity swelling as a function of Cr concentration in Fe and Fe-Cr alloys at (a) ion irradiation-equivalent temperature <500°C, and (b) ion irradiation-equivalent temperature >500°C. The dose rate of each study was: ~1.4×10^{-3} dpa/s (this work), ~2.6×10^{-3} dpa/s (Bhattacharya et al.), ~8.4×10^{-7} dpa/s (Little et al.), and ~8×10^{-7} dpa/s (Sencer et al.) [34, 39, 108]

is likely dependent on the ratio of biased sink strength to neutral sink strength associated with the evolution of defects or the formation of α' precipitates. As discussed in section 6.6.1, the *in-situ* TEM study demonstrated that the dislocation loop evolution process is more sluggish in Fe-10Cr than in pure Fe, which indicates that Cr may impede dislocation loop motion. The observation of loop strings in Fe-10Cr (Figure 5.25) but not in Fe, also infers that the addition of Cr can obstruct the loop coarsening. Besides, the cavity denuded zone width analyses (section 6.1.2) and the higher peak swelling temperature in Fe-Cr alloys (Figure 5.6. and Figure 6.2) both suggest a higher vacancy migration energy in Fe-Cr alloys. In addition, the transformation of 111 to 100 loop types could also potentially alter the total sink strength (section 6.3). The above-mentioned observations can all affect the microstructure evolution under irradiation and thereby impact the defect sink strength.

In summary, cavity swelling varies in different studies and the Cr effects on cavity swelling may not be controlled by a single factor. The swelling in Fe and Fe-Cr is complicated and controlled by several effects, simultaneously. The cavity swelling is not linearly dependent on Cr content, especially at temperatures above 435°C, where the microstructure evolution is accelerated. Positron annihilation spectroscopy (PAS) and small-angle neutron scattering (SANS) studies on neutron-irradiated Fe-Cr alloys reported that the Cr solutes could have a negligible effect on vacancy type defect formation, although the materials were irradiated at a relatively low temperature (300°C) [173]. In addition to effects associated with the irradiation temperature, formation of alpha prime precipitates, and dose rate that could cause an effective cavity swelling temperature shift as well as affect the α' precipitation, other factors such as the dislocation loop density/type [129] and the incubation period of cavities [30] should also be considered. Additional experiments are needed to confirm the overall profile.

6.7 Effect of helium

6.7.1 Bimodal cavity size distribution

Helium stabilizes cavity formation by a pressure effect. Numerous prior studies [122, 174-176] have shown that when He concentration is low, the cavity swelling initially increases with increasing He concentration. For moderate to high He concentrations, relatively small pressurized bubbles and relatively large underpressurized voids lead to bimodal cavity size distributions. As discussed in section 5.2.2 and listed in Table 5.4, the bimodal size distribution of cavities was not found in any of our 0.1 appm He/dpa irradiated Fe or Fe-Cr specimens but observed in the 10 and 50 appm He/dpa conditions. This might be associated with the relatively smaller critical radius in the 0.1 appm He/dpa dual-beam irradiation condition. An ion irradiation study [111] on Fe-10Cr pre-implanted with 300 appm He and then irradiated to a similar dose and temperature (30 dpa and 577°C) as the current study reported a bimodal cavity size distribution with an average bubble diameter of 2.3 nm coexisting with larger cavities (~15 nm diameter) and the critical radius for conversion to bias-driven cavity growth was estimated to be ~2.5 nm.

Based on the critical radius model [16, 26], setting $d\,r_c/t = 0$ in Eq. (2.5) and assume the fluxes of point defects to the sinks are equal, the critical radius as a function of gas pressure gives [101]

$$r_c^{crit} = 2\gamma \Big/ \left\{ p_g + \frac{kT}{\Omega} \ln \left[(1 - Z) \frac{C_v}{C_v^0} + Z \right] \right\} \tag{6.6}$$

where k is the Boltzmann constant, T is the temperature, Ω is the atomic volume, $Z = Z_i^c Z_v^d / Z_v^c Z_i^d$ denotes the capture efficiency ratio, C_v is the vacancy concentration, C_v^0 is the thermal equilibrium vacancy concentration, and the gas pressure (p_g) can be expressed by

$$p_g = n_g kT \Big/ \left(\frac{4}{3} \pi r_c^3 - n_g B \right) \tag{6.7}$$

where n_g is the average number of gas atoms per cavity, r_c is the cavity radius, and B is the Van der Waals coefficient. By plotting the cavity radius as a function of critical radius,

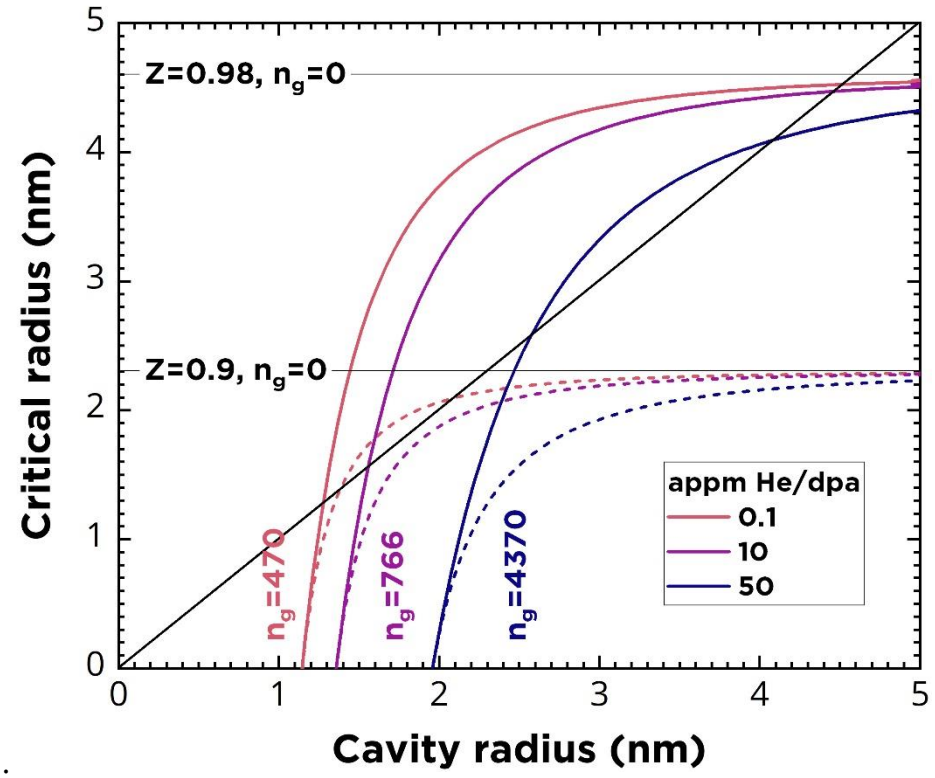

Figure 6.22 Cavity stability map for Fe-10Cr irradiated at 470°C with helium production rates of 0.1-50 appm He/dpa.

Table 6.7 Key parameters for cavity stability map calculation

Parameter	Value
Irradiation temperature (***T***)	470°C (743K)
Surface energy ($\boldsymbol{\gamma}$)	2.3 J/m^2
Atomic volume ($\boldsymbol{\Omega}$)	1.16×10^{-29} m^{-3}
Capture efficiency (***Z***)	0.9, and 0.98
Van der Waals coefficient (B)	2.4×10^{-5} m^3/mol
Number of gas atoms per cavity ($\boldsymbol{n_g}$)	470, 766, and 4370

a cavity stability map can be given as shown in Figure 6.22 for three different He/dpa levels. The colored solid curves were calculated with Z=0.98, and the colored dashed curves were calculated with a Z=0.9. The horizontal lines that are asymptotic with the curves at high cavity radius represent the gas-free critical radius. The values of parameters used in the calculations are summarized in Table 6.7.

In Figure 6.22, the intersection of the curves with the diagonal line (45° line) indicates a possible bimodal cavity size distribution. A cavity containing He atoms would grow along its respective curve until it reaches the stable bubble radius (lower intersection point). For low to intermediate n_g values, the stable bubble radius would increase with increasing n_g. When a large amount of helium atoms is added to the cavities, the curve will no longer intersect with the diagonal line indicating an absence of bimodal size distribution. Figure 6.22 also shows that the critical radius is strongly related to the capture efficiency ratio (Z). Typically, a high capture efficiency ratio above 0.95 is expected for ion-irradiations with high dose rates [177]. Hishinuma and Masure [177] reported that Z is dependent on the temperature and critical radius. With a fixed Z, a high temperature would lead to a higher critical radius. In this sense, the prediction by the cavity stability map (Figure 6.22) is qualitatively in agreement with our experimental results as summarized in Table 5.4. The bubble radius in our 0.1 He appm/dpa samples could be smaller than ~1 nm due to the lower n_g. For the 10 He appm/dpa samples, a bimodal size distribution was not observed in the 400 and 435°C irradiated Fe10Cr and Fe-14Cr samples. This could be because of the bias and temperature effect on the reduction of critical radius. Therefore, at the low helium production rate and several low-temperature conditions, the detection of a bimodal cavity size distribution may not be revealed due to the resolution limit of conventional TEM.

From a different perspective, by considering potential small cavity (bubble) bias effects on the Z ratio (as discussed in section 6.5.3), a variety of different Z ratios may occur. At the low 0.1 appm He/dpa condition, the Z ratio might be dominated by the dislocation bias terms because the dislocation loop nucleation may precede cavity nucleation. This could cause a monomodal cavity size distribution at Z~0.8-0.9 since the

dashed curve in Figure 6.22 would not intersect the diagonal line. At higher He/dpa (10 or 50 appm He/dpa), the large amount of implanted He will accelerate the formation of a high density of small bubbles at the early stages of the irradiation. Considering the large calculated interstitial to vacancy bias ratio for small cavities (Figure 6.15 and Figure 6.16), then a Z ratio of 0.98 (or higher) may quickly develop and lead to the formation of bimodal cavity size distribution at high doses. In other words, a Z ratio near or below 0.9 might be relevant for low He/dpa, whereas a Z ratio near 1.0 might be appropriate for high He/dpa. Assuming the same Z ratio for all He/dpa ratios may be physically incorrect. A related detailed consideration is that the Z ratio will likely change with increasing doses. Historically, researchers assume the microstructure present at low doses (~0.1-1 dpa or so) can be assumed to be relevant for the cavity nucleation phase. This may or may not be a reasonable simplifying assumption.

6.7.1 Effect of He on defects and cavity swelling

The simultaneously implanted He could affect the formation of dislocation loops and cavities. Overall, the dislocation loop size and void size decrease with increasing helium production rate, while their density showed the opposite order (Table 6.8 and Table 6.9). Helium has a considerable effect on voids compared to loops. No pronounced changes in the size or density of the bubbles and dislocation networks were made by different He/dpa levels. Prior research [63, 175, 178] has reported that the addition of helium stabilizes cavity formation by a pressure effect. A possible explanation for the reduction of void size can be the extension of the incubation period by adding helium. Therefore, simultaneous dual-beam (heavy ions plus He ions) irradiations generally result in a smaller size but a higher density of cavities than those in the same material irradiated with a single heavy ion beam. Brimbal et al. [132] reported that cavities were found in dual (Fe and He) ion beam irradiated Fe at 500°C, but cavities could not be detected in thin Fe foils without the presence of helium. In the same report, they also indicated that the addition of helium could reduce loop mobility. Other studies [55, 94] also showed that the presence of He

Table 6.8 Information of dislocations and loops in Fe-10Cr irradiated at 470-500°C with different He/dpa level

appm He/dpa	Dislocation loop diameter (nm)	Dislocation loop density (m^{-3})	Dislocation network density (m^{-2})
0.1	18.76	4.5×10^{20}	1.4×10^{14}
10	16.52	5.1×10^{20}	3.6×10^{14}
50	8.89	8.5×10^{20}	1.8×10^{14}

Table 6.9 Information of cavities in Fe-10Cr irradiated at 500°C with different He/dpa level

appm He/dpa	Void diameter (nm)	Void density (m^{-3})	Bubble diameter (nm)	Bubble density (m^{-3})
0.1	38.61	3.9×10^{20}	--	--
10	11.38	7.8×10^{21}	2.02	2.5×10^{22}
50	6.37	1.1×10^{22}	1.85	1.9×10^{22}

could impede the movement of $\frac{1}{2}\langle 111\rangle$ loops and inhibit the $\frac{1}{2}\langle 111\rangle$ loop to $\langle 100\rangle$ loop transformation. However, recent results reported an opposite trend where more $\langle 100\rangle$ loops formed due to excess He co-implantation in Fe-14Cr [179].

Regarding the effect of helium on cavity swelling (Figure 6.23), the swelling of Fe and Fe-10Cr both peaks at an intermediate He/dpa ratio of ~10 appm He/dpa. The is consistent with other neutron or ion irradiation studies on FCC materials, such as pure Cu [122] and austenitic steels [180, 181], which also reported a maximum swelling occurring at intermediate He/dpa ratios around 10-20 appm He/dpa. For the variation of void size and density (Table 6.9), from 0.1-10 appm He/dpa, the void density rapidly increased and the cavity size decreased with increasing He/dpa ratio. In addition, bubbles can start to be observed at higher He/dpa levels above 10 appm He/dpa. This agrees with the previous theory that low or medium levels of He/dpa can assist the nucleation and growth of cavities and thereby increase the cavity swelling [180]. For higher He/dpa levels, the reduction of swelling is likely due to the increase of the critical radius for the bubble to void conversion or over-nucleation in the number density of cavities [180-182]. From another standpoint, the cavity swelling incubation period is shortened below intermediate He production rates but extended at high He/dpa levels. In this study, although with large uncertainties, a significant increase of the critical radius with increasing He/dpa level from 10-50 appm He/dpa was not observed from the cavity size distribution plots (Figure 5.16, Figure 5.17, and Table 5.4). However, the absence of bubbles in the 0.1 appm He/dpa condition suggests that lower He/dpa levels may result in a smaller stable bubble radius that could not be detected by TEM. From 10 to 50 appm He/dpa, the cavity density seemed to reach saturation, whereas the void size continued decreasing (Table 6.9). The experimental result support the explanation that when the cavity density is sufficiently high, the cavity size and swelling could be suppressed by a sink strength effect.

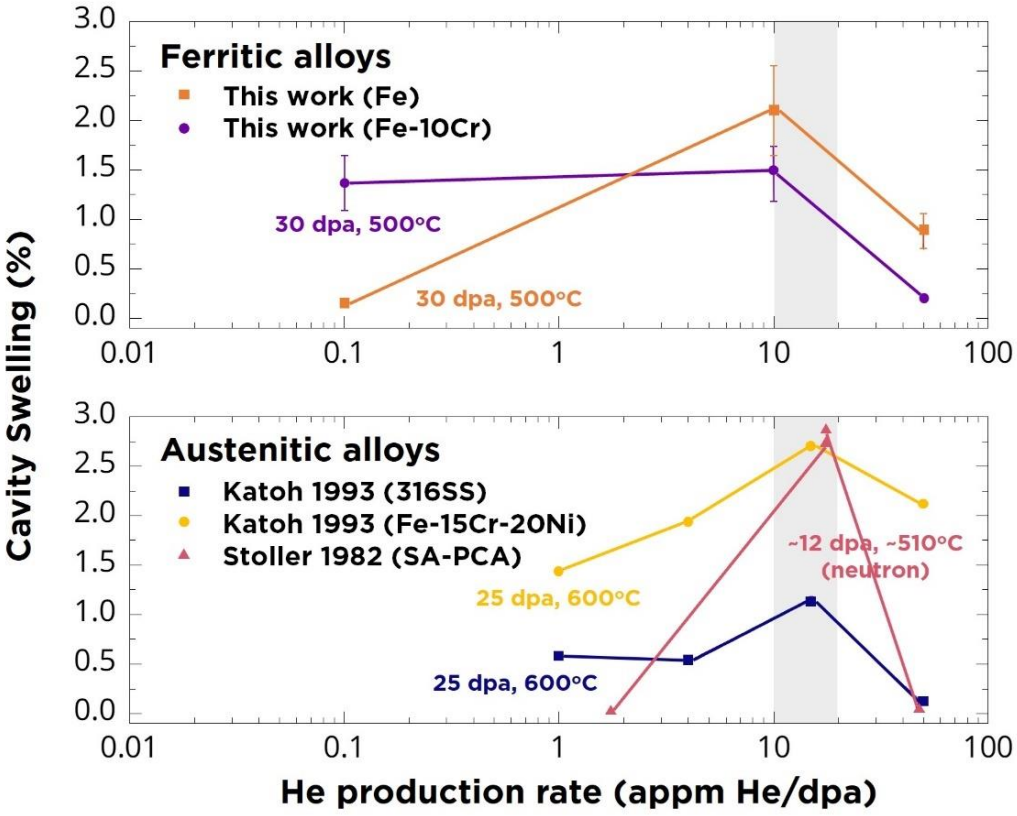

Figure 6.23 Effect of He production rate on cavity swelling in (a) ferritic and (b) austenitic alloys

Chapter 7
Conclusions

The key conclusions resulting from this thesis study are listed below. Suggestions for future studies are given at the end of this chapter.

7.1 Dual-ion beam irradiated Fe and Fe-Cr model alloys

The formation of cavities was observed in high purity Fe-Cr alloys at all five irradiation temperatures (400-550°C) following dual beam (8 MeV Ni + He) ion irradiations at a dose rate of 1.4×10^{-3} dpa/s to midrange doses of ~30 dpa at three different He/dpa levels (0.1, 10, and 50 appm He/dpa). Based on the experimental findings here are the main conclusions:

1. The observed cavity swelling temperature regime for 8 MeV Ni ion irradiated Fe, Fe-Cr alloys is much broader than values suggested by previous ion irradiation studies using low ion energies. This is attributed to several well-known (but maybe not well-avoided) artifacts for ion irradiation research: cavity denuded zones with an adjacent enhanced swelling region and diffusional broadening of injected ions can reduce the breadth of the temperature regime for cavity swelling, and generally shift the cavity swelling regime to higher temperatures with increasing dose rate. The presence of these artifacts is expected to contribute to the extremely narrow observable temperature windows of cavities in ion irradiated FM steels that were previously reported in the literature.

2. When applying ion beams to understand neutron irradiation conditions, the present results highlight that higher heavy-ion energies (>10 MeV) are necessary to provide a sufficiently broad mid-range “safe analysis” region to minimize the above-mentioned artifacts. In addition, our STEM-EDS measurement of the injected Ni profile revealed a mean depth less than the estimated depth calculated by SRIM (~700 nm shift). The error in the stopping power model used in SRIM 2013 can result in incorrect estimates of the location of the safe analysis region if left unchecked.

3. Pure Fe has a ~25-50 °C lower peak swelling temperature difference than Fe-Cr alloys for ion irradiation relevant dose rates. Based on our analysis, this could be related to a potentially lower vacancy migration energy of pure Fe compared to Fe-Cr alloys.

4. The higher He production rate resulted in a higher peak swelling temperature for pure Fe with a temperature difference of ~35°C compared to the 0.1 appm He/dpa case. This could be related to the modification of vacancy thermal emission term by a pressure effect of He gas atoms. The addition of Cr may increase the cavity surface energy and offset the He pressure effect.

5. Despite the large quantitative uncertainty on the estimation of vacancy migration energies from near-surface cavity denuded zone width measurements, the present study revealed that this method is qualitatively robust to explain the experimentally observed peak swelling temperature differences for Fe vs. the Fe-Cr alloys. Further experimental data are needed to improve the uncertainties in the fitted vacancy migration energies.

6. Cr strongly suppresses cavity swelling of ion irradiated Fe-Cr alloys below ~450°C, but seems to have a relatively weak influence at higher temperatures. The Cr content dependence on cavity swelling is associated with the ratio of the biased sink strength to neutral sink strength. The defect sink strength evolution could be related to the Cr solute trapping of defect or the formation of α' precipitates, leading to increased recombination rate of point defects.

7. Cavity swelling peaks at intermediate He/dpa ratios of ~10 appm He/dpa for ion irradiated Fe and Fe-Cr alloys, in agreement with the peak swelling He/dpa ratios of other BCC or FCC materials at 10-20 appm He/dpa. The peak at intermediate He production rate is likely because He assists the nucleation and growth at lower He production rates, but suppress the swelling at very high He production rates due to the over nucleation of cavities.

8. A bimodal cavity size distribution was observed in the 10 and 50 He appm/dpa samples, but not for 0.1 He appm/dpa. It is suggested that a variety of different capture efficiency ratios, Z (depends on temperature, dose rate, and He production rate), may occur and affect the critical radius. Assuming the same Z ratio for all He/dpa ratios may be

physically incorrect. The absence of TEM visible bubbles in the 0.1 appm He/dpa condition attributed to lower amount of He gas atoms in the cavities that led to a smaller stable bubble radius. Small bubbles with diameters <1 nm are typically difficult to be observed due to the resolution limit of TEM, which could contribute to inability in detecting bimodal cavity distributions especially when irradiation temperatures are relatively lower.

7.2 In-situ irradiated Fe and Fe-10Cr model alloys

The dynamic evolution of microstructures in dual-beam (Kr and He ions) irradiated Fe and Fe-10Cr foils at 435°C was investigated. The i*n-situ* TEM videos (total length of ~5.5 hours for each sample) revealed the continuous evolution of loops, network dislocations, and vacancies in the high purity Fe and Fe-10Cr material. The following conclusions have been reached:

1. The loop evolution process is relatively sluggish in Fe-10Cr compared to pure Fe. Several other observations (e.g., dislocation decoration was found to be less pronounced Fe-10Cr, dislocation pinning was observed more frequently in Fe-10Cr, and a longer time required for loop absorption/coarsening as well as a smaller size and higher density of loops were observed in Fe-10Cr) generally support prior observations that Cr impedes dislocation loop motion and suppresses the "111 to 100 loop conversion reaction"

2. In line with previous modeling studies, our experimental results showed that the physical mechanism for the formation of observed ⟨100⟩ dislocation loops may not be a simple dislocation reaction. Some of the observed "111 to 100 loop" reactions violate Frank's energy criterion for one-step dislocation reactions.

3. The significant difference of loop types observed near the grain boundary of the pure Fe foil could be related to the "111 to 100 loop" reaction. The lower loop density in the vicinity of the grain boundary could favor certain types of dislocation loop interactions for ½⟨111⟩ loops to evolve into ⟨100⟩ loops.

4. Cavity formation became visible above 10 to 20 dpa, when the total sink strength of loops and network dislocation fell below ~4×10^{14} m^{-2} due to the physical impingement-induced transformation of loops to network dislocations at intermediate doses.

5. The loop type of the nanoscale black dot defects composing the ⟨100⟩ loop strings observed in Fe-10Cr needs to be confirmed: in particular, whether or not they are ½⟨111⟩ loops arrayed along ⟨100⟩ directions.

7.3 He implanted nanostructured ferritic/martensitic steels

High-temperature cavity formation was examined by TEM and STEM in bulk He-irradiated and in-situ He-irradiated ferritic alloys containing different nanoparticle densities: Fe-9/10Cr (without nanoparticles), CNA3 (intermediate), and 14YWT (highest nanoparticle density). At all temperatures, the cavity density in the He implanted materials was generally in the order of Fe-9/10Cr < CNA3 < 14YWT, which directly corresponds to the nanoparticle density, whereas the cavity size showed the opposite order. Our TEM, EELS and atomic resolution STEM results all suggest that both types of nanoparticles (MX carbides in CNA3 and Y-Ti-O oxides in 14YWT) were quite effective in trapping He-vacancy clusters at temperatures up to ~900°C. Based on the experimental findings the main conclusions are:

1. In agreement with previous studies, the addition of high-density nanoparticles can sequester helium into finely dispersed small bubbles at the particle-matrix interfaces (causing lower overall volumetric swelling compared to conventional alloys) and suppress He diffusion to the grain boundaries. Considering the nanoparticle density and total initial sink strength, the present results suggest that very high He concentrations (up to ~10,000 appm) can be well managed in nanostructured alloys with a high density of nanoparticles (>10^{22} m^{-3}, which corresponds to a sink strength >10^{15} m^{-2}).

2. Distinct from the temperature-dependent effective activation energy for He cavities in particle-free Fe-9/10Cr model alloys, the corresponding activation energies in the CNA3 and 14YWT nanostructured alloys were nearly constant over a wide temperature

range of 500-900°C. This could be related to the suppression of Ostwald ripening by nanoparticles or sufficiently high binding energy of He bubbles attached to nanoparticles that could suppress the helium desorption or migration at high temperatures. The current results suggest that the critical temperature for transitioning from low-temperature migration and coalescence-dominant behavior to high-temperature Ostwald ripening behavior for the cavities could be shifted upwards by ~300°C (from ~600 to >900°C) by introducing finely-dispersed nanoparticles.

3. Both the MX carbides in CNA3 and Y-Ti-O oxides in 14YWT were found to exhibit high (favorable) binding energies for helium cavities up to temperatures as high as 900°C. At 700°C, 14YWT has the most uniform distribution and exhibited an apparent one-to-one relationship for bubble attachment to the Y-Ti-O oxides, while the MX carbide nanoparticles in CNA3 attached ~3-10 small He bubbles to a single particle. This difference is attributed to differences in the particle size (surface area) and density (interparticle distance).

4. There is a strong temperature dependence on the mean free path for He-vacancy cluster diffusion in particle-free Fe-Cr alloys. The CNA3 nanostructured ferritic alloy exhibited intermediate behavior: At temperatures below 600°C, the cavity density in CNA3 did not show an obvious difference compared to single-phase Fe-9/10Cr alloys, whereas a weaker temperature dependence than Fe-9/10Cr was observed at high temperatures. At all investigated temperatures (500-900°C) the 14YWT alloy sequesters the helium into finely dispersed small bubbles, thereby producing a nearly temperature-independent bubble density and a weak temperature variation in bubble size. This may be attributed to the much higher sink strength (smaller interparticle distance) associated with the nanoparticles in the 14YWT alloy, or perhaps a moderate difference in the He trapping ability (binding energy) between Y-Ti-O oxides and MX particles.

7.4 Recommendations for future work

1. Future ion irradiation studies on irradiation-induced defects should beware of the near-surface and implanted ion effects, as well as the SRIM code error for Ni ions. Higher heavy-ion energies (>10 MeV) are necessary to provide a sufficiently broad mid-range safe analysis region to minimize the artifacts. Note that the safe analysis region decreases with increasing irradiation temperature.
2. Additional theoretical studies are needed to bring the Q (biased to unbiased sink strength) and Z (capture efficiency) ratio models into accord with experimental observations. A key question that needs to be resolved is whether all small cavities should be treated as a biased sink or a neutral sink.
3. To provide a better understanding of the cavity formation mechanism, irradiated samples with high cavity density are required to reduce the large uncertainties of experimental measurements (e.g., denuded zone width, critical cavity size, etc.). This could be achieved by long period irradiations or irradiations on low swelling resistant materials.
4. Future irradiation studies on Fe-Cr alloys should concentrate on the formation of α' precipitates and the transformation of dislocation loop types. Several synergistic effects such as temperature, Cr content, dose, and dose rate need to be considered.
5. The potential applications of the STEM imaging technique as applied to irradiation-induced defect analysis should be studied in further detail. STEM imaging can be performed on thicker samples than conventional TEM, and therefore bend contour and auxiliary contrast effects can be suppressed while retaining defect contrast. The combination of ABF, LAADF, and HAADF imaging techniques can improve the identification of the type of defect. The WBDF technique widely used in TEM mode can also be applied in STEM mode for loop type identification.

References

[1] S.J. Zinkle, J.T. Busby, Structural materials for fission & fusion energy, Materials Today 12(11) (2009) 12-19.

[2] A technology roadmap for generation iv nuclear energy systems, U.S. DoE Nuclear Energy Research Advisory Committee and the Generation IV International Forum, 2002.

[3] S.J. Zinkle, L.L. Snead, Opportunities and limitations for ion beams in radiation effects studies: Bridging critical gaps between charged particle and neutron irradiations, Scripta Materialia 143 (2018) 154-160.

[4] S.J. Zinkle, L.L. Snead, Designing Radiation Resistance in Materials for Fusion Energy, Annual Review of Materials Research 44(1) (2014) 241-267.

[5] A. Kohyama, A. Hishinuma, D.S. Gelles, R.L. Klueh, W. Dietz, K. Ehrlich, Low-activation ferritic and martensitic steels for fusion application, Journal of Nuclear Materials 233-237 (1996) 138-147.

[6] V. Kuksenko, C. Pareige, P. Pareige, Cr precipitation in neutron irradiated industrial purity Fe–Cr model alloys, Journal of Nuclear Materials 432(1) (2013) 160-165.

[7] S.J. Zinkle, G.S. Was, Materials challenges in nuclear energy, Acta Materialia 61(3) (2013) 735-758.

[8] M.J. Norgett, M.T. Robinson, I.M. Torrens, A proposed method of calculating displacement dose rates, Nuclear Engineering and Design 33(1) (1975) 50-54.

[9] K. Nordlund, S.J. Zinkle, A.E. Sand, F. Granberg, R.S. Averback, R. Stoller, T. Suzudo, L. Malerba, F. Banhart, W.J. Weber, F. Willaime, S.L. Dudarev, D. Simeone, Improving atomic displacement and replacement calculations with physically realistic damage models, Nature Communications 9(1) (2018) 1084.

[10] J.F. Ziegler, J.P. Biersack, U. Littmark, The Stopping and Range of Ions in Matter, Pergamon Press, New York, 1985.

[11] R.E. Stoller, M.B. Toloczko, G.S. Was, A.G. Certain, S. Dwaraknath, F.A. Garner, On the use of SRIM for computing radiation damage exposure, Nuclear Instruments and Methods in Physics Research Section B: Beam Interactions with Materials and Atoms 310 (2013) 75-80, and erratum NIMB 459 (2019) 196-197.

[12] W.J. Weber, Y. Zhang, Predicting damage production in monoatomic and multi-elemental targets using stopping and range of ions in matter code: Challenges and recommendations, Current Opinion in Solid State and Materials Science 23(4) (2019) 100757.

[13] S. Agarwal, Y. Lin, C. Li, R.E. Stoller, S.J. Zinkle, On the use of SRIM for calculating vacancy production: Quick calculation and full-cascade options, Nuclear

Instruments and Methods in Physics Research Section B: Beam Interactions with Materials and Atoms 503 (2021) 11-29.

[14] L.K. Mansur, The reaction rate theory of radiation effects, JOM 48(12) (1996) 28-32.

[15] A.A. Kohnert, M.A. Cusentino, B.D. Wirth, Molecular statics calculations of the biases and point defect capture volumes of small cavities, Journal of Nuclear Materials 499 (2018) 480-489.

[16] R.E. Stoller, G.R. Odette, Analytical solutions for helium bubble and critical radius parameters using a hard sphere equation of state, Journal of Nuclear Materials 131(2) (1985) 118-125.

[17] L.K. Mansur, Void Swelling in Metals and Alloys Under Irradiation: An Assessment of the Theory, Nuclear Technology 40(1) (1978) 5-34.

[18] W.Z. Han, M.J. Demkowicz, E.G. Fu, Y.Q. Wang, A. Misra, Effect of grain boundary character on sink efficiency, Acta Materialia 60(18) (2012) 6341-6351.

[19] Y.V. Konobeev, A.V. Subbotin, V.N. Bykov, V.I. Tscherbak, Grain boundary void denuded zone in irradiated metals, physica status solidi (a) 29(2) (1975) K121-K124.

[20] S.J. Zinkle, Dislocation Loop Formation in Ion-Irradiated Polycrystalline Spinel and Alumina, in: R.E. Stoller, A.S. Kumar, D.S. Gelles (Eds.), ASTM International, West Conshohocken, PA, 1992, pp. 749-763.

[21] B.N. Singh, S.J. Zinkle, Influence of irradiation parameters on damage accumulation in metals and alloys, Journal of Nuclear Materials 217(1) (1994) 161-171.

[22] H. Trinkaus, B.N. Singh, A.J.E. Foreman, Impact of glissile interstitial loop production in cascades on defect accumulation in the transient, Journal of Nuclear Materials 206(2) (1993) 200-211.

[23] M. Kiritani, Radiation rate dependence of microstructure evolution, Journal of Nuclear Materials 169 (1989) 89-94.

[24] S.J. Zinkle, G.L. Kulcinski, R.W. Knoll, Microstructure of copper following high dose 14-MeV Cu ion irradiation, Journal of Nuclear Materials 138(1) (1986) 46-56.

[25] S.J. Zinkle, K. Farrell, Void swelling and defect cluster formation in reactor-irradiated copper, Journal of Nuclear Materials 168(3) (1989) 262-267.

[26] L.K. Mansur, Theory and experimental background on dimensional changes in irradiated alloys, Journal of Nuclear Materials 216 (1994) 97-123.

[27] S.J. Zinkle, UTK MSE 540 lecture notes.

[28] G.L. Kulcinski, B. Mastel, J.L. Brimhall, Formation of voids in iron during high temperature neutron irradation, Radiation Effects 2(1) (1969) 57-59.

[29] K. Farrell, J.T. Houston, Heterogeneous distribution of irradiation voids in iron, Journal of Nuclear Materials 35(3) (1970) 352-355.

[30] F.A. Garner, M.B. Toloczko, B.H. Sencer, Comparison of swelling and irradiation creep behavior of fcc-austenitic and bcc-ferritic/martensitic alloys at high neutron exposure, Journal of Nuclear Materials 276(1) (2000) 123-142.

[31] M.L. Jenkins, M.A. Kirk, W.J. Phythian, Experimental studies of cascade phenomena in metals, Journal of Nuclear Materials 205 (1993) 16-30.

[32] W.G. Wolfer, Advances in void swelling and helium bubble physics, Journal of Nuclear Materials 122(1) (1984) 367-378.

[33] S.I. Porollo, A.M. Dvoriashin, A.N. Vorobyev, Y.V. Konobeev, The microstructure and tensile properties of Fe–Cr alloys after neutron irradiation at 400°C to 5.5–7.1 dpa, Journal of Nuclear Materials 256(2) (1998) 247-253.

[34] E.A. Little, D.A. Stow, Void-swelling in irons and ferritic steels: I. Mechanisms of swelling suppression, Journal of Nuclear Materials 87(1) (1979) 11-24.

[35] D.S. Gelles, Microstructural examination of neutron-irradiated simple ferritic alloys, Journal of Nuclear Materials 108-109 (1982) 515-526.

[36] D.S. Gelles, Effects of irradiation on ferritic alloys and implications for fusion reactor applications, Journal of Nuclear Materials 149(2) (1987) 192-199.

[37] Y. Katoh, A. Kohyama, D.S. Gelles, Swelling and dislocation evolution in simple ferritic alloys irradiated to high fluence in FFTF/MOTA, Journal of Nuclear Materials 225 (1995) 154-162.

[38] D.S. Gelles, Void swelling in binary FeCr alloys at 200 dpa, Journal of Nuclear Materials 225 (1995) 163-174.

[39] A. Bhattacharya, E. Meslin, J. Henry, A. Barbu, S. Poissonnet, B. Décamps, Effect of chromium on void swelling in ion irradiated high purity Fe–Cr alloys, Acta Materialia 108 (2016) 241-251.

[40] D. Brimbal, E. Meslin, J. Henry, B. Décamps, A. Barbu, He and Cr effects on radiation damage formation in ion-irradiated pure iron and Fe–5.40wt.% Cr: A transmission electron microscopy study, Acta Materialia 61(13) (2013) 4757-4764.

[41] W.G. Johnston, T. Lauritzen, J.H. Rosolowski, A.M. Turkalo, Void Swelling of Ferritic Alloys Bombarded with Nickel Ions, in: H.R. Brager, J.S. Perrin (Eds.), ASTM International, West Conshohocken, PA, 1982, pp. 809-823.

[42] L.L. Horton, J. Bentley, K. Farrell, A TEM study of neutron-irradiated iron, Journal of Nuclear Materials 108-109 (1982) 222-233.

[43] E. Getto, G. Vancoevering, G.S. Was, The co-evolution of microstructure features in self-ion irradiated HT9 at very high damage levels, Journal of Nuclear Materials 484 (2017) 193-208.

[44] E. Aydogan, T. Chen, J.G. Gigax, D. Chen, X. Wang, P.S. Dzhumaev, O.V. Emelyanova, M.G. Ganchenkova, B.A. Kalin, M. Leontiva-Smirnova, R.Z. Valiev, N.A. Enikeev, M.M. Abramova, Y. Wu, W.Y. Lo, Y. Yang, M. Short, S.A. Maloy, F.A. Garner, L. Shao, Effect of self-ion irradiation on the microstructural changes of alloy EK-181 in annealed and severely deformed conditions, Journal of Nuclear Materials 487 (2017) 96-104.

[45] T. Tanaka, K. Oka, S. Ohnuki, S. Yamashita, T. Suda, S. Watanabe, E. Wakai, Synergistic effect of helium and hydrogen for defect evolution under multi-ion irradiation of Fe–Cr ferritic alloys, Journal of Nuclear Materials 329-333 (2004) 294-298.

[46] Y.-R. Lin, A. Bhattacharya, D. Chen, J.-J. Kai, J. Henry, S.J. Zinkle, Temperature-dependent cavity swelling in dual-ion irradiated Fe and Fe-Cr ferritic alloys, Acta Materialia 207 (2021) 116660.

[47] B.L. Eyre, Direct observations of neutron irradiation damage in α-iron, The Philosophical Magazine: A Journal of Theoretical Experimental and Applied Physics 7(84) (1962) 2107-2113.

[48] B.C. Masters, Dislocation Loops in Irradiated Iron, Nature 200(4903) (1963) 254-254.

[49] B.L. Eyre, R. Bullough, On the formation of interstitial loops in b.c.c. metals, The Philosophical Magazine: A Journal of Theoretical Experimental and Applied Physics 12(115) (1965) 31-39.

[50] S.J. Zinkle, B.N. Singh, Microstructure of neutron-irradiated iron before and after tensile deformation, Journal of Nuclear Materials 351(1) (2006) 269-284.

[51] I.M. Robertson, M.L. Jenkins, C.A. English, Low-dose neutron-irradiation damage in α-iron, Journal of Nuclear Materials 108-109 (1982) 209-221.

[52] A.C. Nicol, M.L. Jenkins, M.A. Kirk, Matrix Damage in Iron, MRS Proceedings 650 (2000) R1.3.

[53] M. Hernández-Mayoral, D. Gómez-Briceño, Transmission electron microscopy study on neutron irradiated pure iron and RPV model alloys, Journal of Nuclear Materials 399(2) (2010) 146-153.

[54] M. Matijasevic, W. Van Renterghem, A. Almazouzi, Characterization of irradiated single crystals of Fe and Fe–15Cr, Acta Materialia 57(5) (2009) 1577-1585.

[55] A. Prokhodtseva, B. Décamps, R. Schäublin, Comparison between bulk and thin foil ion irradiation of ultra high purity Fe, Journal of Nuclear Materials 442(1, Supplement 1) (2013) S786-S789.

[56] Z. Yao, M.L. Jenkins, M. Hernández-Mayoral, M.A. Kirk, The temperature dependence of heavy-ion damage in iron: A microstructural transition at elevated temperatures, Philosophical Magazine 90(35-36) (2010) 4623-4634.

[57] S.L. Dudarev, R. Bullough, P.M. Derlet, Effect of the alpha-gamma phase transition on the stability of dislocation loops in bcc Iron, Physical Review Letters 100(13) (2008) 135503.

[58] S.L. Dudarev, P.M. Derlet, R. Bullough, The magnetic origin of anomalous high-temperature stability of dislocation loops in iron and iron-based alloys, Journal of Nuclear Materials 386-388 (2009) 45-48.

[59] J.C. Haley, S.A. Briggs, P.D. Edmondson, K. Sridharan, S.G. Roberts, S. Lozano-Perez, K.G. Field, Dislocation loop evolution during in-situ ion irradiation of model FeCrAl alloys, Acta Materialia 136 (2017) 390-401.

[60] K.G. Field, S.A. Briggs, X. Hu, Y. Yamamoto, R.H. Howard, K. Sridharan, Heterogeneous dislocation loop formation near grain boundaries in a neutron-irradiated commercial FeCrAl alloy, Journal of Nuclear Materials 483 (2017) 54-61.

[61] K.G. Field, S.A. Briggs, K. Sridharan, Y. Yamamoto, R.H. Howard, Dislocation loop formation in model FeCrAl alloys after neutron irradiation below 1 dpa, Journal of Nuclear Materials 495 (2017) 20-26.

[62] M. Hernández-Mayoral, Z. Yao, M.L. Jenkins, M.A. Kirk, Heavy-ion irradiations of Fe and Fe–Cr model alloys Part 2: Damage evolution in thin-foils at higher doses, Philosophical Magazine 88(21) (2008) 2881-2897.

[63] A. Prokhodtseva, B. Décamps, A. Ramar, R. Schäublin, Impact of He and Cr on defect accumulation in ion-irradiated ultrahigh-purity Fe(Cr) alloys, Acta Materialia 61(18) (2013) 6958-6971.

[64] S. Xu, Z. Yao, M.L. Jenkins, TEM characterisation of heavy-ion irradiation damage in FeCr alloys, Journal of Nuclear Materials 386-388 (2009) 161-164.

[65] M. Hernández-Mayoral, C. Heintze, E. Oñorbe, Transmission electron microscopy investigation of the microstructure of Fe–Cr alloys induced by neutron and ion irradiation at 300 °C, Journal of Nuclear Materials 474 (2016) 88-98.

[66] D. Terentyev, L. Malerba, A.V. Barashev, On the correlation between self-interstitial cluster diffusivity and irradiation-induced swelling in Fe–Cr alloys, Philosophical Magazine Letters 85(11) (2005) 587-594.

[67] K. Arakawa, M. Hatanaka, H. Mori, K. Ono, Effects of chromium on the one-dimensional motion of interstitial-type dislocation loops in iron, Journal of Nuclear Materials 329-333 (2004) 1194-1198.

[68] H. Xu, R.E. Stoller, Y.N. Osetsky, D. Terentyev, Solving the Puzzle of ⟨100⟩ Interstitial Loop Formation in bcc Iron, Physical Review Letters 110(26) (2013) 265503.

[69] A. Okada, N. Kawaguchi, M.L. Hamilton, K. Hamada, T. Yoshiie, I. Ishida, E. Hirota, Mechanical property change in neutron irradiated Fe-Cr and Fe-Mn alloys, and their defect structures, Journal of Nuclear Materials 212-215 (1994) 382-387.

[70] Y.V. Konobeev, A.M. Dvoriashin, S.I. Porollo, F.A. Garner, Swelling and microstructure of pure Fe and Fe–Cr alloys after neutron irradiation to ~26dpa at 400°C, Journal of Nuclear Materials 355(1) (2006) 124-130.

[71] M. Matijasevic, A. Almazouzi, Effect of Cr on the mechanical properties and microstructure of Fe–Cr model alloys after n-irradiation, Journal of Nuclear Materials 377(1) (2008) 147-154.

[72] Z. Yao, M. Hernández-Mayoral, M.L. Jenkins, M.A. Kirk, Heavy-ion irradiations of Fe and Fe–Cr model alloys Part 1: Damage evolution in thin-foils at lower doses, Philosophical Magazine 88(21) (2008) 2851-2880.

[73] A. Almazouzi, T. Díaz de la Rubia, B.N. Singh, M. Victoria, Basic aspects of differences in irradiation effects between fcc, bcc and hcp metals and alloys, Journal of Nuclear Materials 276(1) (2000) 295-296.

[74] G. Bonny, D. Terentyev, L. Malerba, On the $\alpha - \alpha'$ miscibility gap of Fe–Cr alloys, Scripta Materialia 59(11) (2008) 1193-1196.

[75] W. Xiong, M. Selleby, Q. Chen, J. Odqvist, Y. Du, Phase Equilibria and Thermodynamic Properties in the Fe-Cr System, Critical Reviews in Solid State and Materials Sciences 35(2) (2010) 125-152.

[76] M. Pohl, O. Storz, T. Glogowski, Effect of intermetallic precipitations on the properties of duplex stainless steel, Materials Characterization 58(1) (2007) 65-71.

[77] F. Danoix, P. Auger, Atom Probe Studies of the Fe–Cr System and Stainless Steels Aged at Intermediate Temperature: A Review, Materials Characterization 44(1) (2000) 177-201.

[78] Zhao, S.J. Zinkle, A. Bhattacharya, Alpha-prime precipitate formation in ion irradiated Fe14Cr and Fe18Cr alloys Fusion Materials Semiannual Progress Reports 66 (2019) 3.

[79] C. Pareige, V. Kuksenko, P. Pareige, Behaviour of P, Si, Ni impurities and Cr in self ion irradiated Fe–Cr alloys – Comparison to neutron irradiation, Journal of Nuclear Materials 456 (2015) 471-476.

[80] Z. Jiao, V. Shankar, G.S. Was, Phase stability in proton and heavy ion irradiated ferritic–martensitic alloys, Journal of Nuclear Materials 419(1) (2011) 52-62.

[81] O. Tissot, C. Pareige, E. Meslin, B. Décamps, J. Henry, Influence of injected interstitials on α' precipitation in Fe – Cr alloys under self-ion irradiation, Materials Research Letters 5(2) (2017) 117-123.

[82] Y. Zhao, S.J. Zinkle, A. Bhattacharya, ALPHA-PRIME PRECIPITATE FORMATION IN ION IRRADIATED Fe14Cr
AND Fe18Cr ALLOYS, Fusion Materials Semiannual Progress Reports 66 (2019) 3.

[83] J. Coze Le, Final report on model alloy preparation, EFDA - Contract 06 - 1901 TW6 - TTMS
007- PUREFE., ARMINE: Ecole Nationale Supérieure des Mines de Saint Etienne, 2007.

[84] L. Tan, L.L. Snead, Y. Katoh, Development of new generation reduced activation ferritic-martensitic steels for advanced fusion reactors, Journal of Nuclear Materials 478 (2016) 42-49.

[85] L. Tan, J.D. Poplawsky, Y. Yang, Effects of niobium and tantalum on the microstructure and strength of ferritic-martensitic steels, Materials Science and Engineering: A 807 (2021) 140900.

[86] M.K. Miller, K.F. Russell, D.T. Hoelzer, Characterization of precipitates in MA/ODS ferritic alloys, Journal of Nuclear Materials 351(1) (2006) 261-268.

[87] Z. Yan, T. Yang, Y. Lin, Y. Lu, Y. Su, S.J. Zinkle, Y. Wang, Effects of temperature on helium bubble behaviour in Fe–9Cr alloy, Journal of Nuclear Materials 532 (2020) 152045.

[88] S. Taller, D. Woodley, E. Getto, A.M. Monterrosa, Z. Jiao, O. Toader, F. Naab, T. Kubley, S. Dwaraknath, G.S. Was, Multiple ion beam irradiation for the study of radiation damage in materials, Nuclear Instruments and Methods in Physics Research Section B: Beam Interactions with Materials and Atoms 412 (2017) 1-10.

[89] G.S. Was, S. Taller, Z. Jiao, A.M. Monterrosa, D. Woodley, D. Jennings, T. Kubley, F. Naab, O. Toader, E. Uberseder, Resolution of the carbon contamination problem in ion

irradiation experiments, Nuclear Instruments and Methods in Physics Research Section B: Beam Interactions with Materials and Atoms 412 (2017) 58-65.

[90] P.J. Doyle, K.M. Benensky, S.J. Zinkle, Modeling the impact of radiation-enhanced diffusion on implanted ion profiles, Journal of Nuclear Materials 509 (2018) 168-180.

[91] R.C. Birtcher, M.A. Kirk, K. Furuya, G.R. Lumpkin, M.O. Ruault, In situ Transmission Electron Microscopy Investigation of Radiation Effects, Journal of Materials Research 20(7) (2005) 1654-1683.

[92] D.B. Williams, C.B. Carter, Transmission Electron Microscopy, Springer US2009.

[93] B. Yao, D. Edwards, R.J. Kurtz, TEM characterization of dislocation loops in irradiated bcc Fe-based steels, Journal of Nuclear Materials 434 (2013) 402–410.

[94] R. Schäublin, B. Décamps, A. Prokhodtseva, J.F. Löffler, On the origin of primary ½ a0 <111> and a0 <100> loops in irradiated Fe(Cr) alloys, Acta Materialia 133 (2017) 427-439.

[95] K. Arakawa, K. Ono, M. Isshiki, K. Mimura, M. Uchikoshi, H. Mori, Observation of the One-Dimensional Diffusion of Nanometer-Sized Dislocation Loops, Science 318(5852) (2007) 956.

[96] F.A. Garner, Impact of the injected interstitial on the correlation of charged particle and neutron-induced radiation damage, Journal of Nuclear Materials 117 (1983) 177-197.

[97] D.L. Plumton, W.G. Wolfer, Suppression of void nucleation by injected interstitials during heavy ion bombardment, Journal of Nuclear Materials 120(2) (1984) 245-253.

[98] J.F. Ziegler, M.D. Ziegler, J.P. Biersack, SRIM – The stopping and range of ions in matter (2010), Nuclear Instruments and Methods in Physics Research Section B: Beam Interactions with Materials and Atoms 268(11) (2010) 1818-1823.

[99] D. Brimbal, B. Décamps, A. Barbu, E. Meslin, J. Henry, Dual-beam irradiation of α-iron: Heterogeneous bubble formation on dislocation loops, Journal of Nuclear Materials 418(1) (2011) 313-315.

[100] D.S. Gelles, R.M. Claudson, L.E. Thomas, Quantitative analysis of void swelling, Fusion Reactor Materials Semiannual Progress Report DOE/ER-0313/3 (1987) 131-136.

[101] L.K. Mansur, W.A. Coghlan, Mechanisms of helium interaction with radiation effects in metals and alloys: A review, Journal of Nuclear Materials 119(1) (1983) 1-25.

[102] D.B. Williams, C.B. Carter, Low-Loss and No-Loss Spectra and Images, in: D.B. Williams, C.B. Carter (Eds.), Transmission Electron Microscopy: A Textbook for Materials Science, Springer US, Boston, MA, 2009, pp. 699-713.

[103] S.J. Zinkle, A Brief Review of Radiation-Induced Cavity Swelling and Hardening in Copper and Copper Alloys, in: R.E. Stoller, A.S. Kumar, D.S. Gelles (Eds.), ASTM International, West Conshohocken, PA, 1992, pp. 813-834.

[104] L.L. Horton, J. Bentley, W.A. Jesser, The microstructure of "triple-beam" ion irradiated Fe and Fe-Cr alloys, Journal of Nuclear Materials 104 (1981) 1085-1089.

[105] E. Kuramoto, N. Yoshida, N. Tsukuda, K. Kitajima, N.H. Packan, M.B. Lewis, L.K. Mansur, Simulation irradiation studies on iron, Journal of Nuclear Materials 104 (1981) 1091-1095.

[106] M. Roldán, P. Fernández, R. Vila, A. Gómez-Herrero, F.J. Sánchez, The effect of triple ion beam irradiation on cavity formation on pure EFDA iron, Journal of Nuclear Materials 479 (2016) 100-111.

[107] B. Kaiser, C. Dethloff, E. Gaganidze, D. Brimbal, M. Payet, P. Trocellier, L. Beck, J. Aktaa, TEM study and modeling of bubble formation in dual-beam He+/Fe3+ ion irradiated EUROFER97, Journal of Nuclear Materials 484 (2017) 59-67.

[108] B.H. Sencer, F.A. Garner, Compositional and temperature dependence of void swelling in model Fe–Cr base alloys irradiated in the EBR-II fast reactor, Journal of Nuclear Materials 283-287 (2000) 164-168.

[109] Y.E. Kupriiyanova, V.V. Bryk, O.V. Borodin, A.S. Kalchenko, V.N. Voyevodin, G.D. Tolstolutskaya, F.A. Garner, Use of double and triple-ion irradiation to study the influence of high levels of helium and hydrogen on void swelling of 8–12% Cr ferritic-martensitic steels, Journal of Nuclear Materials 468 (2016) 264-273.

[110] A.M. Monterrosa, Z. Jiao, G.S. Was, The influence of helium on cavity evolution in ion-irradiated T91, Journal of Nuclear Materials 509 (2018) 707-721.

[111] L.L. Horton, L.K. Mansur, Experimental Determination of the Critical Cavity Radius in Fe-10Cr for Ion Irradiation, in: F.A. Garner, J.S. Perrin (Eds.), ASTM International, West Conshohocken, PA, 1985, pp. 344-362.

[112] Y.-R. Lin, L.-G. Chen, C.-Y. Hsieh, A. Hu, S.-C. Lo, F.-R. Chen, J.-J. Kai, Atomic structure of nano voids in irradiated 3C-SiC, Journal of Nuclear Materials 498 (2018) 71-75.

[113] Y.R. Lin, L.G. Chen, C.Y. Hsieh, M.T. Chang, K.Y. Fung, A. Hu, S.C. Lo, F.R. Chen, J.J. Kai, Atomic Configuration of Point Defect Clusters in Ion-Irradiated Silicon Carbide, Scientific Reports 7(1) (2017) 14635.

[114] S. Van Aert, K.J. Batenburg, M.D. Rossell, R. Erni, G. Van Tendeloo, Three-dimensional atomic imaging of crystalline nanoparticles, Nature 470(7334) (2011) 374-377.

[115] K. Farrell, E.H. Lee, Ion bombardment damage in a modified Fe-9Cr-1Mo steel, 12th Int. Symp. on Effects of Radiation on Materials ASTM STP 870 (1985) 383-393.

[116] C.J. Baroch, Properties of Reactor Structural Alloys After Neutron or Particle Irradiation, ASTM International, West Conshohocken, PA, 1975.

[117] D. Costa, G. Adjanor, C.S. Becquart, P. Olsson, C. Domain, Vacancy migration energy dependence on local chemical environment in Fe–Cr alloys: A Density Functional Theory study, Journal of Nuclear Materials 452(1) (2014) 425-433.

[118] C.-C. Fu, J.D. Torre, F. Willaime, J.-L. Bocquet, A. Barbu, Multiscale modelling of defect kinetics in irradiated iron, Nature Materials 4(1) (2005) 68-74.

[119] S.L. Dudarev, Density Functional Theory Models for Radiation Damage, Annual Review of Materials Research 43(1) (2013) 35-61.

[120] W.G. Wolfer, 1.01 Fundamental Properties of Defects in Metals., in: R.J.M. Konings (Ed.), Comprehensive Nuclear Materials, Elsevier2012, pp. 1-45.

[121] E. Aydogan, E. Martinez, K. March, O. El-Atwani, D.L. Krumwiede, P. Hosemann, T. Saleh, S.A. Maloy, α' formation kinetics and radiation induced segregation in neutron irradiated 14YWT nanostructured ferritic alloys, Scientific Reports 9(1) (2019) 8345.

[122] A. Bhattacharya, S.J. Zinkle, 1.12 - Cavity Swelling in Irradiated Materials, in: R.J.M. Konings, R.E. Stoller (Eds.), Comprehensive Nuclear Materials (Second Edition), Elsevier, Oxford, 2020, pp. 406-455.

[123] N.I. Budylkin, E.G. Mironova, V.M. Chernov, V.A. Krasnoselov, S.I. Porollo, F.A. Garner, Neutron-induced swelling and embrittlement of pure iron and pure nickel irradiated in the BN-350 and BOR-60 fast reactors, Journal of Nuclear Materials 375(3) (2008) 359-364.

[124] V.K. Sikka, J. Moteff, Damage in neutron-irradiated molybdenum: (I). Characterization of as-irradiated microstructure, Journal of Nuclear Materials 54(2) (1974) 325-345.

[125] P. Olsson, T.P.C. Klaver, C. Domain, Ab initio study of solute transition-metal interactions with point defects in bcc Fe, Physical Review B 81(5) (2010) 054102.

[126] L.K. Mansur, Correlation of neutron and heavy-ion damage: II. The predicted temperature shift if swelling with changes in radiation dose rate, Journal of Nuclear Materials 78(1) (1978) 156-160.

[127] B.C. Masters, Dislocation loops in irradiated iron, The Philosophical Magazine: A Journal of Theoretical Experimental and Applied Physics 11(113) (1965) 881-893.

[128] J. Marian, B.D. Wirth, J.M. Perlado, Mechanism of Formation and Growth of <100> Interstitial Loops in Ferritic Materials, Physical Review Letters 88(25) (2002) 255507.

[129] M.L. Jenkins, Z. Yao, M. Hernández-Mayoral, M.A. Kirk, Dynamic observations of heavy-ion damage in Fe and Fe–Cr alloys, Journal of Nuclear Materials 389(2) (2009) 197-202.

[130] Y.-R. Lin, A. Bhattacharya, D. Chen, J.-J. Kai, J. Henry, S.J. Zinkle, Temperature-dependent cavity swelling in dual-ion irradiated Fe and Fe-Cr alloys, Acta Materialia submitted (2020).

[131] K. Arakawa, T. Amino, H. Mori, Direct observation of the coalescence process between nanoscale dislocation loops with different Burgers vectors, Acta Materialia 59(1) (2011) 141-145.

[132] D. Brimbal, B. Décamps, J. Henry, E. Meslin, A. Barbu, Single- and dual-beam in situ irradiations of high-purity iron in a transmission electron microscope: Effects of heavy ion irradiation and helium injection, Acta Materialia 64 (2014) 391-401.

[133] N. Gao, Z.W. Yao, G.H. Lu, H.Q. Deng, F. Gao, Mechanisms for <100> interstitial dislocation loops to diffuse in BCC iron, Nature Communications 12(1) (2021) 225.

[134] J.C. Haley, F. Liu, E. Tarleton, A.C.F. Cocks, G.R. Odette, S. Lozano-Perez, S.G. Roberts, Helical dislocations: Observation of vacancy defect bias of screw dislocations in neutron irradiated Fe–9Cr, Acta Materialia 181 (2019) 173-184.

[135] M.A. Kirk, P.M. Baldo, A.C.Y. Liu, E.A. Ryan, R.C. Birtcher, Z. Yao, S. Xu, M.L. Jenkins, M. Hernandez-Mayoral, D. Kaoumi, A.T. Motta, In situ transmission electron microscopy and ion irradiation of ferritic materials, Microscopy Research and Technique 72(3) (2009) 182-186.

[136] S.J. Zinkle, 1.03 - Radiation-Induced Effects on Microstructure, in: R.J.M. Konings (Ed.), Comprehensive Nuclear Materials, Elsevier, Oxford, 2012, pp. 65-98.

[137] E.A. Little, R. Bullough, M.H. Wood, W.C. Marshall, On the swelling resistance of ferritic steel, Proceedings of the Royal Society of London. A. Mathematical and Physical Sciences 372(1751) (1980) 565-579.

[138] Y.-R. Lin, W.-Y. Chen, M. Li, J. Henry, S.J. Zinkle, Dynamic observation of dual-beam irradiated Fe and Fe-10Cr alloys at 435 °C, Acta Materialia 209 (2021) 116793.

[139] O. El-Atwani, J.A. Hinks, G. Greaves, S. Gonderman, T. Qiu, M. Efe, J.P. Allain, In-situ TEM observation of the response of ultrafine- and nanocrystalline-grained tungsten to extreme irradiation environments, Scientific Reports 4(1) (2014) 4716.

[140] E. Aydogan, O. El-Atwani, M. Li, S.A. Maloy, In-situ observation of nano-oxide and defect evolution in 14YWT alloys, Materials Characterization 170 (2020) 110686.

[141] R. Bullough, M.R. Hayns, M.H. Wood, Sink strengths for thin film surfaces and grain boundaries, Journal of Nuclear Materials 90(1) (1980) 44-59.

[142] P. Dauben, R.P. Wahi, H. Wollenberger, Bubble nucleation and growth in an Fe-12 at% Cr ferritic alloy under He+ implantation and Fe+ irradiation, Journal of Nuclear Materials 141-143 (1986) 723-726.

[143] K. Ono, K. Arakawa, H. Shibasaki, H. Kurata, I. Nakamichi, N. Yoshida, Release of helium from irradiation damage in Fe–9Cr ferritic alloy, Journal of Nuclear Materials 329-333 (2004) 933-937.

[144] H. Schroeder, P.F.P. Fichtner, On the coarsening mechanisms of helium bubbles — Ostwald ripening versus migration and coalescence, Journal of Nuclear Materials 179-181 (1991) 1007-1010.

[145] H. Trinkaus, B.N. Singh, Helium accumulation in metals during irradiation – where do we stand?, Journal of Nuclear Materials 323(2) (2003) 229-242.

[146] X. Hu, D. Xu, B.D. Wirth, Quantifying He-point defect interactions in Fe through coordinated experimental and modeling studies of He-ion implanted single-crystal Fe, Journal of Nuclear Materials 442(1, Supplement 1) (2013) S649-S654.

[147] N.L. Peterson, Grain-boundary diffusion in metals, International Metals Reviews 28(1) (1983) 65-91.

[148] B.N. Singh, A.J.E. Foreman, Some limitations of simulation studies using the ppm to dpa ratio as the helium generation rate, Journal of Nuclear Materials 179-181 (1991) 990-993.

[149] P.L. Lane, P.J. Goodhew, Helium bubble nucleation at grain boundaries, Philosophical Magazine A 48(6) (1983) 965-986.

[150] P.D. Edmondson, C.M. Parish, Q. Li, M.K. Miller, Thermal stability of nanoscale helium bubbles in a 14YWT nanostructured ferritic alloy, Journal of Nuclear Materials 445(1) (2014) 84-90.

[151] C. Lu, Z. Lu, X. Wang, R. Xie, Z. Li, M. Higgins, C. Liu, F. Gao, L. Wang, Enhanced Radiation-tolerant Oxide Dispersion Strengthened Steel and its Microstructure Evolution under Helium-implantation and Heavy-ion Irradiation, Scientific Reports 7(1) (2017) 40343.

[152] C.M. Parish, K.A. Unocic, L. Tan, S.J. Zinkle, S. Kondo, L.L. Snead, D.T. Hoelzer, Y. Katoh, Helium sequestration at nanoparticle-matrix interfaces in helium + heavy ion irradiated nanostructured ferritic alloys, Journal of Nuclear Materials 483 (2017) 21-34.

[153] D. Brimbal, L. Beck, O. Troeber, E. Gaganidze, P. Trocellier, J. Aktaa, R. Lindau, Microstructural characterization of Eurofer-97 and Eurofer-ODS steels before and after multi-beam ion irradiations at JANNUS Saclay facility, Journal of Nuclear Materials 465 (2015) 236-244.

[154] T. Yamamoto, G.R. Odette, P. Miao, D.T. Hoelzer, J. Bentley, N. Hashimoto, H. Tanigawa, R.J. Kurtz, The transport and fate of helium in nanostructured ferritic alloys at fusion relevant He/dpa ratios and dpa rates, Journal of Nuclear Materials 367-370 (2007) 399-410.

[155] T. Yamamoto, Y. Wu, G. Robert Odette, K. Yabuuchi, S. Kondo, A. Kimura, A dual ion irradiation study of helium–dpa interactions on cavity evolution in tempered martensitic steels and nanostructured ferritic alloys, Journal of Nuclear Materials 449(1) (2014) 190-199.

[156] P.D. Edmondson, C.M. Parish, Y. Zhang, A. Hallén, M.K. Miller, Helium bubble distributions in a nanostructured ferritic alloy, Journal of Nuclear Materials 434(1) (2013) 210-216.

[157] L.K. Mansur, E.H. Lee, Theoretical basis for unified analysis of experimental data and design of swelling-resistant alloys, Journal of Nuclear Materials 179-181 (1991) 105-110.

[158] T. Stan, Y. Wu, J. Ciston, T. Yamamoto, G.R. Odette, Characterization of polyhedral nano-oxides and helium bubbles in an annealed nanostructured ferritic alloy, Acta Materialia 183 (2020) 484-492.

[159] D. Terentyev, N. Juslin, K. Nordlund, N. Sandberg, Fast three dimensional migration of He clusters in bcc Fe and Fe–Cr alloys, Journal of Applied Physics 105(10) (2009) 103509.

[160] M.L. Jenkins, C.A. English, B.L. Eyre, Heavy-ion irradiation of α-iron, Philosophical Magazine A 38(1) (1978) 97-114.

[161] M.A. Kirk, I.M. Robertson, M.L. Jenkins, C.A. English, T.J. Black, J.S. Vetrano, The collapse of defect cascades to dislocation loops, Journal of Nuclear Materials 149(1) (1987) 21-28.

[162] R.E. Stoller, The role of cascade energy and temperature in primary defect formation in iron, Journal of Nuclear Materials 276(1) (2000) 22-32.

[163] D.J. Bacon, Y.N. Osetsky, R. Stoller, R.E. Voskoboinikov, MD description of damage production in displacement cascades in copper and α-iron, Journal of Nuclear Materials 323(2) (2003) 152-162.

[164] J. Chen, F. Duval, P. Jung, R. Schäublin, N. Gao, M.F. Barthe, Dislocation loops in ultra-high purity Fe(Cr) alloys after 7.2 MeV proton irradiation, Journal of Nuclear Materials 503 (2018) 81-90.

[165] W.-Y. Chen, Irradiation damage in neutron-irradiated Fe-Cr model alloys, Nuclear, Plasma, & Rad Engr, University of Illinois at Urbana-Champaign, 2014.

[166] W.-Y. Chen, Y. Miao, J. Gan, M.A. Okuniewski, S.A. Maloy, J.F. Stubbins, Neutron irradiation effects in Fe and Fe-Cr at 300 °C, Acta Materialia 111 (2016) 407-416.

[167] K.L. Wong, J.H. Shim, B.D. Wirth, Molecular dynamics simulations of point defect interactions in Fe–Cr alloys, Journal of Nuclear Materials 367-370 (2007) 276-281.

[168] N. Yoshida, M. Kiritani, Point Defect Clusters in Electron-Irradiated Gold, Journal of the Physical Society of Japan 35(5) (1973) 1418-1429.

[169] M.L. Jenkins, Characterisation of radiation-damage microstructures by TEM, Journal of Nuclear Materials 216 (1994) 124-156.

[170] M.J. Aliaga, R. Schäublin, J.F. Löffler, M.J. Caturla, Surface-induced vacancy loops and damage dispersion in irradiated Fe thin films, Acta Materialia 101 (2015) 22-30.

[171] A. Bhattacharya, E. Meslin, J. Henry, B. Décamps, A. Barbu, Dramatic reduction of void swelling by helium in ion-irradiated high purity α-iron, Materials Research Letters 6(7) (2018) 372-377.

[172] E.R. Reese, N. Almirall, T. Yamamoto, S. Tumey, G. Robert Odette, E.A. Marquis, Dose rate dependence of Cr precipitation in an ion-irradiated Fe18Cr alloy, Scripta Materialia 146 (2018) 213-217.

[173] M.J. Konstantinović, A. Ulbricht, T. Brodziansky, N. Castin, L. Malerba, Vacancy-solute clustering in Fe–Cr alloys after neutron irradiation, Journal of Nuclear Materials 540 (2020) 152341.

[174] A. Kohyama, G. Ayrault, N. Igata, Microstructural evolution in dual-ion irradiated 316ss under various helium injection schedules, Journal of Nuclear Materials 122(1) (1984) 224-229.

[175] K. Farrell, Experimental effects of helium on cavity formation during irradiation—a review, Radiation Effects 53(3-4) (1980) 175-194.

[176] K. Farrell, P.J. Maziasz, E.H. Lee, L.K. Mansur, Modification of radiation damage microstructure by helium, Radiation Effects 78(1-4) (1983) 277-295.

[177] A. Hishinuma, L.K. Mansur, Critical radius for bias-driven swelling — a further analysis and its application to bimodal cavity size distributions, Journal of Nuclear Materials 118(1) (1983) 91-99.

[178] S.J. Zinkle, W.G. Wolfer, G.L. Kulcinski, L.E. Seitzman, II. Effect of oxygen and helium on void formation in metals, Philosophical Magazine A 55(1) (1987) 127-140.

[179] A. Bhattacharya, J. Henry, B. Décamps, S.J. Zinkle, E. Meslin, Helium causing disappearance of a/2<111> dislocation loops in binary Fe-Cr ferritic alloys, Journal of Nuclear Materials 556 (2021) 153213.

[180] R.E. Stoller, The influence of helium on microstructural evolution: Implications for DT fusion reactors, Journal of Nuclear Materials 174(2) (1990) 289-310.

[181] Y. Katoh, Y. Kohno, A. Kohyama, Dual-ion irradiation effects on microstructure of austenitic alloys, Journal of Nuclear Materials 205 (1993) 354-360.

[182] E.H. Lee, L.K. Mansur, Unified theoretical analysis of experimental swelling data for irradiated austenitic and ferritic/martensitic alloys, Metallurgical Transactions A 21(5) (1990) 1021-1035.

Appendix

A. Supplemental Information for Chapter 5.1

1. SEM and EDS analysis of pre-irradiated material

To check the sample preparation quality, SEM images (Fig. A.1.) with Bruker ARGUS FSE/BSE imaging system were taken by a Zeiss EVO MA15 for fast characterization. The colored SEM images applying the e-flash detector are usually used for preview of regions of interest for EBSD (Electron backscatter diffraction) analysis. However, the image quality is sufficiently good for a quick check of the microstructural homogeneity and mean grain size of each material. EDS (Energy dispersive x-ray spectroscopy) element analysis was conducted after ion irradiation to confirm that the 30 samples were not mixed up during irradiation. The mean grain size and element composition result of the high purity Fe-Cr alloys agree with the material processing report. Lath structures with grain size <1 μm were observed in the Fe-10Cr-C material. These structures are in accordance with martensite characteristic features that could form in steels due to supersaturated carbon. The main solute compositions of the Eurofer97 material (without ODS) detected via SEM-EDS were Cr (8.95 wt%), W (1.04 wt%), Mn (0.55 wt%), V (0.20 wt%), and C (0.1 wt%). The measured mean grain size was ~10 μm.

2. Secondary Ion Mass Spectrometry (SIMS) measurement

The SIMS measurements were conducted by Eurofins EAG Materials Science company using a Cameca IMS 6F. A Cs^+ beam was used as a sputter beam scanned on an area ~200 x 200 μm^2, and the detecting area was ~30-60 μm diameter. The data spacing was ~15-20 nm up to a depth of 3 μm. Fig. A.2. shows depth profiling of the carbon and oxygen concentration as determined by SIMS in the unirradiated Fe, and the same Fe material irradiated at 470°C. It can be seen that significant carbon and oxygen contamination exists in the irradiated regions of the ion irradiated Fe specimen, despite the use of plasma cleaning and other recommended practices to minimize carbon contamination. At a depth of ~1 μm, the carbon and oxygen concentrations are ~1.2 at%

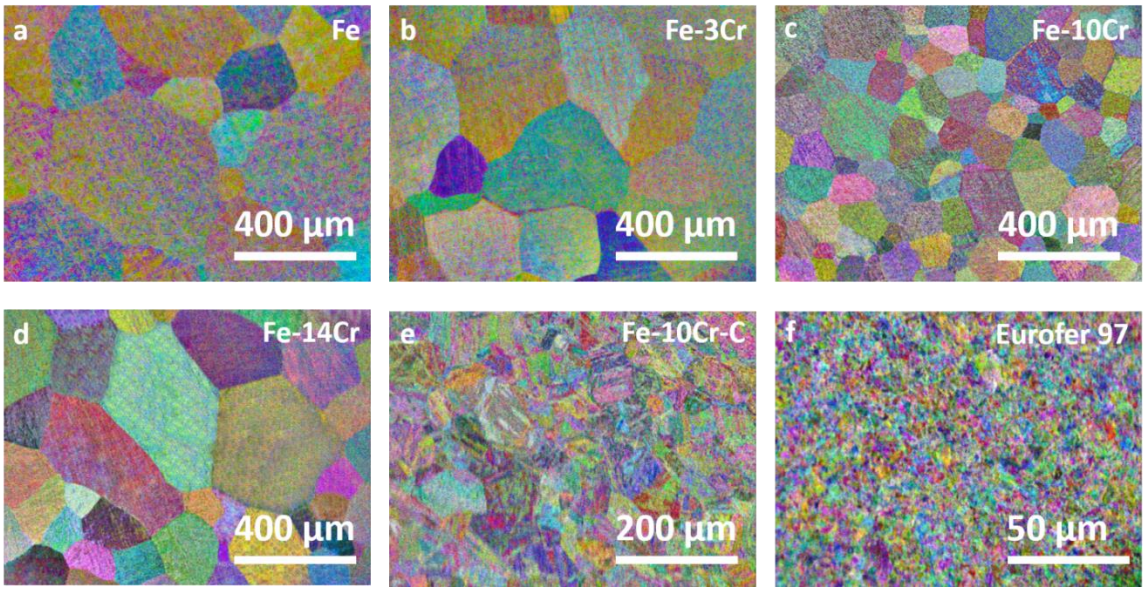

Fig. A.1. Colored SEM image of pre-irradiated (a) Fe, (b) Fe-3Cr, (c) Fe-10Cr, (d) Fe-14Cr, (e) Fe-10Cr-C, and (f) Eurofer97 materials.

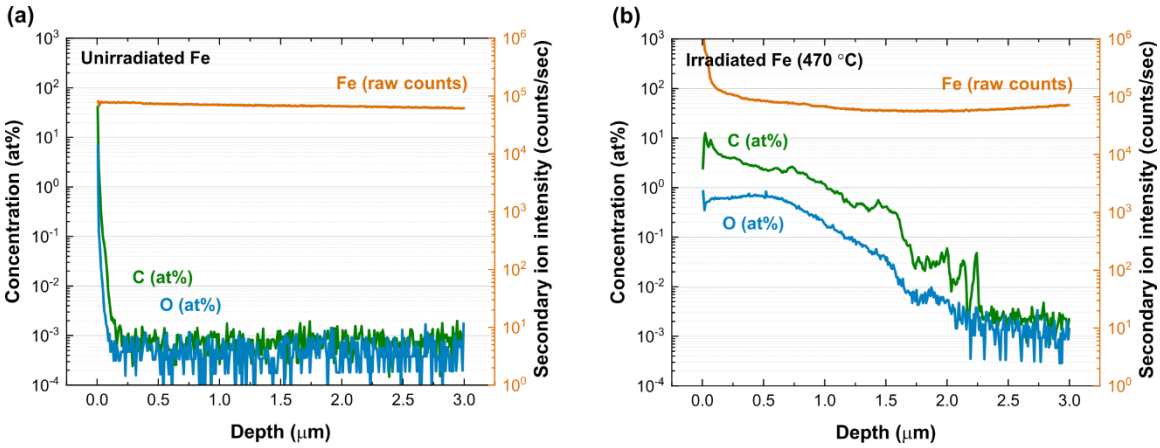

Fig. A.2. SIMS measured depth profile of carbon and oxygen concentration in (a) unirradiated Fe and (b) Fe irradiated at 470 °C.

and 0.2 at%, respectively, which are two to three orders of magnitude higher than the nominal value of 10^{-3} at% in the unirradiated pure Fe.

3. Irradiation temperature control

For each set of irradiations, 4 thermocouple wires were welded on four of the samples (outside the area of interest). At 400-550°C, an IR thermal imager that collects the infrared radiation from objects was first calibrated by the thermocouple signal before the temperature was increased and held stable for the irradiation. During the irradiation, each sample was set up with three AOI (area of interest) spots for temperature reading by the thermal imager. As shown in Fig. A.3, the standard deviation of the continuously recorded temperatures during each irradiation exhibited good stability, with a relatively low deviation of ~±5-10°C over the entire irradiation period.

4. Dislocation loops and dislocation networks

To investigate the possible interconnection between the depth-dependent evolution of dislocation loops and the formation of cavities, the dislocation loops in Fe-10Cr at 470°C were characterized by STEM bright-field images along [100] zone-axis (Fig. A.4). With increasing depth below the surface, within the depth interval 400-1750 nm, the dislocation loop density increased, and dislocation networks were observed at deeper regions beyond ~1000nm. Based on simple geometric considerations, Yao et al. noted that along the [100] zone axis, a/2 ⟨111⟩ loops would exhibit elliptical shape and a⟨100⟩ loops would be either plan-view (circular) or edge-on orientation under S/TEM. Following this geometric guideline, we found that the loops in Fe-10Cr at 470°C were mainly a⟨100⟩ loops (indicated by orange arrows in Fig. A.4b). Only a few a/2 ⟨111⟩ loops (<10%) were observed (indicated by blue arrows in Fig. A.4b). In addition, we also examined the Q value which is the ratio of dislocation sink strength to void sink strength. The calculated Q values were 3.2, 2.5, and 7.9 with increasing depth for the three depth intervals. The maximum observed swelling in the three intervals was S=0.28% at 750-1350 nm with a Q value of 2.5. The

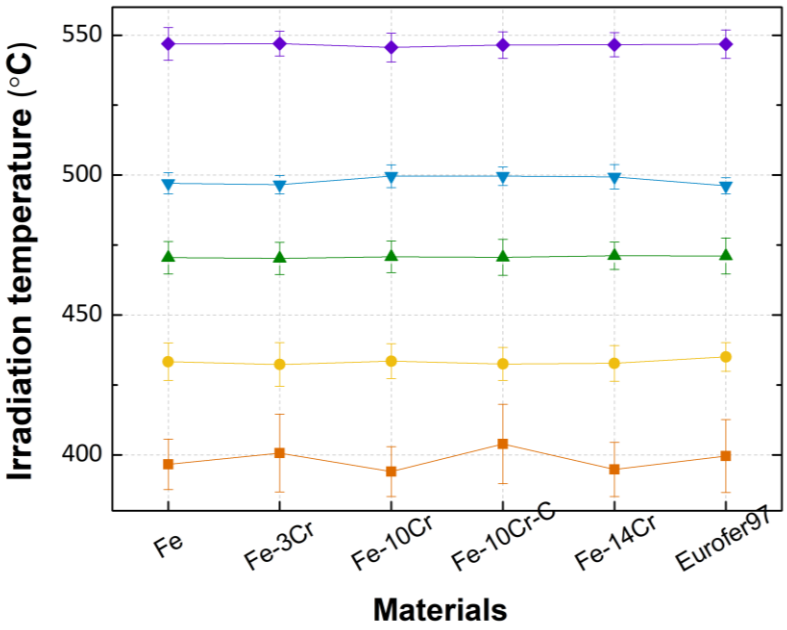

Fig. A.3. Average temperature on each sample measured by the thermal imager.

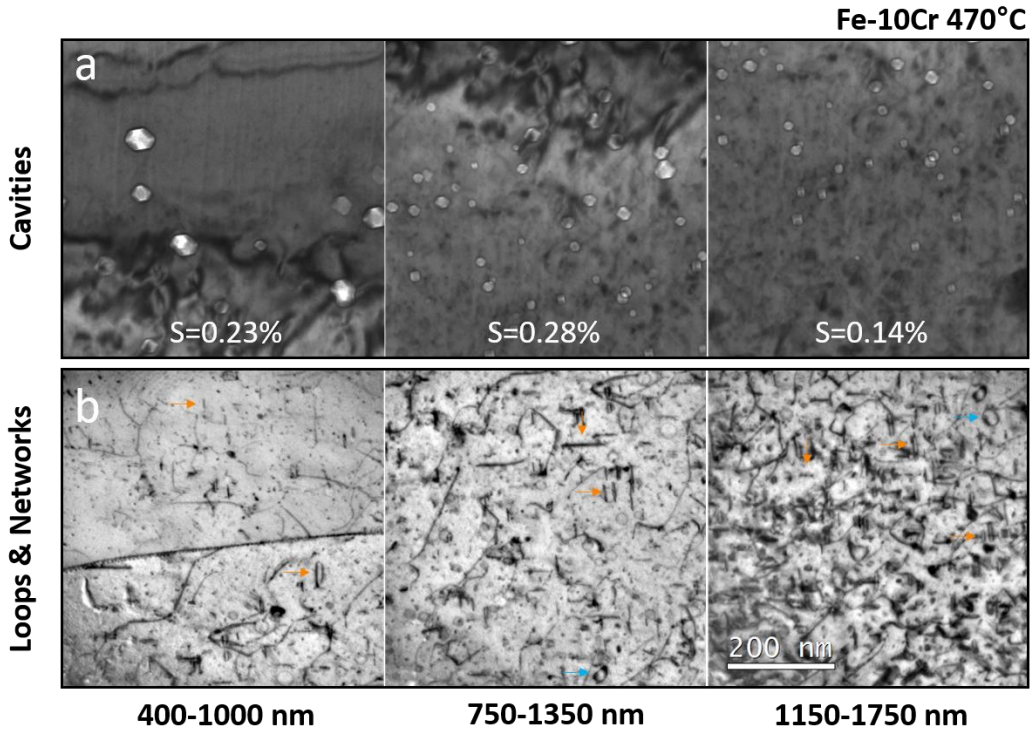

Fig. A.4. Microstructures observed in irradiated Fe-10Cr at 470 (a) Cavities (b) Dislocation loops and dislocation networks. The dislocation images were taken along [100] zone-axis.

swelling behavior agrees with the general trend that maximum swelling should occur at Q~1. A comparison of the depth distribution of the cavities, dislocation loops (or dislocation networks), and Ni profile are summarized in Fig. A.5.

5. Vacancy migration energy estimation

The vacancy migration energy estimation from denuded zones and relation to peak swelling temperature, and temperature shift values are summarized in Table. A.1.

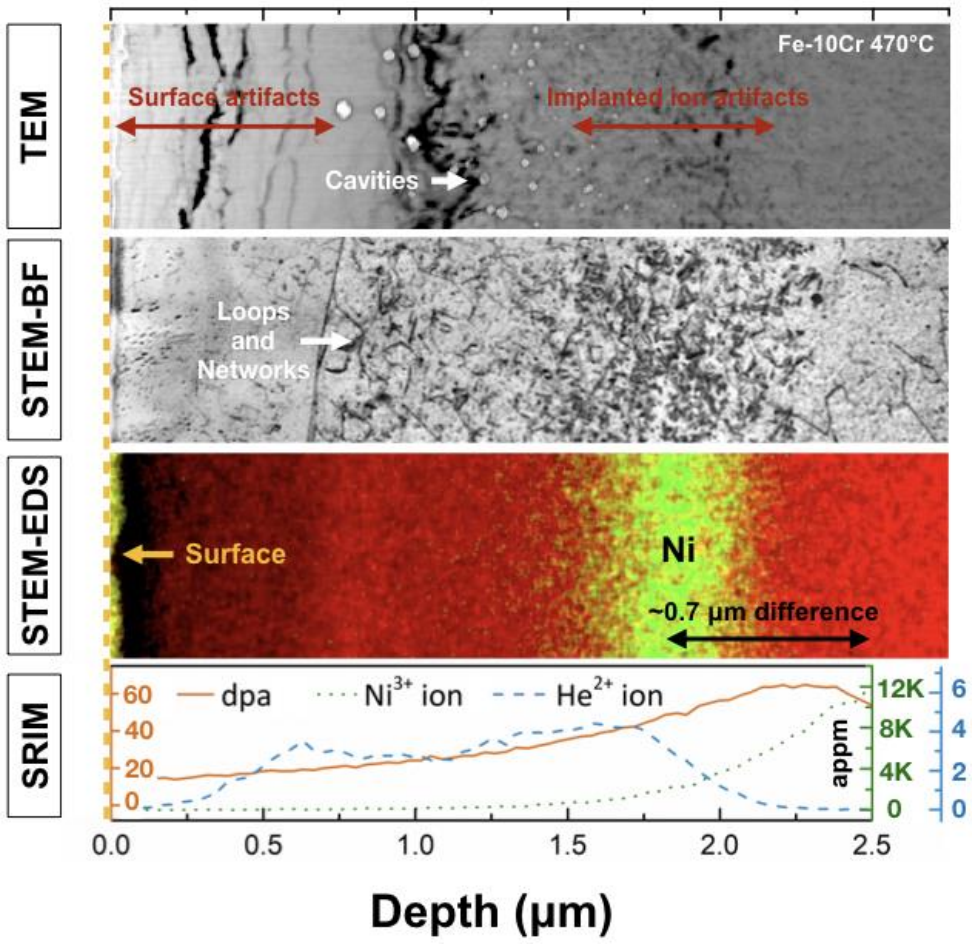

Fig. A.5. Depth distribution of (a) cavities, (b) dislocation loops and network dislocations in irradiated Fe-10Cr at 470 °C, (c) STEM-EDS mapping of implanted Ni profile, and (d) SRIM simulation. The dislocation images were taken along [100] zone-axis.

Table A.1 Mono-vacancy migration energy and peak swelling temperature shift of Fe, Fe-10Cr, and Fe-14Cr alloys. The value in the bracket is the recently reported E_m (0.67 eV) of Fe.

Material	Vacancy migration energy, E_m (eV)		Peak swelling temperature shift (°C)		
	This study	DFT study	Experimental temperature difference	Using rate theory estimation	Using DFT values
Fe	0.96 ± 0.33	0.71 (0.67)	54	61 ± 10	64
Fe-10Cr	1.22 ± 0.61	0.43	78	67 ± 17	74
Fe-14Cr	1.31 ± 0.82	0.51	73	65 ± 21	74

B. Supplemental Information for Chapter 5.2

1. Irradiation temperature and stage pressure

The dual ion beam irradiation experiments were done in beamline the MBC (multi beam Chamber) at MIBL. The thermal imaging system was calibrated prior to the start of the irradiation. Three AOIs were set per sample to measure the sample temperature with the thermal imager. Plasma Cleaner was used to clean the chamber for 2 hours, and cold trap was used during the experiment to eliminate contaminates. An overview of the average temperature and average stage pressure is summarized in Fig. B.1. Five irradiation temperatures were chosen between 400-550°C. The fluctuation of continuously recorded temperatures during each irradiation remained stable, with a relatively low deviation below 10°C (over the entire irradiation period). The average stage pressure of each irradiation was between 1×10^{-8} to 5×10^{-7} torr, as shown by the color heat-map of the stage pressure in Fig. B.1.

2. Energy degrader for multiple ion beam irradiation

For the dual-beam irradiation experiments at MIBL, a tiltable aluminum foil was used to degrade the 3.55 MeV He ion beam to provide the desired depth-dependent He implantation in the ion irradiated midrange region. By a programmable stepper motor (rotating in 0.01° increments), the ratable aluminum foil (6.2 μm thick) could rotate from 0-60° degrees in either clockwise or counterclockwise during the irradiation.

As shown in Fig. B.2, with known injected ion energy, energy degrader (Al foil) thickness and rotation angle, the distance between the foil to the sample surface (26.04 cm for our case), and the irradiation area, the scatter factor and residual energy could be estimated by the SRIM output file “transmit.txt.” The scattering factor is the ratio of the sample irradiated region to the scattering area. The scattering factor counts for the flux of injected helium ions that can hit the sample surface after penetrating the Al foil, based on the divergence angle of the injected ion beam. Next step, with known residual energy and scattering factor for each rotation angle as well as the hold time (time spent at each angle), the depth profile of He concentration for each rotation angle could be simulated

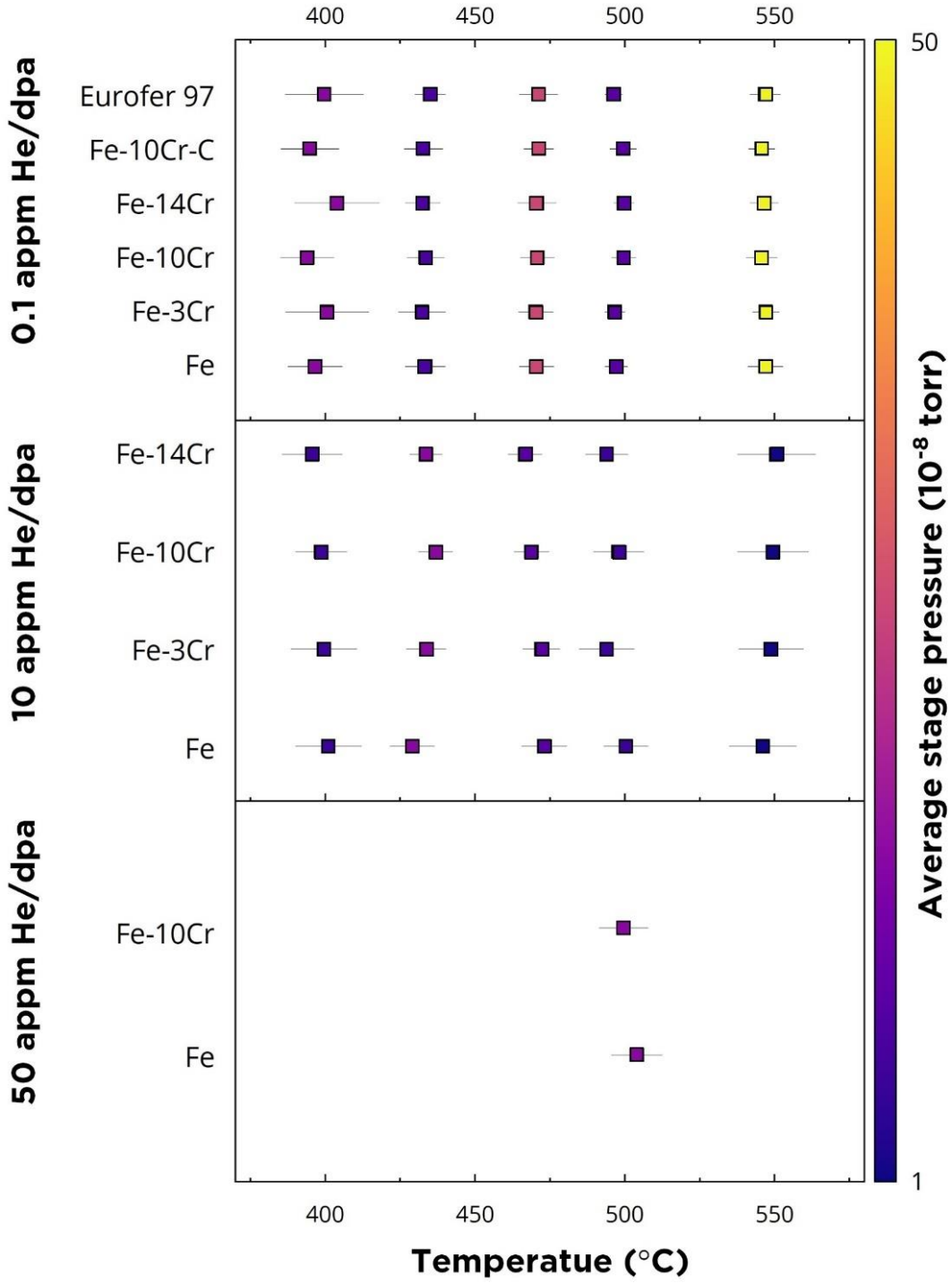

Fig. B.1. Average temperature and pressure of each irradiation condition.

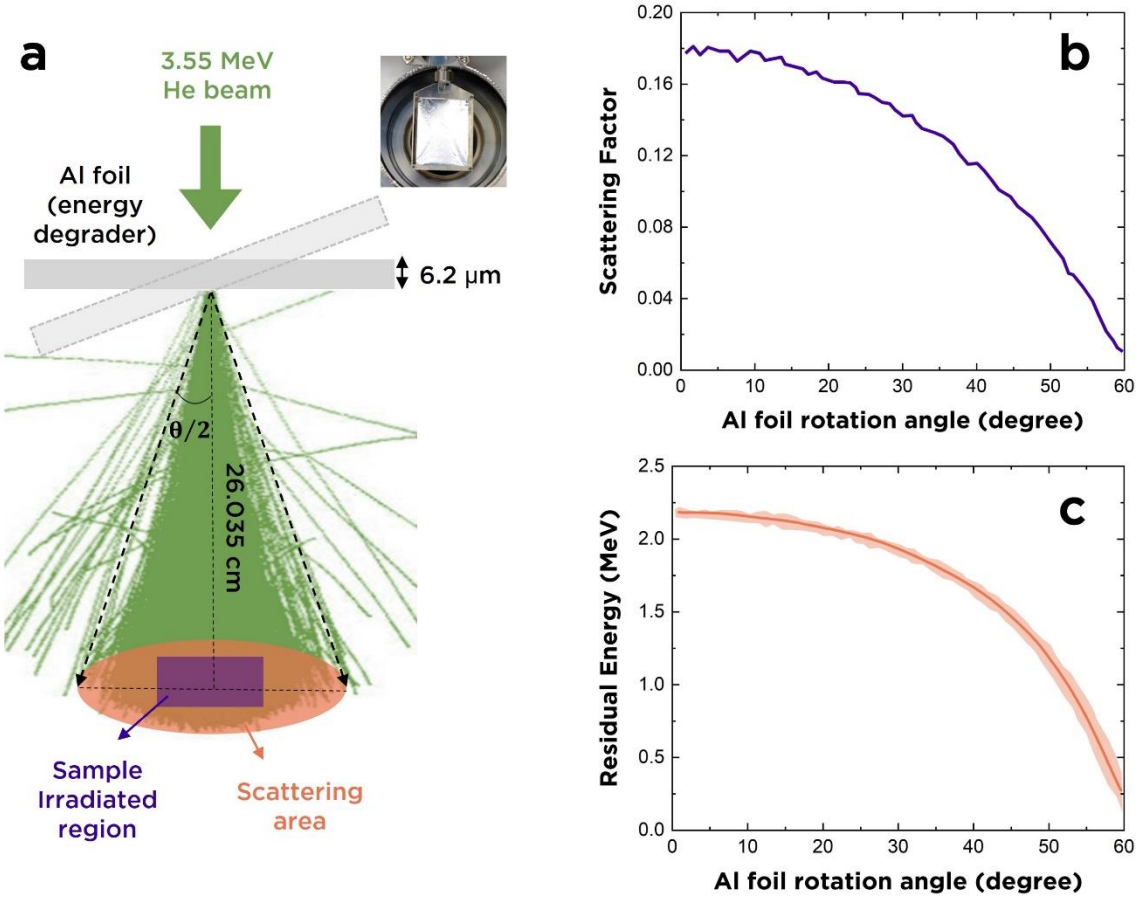

Fig. B.2. (a) Schematic diagram of the beam energy control by energy degrader at MIBL. (b) scattering factor and (c) residual energy as a function of the rotation angle.

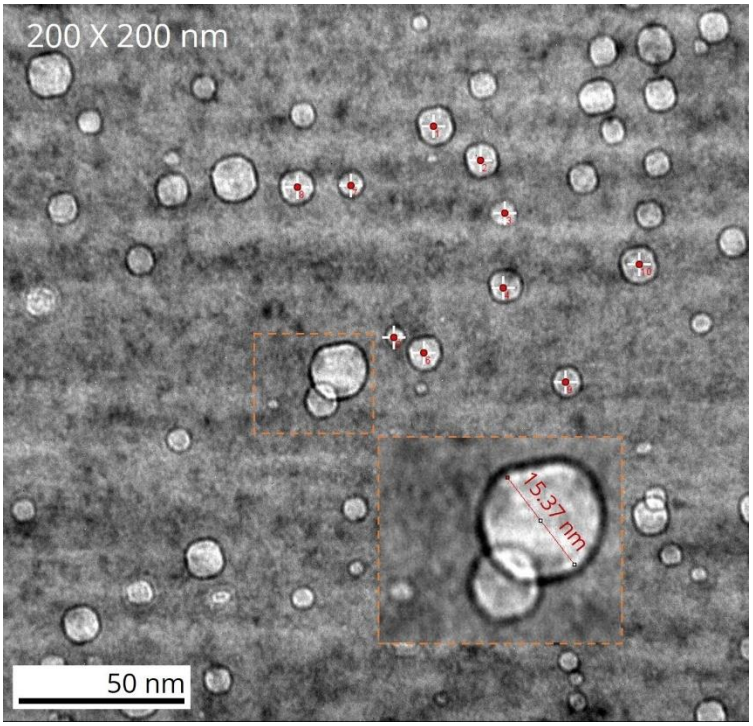

Fig. B.3. High magnification TEM image (100-200 kX) for cavity size and area density measurement

individually by SRIM. Finally, by summing up all He profiles with different combinations of rotation angles, the ultimate depth profile of He concentration can be manipulated.

3. Cavity size and density measurement

TEM magnifications of 100-200 kX were used for measuring the size of cavities that are assumed to be spherical. As shown in Fig. B.3, the inner diameter of cavities (excluding the border thickness) of each cavity was measure by ImageJ. The area density of cavities was also counted under high magnification TEM images to improve the visibility of small bubbles with a diameter ~2 nm.

As for the depth profile of cavity swelling, TEM images were cut into strips with a bin size of 250 nm. In order to obtain a continuous TEM image from the surface to the depth of ~3 μm, lower magnification (~8-15 kX) TEM images were used to calculate the cavity swelling (Fig. B.4). Under lower magnifications, some of the small bubbles with diameters below ~2 nm may not be observable or identified. However, the differences between the swelling values calculated under higher and low magnification images at the same depth are negatable for our case. As shown in Fig. B.5, EELS thickness mappings were conducted for each sample to evaluate the sample thickness at a specific depth. This would improve the accuracy of cavity density estimation when dividing the cavity areal density by the measured foil thickness. The overall thickness of the FIB samples in the midrange (depth of ~1 μm) is around 50-80 nm.

4. SRIM Profile Correction

The SRIM output results of the ion range and implanted peak center could be modified by changing the target density or correction factor. Based on the SRIM program, the compound correction approach separates out the stopping contributions from the binding electrons (bonds) from inner shell electrons (core), then alters the stopping for the bonding electrons based on the bonds found in the compound. As shown in Fig. B.6, increasing the target density or correction factor shifts the implanted ion profile toward the surface and narrows the width of the profile. In addition, the dpa profile would also be modified (as shown in Fig. B.7).

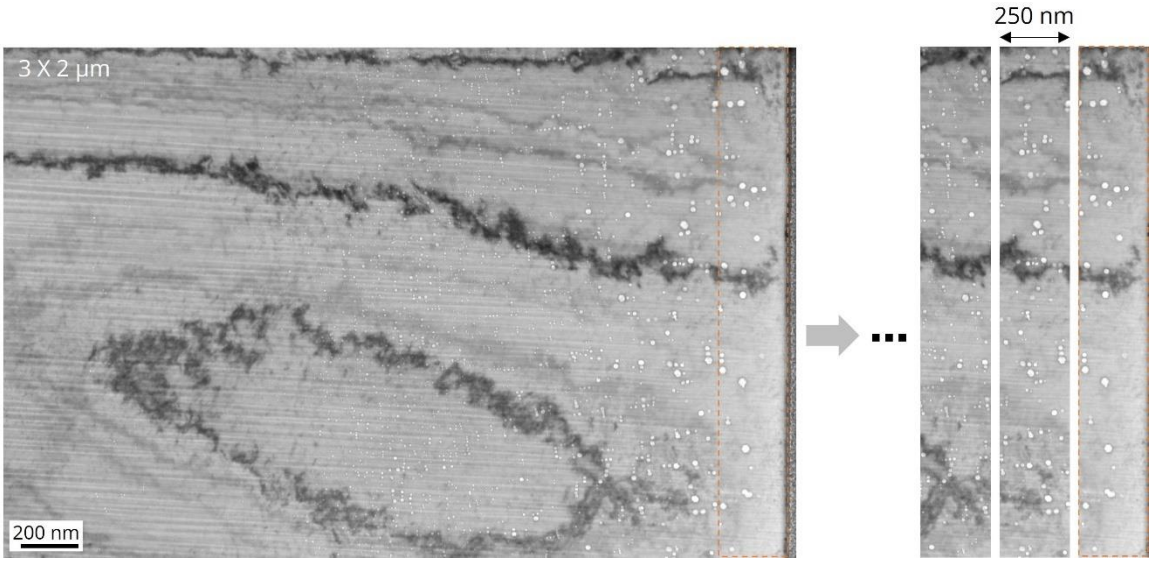

Fig. B.4 Low magnification TEM image (~8-15 kX) for depth distribution of cavity swelling evaluation.

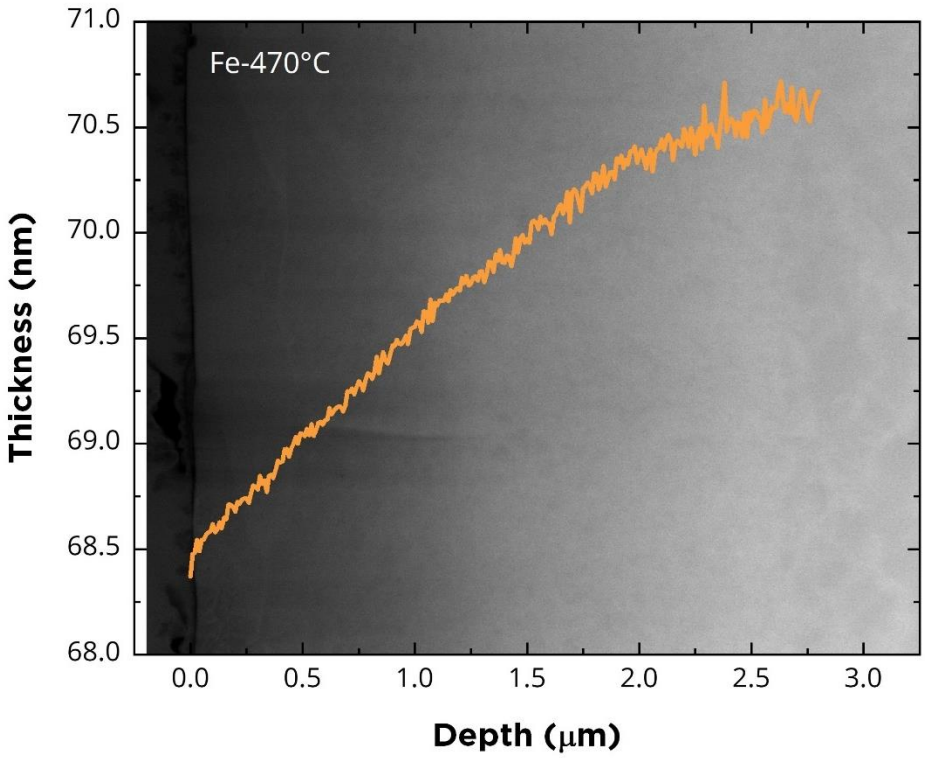

Fig. B.5 EELS thickness mapping of a dual-beam irradiated Fe sample superimposed on the STEM-ADF image of the investigated area.

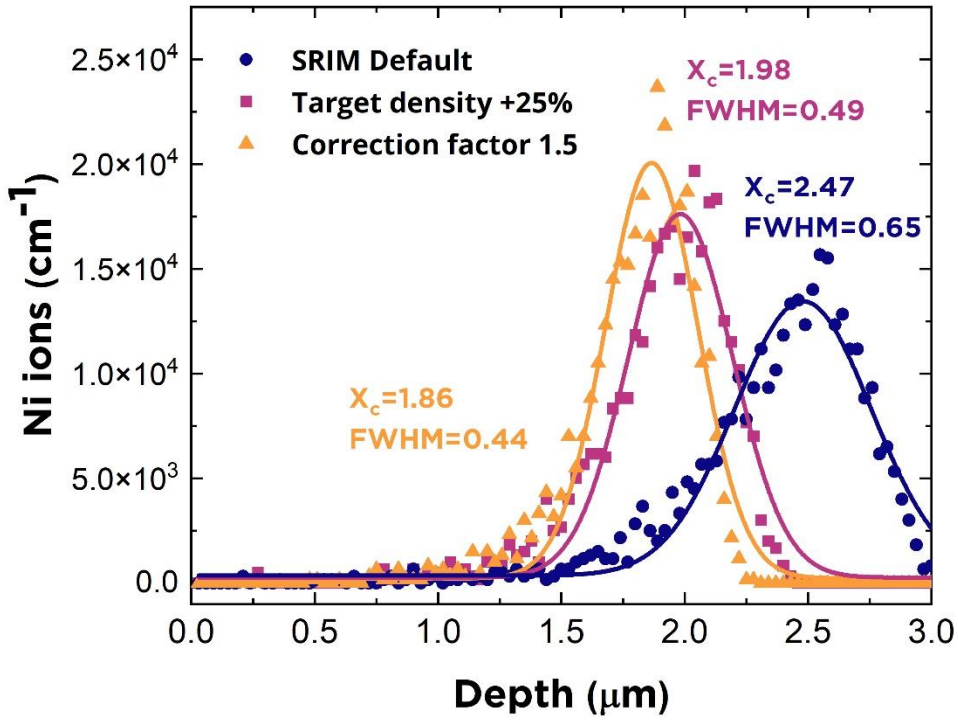

Fig. B.6 Demonstration of SRIM output profile with modified compound correction factor and target density

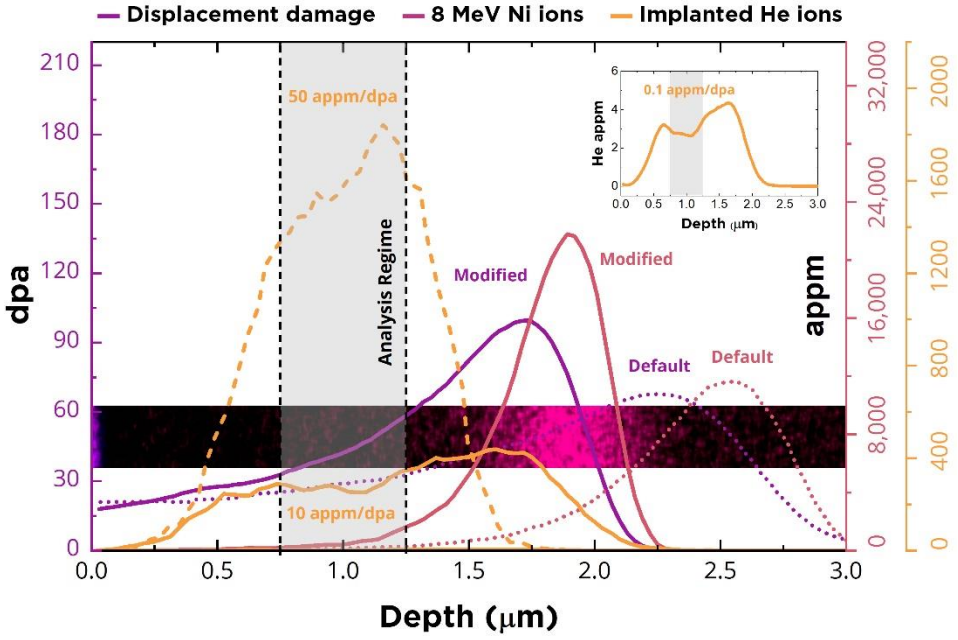

Fig. B.7 SRIM default and modified (with correction factor of 1.5) profiles of implanted ion concentration and dpa.

C. Supplemental Information for Chapter 5.3

1. Foil thickness measurement

The foil thickness of the irradiated post samples was determined by the log-ratio model of electron energy loss spectroscopy (EELS). Thickness fringes in DF images were used to measure the thickness of investigated areas that were slowly diminished (mostly due to surface diffusion of atoms from the very thin edge) during the high-temperature irradiation. The extinction distance (ζ) of the 110 reflection in Fe for 300 kV electron is approximately 35 nm. In Fig. C.1., the TEM image was taken before irradiation showing the increment of thickness from the top (sample edge) to bottom. The measured foil thickness at the same area given by the thickness fringe method and the EELS method were 122.5 nm and 127.8 nm, respectively (within an error of roughly 4 %).

2. In-situ TEM videos

The dynamic evolution of defects was recorded consistently using g=011 near a zone axis of [100] in both irradiated Fe and Fe-10Cr samples at 435°C. To investigate the formation of cavities, the image condition was set up to under-focused images (defocus value ~ -500 to -1000 nm). The original TEM video was collected simultaneously during the irradiation at 1 frame per second (fps). Irradiations were paused to re-align the electron beam condition at doses of 0.5, 1, 3, 5, 8.5, 10, 15, and 20 dpa. The accumulated irradiation time was around 5.5 hours for each sample. In the supplemental video files, the videos were speeded up 30 times with 30 fps. The real irradiation time and its corresponding damage level are indicated in the upper right corner of each video.

3. Irradiation conditions of the references

Table. C.1. summarizes the irradiation conditions (including irradiation species, dose, dose rate, temperature, etc.) of the references in Chapter 6.3 in the main text.

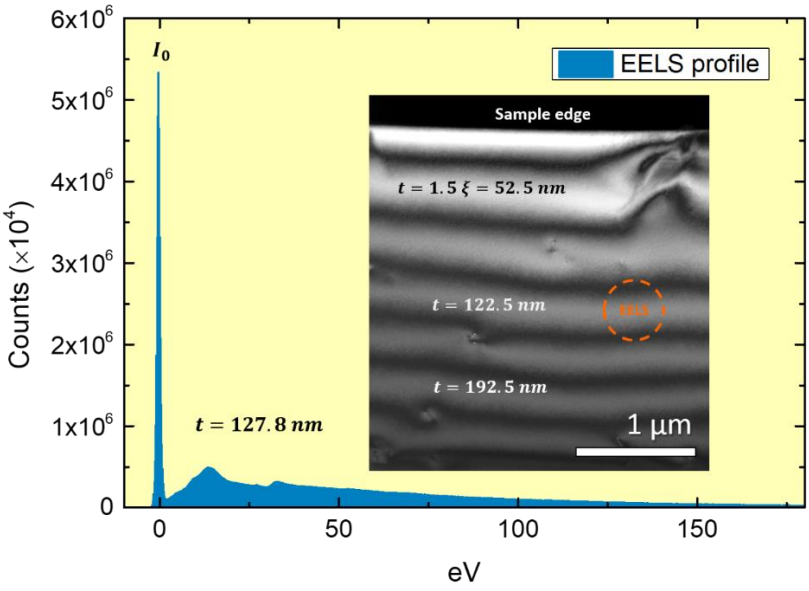

Fig. C.1. Foil thickness measurement: EELS profile was taken from the same marked area (orange, dashed line) on the embedded dark-field TEM image of the UHP Fe sample.

Table C.1. Irradiation conditions of the references

Material	Irradiated Temperature (°C)	Irradiation species	Dose (dpa & appm He/dpa)	Dose rate (dpa/s)	Notation
Fe (foil)	RT	500 KeV Fe + 10 KeV He	0.8 (900)	N/A	Prokhodtseva (2013)
Fe (bulk)	RT	24 MeV Fe + 2 MeV He	0.8 (900)	N/A	Prokhodtseva (2013)
Fe and Fe-Cr alloys (foil)	270-500	0-7.2 MeV protons	0.3	3.2×10^{-6}	Chen (2018)
Fe and Fe-8Cr (foil)	300	150 KeV Fe	0-13	2×10^{-4}	Hernandez (2008)
Fe (foil)	300-500	150 KeV Fe	0-13	N/A	Yao (2010)

Table C.1. continued

Fe (foil)	500	1 MeV Fe	0-0.8	3×10^{-4}	Brimbal (2014)
Fe (foil)	500	1MeV Fe + 15 KeV He	0-0.8 (670)	3×10^{-4}	Brimbal (2014)
Fe (bulk)	50-70	neutron (HFIR)	0.0001-0.79	7×10^{-7}	Zinkle (2006)
Fe (bulk)	80	neutron (PLUTO)	0.001-0.1	10^{-5}-10^{-7}	Robertson (1982)
Fe (bulk)	182-740	neutron (ORR)	~1	2×10^{-7}	Horton (1982)
Fe (bulk)	280	neutron (Magnox)	0.06	N/A	Nicol (2000)
Fe (bulk)	300	neutron (BR2)	0-0.19	$\sim7\times10^{-7}$	Hernandez (2010)
Fe and Fe-Cr alloys (bulk)	300-450	neutron (ATR)	0.01-1	$\sim2\times10^{-7}$	Chen (2014)
Fe and Fe-Cr alloys (bulk)	400	neutron (BR-10)	25.8	4×10^{-7}	Konobeev (2006)
Fe and Fe-Cr alloys (bulk)	400	neutron (BR-10)	5.5-7.1	1×10^{-7}	Porollo (1998)

D. Supplemental Information for Chapter 5.4

1. Material information

For the in-situ TEM study, TEM images were taken from electropolished samples. During the electropolishing process, pits may form due to etching effects. If left unchecked, these pits may be confused with radiation-induced cavities. Before irradiation, we confirmed that all of the investigated areas are pit-free. The chemical compositions of the materials are summarized in Table D.1. The chemical composition was measured by atom probe tomography (APT), inductively coupled plasma optical emission spectroscopy (ICP-OES), or glow discharge mass spectrometry.

2. Sample thickness measurement and denuded zone effect

The thickness of the sample was estimated by using the intensity of zero loss and plasma loss in EELS spectra. Figs. D.1 and D.2, show the EELS thickness mapping result, from the surface to the depth of 1.6 μm, of the ex-situ irradiated CNA3 and 14YWT samples prepared by FIB. Subtracting the Pt protection layer thickness of the highlighted yellow boxes in Figs. D.1b and D.2b, the cavity analysis regime was at the depth of 0.6-0.8 μm, corresponding to the sample thickness of 55 and 40 nm for CNA3 and 14YWT, respectively.

For the in-situ TEM study, the thickness of wedge-shaped electropolished TEM samples is generally thinnest near the perforated hole and thicker away from the hole. As shown in Fig. D.3, EELS thickness mappings were performed from the thin to thick areas. Due to the well-known surface effect in thin foil in-situ irradiations, we quantified the bubble density at each thickness area. At the relatively thin areas (near the perforated hole) the bubble density is lower. In Fig. D.3, the bubble density increases with increasing thickness until hitting a plateau at the thickness around 90 nm. While at the thicker areas (thickness > 90 nm), bubbles that are too small may not be observed under TEM images and result in a lower bubble density (Fig D.3c). Based on the thickness mapping result, we selected the areas with a thickness of 70-90 nm for bubble analysis of the in-situ study.

Table D.1. Compositions (wt%) with balance of iron of the F/M steels used in this study.

	Materials			
Element	Fe-9Cr	Fe-10Cr	CNA3	14YWT-SM10
Cr	8.95	10.10	8.6	13.190
C	0.0004	0.0004	0.1	0.065
Mn	0.6	--	1	0.06
Mo	0.2	--	--	0.002
N	--	0.0003	0.004	0.131
Nb	--	--	--	< 0.02
Ni	--	--	--	0.03
Si	0.22	--	0.15	0.04
Ta	--	--	0.1	--
Ti	--	--	0.15	0.24
V	0.12	--	0.1	< 0.002
W	0.3	--	1.3	1.94
Y	--	--	--	0.199

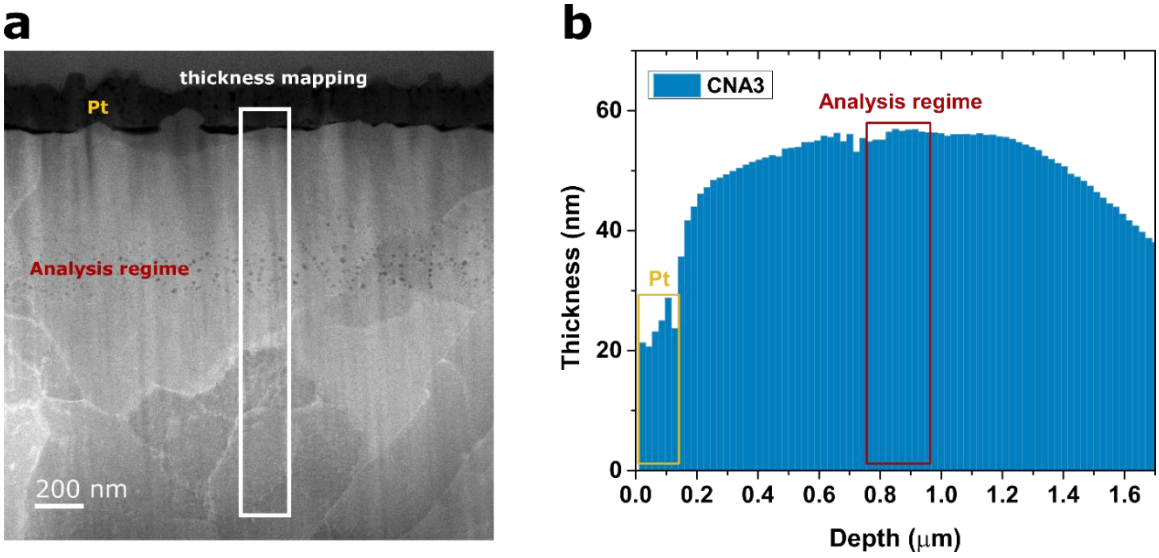

Fig. D.1. (a) STEM-ADF image of irradiated CNA3 at 700°C. (b) Thickness mapping result (as a function of depth) of the boxed area in Fig. a.

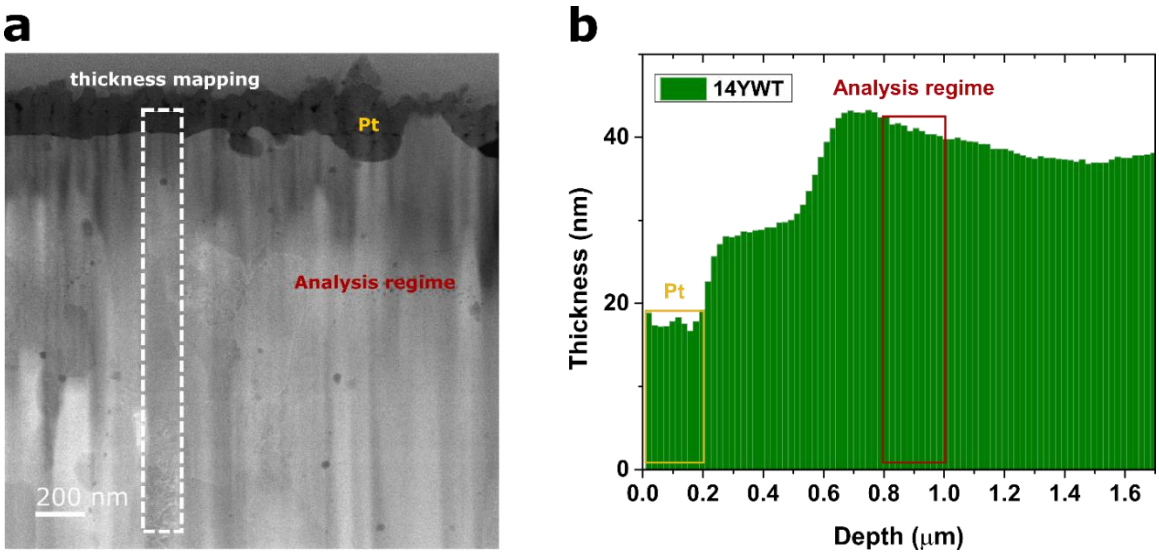

Fig. D.2. (a) STEM-ADF image of irradiated 14YWT at 700°C. (b) Thickness mapping result (as a function of depth) of the boxed area in Fig. a.

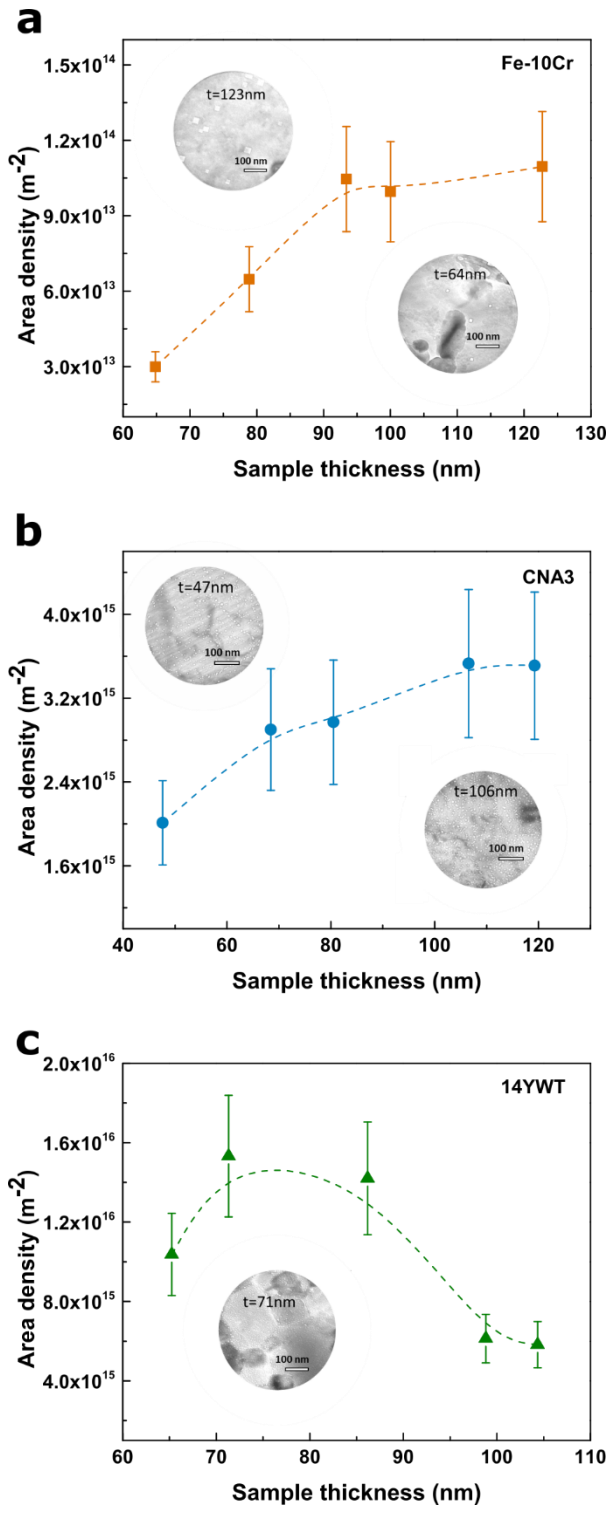

Fig. D.3. He bubble density as a function of sample thickness. (a) Fe-10Cr, (b) CNA3, and (c) 14YWT thin foils irradiated at 600°C and annealed at 900°C.

Table D.2. Grain boundary cavity denuded zone width of the in-situ irradiated thin foils measured under TEM images.

	Fe-10Cr	CNA3	14YWT
600°C	25±10 nm	13±2 nm	7±1 nm
900°C	31±9 nm	14±3 nm	9±4 nm

In addition, the slope of the plot of cavity areal density as a function of thickness (Fig. D3) provides a check whether there is a significant denuded zone effect, which would be visible as a y-intercept offset. From a rough estimate of Fig. D.3a, there might be ~57 nm denuded zone width (i.e., ~28 nm at each surface) for this 900°C implantation condition. However, the denuded zone width seems to be undetectable within experimental uncertainties for the nanostructured alloys in Figs. D.3b and D.3c. The denuded zone width estimated by Fig. D.3a is in agreement with the grain boundary denuded zone width of Fe-10Cr (Table D.2.) measured under TEM images. The possible surface denuded zone effect would be expected to be most pronounced at 900°C due to the high diffusivity at this temperature. In Fig. D.3, any deviation from a linear relationship of the areal density vs. thickness (ideally going through the origin) is an indication of either defect invisibility issues (curvature or plateau in areal density at higher thicknesses) or surface denuded zone issues (non-zero intercept), respectively.

From a rigorous perspective, the denuded zone thickness should be subtracted from the overall foil thickness in order to determine the "bulk" He bubble density without denuded zone effects. Considering the denuded zone thickness (double of the grain boundary denuded zone width in Table D.2.), for the 900°C Fe-10Cr specimens the effective sample thickness would decrease by a factor of 0.45, thereby increasing the bubble density by a factor of 2.2. For the nanostructured alloys, the increase is less significant. The corrected bubble density of CNA3 and 14YWT would increase by a factor of 1.38 and 1.25, respectively. This correction would not have any impact on the points discussed in the manuscript other than a small reduction in activation energy, an increase in the cavity swelling, and a decrease by a factor of ~0.7 in the value of L. Cross-sectional TEM study on the bubble distribution in thin foil irradiated samples would be useful to confirm the magnitude of the surface effect and denuded zone thickness for the He-filled cavities.

3. Fresnel-defocused bright-field TEM images

Fresnel fringes in TEM are produced by the interference of electrons scattered from the edge of the specimen with the incident electron beam. Likewise, Fresnel fringes would also appear around the He bubbles (or cavity) in irradiated materials, when electron beam scattered from the edge of the bubbles. As shown in Fig. D.4, for under-focused images (negative defocus value, $\Delta f < 0$), the bubbles generally appear as white dots surrounded by a dark fringe, while for over-focused images ($\Delta f > 0$), fringe contrast is reversed. When the TEM image is in-focus ($\Delta f = 0$), the bubble is almost invisible (no significant contrast). In Fig. D.4, the under- and over-focused images were taken at $\Delta f = -3\ \mu m$ and $\Delta f = +3\ \mu m$, respectively. Figs. D5-4 shows other low magnification TEM images.

4. Vacancy concentration & cavity growth rate

When neglecting the vacancy migration entropy and hydrostatic pressure terms, the thermal equilibrium vacancy concentration is approximately:

$$C_v^{eq} = \exp\left(\frac{-E_v^f}{kT}\right)$$

where E_v^f is the vacancy formation energy (~1.6 eV for iron), k is the Boltzmann constant, and T is the temperature. In addition, the vacancy diffusivity D_V is given by:

$$D_v = D_0\ exp\left(\frac{-E_v^m}{kT}\right)$$

where E_v^m is the vacancy migration energy (~0.6 eV for iron) and $D_0 = \alpha {a_0}^2 \upsilon$ is a temperature-independent term. Here, α is related to the crystal structure (1 for vacancy diffusion in bcc structure), a_0 is the lattice constant (~2.87 Å for bcc iron), and υ is the Debye frequency (~10^{13} s^{-1}). For recombination-dominant conditions with low or intermediate sink strength the corresponding steady-state vacancy concentration can be estimated by:

$$C_v = (K_0 K_{is}/K_{iv}K_{vs})^{1/2}$$

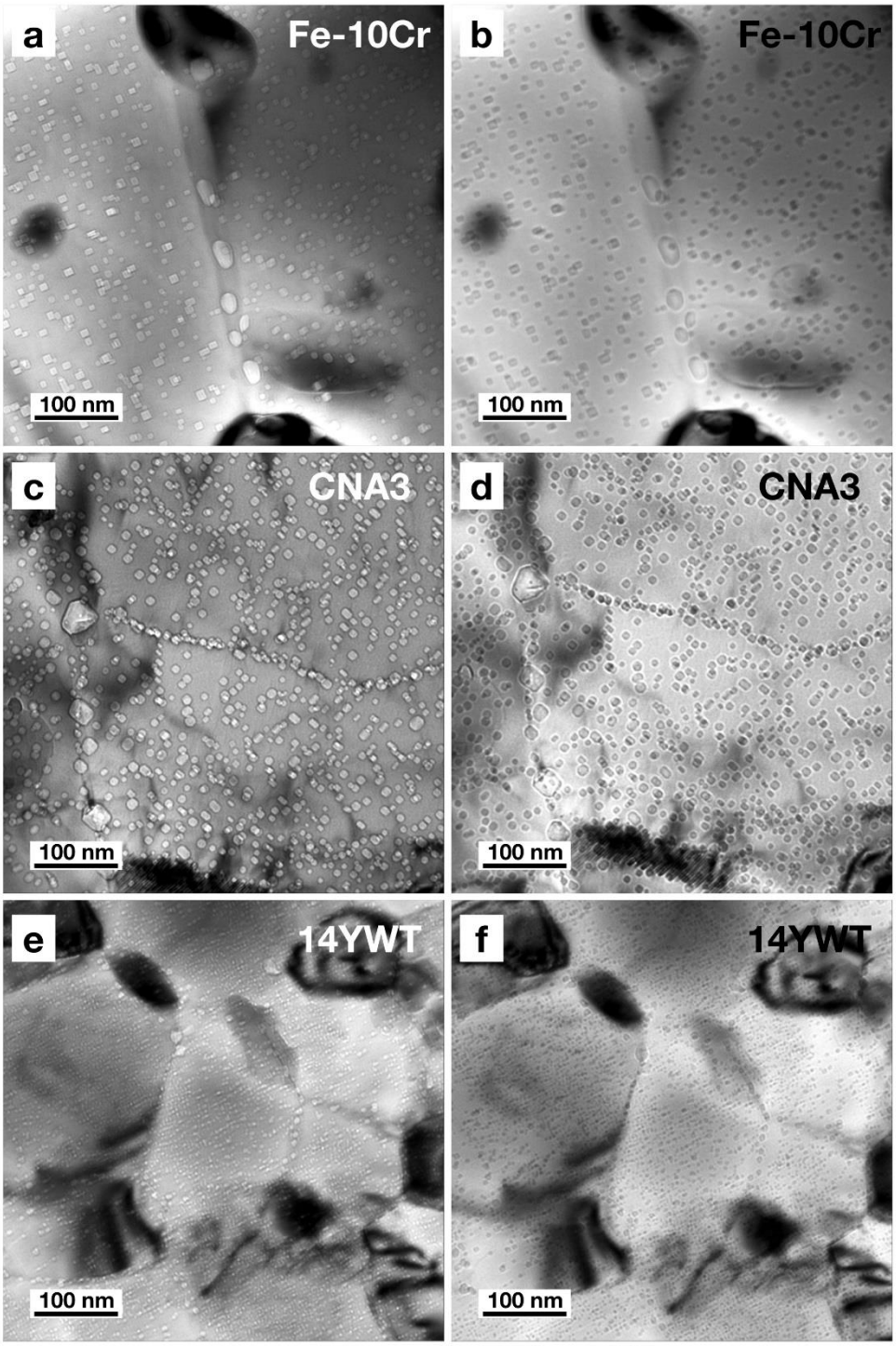

Fig. D.4. Under-focused (a, c, e) and over-focused (b, d, e) TEM images of He bubbles in Fe-10Cr, CNA3, and 14YWT.

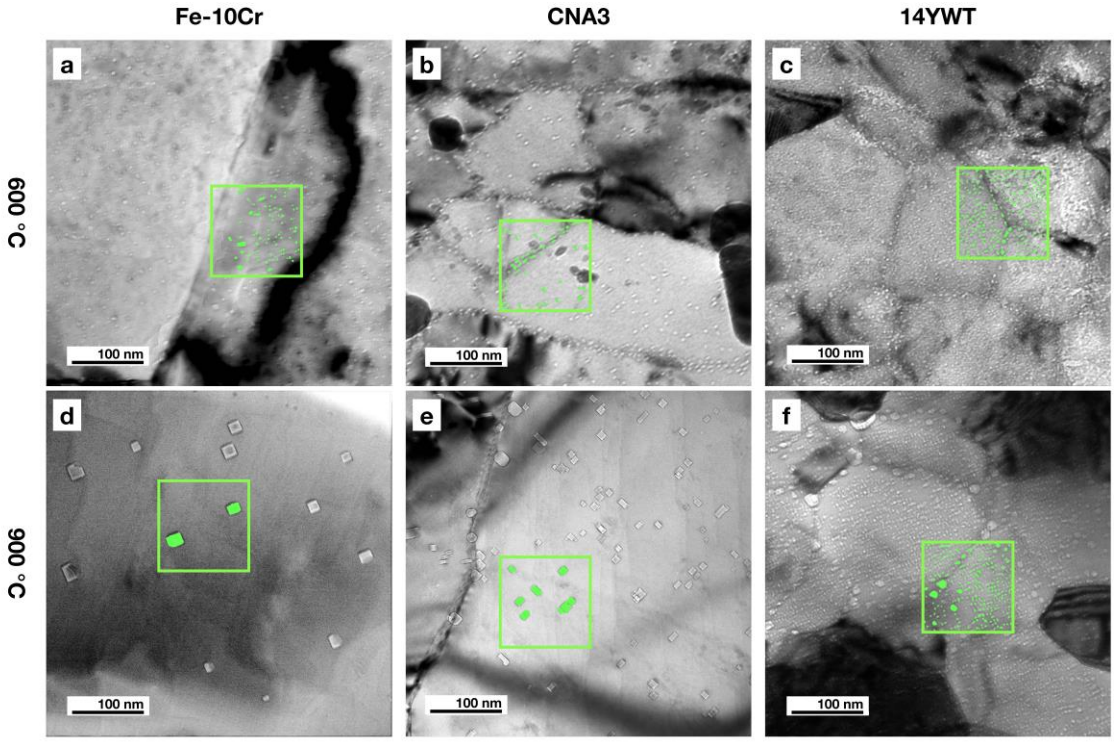

Fig. D.5. Defocused TEM images of bubbles in in-situ He implanted Fe-10Cr and NFA thin foils at 600°C (a-c) and 900°C (d-f).

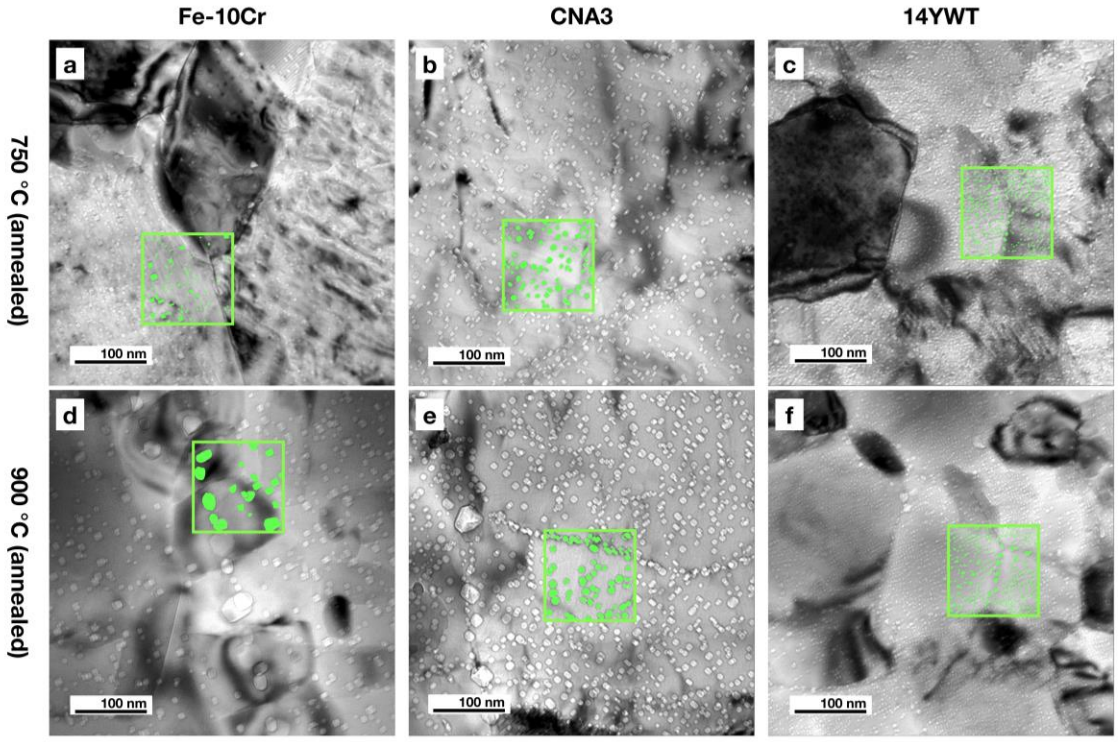

Fig. D.6. Defocused TEM images of bubbles in post-irradiation annealed Fe-10Cr and NFA thin foils at 750°C (a-c) and 900°C (d-f).

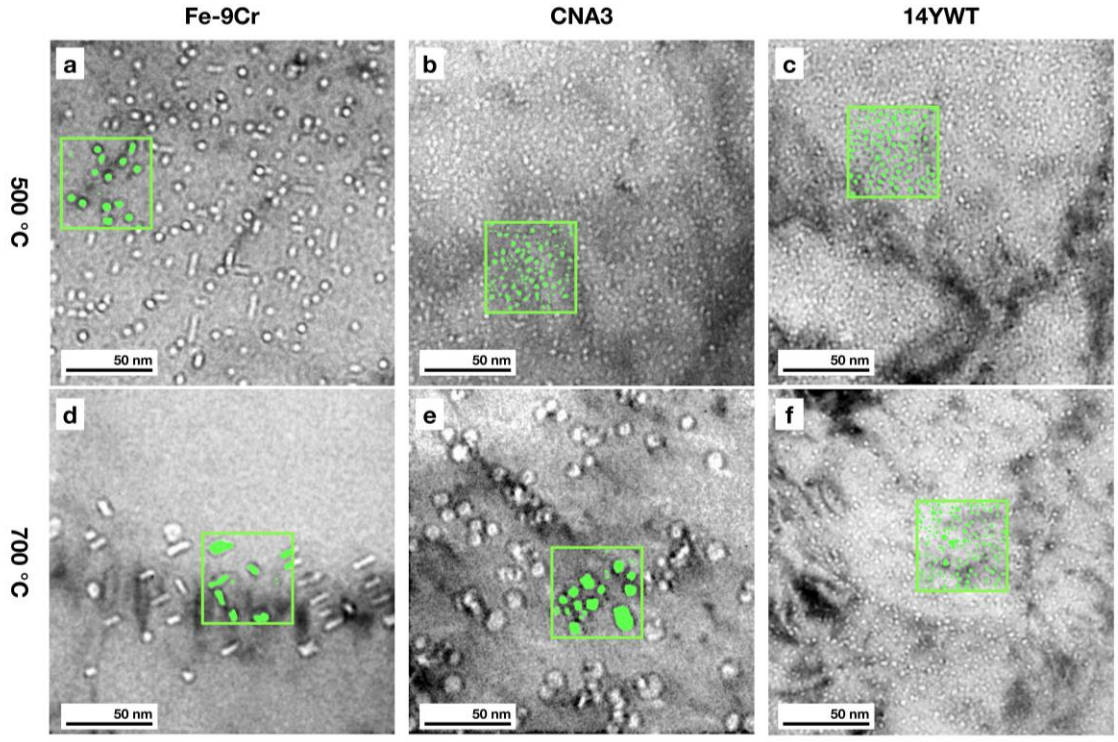

Fig. D.7. Defocused TEM images of bubbles in He implanted bulk Fe-9Cr and NFAs at 500 and 700°C

where K_0 is the defect production rate (~1×10^{-4} dpa/s for our in-situ irradiation), K_{is} is the interstitial-sink reaction rate coefficient, K_{iv} is the vacancy-interstitial recombination rate coefficient, K_{vs} is the vacancy-sink reaction rate coefficient. Assuming $D_i \gg D_v$, then

$$C_v = (K_0\Omega/4\pi r_{vs}D_v)^{1/2}$$

where $\Omega = {a_0}^3/2$ for bcc structures, and $r_{vs} \approx 10a_0$.

For high temperature sink dominant conditions, the steady state vacancy concentration may transition to the value of

$$C_v = K_0/K_{vs}C_s$$

where the sink concentration $C_s = S/4\pi r_{vs}$, and S is the sink strength. At this condition, the time constant τ_3 is

$$\tau_3 = (K_{vs}C_s)^{-1}$$

Based on the equations listed above, Fig. D.8. shows the steady-state and thermal vacancy concentration as a function of temperature in Fe. At temperatures near or above 750°C, the steady-state vacancy population produced by ion bombardment is comparable to the thermal-equilibrium vacancy concentration. The calculated time constant τ_3 ~ 10^{-8} s using the microstructure information indicates that the final steady state should have been achieved during the 900 s irradiations.

Besides, a cavity with gas can grow by absorbing vacancies to reduce the pressure. The radial growth rate of cavities is

$$dR/dt = (\Omega/R)\left[D_v\left(C_v - C_v^{eq}e^{y}\right) - D_iC_i\right]$$

where R is the cavity radius, $y = [(2\gamma/R) - p]\,\Omega/kT$, γ is the surface energy, and p is the gas pressure in the cavity ($p = 3mkT/4\pi R^3$ for ideal gas). For the post-irradiation annealing conditions, in the absence of irradiation, the vacancy concentration C_v rapidly approaches the thermal equilibrium value C_v^{eq}. At such condition, we assume $C_v = C_v^{eq}$. The calculated cavity growth rates for the two annealing conditions are ~10^{-3} nm/s.

5. Sink strength

The estimated sink strength for different microstructural features in the materials used in the study is summarized in Table D.3. The grain size, dislocation density, particle density, and particle size are extracted from previous studies.

6. STEM EELS and imaging condition

The beam convergence angle was 15 mrad and the collection angle at the entrance of the EELS spectrometer was 27 mrad. A dispersion of 0.5 eV/channel was employed. With a camera length of 8 cm, the HAADF detector was set to collect electrons scattered between 68 and 280 mrad, the LAADF detector was set to collect electrons scattered between 30 and 120 mrad, and the ABF detector was set to collect electrons scattered between 17 and 34 mrad.

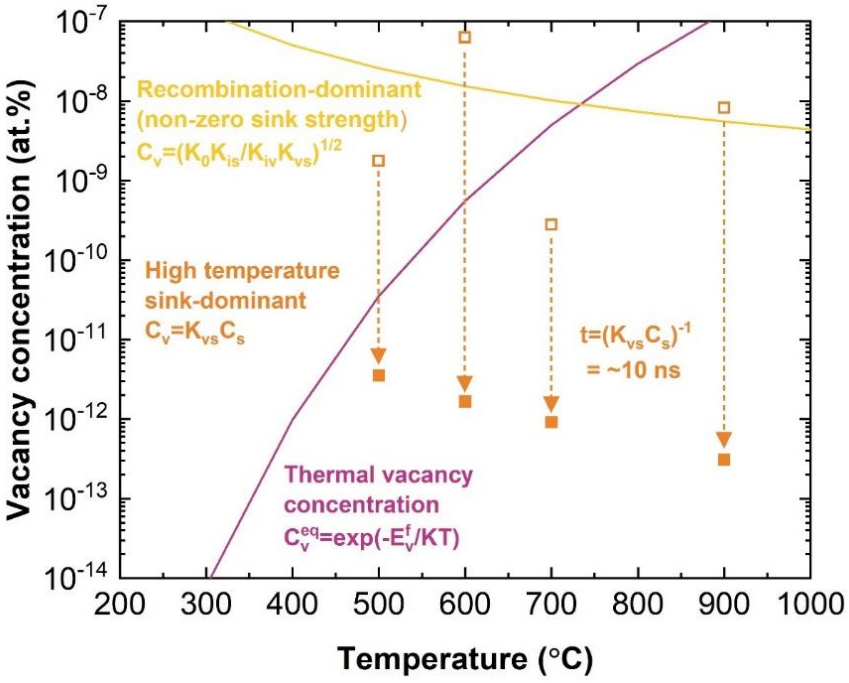

Fig. D.8. Steady-state and thermal vacancy concentration as a function of temperature in Fe. The open and closed symbols considered the initial sink strength and the sink strength after irradiation, respectively.

Table D.3. Initial sink strengths for different microstructural features.

	Fe-9Cr	Fe-10Cr	CNA3	14YWT
Grain size (μm)	~0.6	~82	~1	~0.3
Primitive dislocation density (m^{-2})	~1×10^{12}	~1×10^{12}	~3×10^{14}	~2×10^{14}
Fine particle density (m^{-3})	No particles	No particles	~7×10^{21}	~8×10^{23}
Fine particle size (nm)	No particles	No particles	~8	~4
Total sink strength (m^{-2})	~1×10^{14}	~1×10^{12}	~2×10^{15}	~3×10^{16}

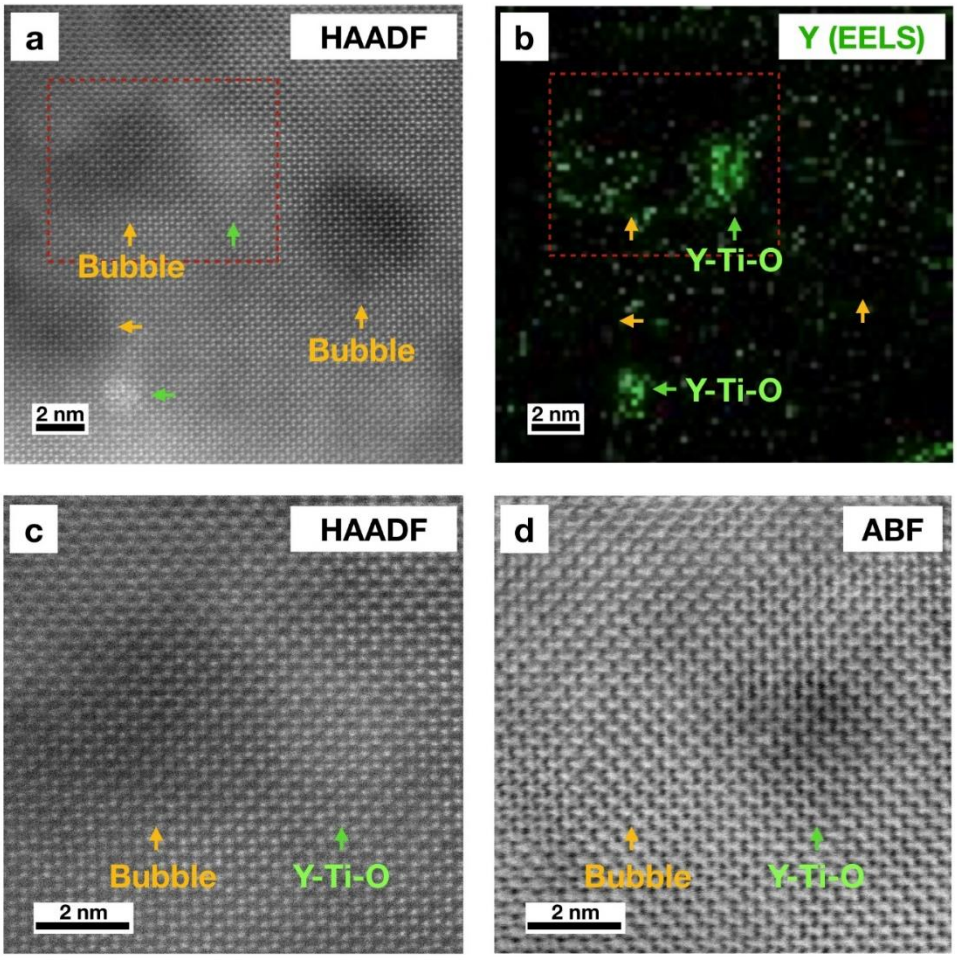

Fig. D.9. (a) STEM-HAADF image of bubble and Y-Ti-O particles in 14YWT and (b) corresponding EELS elemental mappings of Yttrium. Enlarged (c) HAADF and (d) ABF images of the boxed area in Fig. a.

Vita

Yan-Ru Lin was born in Taichung, Taiwan, where he finished his primary and secondary education. Yan-Ru earned his Bachelor's degree in the Department of Engineering and System Science (major in Material Science and Nuclear Engineering) from National Tsing-Hua University (NTHU), Taiwan, in 2012. After being awarded with a Bureau of Energy (Taiwan) and National Synchrotron Radiation Research Center (Taiwan) fellowship, Yan-Ru continued his education at NTHU through enrollment in the university's College of Sciences graduate program. Under the mentorship of Prof. Ji-Jung Kai, Yan-Ru researched the microstructural evolution and swelling of irradiated silicon carbide, and graduated with Master's degree in 2014. After that, Yan-Ru enrolled at the University of Tennessee, Knoxville, as a graduate research assistant in the Department of Materials Science and Engineering in 2017. Supervised by Prof. Steven Zinkle, Yan-Ru studied structural materials for nuclear applications. His dissertation research focuses on the formation of cavities in Fe and Fe-Cr alloys. The research leading up to this thesis has resulted in 24 publications, including 6 peer-reviewed journals in Acta Materialia, Journal of Nuclear Materials, and Nuclear Instruments and Methods in Physics Research, etc.